THE NEAR WAKE OF A TWO-DIMENSIONAL HYPERSONIC BLUNT BODY WITH MASS ADDITION

Thesis by

Donald James Collins

In Partial Fulfillment of the Requirements

For the Degree of

Doctor of Philosophy

California Institute of Technology

Pasadena, California

1969

Submitted December, 1968

ACKNOWLEDGMENTS

The author wishes to express his most sincere appreciation and thanks to Professors Anatol Roshko and Lester Lees for their joint cooperation, guidance and support throughout this research, and to Professor Toshi Kubota for his continuing interest and invaluable advice.

My grateful appreciate is extended to Mrs. T. Van Harreveld for her conscientious efforts in the reduction of the data; to the staff of the GALCIT Hypersonic Wind Tunnel, P. Baloga, G. Van Halewyn, S. Roman, J. Van Dijk and H. Mazurowski for their cooperative assistance during the wind tunnel tests; to the staff of the Aeronautics Shop under G. Carlson for the construction of the models and equipment; and to Mrs. V. Conner for her expert typing of this thesis.

I wish to acknowledge the receipt of financial support from the National Science Foundation (1963-1966), the Rand Corporation (1966-1967), and from the California Institute of Technology (1967-1968). The work discussed in this thesis was carried out under the sponsorship and with the financial support of the U. S. Army Research Office and the Advanced Research Projects Agency, Contract No. DA-31-124-ARO(D)-33.

My deepest gratitude belongs to my wife, Judy, for her sacrifices and encouragement, which have made this work possible, and to my sons, Scott and Bruce, who will gain a father with the completion of this work.

ABSTRACT

An experimental investigation of the steady, laminar near-wake flow field of a two-dimensional, adiabatic, circular cylinder with surface mass transfer has been made at a free-stream Mach number of 6.0, and free-stream Reynolds numbers $Re_{\infty, d} = 0.9$ and 3.0×10^4.

A flush-mounted porous section was used to transfer argon, nitrogen or helium into the near wake of the circular cylinder to determine the flow field associated with the addition of a passive scalar. Two cases were studied: mass transfer from the forward stagnation region, and mass transfer from the base. The pressure field was mapped by standard Pitot- and static-pressure measurements. The mass-concentration field was monitored by a continuous sampling mass-spectrometer system which utilized the output of a single mass peak to determine the relative mass-concentration levels.

For mass addition from the base, a recirculating vortex remains in the near-wake flow and the characteristic near-wake pressure is the pressure at the stagnation point created by the interaction of the reversed flow with the injected fluid. This pressure, and the entire near-wake flow field, correlates with the ratio of the momentum flux of the injected fluid to the momentum flux in the cylinder boundary layer upstream of separation, and not the mass flow of the injected fluid as predicted by Chapman.

For mass addition from the base, the axial mass concentration decays rapidly away from the base as a consequence of the counter-current diffusion of mass into the oncoming recirculating flow. In

addition, strong transverse mass-concentration gradients exist in the region between the two stagnation points and a local maximum occurs in the vicinity of the $u = 0$ locus for those cases in which $ReSc > 0(1)$ for the reversed flow.

With moderate mass addition from the forward stagnation region, the near-wake pressure field is unperturbed. In addition, because there is no source in the base region, the near-wake mass-concentration field is nearly uniform in the region of reversed flow. Bounding the uniform region, in the vicinity of the viscous shear layers, narrow diffusion layers govern the transport of mass into the outer flow.

In the intermediate-wake region, immediately downstream of the neck, the mass-concentration fields for both forward and base injection are explained by a single model which incorporates the influence both of the accelerating axial velocity and of an assumed Gaussian distribution for the mass-concentration of argon. This model predicts the axial decay of mass concentration in the intermediate wake, and establishes the location of the virtual origin of the asymptotic far wake in terms of the mass-concentration profile parameters at the neck.

TABLE OF CONTENTS

TABLE OF CONTENTS (Cont'd)

LIST OF TABLES

LIST OF FIGURES

LIST OF FIGURES (Cont'd)

LIST OF FIGURES (Cont'd)

LIST OF SYMBOLS

a	sound speed; axial velocity profile constant
A, B, C, D	constants
A_e	effective probe cross-sectional area
A_p	probe cross-sectional area
$\mathcal{AR}$	ℓ/d - aspect ratio
b	$\dfrac{\int_0^\infty F(\eta_c)\,d\eta_c}{\int_0^\infty F(\eta_c)F^*(\eta_u)d\eta_c} - 1$ - mass-concentration profile constant
C_∞	$\dfrac{\mu}{\mu_\infty}\dfrac{T_\infty}{T}$ - Chapman-Rubesin factor
C, C_i	ρ_i/ρ - mass concentration
C_p	specific heat at constant pressure
d	cylinder diameter
D	binary diffusion coefficient
$E(\tilde{X})$	$\exp\int_0^{\tilde{X}} \tilde{U}(\xi)d\xi$
$F(\eta_c)$	self-similar mass-concentration profile function
$F^*(\eta_u)$	self-similar velocity profile function
$G(M_\infty)$	$\dfrac{P_o}{P_\infty}\dfrac{1}{M_\infty}\left[\dfrac{T_\infty}{T_o}\right]^{\frac{1}{2}} = \dfrac{1}{M_\infty}\left[1+\dfrac{\gamma-1}{2}M_\infty^2\right]^{\frac{\gamma+1}{2(\gamma-1)}}$
H	C_pT_o - total enthalpy; $\dfrac{\dot{m}_i}{\dot{m}_f}G(M_\infty)$ - Korst injection parameter
H^*	$H\left[\dfrac{\mathcal{M}_{Air}}{\mathcal{M}_i}\right]^{\frac{1}{2}}$ - modified Korst parameter
$\mathcal{H}$	θ_i/δ_i^* - incompressible boundary-layer form parameter
h_p	characteristic probe dimension

LIST OF SYMBOLS (Cont'd)

I	$\frac{\dot{m}_i}{2\dot{m}_{B.L.}}\left[\frac{\mathcal{M}_{Air}}{\mathcal{M}_i}\right]^{\frac{1}{2}}$ - mass transfer parameter
k	thermal conductivity
ℓ	model span between fences
l	length
l_s	length scale of separation interaction
m/e	mass/charge ratio for an ionized species
$\dot{m}_{B.L.}$	$\left[\int_0^{\delta} \rho u\, dy\right]_s = \rho_e u_e(\delta - \delta^*)$ - mass flux per unit span in cylinder boundary layer upstream of separation
$\dot{m}_f$	$\rho_\infty u_\infty d$ - intercepted free-stream mass flux per unit span
$\dot{m}_i$	mass flux per unit span of injectant
$\dot{M}$	$\frac{\dot{m}_i}{2\dot{m}_{B.L.}}$ - mass transfer parameter
M	Mach number
$\mathcal{M}$	molecular weight
P	pressure
P_b	base pressure
$P_{b,\infty}$	base pressure with the probe at infinity.
$P_b(0)$	base pressure with zero mass transfer
P_{o_2}	Pitot pressure, impact pressure
P_{t_2}	stagnation pressure behind normal shock at M_∞
Pr	$\frac{\mu C_p}{k}$ - Prandtl number
r	cylinder radius

LIST OF SYMBOLS (Cont'd)

R	$\frac{\mathbb{R}}{\mathcal{M}}$ - gas constant	
$\mathbb{R}$	universal gas constant	
Re	$\frac{ul}{\nu}$	Reynolds numbers
$Re_{\infty, d}$	$\frac{u_\infty d}{\nu_\infty}$	
$Re_{\infty, x}$	$\frac{u_\infty x}{\nu_\infty}$	
$Re_{N, d}$	$\frac{u_N d}{\nu_N}$	
Re_x	$\frac{u_e x}{\nu_e}$	
$Re_{o, d}$	$\frac{\rho_\infty u_\infty d}{\mu_o} = \frac{\mu_\infty}{\mu_o} Re_{\infty, d}$	
Re_p	$\frac{u}{\nu} h_p$	
s	curvilinear coordinate tangential to cylinder surface	
S	$\frac{H-H_e}{H_e}$ - total enthalpy defect parameter	
Sc	$\frac{\nu}{D}$ - Schmidt number	
T	temperature	
u, v	physical velocity components	
u*	$\frac{u_{\psi=0}}{u_e}$ - dividing streamline velocity ratio	
U	u/u_e - transformed velocity	
$\tilde{U}(\tilde{X})$	$\frac{u(\tilde{X})}{u_{max}} \cdot \frac{\lvert u_{max} \rvert (x_r - x_b)}{D} = Re(\tilde{X})Sc$	
V	volume flow rate (cc/sec)	

LIST OF SYMBOLS (Cont'd)

w	$1-U$ - transformed velocity defect
$W_{\frac{I}{2}}$	physical mass-concentration profile half-width
x, y, z	physical coordinates
$\tilde{X}$	$\frac{x-x_b}{x_r-x_b}$ - transformed physical x
X	$\int_0^{x/d} \frac{\rho_e u_e \mu_e}{\rho_\infty u_\infty \mu_\infty} d(x/d)$ - modified Howarth coordinate
x_r	location of reattachment
X_i	$\frac{P_i}{P}$ - mole fraction of injectant
$\tilde{Y}$	$\frac{y}{x_r-x_b}$ - transformed physical y
$\overline{Y}$	$\int_0^{y} \frac{\rho a_e}{\rho_N a_N} dy$ - Stewartson transformed y
Y	$[C_\infty \, Re_{\infty, d}]^{\frac{1}{2}} \int_0^{y/d} \frac{\rho_e u_e}{\rho_\infty u_\infty} \frac{\rho}{\rho_e} d(y/d)$ - modified Howarth coordinate
$(y/d)_e$	edge location
$\overline{(y/d)}_s$	mean shock location, profile average
α	$\left[1 - \frac{4\Delta}{\tilde{U}^2}\right]^{\frac{1}{2}}$
β^*	$\frac{8}{Sc\, \sigma_N^2} [b+U_N]^2$
γ	$\frac{C_p}{C_v}$ - specific heat ratio
δ	boundary-layer thickness; shock wave angle
$\Delta(\tilde{X})$	$\frac{F(0)''}{\sigma(\tilde{X})^2}$ - self-similar profile curvature at $\eta = 0$
δ_b	base boundary-layer thickness

LIST OF SYMBOLS (Cont'd)

δ^*	$\int_o^\delta \left(1 - \frac{\rho u}{\rho_c u_c}\right) dy$	boundary-layer displacement thickness
δ_{max}	shock wave detachment angle	
δ_i	Stewartson transformed boundary-layer thickness	
δ_i^*	$\int_o^{\delta_i} (1 - U)\, dY$	Stewartson transformed boundary-layer displacement thickness
δ_r^*	$Re_{N,r} \left[\frac{\delta_i^*}{r}\right]^2$	
ζ	$\frac{\psi}{\sqrt{u_e \nu_e x C_\infty}}$	dimensionless stream function
ζ_o	Chapman mass entrainment rate	
η	$\tilde{Y}/\sigma(\tilde{X})$, $Y/\sigma(X)$	profile similarity variable
θ_i	$\int_o^{\delta_i} U(1-U)dy$	Stewartson transformed momentum thickness
θ	momentum thickness; angle from forward stagnation point	
κ	ratio of the spectrometer output voltage for a mixture to that for the pure species	
λ_e	$\frac{\rho_{-\infty} v_{-\infty}}{\rho_e u_e}$	mass entrainment parameter
μ	dynamic viscosity coefficient	
ν	μ/ρ	kinematic viscosity coefficient
ξ	$X - X_N$	transformed Howarth coordinate
ξ_o	virtual origin for the asymptotic far wake	
Π	ratio of momentum flux of the injected fluid to that in the boundary layer upstream of separation	

LIST OF SYMBOLS (Cont'd)

ρ	density
$\sigma(\tilde{X}), \sigma(X)$	non-dimensional length scale for the self-similar profiles
$\bar{\chi}$	$\frac{M^3\sqrt{C_\infty}}{\sqrt{Re_{\infty, x}}}$ - hypersonic viscous-interaction parameter
ψ	stream function

Subscripts

aw	adiabatic wall
b	base stagnation point
c	pertaining to mass concentration
$\mathfrak{C}$	centerline
e	edge of viscous layer; external
i	injected fluid
meas	measured
max	maximum
N	neck
p	probe
r	reference state
s	boundary layer immediately upstream of separation
u	pertaining to transformed velocity U
w	wall
o	total or stagnation condition; origin
∞	undisturbed free-stream conditions
$-\infty$	far field in Chapman mixing layer solution

I. INTRODUCTION

In the past several years, considerable attention has been given to problems associated with separated flows. Initially, the interest was centered on the "base pressure problem;" however, more recently, both the level of understanding and the sophistication involved in these investigations has increased and the emphasis has shifted to a more detailed description of the physical processes occurring in these highly complex flows. With the advent of high performance re-entry vehicles, a primary emphasis has centered on the near- and far-wake flows as they relate to the wake discrimination problem. For wake discrimination, the production and quenching of observables in the wake are associated with the diffusion of scalar quantities, e.g., mass, temperature, within the near-wake flow, which generates the initial conditions for the development of the far-wake flow field.

The primary emphasis at GALCIT over the past few years has been on the fundamental physical processes associated with the wakes behind elementary hypersonic, two-dimensional bodies, in particular the structure of the flow over a circular cylinder (Figure (1)), first described theoretically by Reeves and Lees[1] and later in more detail by Grange, et. al.,[2] and by Klineberg.[3] These theoretical investigations are based on the use of moment methods, and employ the mixing theories outlined by Crocco and Lees[4] to describe the flow which originates at the forward stagnation point and proceeds downstream through the wake neck into the asymptotic far wake, discussed by Kubota,[5] and by Gold.[6] These theoretical models include the effects of heat transfer on the flow, but do not consider the effects of mass

addition.

Experimentally, the work of McCarthy,[7] Dewey[8] and Behrens[9] on the adiabatic cylinder without mass addition has provided detailed information on the near- and far-wake flow field behavior, and on the stability of these flows. Mohlenhoff,[10] and later Kingsland,[11] experimentally investigated the problem of mass diffusion in the far wake of a uniformly porous cylinder, using argon and helium tracers to determine the distribution of the injected species in the equilibrium far wake. In addition, Herzog[12] has investigated the near-wake flow field with mass addition at the base, using nitrogen as an injectant, for a range of mass transfer extending beyond the value required to eliminate the recirculating flow. Herzog's investigation demonstrated that for mass transfer equivalent to 1.5-2.0% of the free-stream frontal-area mass flux, the mass entrainment requirements of the shear layers are satisfied, and the recirculation zone vanishes. Elsewhere, the problem of mass transfer in separated flows has been investigated by Ginoux,[13] Chapkis, et. al.,[14] and others.

Several questions remain, however, and this thesis will address itself to two of the primary problems: (1) the behavior of the base pressure with mass addition, and (2) the question of the distribution in the near-wake flow of foreign species transferred to the flow from the body surface.

1. Base Pressure

Perhaps the oldest question, and that which has led to much of the current research in separated flows, is that of the base pressure, or characteristic near-wake pressure. A theoretical development by

Reeves and Lees[1] has established that, in the absence of mass addition, the base pressure for the circular cylinder is weakly dependent on Reynolds number through the viscous-inviscid interaction. The determination of the base pressure with mass addition becomes even more complex, however, and no satisfactory theory is currently available. It is obvious, a priori, that mass addition into the near wake, via the base stagnation region, will produce some perturbation of that basic flow field; however, it is not obvious what effects, if any, will be produced by mass addition from the forward stagnation region. It is anticipated that the effects of mass addition will be dependent on both Reynolds number and the molecular weight of the injectant.

For mass addition from the base, two fundamentally different mechanisms have been proposed to describe the influence of base mass addition on the base pressure. These will be briefly summarized:

a. Korst, et. al.[15] proposed that the base pressure is established by an expansion of the gas from the free-stream direction to a direction parallel to an assumed, straight $\psi = 0$ streamline which bounds the recirculating flow, and that the change in base pressure with mass addition can be calculated by considering the spread of the $\psi = 0$ streamline to accomodate the added mass.

b. The arguments advanced by Chapman,[16][17] for a fully-developed mixing-layer profile, establish the base pressure in terms of the velocity u^* on the stagnating streamline. When the mass entrainment in the shear layer is partially satisfied by mass addition, u^* is less than 0.587, the value for a fully-developed free shear layer, and as a result, the less energetic compression supports a smaller pressure

rise to reattachment, and the base pressure is increased. In the absence of definitive experiments, it has been generally believed that this criterion is correct when modified to include the influence of a finite initial boundary layer on the development of the non-similar mixing profile.

The arguments by Korst, et. al., and by Chapman, both conclude that the base pressure, and hence the near-wake structure, depend only on the properly normalized mass flux of the injected fluid. These arguments seem to be supported by the experiments of Ginoux[13] who examined the effects of mass addition on the separated flow over a rearward facing step and concluded that, for the case of small momentum in the injected fluid, the dominant parameter controlling the near-wake pressure field is the mass of the injected fluid.

The present experiments will examine the effects of mass addition on the laminar near-wake flow in order to determine the physical mechanism associated with the influence of mass addition on the base pressure and the near-wake pressure field, and the correlation, if any, of these effects with Reynolds number and molecular weight.

2. Distribution of the Injected Species

To the present time, no theoretical or experimental investigations have been performed to determine the distribution in the near-wake flow field of mass species transferred to the flow from the body.

In the present investigation, the distributions of the injected species were measured in the steady near-wake flow of an adiabatic circular cylinder at a free-stream Mach number of 6.0, and free-stream Reynolds numbers $Re_{\infty, d} = 0.9$ and 3.0×10^4, and the important

mechanisms that determine the distribution of passive scalars (i. e. mass) in the near wake are examined. In addition, to understand the behavior of the asymptotic far-wake distribution of the injected species, an intermediate-wake region, immediately downstream of the wake neck, is examined to determine the influence of the boundary conditions on the body on the development of the asymptotic far wake.

To investigate these points, a flush-mounted, spanwise-uniform porous section of 88.5° included angle was used to transfer argon, nitrogen or helium into the near-wake flow field at mass rates up to 30% of the mass flux in the cylinder boundary layer upstream of separation. Two cases were studied: mass transfer from the forward stagnation region, and mass transfer from the base. The pressure field was mapped by standard Pitot- and static-pressure measurements outlined in Chapter II. The mass-concentration field was monitored by a continuous sampling mass-spectrometer system which utilized the output of a single mass peak to determine the relative mass-concentration levels. This mass-spectrometer configuration has not been used previously, and was found to be more accurate than that used by Chow,[18] for example, for the determination of the diffusive separation in a free jet of nitrogen and oxygen.

The results for the influence of mass addition on the pressure field are given in Chapter III and the results of measurements of the mass-concentration field are given in Chapter IV. In addition, an analogy between heat and mass transfer, and some aspects of the heat transfer models of Chapman[16] and of Scott and Eckert[19] are discussed in Chapter IV, and a complete analogy is outlined in Appendix A.

II. EXPERIMENTAL TECHNIQUE

II. 1. Flow Facilities

The experiments were performed in the M = 6 leg of the GALCIT hypersonic facility. This facility is a closed return, continuous flow tunnel with a 5 in. x 5 in. test section. The stagnation pressure is variable from 25 psia to 115 psia with an accuracy of ± .02 psia, and the stagnation temperature is maintained at 735°R, with an accuracy of ± 1°R, to avoid nitrogen condensation in the test section. The models were located 23 inches downstream of the throat on the horizontal centerplane of the tunnel, in the forward portion of the 10 inch long test rhombus. The tunnel empty distribution of free-stream Mach number and static pressure within the rhombus possess gradients, as given in the work by Batt[20] and Behrens,[9] which amount to at most 3% of the measured static pressure at the model station. Corrections for these gradients have been applied to the measured pressure data as discussed in the following sections.

II. 2. Models

The wind tunnel models used in this investigation (Figure (2)) consisted of 0.200 inch diameter stainless-steel tubes which spanned the 5 inch test section and were supported by dual O-ring seals in lucite or glass ports on either side wall, as shown in the figure. This configuration has been adapted from the design used by Herzog.[12] To relieve the interaction of the cylinder with the wind tunnel wall boundary layer, 20°, 5/8" long, wedges have been mounted on the cylinders in the vicinity of the wall, in the manner described

by Behrens.[9] Ramaswamy* has shown that the use of these wedges leaves the central portion of the near-wake pressure field unchanged (see Appendix B). To isolate the flow in the uniform core in the tunnel from the wall boundary-layer flow, triangular cross-flow fences were installed on the model with a spacing of 3 inches, as illustrated in the figure. The influence of these fences on the spanwise distribution of base pressure and mass concentration is discussed in Appendix B.

The angle of attack of the models was controlled using a flat portion machined on the model extremity to externally align the model with the free-stream flow direction. An angle of attack of $\pm 5^{\circ}$ gave no measurable change in the Pitot-pressure field for moderate mass transfer rates; however, an angle of attack renders the mass-concentration field, discussed in Chapter IV, asymmetric through the asymmetric boundary conditions. This asymmetry was manifested in the levels of the mass concentration occurring in the vicinity of the shear layers for either mode of mass addition, and was used to align the model with the flow direction.

A summary of the flow conditions used in the present investigation is given in Table 1. The free-stream Reynolds numbers used were $Re_{\infty, d} = 0.905 \times 10^4$, 2.95×10^4, for a nominal free-stream Mach number of 6.0. Other constants of the flow are given in the table.

---

* Ramaswamy, M. A. - Private Communication

Pressure Model

Model C-5 (Figure (2b)) has an internal O-ring designed to seal the Pitot probes shown in the figure to the model, which formed the pressure lead to a silicone-oil micromanometer for the measurement of the reversed flow Pitot pressure. The Pitot probes listed in the table in Figure (2b) have a shank 0.032" O.D. and a probe body 0.012" O.D. x 0.006" I.D., with a chamfered tip. As a consequence of these dimensions and the low base pressures, the response times for the reversed flow measurements were of the order of minutes. The Pitot-pressure distribution on the axis was measured by interrupting the flow and interchanging the family of probes. The model was subsequently realigned using a Gaertner* cathetometer, which allows an alignment of the probe tip of within ± .002" of the flow axis. Measurement of the off-axis distribution was attempted by rotating the model through an angle of attack; however, probe interference and angle of attack effects cause difficulties in the interpretation of the data, and it will not be shown here.

The centerline static pressure was measured using the insert static-pressure probes shown in Figure (2b), for the reversed flow measurements on Model C-5. The interchangeable probe tips used two 0.0135"D orifices, spaced at 180°, with their axis aligned parallel to the model span, to measure the axial distribution of static pressure for $0.5 \leq x/d \leq 2.75$, using the tunnel horizontal actuator. The static pressure was conducted by a lead through the tunnel side wall to a silicone-oil micromanometer.

* Gaertner Scientific Corp., Chicago, Ill.

Mass-Transfer Model

For the mass-transfer model (see Figure (2a)), a machineable porous ceramic insert of Al Si Mag-222* was bonded into an opening in the stainless-steel cylinder using Eccobond-26† epoxy. The individual ceramic inserts were carefully selected for uniformity before machining to 3" x 0.140" sections and bonding into the model shell. Pressure taps were not included in the model because of the possibility of interference with the flow through the ceramic material.

In the GALCIT M = 6 facility, oil vapor present in the free stream accumulated on the model surface and contaminated the ceramic material, altering the distribution of the injected gas. To alleviate this problem, Xylene was periodically injected through the porous ceramic to remove the accumulated oil. The model cleaning procedure and the use of Eccobond-26 epoxy were chosen specifically because of the degradation of other epoxy resins by the use of Xylene. With periodic removal of the oil, repeatable data were obtained for the mass-concentration field.

In order to understand the exit condition of the gas from the model, a brief description of the flow through the ceramic material is necessary. The mass flux per unit area through the material is given by D'Arcy's Law,

$$\dot{m}_i = \frac{K}{2\mu t R T}(P_o^2 - P_e^2),$$

where K is the porosity and t is the thickness of a plane slab. Then, for $P_o^2 >> P_e^2$, the material is choked and the mass flux per unit area is independent of external pressure. Hence, the spanwise plenum-

* American Lava Corp., City of Industry, Calif.

† Emerson and Cuming, Inc., Canton, Mass.

pressure distribution is expected to be uniform.

The spanwise distributions of the plenum pressure and temperature were measured by inserting small diameter pressure and thermocouple probes into the model plenum in such a way that the gas flow was essentially undisturbed. The model plenum pressure, found to be spanwise uniform within less than $\pm 0.5\%$, is shown in Figure (3) as a function of volume flow rate at 30" Hg. and 30°C for the two models, C-1 and C-4. These models differ only in the nature of the ceramic material, the porosity being different by a factor of nearly 7 between the two. Figure (3) shows that the flow through the ceramic material is choked for both argon and helium, i.e., the mass flux is independent of the external pressure. Figure (18) demonstrates that the porosity has no effect on the external flow field associated with mass addition.

Measurements of the model plenum temperature, given in Figure (4) as a function of spanwise position, with mass transfer rate as a parameter, show that the gas temperature in the plenum is very nearly the adiabatic-wall temperature of the model. The primary influence on the temperature distribution is conduction toward the side walls by the model. From a simple calculation of the heat transferred to the gas during its expansion through the ceramic material, it is concluded that the flow through the ceramic approaches an isothermal, choked flow, and as a consequence, the exit Mach number $M_i \rightarrow \frac{1}{\sqrt{\gamma_i}}$. The infinite heat transfer rates required in the limit invalidate an equality; however, this approximation is expected to closely represent the flow from the model, and will be used in Section III. 2.

Mass transfer from the model occurs through a random, closely-spaced distribution of low Reynolds number jets which interact and decay by viscous dissipation. The Mach-number distribution in this flow is shown in Figure (19). Because of the random jets, attempts to measure the spanwise uniformity of the model by using a hot wire give a highly non-uniform profile; whereas, measurements of the spanwise pressure and mass-concentration fields using sampling probes yield a very uniform profile because of the integrating effect of the probe. The spanwise pressure and mass-concentration measurements shown in Figures (5) and (6) demonstrate the spanwise model uniformity. A further description of the uniformity of the flow field is given in Appendix B.

Gas Handling Apparatus

Figure (7) is a sketch of the apparatus constructed to monitor the transfer of gas to the model. The flow rate of the filtered, pure gas was regulated with a Brooks* model 1355 flow meter at a constant pressure of 30" Hg. and 30° C. Figure (7) shows the Xylene injection system and a system for mixing calibration samples of liquid-nitrogen trapped air and the test gas by partial pressure. These samples are stored in the volume illustrated in Figure (7) for calibration of the instrumentation. A further description of this process is given in Section II. 4.

II. 3. Pressure Measurement

Probes and Equipment

The pressure field was measured using a 0-5 psia Statham†

* Brooks Instrument Co., Hatfield Pennsylvania
† Statham Instrument Co., Los Angeles, California

pressure transducer, shown in Figure (7), and a vacuum reference silicone-oil micromanometer. Both instruments had a reference pressure less than 0.5 μ, and for each the measurement errors are less than 1%.

All measurements in the vertical centerplane of the tunnel were performed using the existing tunnel actuator system, which is repeatable within ± 0.001" in both the x and y directions. Measurements made in the spanwise direction, and at spanwise stations away from the vertical centerplane of the tunnel, used the spanwise tranverse mechanism shown in Figure (8). This device mounts in an aft wind tunnel access port and possesses freedom of motion along the three coordinate axes, two of which are externally controllable. The gear driven lead screw sets the y position to ± .002", using the micrometer head for calibration. The spanwise (z) position is given to ± .010" by a manual drive and a counter, while the x position is provided only by set screw adjustments using feeler gauges, within the tunnel, with an accuracy of ± .003". The probes are mounted in a dual O-ring seal, shown in detail in Figure (8), and are secured by two set screws to the drive arm which serves as a pressure lead to the monitoring system.

The static-pressure and Pitot-sampling probes used in this investigation are illustrated in Figure (9). The family of Pitot-sampling probes shown in the figure were constructed to investigate the effects of probe Reynolds number on the sampling problem, discussed in Section II. 4, and to provide an adequate sample with a

minimum probe dimension and minimum response time for each value of $Re_{\infty,d}$. For $Re_{\infty,d} = 3 \times 10^4$, the 0.005" probe was required for mass sampling, whereas for $Re_{\infty,d} = 0.9 \times 10^4$, the 0.009" probe was necessary to obtain an adequate sample in the vicinity of the base.

Three separate static-pressure probes were used in this investigation. First, the probes described in Section II.2 allowed measurement of the axial static pressure for model C-5, without mass addition. Second, the far-wake axial static pressure, downstream of the neck, was measured with the cone-tipped static-pressure probe illustrated in Figure (9), and used by Behrens[9]. The third static-pressure probe used interchangeable tip sleeves (see Figure (9)) to measure the axial static-pressure distribution near the base with mass addition. The axial position was varied by interrupting the flow and changing the tip sleeve, which was positioned against the base to provide a continuous probe diameter from the orifice to the model base. The axial static pressure from this probe agrees within 1% with the pressure measured by the cone-tipped probe for $2.5 \leq x/d \leq 3.0$, the vicinity of the neck.

Both the static and Pitot-sampling probes exit from the tunnel through a bellows seal on the tunnel side wall aft of the model station, where a teflon Swagelok fitting allows a sliding seal for the pressure lead, and are connected directly to either the micromanometer or the sampling inlet system shown in Figure (7).

Data Reduction

To estimate the influence of the presence of a probe on the

measured pressure field, the base pressure on model C-5 was measured as a function of the distance of the tip of the insert static-pressure probe from the model base. The results are shown in Figure (10), with $Re_{\infty, d}$ as a parameter, where $P_{b, \infty}$ is the undistrubed base pressure. The corrections implied by these measurements were used in computing the axial Mach-number distribution given in Figure (19). No other corrections for probe influence were used.

Using the 0.005" probe to measure the Pitot-pressure profiles, no correction for finite probe size is required, except in the definition of the shock wave locations. The measured Pitot-pressure distribution through a thin, steady, oblique shock wave exhibits a thickness greater than the probe dimension because of the interaction of the oblique wave with the subsonic region behind the bow shock on the probe. In addition, from hot-wire measurements by Behrens,* the shock system associated with the separated flow has a non-steady behavior, which further broadens its Pitot-pressure profile. Therefore, the shock wave location is assumed to be given by the location of the mean of the intersections of the maximum slope with the maximum and the minimum of the measured Pitot-pressure profile through the shock wave. Because the distribution is not symmetric, this value does not correspond to the midpoint in the pressure rise through the shock, but correlates well with the location of the peak in the hot-wire fluctuation traces (cf. Behrens*).

As a consequence of the low Reynolds numbers in the near-wake flow field, viscous corrections are required for both the Pitot- and the static-pressure data. The viscous corrections to the Pitot-

* Behrens, W. Private Communication.

pressure data are taken from the work of Sherman[21], and result in a maximum correction of $\approx 3.5\%$ for the larger value of $Re_{\infty, d}$, whereas, for the lower value of $Re_{\infty, d}$, the maximum correction is $\approx 18\%$ of the measured Pitot pressure. This correction is only applicable in the region of forward-facing flow, and rapidly decreases to zero away from the plane of symmetry in the near-wake region.

Corrections to the axial static pressure account both for the tunnel-empty gradients, by normalization with the local tunnel-empty static pressure, and for viscous interaction effects on the probe in the same manner as described by Behrens.[9],[22] Behrens has shown that,

$$\frac{P_{meas}}{P} = 1 + A\bar{\chi} + B\bar{\chi}^2$$

where $\bar{\chi} = \dfrac{M^3 \sqrt{C_\infty}}{\sqrt{Re_{\infty, x}}}$, and the constants A, B are given in Ref. (22). The cumulative effects of both corrections amount to at most 2% of the axial static pressure.

In addition to the above corrections, the influence of angle of attack on the measurement of Pitot pressure must be considered. The results of Dewey[8] indicate that for angles of attack less than 12°, no measurable influence is found on the Pitot pressure. Since the maximum flow inclination in the near wake is $\approx 14°$, no attempt was made to correct for this effect in the measured Pitot-pressure profiles.

The location of the u = 0 locus, shown in Figure (32), was found by a comparison of the corrected Pitot- and static-pressure profiles. The corrected static pressure is assumed to be constant and

equal to its value on the centerline of the reversed flow. This pressure is equated to the Pitot pressure, and the location of the u = 0 locus is determined from the transverse Pitot-pressure profiles. The same technique is used in defining the rear stagnation point, as shown in Figure (25).

Where required, half profiles are formed by averaging the measured pressure from opposite sides of the wake at a fixed y/d. This technique assumes that any differences arise from the flow and from measurement errors, not from errors in probe position.

The overall accuracy of the pressure measurements is ± 1% for the region of forward-facing flow. Within the reversed flow, the measurements of the centerline Mach-number distribution are within ± 3%. Measurements in the reversed flow using a standard Pitot-tube configuration must be carefully interpreted because they result in the measurement of a base flow on the probe. Consequently, no corrections have been placed on these measurements.

II. 4. Mass-Concentration Measurement

Sampling Process

In any investigation involving the removal of a sample from a flow, a primary difficulty arises in insuring that the sample collected for analysis is representative of the undisturbed flow. Chow,[18] Masson,[23] and later Reis and Fenn[24] have demonstrated that for the flow of a binary mixture of gases of disparate molecular weights, the presence of a sampling probe can cause barotropic species separation by virtue of the existence of a strong lateral pressure gradient

in the vicinity of the probe tip. Strong streamline curvature causes the heavier particles to diffuse across streamlines, creating a significant perturbation in the local mass-concentration field.

From the work of Masson, and that of Reis and Fenn, the magnitude of the species separation is a function of Mach number, Reynolds number, the disparity between the constituent molecular weights, and the mass-transfer boundary condition at the probe. Of these effects, the latter is the most important. Because Masson assumed the surface mass flux to be negligible, his work is not applicable in the present investigation, and hence no criterion exists with which to estimate the separation effects, a priori. These effects were investigated experimentally in the flow regime of interest.

The mass-sampling configuration, shown in Figure (7), uses the Pitot-sampling probe to measure either Pitot pressure or mass concentration, using the same apparatus. The gas sample to be analyzed is extracted by a 15 CFM mechanical pump, both to insure a short response time and to provide the desired mass flux through the probe. A small portion of the sample is liquid-nitrogen trapped and expanded into the mass-spectrometer inlet, as shown in the figure.

An important parameter in the mass-sampling problem is the ratio of the effective probe area to the actual probe area, A_e/A_p, i.e., the size of the sampled stream tube compared to the incident cross-section of the probe. This quantity is deduced from the equation

$$\frac{A_e}{A_p} = \frac{\dot{m}_{probe}}{\rho_\infty u_\infty} \quad ,$$

where $\dot{m}_{probe}$ is the mass flux per unit area through the sampling probe, calculated by measuring the inlet pressure to the mechanical pump with the Vacustat McLeod gauge, shown in Figure (7), and comparing the results to a calibration for known mass flow rates. To obtain the proper range of Mach number and Reynolds number, the flow was investigated on the axis downstream of the rear stagnation point. The results, plotted in Figure (11) against the local Pitot pressure, demonstrate that the probe tip is choked by viscous effects, and that the sampled stream-tube area is much less (0.2) than the incident probe cross-sectional area. Included in Figure (11) are the locations of the rear stagnation point in the flow ($A_e \rightarrow \infty$), the sonic point on the axis, and the location of the point of shock detachment ($\delta = \delta_{max}$) for the individual probes. These results are consistent with the results of Coles,[25] who found a reduction in the sampled stream-tube area with decreasing probe Reynolds number, for probe Reynolds numbers nearly two orders of magnitude greater than the present case.

To verify that the measured mass concentration is correct under these conditions, two experiments were performed. A blow-down jet facility was constructed to give Mach and Reynolds numbers in the desired range, using a known binary mixture as a working fluid. No measurable barotropic species separation was found in this device for $M_\infty = 1.3, 2.6$ and for $25 \leq Re_p \leq 1000$, using a 0.5 mole fraction of argon in air.

In addition, measurements were performed on the axis of the near wake behind the cylinder, with mass addition from the base, and

at selected off-axis stations. For these measurements, the mass concentration at a point, for a constant set of flow conditions, was measured as a function of probe Reynolds number (by changing probe size), and the mass flux through the probe, for argon and helium addition. Neither an increase in probe Reynolds number by a factor of five, nor a change in probe mass flux by a factor of ten gave a measurable change in the mass concentration for either gas, or for different mass concentrations at a given point in the flow.

On the basis of these measurements, it is concluded that, by virtue of the low Mach numbers and the large probe mass flux, barotropic species separation does not occur for the present measurements and the sample obtained is representative of the undisturbed flow field.

Mass-Analysis System

The heart of the mass-analysis system, shown in Figure (12), is the Varian Partial Pressure Gauge,* a small magnetic mass spectrometer utilizing a modified Bayard-Alpert source with a thoriated-iridium filament. This design allows the measurement of the system total pressure with the standard Bayard-Alpert technique, and the mass spectrum for $2 \leq m/e \leq 70$, with the same device. The thoriated-iridium filament reduces the presence of CO, formed when tungsten filaments are used in the presence of hydrocarbons and oxygen, and prolongs the filament life. The spectrometer is maintained by a liquid-nitrogen-trapped oil diffusion pump using Convalex-10† fluid to reduce back streaming and keep the entire system free of silicones,

* Varian Associates, Palo Alto, Calif.

† Consolidated Vacuum Corp., Rochester, N. Y.

which have a detrimental effect on the spectrometer. The LN_2 trap is an internally silvered concentric sphere type with an internal volume of 1 liter and a total life time of > 44 hours under vacuum. During operation of the spectrometer, the system pressure is monitored by a CVC* discharge gauge. The spectrometer operating pressure is $\approx 2 \times 10^{-8}$ torr; the background pressure is $\approx 2 \times 10^{-8}$ torr, and is principally water vapor, as is the case for all such vacuum systems.

In principle, the output from a mass spectrometer is proportional to the product of the collision cross-section for ionization at the given m/e, and the number density of the species. For the Varian spectrometer this is in fact not the case, as a non-linearity is introduced by the existence of pressure dependent space charge effects within the source. This effect appears to be reproducible and has been included in the calibration procedure. Because of the dependence of the output on number density, the mode of operation selected establishes a known spectrometer pressure and monitors the output as a function of mass concentration, or mole fraction, by means of a calibration technique.

To provide the known pressure in the spectrometer, the gas sample from the inlet is throttled by the inlet valves to a constant pressure (25μ), monitored on a Pirani* gauge, and maintained by the mechanical pump shown in Figure (12). Back streaming of oil from the mechanical pump is eliminated by a second LN_2 trap. A portion of this sample is expanded from the constant pressure region into the

---

* Consolidated Vacuum Corp., Rochester, N. Y.

spectrometer inlet section through a fixed geometry capillary. Because the pumping system is stable, the maintenance of a constant Pirani gauge pressure provides a stable, known reference pressure. The Pirani gauge is a temperature compensated thermal-conductivity device, and hence the measured gauge pressure is a function of mass concentration. However, this effect can be included in the calibration, along with any differential pumping caused by the influence of molecular weight.

The system as illustrated in Figure (12) suffers from a coupling between the inlet system and the spectrometer through the diffusion pump. This coupling occurs only for the case of helium mixtures as a result of the high diffusion coefficient for helium and the consequent backstreaming of helium through the diffusion pump. For the measurement of helium, the m/e = 4 peak is unsteady, as a result of this backstreaming, and consequently the m/e = 32 peak, characteristic of the primary stream, was used for the measurements of helium concentration. This technique has the disadvantage of a decreased accuracy at the lower values of mass concentration, but is otherwise acceptable. The coupling can be remedied by the installation of a second mechanical pump in the inlet system, uncoupling the inlet and spectrometer systems, except through the capillary.

Calibration and Data Acquisition

The spectrometer system described above is calibrated by introducing, through the inlet system shown in Figure (7), known sample mixtures, prepared by partial pressure. To calibrate the instrument, a single peak is chosen for the mixture, i.e., m/e = 40

for argon-air, m/e = 32 for helium-air, m/e = 28 for nitrogen-air and the output of the spectrometer is recorded under the inlet conditions $P_{Pirani} = 25\mu$, normalized with the spectrometer output for the pure gas under the same inlet conditions. The normalization removes any dependence of the absolute output on system pressure, long time drift, and other random effects. The calibration process relies on the fixed cracking pattern for any molecule at a given ionization beam energy, and the short term stability of the overall electronics and pumping systems. The dependence of the inlet pressure on the mass composition of the sample is included in the calibration procedure.

To facilitate the data handling, the electronic control for the Varian spectrometer was modified in the manner illustrated in Figure (13). The figure shows the entire electronics system used to measure mass concentration, including the spectrometer modifications required to display the m/e output on a digital voltmeter and the modification to allow remote operation of the mass-scan circuitry. The remaining circuitry provides the inversion and bucking of the output signal to allow amplification of the signal for small mass concentration.

The results of the calibration are shown in Figures (14), where both the mole fraction, X_i, and the mass fraction, C_i, are plotted as a function of K, the normalized spectrometer output. The repeatability of the calibration is largely dependent on the accuracy with which the calibration sample is mixed. Each data point in Figure (14) represents the mean of 10-20 measurements taken from a given gas sample. The scatter between points for a given sample is uniformly less than 1% for all but the lowest mass concentrations, and everywhere

less than 1.5%. The scatter between samples accounts for the scatter shown in the curves. For argon, the maximum scatter is ~ 1.5%; for nitrogen, < 1%; for helium ~ 1.5%. However, the error in the measured mass concentration differs from the experimental scatter in the calibration curves. For argon, because the primary peak m/e = 40 is used, the error in the measurements is at most 1.5% of the measured value over the entire range of mass concentrations. This is a consequence of the fact that the background gas contains only a trace (< 1%) of argon. For a 1% error in the measurement of nitrogen, the percent error in the mass concentration of the injected species becomes unbounded as the injected species approaches zero concentration because the background gas (air) contains ~ 80% nitrogen. For measurement of transverse profiles, this effect is offset by the fact that the mass concentration of the injected species decays to zero at the outer edge of the profile, allowing the establishment of a distinct zero level, and thus a greater accuracy in the description of the mass-concentration field.

The primary sources of error in the measurement of mass concentrations result from the scatter in the data for the various calibration samples and in the inherent error in the manual control of the inlet pressure to 25μ, using the Pirani gauge. This pressure can be repeated to within ± 0.25μ, or within ±1% in the spectrometer output. In addition, electronic drift and fluctuations in system pressure account for some measurement errors. By scanning the desired mass peak, the error associated with the shift in the mass peak with pressure is avoided. If the peak is not scanned, this error can be serious

for the Varian instrument, as the mass peak acceleration voltage is a function of pressure.

Errors in the measured mass-concentration field, resulting from the flow system itself, must also be considered. The flow-meter system is rated at ± 3% accuracy; however, careful handling allows a repeatability of the injection rate to ≈ 1%, for the injection rates used. Because the hypersonic tunnel is a closed-return system, some concern for the stability of the background concentration is justified. Continual monitoring of the background concentration for argon shows that over an eight hour run, no measurable change in the background mass concentration of argon was found. This is a consequence of the low mass transfer rates compared to the very large mass flow in the tunnel (typically $\dot{m}_i \ell / \dot{m}_T \approx 8 \times 10^{-5}$), and the rather large exchange rate for the primary fluid as a consequence of the process of venting and the addition of makeup air to stabilize the total pressure in the tunnel.

The measurement of mass concentrations in the near wake, using the experimental systems shown in Figures (7) and (12), follows the reverse of the calibration procedure. The system response time is determined by the purging time for the system, and the time required to restabilize the constant pressure system for a change in the input pressure to the mass-sampling probe. For the near-wake field, where the gradients in Pitot pressure and mass concentration are large, the response times are of the order of 30-45 seconds per data point.

For the near-wake mass-concentration field, each mass-concentration profile is individually normalized using the pure gas, and the zero level of mass concentration is verified at the extremities of each profile by sampling the free-stream component. The data are transformed to mass concentrations using the calibration curves shown in Figures (14) and are reduced to mean profiles, where applicable, by averaging the value of C_i from opposite sides of the wake at constant values of y/d.

III. THE STRUCTURE OF THE FLOW FIELD WITH MASS ADDITION

The purpose of the present experiments is to determine the interrelationship between the basic transport mechanisms of convection and diffusion for a scalar quantity, i. e. mass, within the framework of the near-wake flow field of the circular cylinder at hypersonic speeds, illustrated in the Schlieren photograph and sketch in Figure (1). The Pitot-pressure profiles, overlaid on the basic flow-field structure in Figure (15), serve to illustrate the more salient features of the undisturbed near-wake flow field.

It is obvious, a priori, that mass addition into the near wake, via the base stagnation region, will produce some perturbation of that basic flow field, and thus influence the convection and diffusion mechanisms. However, it is not obvious what effects, if any, will be produced by mass addition from the forward stagnation region because the near-wake boundary conditions are entirely different for this case. The present discussion will investigate the nature of the change in the near-wake pressure field caused by mass addition, and will evaluate its effect on the measured mass-concentration field to be discussed in Chapter IV.

III. 1. Mass Addition From the Forward Stagnation Region

Measurements of the near-wake pressure field for mass addition from the forward stagnation region demonstrate that the Pitot-pressure distributions (Figures (16), (17)) and the base pressure (Figure (18)) are completely independent of mass addition, i. e., that no discernible perturbations of the flow field exist although the mass

addition rates are large compared to the local boundary-layer mass flux in the vicinity of the stagnation point.

Measurements in the outer, inviscid, rotational flow generated by the curved bow shock wave show that, for the range of the mass transfer parameter $\dot{M} = \frac{\dot{m}_i}{2\dot{m}_{B.L.}}$ used in this investigation, the location of the bow shock wave is not measurably altered by mass addition as a result of the accomodation afforded by the existence of a large standoff distance for the bow shock wave (Figure (1)). Further, because of the existence of the strong favorable pressure gradient on the cylinder, disturbances of the boundary layer caused by injection in the stagnation region decay rapidly as the flow expands and do not change the boundary-layer profile near the separation point on the cylinder (cf. Figure (16)). Finally, the dynamics of the flow along the dividing streamline are not significantly altered by moderate mass addition rates because the near-wake mass concentrations are sufficiciently low that the density and specific heats ratio γ are essentially constant (Section IV. 2, Appendix D).

Large mass transfer rates were not studied in this investigation; however, it is certain that as the mass transfer rate is increased, the near-wake flow will be affected, both through perturbations on the boundary conditions on the body, and through the influence of finite mass concentrations on the recompression process by their effect both on density and on γ.

It is concluded, on the basis of these measurements, that the mass-concentration field corresponding to moderate rates of mass addition from the forward stagnation region is representative of the field

of a scalar quantity diffusing in the otherwise undisturbed near-wake flow, where the presence of the scalar introduces no perturbation into the fundamental flow field.

III. 2. Mass Addition from the Base - Base Pressure

The most important result of the present experiments is that neither the Korst nor the Chapman theory outlined in the Introduction gives a proper description of the behavior of the base pressure with base mass transfer. The present experiments show that, under the condition that a non-vanishing recirculating flow exists in the near wake, the base pressure, and the entire near-wake pressure field correlates with the momentum flux of the injected fluid. Figure (18) demonstrates that the base pressure, normalized by its undisturbed value, $P_b/P_b(0)$, depends only on the injection parameter

$$I = \frac{\dot{m}_i}{2\dot{m}_{B.L.}}\sqrt{\frac{m_{Air}}{m_i}}$$

This parameter is the momentum flux of the injected fluid, properly normalized to account for the influence of free-stream Reynolds number and the molecular weight of the injectant. Its origin and derivation will be discussed in the following paragraphs. The correlation, shown in Figure (18), holds within $\pm 2\%$ for $I \leq 16 \times 10^{-2}$ for argon, nitrogen and helium addition at both values of $Re_{\infty, d}$ and includes two different models, C-1 and C-4, which differ by a factor of nearly seven in porosity. The complete correlation of the near-wake pressure field with the parameter I will be demonstrated in Section III. 3.

Since the predictions given by the Chapman[16], [17] model are incorrect for this flow, it is necessary to construct a physical model

for the behavior of the base pressure with mass addition which includes the interaction of the injected gas with the near-wake flow field.

Base Pressure Model

The present experiments suggest a physical model for the base pressure which depends on the dynamics of the interaction of the injected gas with the recirculating near-wake flow field. This model possesses two aspects: (1) the interaction of the injected fluid with the reversed flow forms a stagnation point off of the body, and consequently (2) the injected fluid is turned away from the axis and is impressed on the free shear layer near its origin, inducing an increase in pressure. Both aspects are coupled and result in a momentum flux dependence for the base pressure. Each of these aspects will be examined separately below.

The first aspect of this model is the interaction between the injected fluid and the reversed flow. For moderate mass addition rates, a recirculating vortex remains in the near wake, and hence two stagnation points exist on the axial streamline: the rear stagnation point, and a stagnation point in the vicinity of the base. Figures (19), (20) demonstrate that the total pressure of the injected gas is comparable with the total pressure on the centerline of the recirculating vortex, and hence the base stagnation point is formed off the body by a balance between the total pressures of the two interacting streams. The generalization of the base pressure, or characteristic near-wake pressure, is the stagnation pressure of the highly dissipative reversed flow at the base stagnation point, as measured by the plateau in the axial Pitot-pressure profiles near the base (Figure (20)), and is therefore

determined by the momentum flux of the injected fluid.

The total pressure on the axial streamline decays monotonically from its value at the rear stagnation point to its value at the base stagnation point as a consequence of viscous dissipation (Figures (23), (25)). Therefore, as the momentum flux of the injected gas, and hence its total pressure, is increased, the base stagnation point moves toward the rear stagnation point into a region of increasing total pressure for the reversed flow. For this reason, the base pressure increases with increasing mass addition. When the total pressure of the injected fluid exceeds the maximum available total pressure in the reversed flow, the entrainment required by the shear layers is satisfied by the injected gas and the reversed flow vanishes. This case was examined by Herzog,[12] and will be discussed further in Chapter V.

The flow in the immediate vicinity of the base is a stagnation point boundary layer for which, for moderate mass addition rates, the stagnation point is estimated to lie in the region $0.05 \leq \frac{\delta_b}{d} \leq 0.10$, as indicated by the Pitot-pressure profiles in Figure (20). However, no exact measurements have been made of the location of this stagnation point for moderate mass transfer rates because of the difficulty of making static-pressure measurements very near the base. For large mass transfer rates, the data of Herzog[12] may be used to determine the motion of the base stagnation point.

From the above discussion it is concluded that the generalized base pressure increases with increasing mass addition, and that the entire near-wake pressure field is governed by the momentum flux of the injected gas. The proper scaling for this momentum flux is given

by the momentum flux of the reversed flow.

The second aspect of the model involves the interaction between the injected gas and the separating free shear layer. A physical model will be proposed for this interaction; however, its complete analytical formulation is, as yet, not evident.

The boundary layer on the cylinder proceeds smoothly to a subcritical non-similar, constant pressure free shear layer whose initial profiles are not strongly distorted from their form in the boundary layer upstream of separation (cf. Klineberg[3]). In the present model, the gas injected from the base is turned by the reversed flow in a distance $L \sim \delta_b = \delta_b (\dot{m}_i / \sqrt{\dot{m}_i})$, the distance from the body to the base stagnation point, and is impressed on the separating free shear layer over a distance of the order of L. The effects on the free shear layer caused by the impressed mass are determined by the amount of mass that the layer is required to entrain. For a compressible laminar mixing layer, the entrainment is given by

$$-\zeta_0 = \lambda_e \sqrt{\frac{Re_x}{C_\infty}} \quad ,$$

where

$$\lambda_e = \frac{\rho_{-\infty} v_{-\infty}}{\rho_e u_e} \quad ,$$

and $\zeta - \zeta_0$ is the value of the stream function for $u/u_e \to 0$. In the present model, on the u = 0 locus,

$$\rho_{-\infty} v_{-\infty} \approx \frac{\dot{m}_i}{2L} \quad .$$

The Reynolds number for the non-similar free shear layer is undetermined and will be arbitrarily assumed to be characterized by $Re_{\infty, d}$.

Taking the Chapman-Rubesin factor $C_\infty = 1$, and a mass flux $\dot{m}_i/2\dot{m}_{B.L.} = 0.05$ as a typical example, then from the experiments, $4 < \lambda_e \sqrt{Re_{\infty,d}} < 8.6$. For comparison, if the idealization proposed by Chapman[26] is used, an upper bound can be determined for the mass entrainment resulting from viscous stresses. From Chapman's solution, viscous stresses in a constant pressure free shear layer produce a unique value of mass entrainment given by

$$-\zeta_o = -\zeta_o(M_e) \quad ,$$

where $-\zeta_o = 1.10$

for $M_e = 3.0$.

It is concluded from these arguments that in the present experiments viscous stresses are no longer sufficient to turn the flow and a pressure increase is induced by the interaction which turns both the impressed flow and the flow in the free shear layer. The amount of the turning of the shear layer flow, and hence the induced pressure, is determined from a balance between the momentum flux of the impressed flow and some characteristic momentum flux associated with the free shear layer. The proper normalization cannot be determined from these rough arguments, but is obtained from the previous discussion and from experiment.

The relationship between the momentum flux of the flow impressed on the free shear layer and the momentum flux of the gas injected from the base is simply

$$\frac{\dot{m}_i v_{-\infty}}{\dot{m}_i u_i} \approx \frac{d}{2L} \quad ,$$

where $\frac{d}{2L}$ is an undetermined, non-linear function of the momentum flux from the base. Therefore, so long as the entrainment is large compared to the entrainment specified by the Chapman solution, and so long as a recirculating vortex exists in the near wake, the change in the near-wake pressure field with base mass addition will be a function only of the momentum flux of the injected gas, properly normalized, as discussed previously. The validity of this model for low mass transfer rates and the validity of the Chapman model, will be discussed further following the derivation of the mass transfer parameter.

Mass Transfer Parameter

Both aspects of the base pressure model described above depend only on the properly normalized momentum flux of the injected fluid and are independent of the model porosity, as long as the ceramic is choked. In addition, the base stagnation point interaction determines that the proper scaling is given by the momentum flux in the reversed flow. However, for the circular cylinder, because the subcritical separation process allows a smooth transition from the cylinder boundary layer to the non-similar laminar free shear layer, the Reynolds number scaling is the same for both the reversed flow and the cylinder boundary layer. Therefore, the characteristic near-wake momentum flux has been taken as that associated with the cylinder boundary layer upstream of separation and is justified entirely on the basis of the proper Reynolds number scaling.

Using these ideas, an injection parameter is formulated from the ratio of the momentum flux of the injected gas to the momentum

flux in the boundary layer upstream of separation, given by

$$\Pi = \frac{\dot{m}_i u_i}{2(\rho_e u_e^2)_s \int_0^{\delta} \left(\frac{\rho u^2}{\rho_e u_e^2}_s\right) dy}$$

Evaluating the integral,

$$\Pi = \frac{\dot{m}_i}{2\dot{m}_{B.L.}} \left[\frac{\mathcal{M}_{Air}}{\mathcal{M}_i}\right]^{\frac{1}{2}} \left\{ \frac{M_i}{M_e} \left[\frac{\delta - \delta^*}{\delta - \delta^* - \theta}\right] \left[\frac{T_i}{T_e} \frac{\gamma_i}{\gamma_e}\right]^{\frac{1}{2}} \right\}_s$$

As in Chapter II, the porous ceramic is assumed to be isothermally choked, hence $M_i \rightarrow \frac{1}{\sqrt{\gamma_i}}$, and $T_i = T_{0_i}$, where T_{0_i} is the measured plenum temperature of the injectant given in Figure (4). Therefore,

$$\Pi = \left\{ \frac{1}{M_e \sqrt{\gamma_e}} \left[\frac{\delta - \delta^*}{\delta - \delta^* - \theta}\right] \left[\frac{T_{0_i}}{T_0} \frac{T_0}{T_e}\right]^{\frac{1}{2}} \right\}_s I \quad ,$$

where

$$I = \frac{\dot{m}}{2\dot{m}_{B.L.}} \left[\frac{\mathcal{M}_{Air}}{\mathcal{M}_i}\right]^{\frac{1}{2}}$$

is taken as the injection parameter for the momentum dominated mass transfer problem. For large Reynolds numbers, where the boundary layer on the cylinder is small compared to the cylinder diameter, and for hypersonic Mach numbers, the quantity

$$\left\{ \frac{1}{M_e \sqrt{\gamma_e}} \left[\frac{\delta - \delta^*}{\delta - \delta^* - \theta}\right] \left[\frac{T_{0_i}}{T_0} \frac{T_0}{T_e}\right]^{\frac{1}{2}} \right\}_s = F(M_e, \gamma_e)$$

and is dependent on $Re_{\infty, d}$ only through the weak dependence of the location of the separation point on $Re_{\infty, d}$, and is assumed to be invariant. The temperature ratio is given by $T_{0_i}/T_0 \approx T_{aw}/T_0$, the recovery temperature ratio. The quantity $\dot{m}_{B.L.}$, the boundary-layer mass flux per unit span upstream of separation, is calculated from a locally

similar solution given by Klineberg,[3] and is given in Appendix C. Therefore, according to the model proposed above, the injection parameter I possesses both the proper Reynolds number and the proper molecular weight scaling for the momentum dominated mass transfer problem (cf. Figure (18)).

The Results of Experiment

A number of comparisons with experiment are possible in order to verify the ideas presented above. To establish the interaction between the injectant and the reversed flow, the axial Mach-number distribution given in Figure (19) was obtained using the insert Pitot- and static-pressure probes shown in Figure (2) and the viscous and probe-interference corrections described in Chapter II.

In the absence of mass addition, the axial Mach-number distribution between the two stagnation points exhibits an initial acceleration from the rear stagnation point to a pronounced maximum in the low subsonic range, and a subsequent deceleration to the base stagnation point (Figure (19)). Theoretical estimates of the maximum centerline Mach number in the reversed flow, calculated from the work of Reeves and Lees[1] for the Reynolds numbers of interest, are compared to the measured data in Figure (19). The theoretical estimates are based on a Taylor series expansion in the neighborhood of the rear stagnation point, which yields the result $u_{\ell}/u_{\psi=0} = 0.5$, coupled with an estimate of u^*_{max} as a function of $Re_{\infty, d}$; i. e., for the adiabatic case, $u^*_{max} = 0.28,\ 0.38$ for $Re_{\infty, d} = 0.9\times10^4,\ 3\times10^4$, respectively. These results, together with an assumption of the uniformity of the static pressure in the transverse direction, and an estimate for the

total temperature in the recirculating zone, $T_{0_{\mathcal{L}}}/T_0 = 0.90$, from the data of Herzog,[12] give the estimate of the maximum centerline Mach number. This estimate is greater than the measured centerline maximum value in each case. The effect of free-stream Reynolds number is evident in the figure, the maximum centerline Mach number decreasing and moving toward the base with decreasing $Re_{\infty, d}$, and hence increasing viscous effects. No direct measurements of the reversed flow have been attempted with mass addition. However, Figures (23), (24) indicate qualitatively that, in the vicinity of the rear stagnation point, the axial Mach-number distribution for moderate mass addition rates must be nearly that for zero mass transfer; whereas, as the base is approached, the centerline Mach number will be significantly reduced from the zero mass transfer value.

The profiles of Pitot pressure in the vicinity of the base, obtained from a probe facing the base, are shown in Figure (20). To demonstrate the dissipative viscous effects in the expansion away from the base, a similar profile was taken under conditions in which the test section was evacuated to a pressure representative of the base pressures, but without flow in the tunnel (Figure (20)). Figure (19) illustrates the Mach-number distribution in the base layer, using the measured, uncorrected, Pitot pressure from Figure (20) and an estimated static pressure, which is taken to be equal to the static pressure at the base stagnation point. This figure clearly demonstrates that the momentum flux of the injectant is comparable to the momentum flux in the reversed flow, and that the pressure and location of the base stagnation point are determined by a balance of the total pressures of

the interacting streams.

The results of the physical model proposed above can now be compared to the predictions of the theories by Korst, et. al.,[15] and by Chapman,[16] and to the available experimental data. In this regard, it is interesting to note that the Korst parameter has been used by Herzog,[12] Ginoux[13] and others without attempting to check the dependence on either Reynolds number or molecular weight.

Two fundamental differences exist between the present mass transfer criterion and those proposed by Korst, et. al.[15] and by Chapman:[16]

1. The present parameter,

$$I = \frac{\dot{m}}{2\dot{m}_{B.L.}} \left[\frac{\mathcal{M}_{Air}}{\mathcal{M}_i}\right]^{\frac{1}{2}} ,$$

is based on the momentum flux of the injected fluid, while the previous discussions have assumed that the mass flow of the injected fluid establishes the change in the near-wake pressure field.

2. The present discussion assumes that the proper normalization of the momentum flux of the injected fluid is the momentum flux in the boundary layer upstream of separation, while the Korst parameter,

$$H = \frac{\dot{m}_i}{\dot{m}_f} \; G(M_\infty) ,$$

for example, assumes that the proper mass flux normalization is the free-stream mass flux, $\dot{m}_f$.

The first point accounts for the molecular weight scaling and depends on the nature of the interaction between the injected mass and

the reversed flow. The second point involves the correct Reynolds number scaling for the mass transfer parameter, as

$$I \sim [Re_{\infty, d}]^{-\frac{1}{2}}$$

whereas $$H \sim [Rc_{\infty, d}]^{-1}$$

Figure (18) clearly demonstrates that both the Reynolds number and molecular weight scaling are properly included in the momentum criterion for the mass transfer regime considered.

The Korst theory is invalid in the present experiments. To demonstrate the discrepancy, the Korst theory, with an assumed, straight $\psi=0$ line, has been used to estimate the change in base pressure for a given mass transfer rate by calculating the lateral displacement of the $\psi=0$ streamline at the neck according to the relation

$$\dot{m}_i = 2 \int_0^{(y/d)_{\psi=0}} \rho u \, dy \quad ,$$

where ρu is calculated from the measured pressure distributions given in Figures (23), (29). For example, for $x/d = 3.0$, $Re_{\infty, d} = 3 \times 10^4$, $I = 4.28 \times 10^{-2}$ (argon), then $(y/d)_{\psi=0} = 0.005$ and the calculated value is $\frac{\Delta P_b}{P_N - P_b} = 0.010$. Under these same conditions, however, the measured base pressure change is $\frac{\Delta P_b}{P_N - P_b} = 0.085$. It should be noted that a similar calculation using the streamline displacement in the immediate vicinity of separation, as measured by the displacement of the shear-layer edge, yields good agreement with the measured base pressure change. This is a consequence of the fact that the shear-layer edge is curved and that the free shear layer cannot support a large transverse pressure gradient.

The Chapman criterion for the change in base pressure with mass addition contains the assumption that the single effect of mass addition is a displacement of the dividing streamline within the shear-layer profile (which need not be assumed self-similar, i. e., independent of initial conditions). Under these conditions, changes in the inviscid recompression pressure rise, and hence in the base pressure, are determined by the changes in the kinetic energy on the dividing streamline. However, the present experiments imply that the primary influence of mass addition is the impression of the injected fluid on the free shear layer near its origin by the recirculating flow, thus changing the boundary conditions on the development of the non-similar layer. This effect is dominant and obviates the use of the Chapman criterion for finite base mass addition rates.

The upper bound on the region of validity of the present model is that value of mass addition for which the recirculating vortex ceases to exist. The lower bound on the region of validity, and hence the upper bound on the region of validity of the Chapman model is that value of mass addition for which the mass impressed on the shear layer can be accomodated entirely by a viscous entrainment process. As an upper bound, this condition is given by

$$\lambda_e \sqrt{Re_x} = -\zeta_0 (M_e) \quad ,$$

where $\zeta_0 (M_e)$ is given by the ideal model proposed by Chapman.[26] For the non-similar free shear layer encountered in experiment, the entrainment will be even less than the Chapman value. For finite mass transfer rates, this condition will be satisfied only if

$$\rho_{-\infty} v_{-\infty} \approx \frac{\dot{m}_i}{2L}$$

becomes sufficiently small with decreasing $\dot{m}_i$. Since $L \to 0$ as $\dot{m}_i \to 0$, however, $\dot{m}_i/2L$ may remain large in comparison with the Chapman value for small values of $\dot{m}_i$. On the basis of the present experiments, it is expected that

$$\lim_{\dot{m}_i \to 0} \left(\frac{\dot{m}_i}{2L}\right) = 0$$

and that the Chapman model will be valid only in the limit of vanishing mass transfer, and hence vanishing change in base pressure; a physically unimportant though theoretically interesting case. Further experiments are necessary to verify this hypothesis.

For the flow over a rearward facing step, using only air as an injectant, Ginoux[13] has found that for low mass transfer rates the base pressure change is independent of the direction of the momentum vector. These results are inconclusive because, for Ginoux's experiments, the recirculating flow is of sufficient strength to impress the injected mass on the free shear layer near its origin, as discussed in the present model, irrespective of the initial orientation of the momentum vector. In view of the present results, it is clear that the role of momentum can only be determined by an investigation of the effect of molecular weight.

In other experiments, Townend[27] has also investigated the effects of molecular weight on the base pressure by injecting nitrogen and hydrogen into the turbulent near wake of an axisymmetric cone-cylinder, both by means of a series of discrete holes in the base, and

by a peripheral slot immediately upstream of the base. Townend reported the base pressure for a single value of Re_∞ as a function of the Korst[15] parameter

$$H = \frac{\dot{m}_i}{\dot{m}_f} G(M_\infty) \quad ,$$

where $$\dot{m}_f = \rho_\infty u_\infty d \quad ,$$

and $$G(M_\infty) = \frac{P_0}{P_\infty} \frac{1}{M_\infty} \left[\frac{T_\infty}{T_0}\right]^{\frac{1}{2}} \quad .$$

This parameter did <u>not</u> correlate the effects of molecular weight.

Townend's data for the smallest orifice size are replotted in Figure (21) as a function of the momentum flux ratio

$$H^* = H\left[\frac{\mathcal{M}_{Air}}{\mathcal{M}_i}\right]^{\frac{1}{2}}$$

where the Korst parameter is retained because the turbulent flow is insensitive to Re_∞. For base mass addition from orifices with an open area ten times that used to generate the data shown in Figure (21), Townend's data for nitrogen (not shown) no longer satisfy the momentum criterion, while the data for hydrogen correlates well with the results presented in the figure. The significance of the failure of these data to correlate with the rest is not clear.

For the peripheral injection, all values of the effective orifice size yield a momentum criterion. This result further substantiates the proposed model of an induced pressure as a consequence of mass addition into the shear layer in excess of the maximum amount allowed by viscous entrainment.

III. 3. The Pressure Field Similitude with Base Mass Transfer

The laminar cylinder boundary layer upstream of separation forms the upstream boundary conditions for the development of the near-wake flow field. The Pitot-pressure profiles for the boundary layer upstream of separation (x/d = 0.20), uncorrected for either viscous or probe-interference effects, are shown in Figures (15), (16). The measured boundary-layer thicknesses give excellent agreement with theory (see Klineberg[3]), substantiating the assumption $\mathscr{N}$ = const. for $\theta \geq 65^{\circ}$. The slight overshoot at the boundary-layer edge for $Re_{\infty, d} = 3 \times 10^4$ is attributed to probe-interference effects similar to those reported by Kendall,[28] where $h_p/\delta = .191$. These boundary conditions are independent of mass transfer for injection both from the forward stagnation region and from the base, as discussed previously (Figure (16)).

An important feature of the near-wake pressure field is the increase of the static pressure from the base to the neck, caused by the turning of the outer flow, and the subsequent relaxation back to the free-stream value in the far wake. In Figure (22), the axial static-pressure distribution without mass addition has been normalized to correct for tunnel gradients as described previously, and is compared to similar data from Behrens[9] for $x/d \geq 4.0$, and to the data of Herzog[12] for $0.5 \leq x/d \leq 4.0$. Herzog's data have been replotted here without correcting for tunnel gradients, which accounts for the discrepancy noted in the vicinity of the neck.

The maximum in the axial static-pressure distribution, shown in Figures (22), (23), corresponds to the location of the neck, or region in which the flow is parallel to the wake axis. The static-pressure level at the neck is determined by the outer, rotational flow and is independent of the near-wake pressure field, so long as the assumption is valid that the separation and wake shocks are sufficiently weak that the outer flow is isentropic along streamlines. These ideas are verified by the inviscid calculation of the Mach number of the outer, inviscid flow at the neck by Reeves and Lees,[1] who assumed that the outer flow expands isentropically from the forward stagnation point to the free-stream direction according to the static-pressure distribution given by McCarthy.[7] This establishes the stagnation pressure behind the normal portion of the bow shock as the characteristic total pressure and ignores the finite strength of the separation and wake shocks. Using these isentropic assumptions, their estimate of the inviscid flow Mach number at the neck, $M_N = 2.50$, is verified exactly by the measurements of Pitot and static pressure at the neck given in Figures (23) and (29).

The most important feature of the influence of base mass addition on the recompression static pressure rise, shown in Figure (23), is the insensitivity of the static pressure downstream of reattachment to small mass addition rates. For a mass transfer rate sufficient to cause a base pressure ratio $P_b/P_b(0) = 1.09$ (see Figure (18)), the static pressure at the neck experiences a change of less than 1% from the undisturbed level. In contrast, Herzog[12] has reported that for mass injection rates sufficient to greatly disturb the recirculating

vortex, the static pressure at the neck decreases monotonically with increasing injection, decreasing 17% at $\dot{m}_i/\dot{m}_f = 0.02$ ($I = 0.74$ for $Re_{\infty, d} = 3 \times 10^4$, for which the recirculating zone no longer exists); coupled with a measurable aft motion of the neck. This condition occurs for a base pressure ratio $P_b/P_b(0) = 1.50$.

Using the corrected axial distribution of Pitot and static pressure, plotted in Figures (23), (24), the rear stagnation point is defined in Figure (25) by the ratio $P_{0_2}/P = 1.0$. Using this definition, the location of the rear stagnation point as a function of $Re_{\infty, d}$ in the absence of mass addition is given in Figure (26). Also included in Figure (26) are the theoretical predictions of Reeves and Lees,[1] the theoretical predictions of Klineberg,[3] and the experimental data of Dewey[8] and Herzog.[12] Herzog's result fails to correlate with the present data because the pressure measurements from which it was derived were not corrected, either for viscous effects or for tunnel gradients. The discrepancy between the theoretical predictions of Reeves and Lees[1] and those of Klineberg[3] apparently arises because Klineberg considers a subcritical separation phenomena which is coupled to the near-wake flow, whereas Reeves and Lees consider a fixed separation point. In addition, the profile functions used by Klineberg to evaluate the integral equations differ somewhat from those used by Reeves and Lees. For moderate injection rates, the location of the rear stagnation point is not changed (see Figure (25)), whereas, as the mass transfer parameter is increased beyond 0.5% of the frontal-area mass flux ($I = 0.185$), the entire near-wake structure is changed, including both the nature and location of the rear stagnation point, as shown by

Herzog.

The axial Mach-number distribution for $x > x_r$, in the absence of mass addition, has been calculated from the corrected Pitot- and static-pressure distributions, and is shown in Figure (27). The axial Mach number decreases very slowly with increasing mass transfer for moderate mass addition rates, and this effect has not been included in Figure (27).

The Pitot-pressure profiles in Figure (28) were taken at the neck location for a single gas and a single value of $Re_{\infty, d}$ to demonstrate the effects of increasing mass addition on the near-wake pressure field. Three features are of principal importance: the effect on the separation process, the effect on the recompression shock strength, and the effects of mass addition on the structure of the viscous shear layers. The outermost portion of the profiles corresponds to the outer, rotational flow. Proceeding toward the axis, the weak separation shock is followed by a plateau region which is terminated in the wake, or recompression shock. Within the wake shock, the region of nearly uniform Pitot pressure is followed by the characteristic wake "bucket."

A direct consequence of the addition of mass at the base is the upstream migration of the separation point, as demonstrated by Herzog.[12] For moderate mass addition rates the separation shock strength increases with increasing mass transfer rate; however, a significant departure from an isentropic compression does not occur until the distinct character of the recirculating flow begins to change, i.e. for mass addition in excess of 0.5% of the frontal-area mass flux ($I = 0.185$ for $Re_{\infty, d} = 3 \times 10^4$, cf. Herzog[12]).

The most prominent effect of increasing mass addition is the progressive decrease in the strength of the wake, or recompression shock. For the largest mass transfer rate shown in Figure (28), a small but finite recirculation remains in the near wake. At this mass addition rate, the wake shock at the neck location has been reduced to a gentle compression with a strength of less than one third (0.3) of the strength of the wake shock occurring in the absence of mass addition. This fact, coupled with the lateral displacement and decreased shear in the viscous layers for large mass transfer rates, has a significant effect on the development of the intermediate-wake region, immediately downstream of the neck.

The correlation of the transverse Pitot-pressure profiles in the near wake with the mass transfer parameter I is shown in Figure (29) for argon, nitrogen and helium injection at freestream Reynolds numbers $Re_{\infty, d} = 0.9 \times 10^4$ and 3×10^4, compared to the distribution for I = 0. The most prominent features of this correlation are the location and strength of the separation and wake shock waves, and the structure of the flow in the vicinity of the shear-layer edge. Some of the more important of these features, shown in Figure (29) for a single value of I, are replotted in the succeeding figures as functions of the mass transfer parameter.

In Figure (30) the location of the separation shock is given as a function of I, with x/d as a parameter, for $Re_{\infty, d} = 3 \times 10^4$, while Figure (31) illustrates the wake shock location for $Re_{\infty, d} = 0.9 \times 10^4$ and 3×10^4 as a function of the parameter I.

The arguments presented in Section III. 2 which lead to the correlation of the base pressure with the mass transfer parameter I (Figure (18)) involve the momentum flux of the reversed flow. The Pitot-pressure distributions in Figure (29) show that the shear layers are displaced laterally and somewhat broadened as a consequence of mass addition. However, Figure (32) shows that the location of the u=0 locus, and hence the lateral extent of the reversed flow, is unchanged by moderate mass addition rates. Therefore, the net effect of mass addition on the structure of the free shear layer is a reduction in the value of u*, the velocity on the stagnating streamline. By the arguments of Reeves and Lees,[1] this gives a consequent reduction in $\frac{1}{2}\, u^* = u_{\mathcal{L}}/u_e$. Therefore, with increasing mass addition there is a reduction in the strength of the recirculating vortex and an aft motion of the base stagnation point toward the rear stagnation point, a phenomenon first reported by Herzog.[12] By the momentum balance argument, the base pressure increases with increasing mass addition (Figure (18)) both because of an increasing momentum of the injected gas and, as a secondary effect, because of the decreasing momentum in the reversed flow.

III. 4. The Effects of Transition

For a wake, the occurrence of transition from laminar to turbulent flow is distinguished by an increase in the effective diffusivities of the mean flow, and consequently an increase in the growth rate of the wake. From measurements of the growth rate of the mean flow profiles, the location of transition in the wake of a circular cylinder has been estimated by Behrens[29] to occur at x/d = 80 for $Re_{\infty, d} = 0.9 \times 10^4$

and at $x/d = 10$ for $Re_{\infty, d} = 3 \times 10^4$, after the measurements of McCarthy[7] and Behrens.

In Figure (33) the measured wake widths, taken from both the Pitot-pressure profiles and the mass-concentration profiles for argon addition from the forward stagnation region, are compared to a wake width defined by the maximum slope intercept of the mean-square hot-wire voltage fluctuations, obtained by Behrens* for zero mass transfer. The hot-wire measurements show that for $Re_{\infty, d} = 0.9 \times 10^4$, no fluctuations of measurable amplitude persist in the near wake, hence $Re_{\infty, d} = 1.48 \times 10^4$ has been used to define the wake edge for a fully laminar case. For $Re_{\infty, d} = 3 \times 10^4$, fluctuations of measurable amplitude exist and are amplified by the flow, and the growth rate defined by these fluctuations exceeds the fully laminar growth rate for $x/d \geq 3.75$. The first stages of this departure, where the deviations remain small, are shown in Figure (33), where it is also demonstrated that in the initial stages of departure, the increased fluctuations have little effect on the mean-flow measurements.

From this evidence, it is concluded that the near-wake flow field is laminar upstream of the sonic point on the axis, with transition occurring in the far wake for $Re_{\infty, d} = 0.9 \times 10^4$. and moving to the intermediate-wake region, downstream of the sonic point on the axis, for $Re_{\infty, d} = 3 \times 10^4$. Fluctuation measurements have not been made for a circular cylinder with mass transfer; however, it is anticipated that moderate mass transfer rates and their attendant low mass-concentration levels, will have little or no effect on wake transition.

* Behrens, W.: Private Communication.

A second aspect of the effects of transition is shown in Figure (34), where the measurements of the base pressure in the absence of mass addition are given as a function of $Re_{0,d} = \frac{\mu_\infty}{\mu_0} Re_{\infty,d}$. Included in this figure are the experimental curves obtained by Dewey[8] as a function of aspect ratio, and further experimental data by Herzog[12] and Ramaswamy* on circular cylinders with AR = 15, as is the present case. The experimental data indicate that an aspect ratio effect is present at the higher Reynolds numbers; a fact attributed by Dewey to three-dimensional effects. However, in the present experiments it has been found that a correlation exists between the onset of the effect of aspect ratio on the base pressure and the occurence of transition to turbulent flow of the wind-tunnel boundary layers at the model station. This is expected to have little effect on the pressure field measurements in the near wake.

---

* Ramaswamy, M. A.: Private Communication.

IV. THE STRUCTURE OF THE MASS-CONCENTRATION FIELD

The mass-concentration field in the cylinder wake is divided into three distinct regions; the near wake, the asymptotic far wake and an intermediate-wake region. The structure of the near-wake region is governed by the diffusion of the injected species in the reversed flow, subject to the boundary conditions imposed at the base, and by the outer transport layer. The intermediate wake is characterized by a region of viscous acceleration of the centerline velocity, in the absence of axial diffusion, and is a transition zone from the flow in the vicinity of the rear stagnation point to the flow in the asymptotic far wake, for which an Oseen linearization of the velocity is valid, i.e., $u_{\mathcal{C}_L}$ = const., to first order.

In each region of the wake the structure of the mass-concentration field is dependent on both the relative magnitude and the relative orientation of the convective and diffusive velocity vectors. The relative magnitude is given by the parameter $ReSc = u\ell/D$, the ratio of the convective to the diffusive velocities, while the relative orientation is determined by the physics of the wake flow. The consequences of these facts will be examined separately in each region of the wake.

IV. 1. The Near-Wake Flow with Mass Addition at the Base

Transverse Distribution

The mass-concentration field in the near wake with mass addition at the base is illustrated in Figures (35), (36) for argon, nitrogen and helium addition at a single value of the injection parameter I, for $Re_{\infty, d} = 0.9 \times 10^4$ and 3×10^4. Figure (36) shows an isogram of the mass-concentration field, illustrated in the isometric plot in Figure (35),

overlayed on the characteristic features of the corresponding pressure field. In these figures, the mass-concentration profiles are average profiles obtained by averaging the mass concentration from opposite sides of the wake at a given value of the transverse position, as discussed in Chapter II. The dominant feature of the near-wake mass-concentration field is the axial decay of the mass concentrations from the base toward the rear stagnation point, shown in Figures (37), (38), as the result of the existence of a stagnation point in the flow in the vicinity of the base, and the consequent counter-current diffusion of the injected species into the reversed flow in the region between the two stagnation points.

Scott and Eckert[19] have proposed a model for heat transfer in high Reynolds number separated flows which uses two thin layers to describe the transport of heat between the body and the outer flow. This model is directly applicable to flows with mass transfer, using the analogy given in Appendix A. The first layer in this model, a boundary layer at the base, governs the transport of heat or mass at the body surface. The generalization of the concept of this layer to the case of small values of ReSc will be shown below to be represented by the axial profiles in Figure (37).

The second, or outer transport layer in this model occurs in the vicinity of the shear layers, and governs the transport of heat or mass between the recirculating vortex and the outer flow by diffusion across the shear layers. This outer layer sets the outer boundary condition on the inner recirculating flow and is responsible for the establishment of the rear stagnation point boundary condition on the axial

distribution of mass concentration.

For $Re_{\infty, d} = 3 \times 10^4$, the transverse mass-concentration profiles illustrated in Figure (35) are characterized by an off-axis maximum in the vicinity of the u = 0 locus as a result of the convection of the high mass-concentration layer near the base into the shear layer by the recirculating flow. This maximum appears as a folding of the isolines in Figure (36) and isolates the outer transport layer from the mass-concentration field near the axis. Lateral and axial diffusion result both in the decay of this maximum, as the rear stagnation point is approached, and the subsequent development of the profile toward the asymptotic Gaussian form downstream of the rear stagnation point.

For $Re_{\infty, d} = 0.9 \times 10^4$, Figures (35) and (36) demonstrate that the transverse mass-concentration profiles are diffusion dominated within the recirculating zone, as evidenced by the monotonic decay away from the axis, and are convection dominated only in the vicinity of the outer layer. The local maximum does not exist for this case, and the outer transport layer is no longer distinct as a consequence of the reduced Reynolds number. The results for helium, shown in Figures (35) and (36), demonstrate that the decreased Schmidt number, and hence the increased importance of diffusion, similarly reduce the definition of the off-axis maximum for $Re_{\infty, d} = 3 \times 10^4$, and more rapidly transforms the resulting profile to a monotonically decreasing diffusion profile.

The location of the vortex center and the nature of the velocity along the u = 0 locus can be determined for the main body of the recirculating flow with mass addition from the base using the data given in

Figure (35). The species conservation equation, written along the $u = 0$ locus, yields the result that, if $\partial C_i/\partial y < 0$ and $\partial^2 C_i/\partial y^2 \gtrless 0$, then $v \lesssim 0$. Using this result and the measurements of the mass-concentration field shown in Figure (35), for $Re_{\infty, d} = 3 \times 10^4$, $I = 4.28 \times 10^{-2}$, the lateral velocity is directed away from the axis for $x/d < 0.625$ and toward the axis for $x/d > 0.75$. Hence, the vortex center occurs on the $u = 0$ locus for $0.625 < x/d < 0.750$. This location corresponds to the region in which the $u = 0$ locus turns rapidly away from the axis in Figure (36), and for which the wake edge defined by the mass-concentration measurements exhibits a maximum width. Because the pressure field is disturbed only slightly at this mass transfer rate, the location for the vortex center is representative of that for $I = 0$. The influence of mass addition is to displace the vortex center away from the base, and to reduce the vortex strength (cf. Chapter III).

The normalized profiles in Figures (41) show that, in addition to profile shape which is determined from the boundary conditions, the transverse mass-concentration profiles in the near wake are characterized by their centerline mass concentration and a somewhat arbitrary characteristic width. For the near wake, the maximum slope intercept with the zero has been chosen as the characteristic width and has been designated as the wake edge (C_i) in the isograms in Figure (36).

In Figure (36) the location of the wake edge (C_i) may be compared with the location of the shear-layer edge, $(y/d)_e$, defined from the Pitot-pressure profiles given in Figure (29) as the maximum slope intercept with the maximum at the outer edge of the shear layer.

Figure (36) demonstrates that for argon addition the corresponding edges lie nearly parallel to one another, while for helium addition, the decreased Schmidt number causes the mass-concentration wake to spread more rapidly than the corresponding viscous layer. It will be demonstrated in Section IV. 3 that the lateral scale of the mass-concentration wake depends only on the lateral scale of the viscous shear layers and the Schmidt number, independent of the mass transfer rate (Figure (40)). As a consequence, the mass-concentration profiles become extremely narrow in the vicinity of the neck because of the contraction of the viscous shear layers in this region (Figure (41-e)).

The primary influence of increased mass addition on the near-wake pressure field is the downstream motion of the base stagnation point, and the consequent reduction of the strength of the reversed flow, and hence the product ReSc. For the addition of argon, the effects of increasing I are most pronounced for $Re_{\infty, d} = 3 \times 10^4$, in the vicinity of the base (Figure (41-c)). For this case, the data exhibit an increase in the width of the central peak and a reduction, and eventual elimination, of the off-axis maximum with increasing mass transfer. Further increases in the mass transfer change the character of the profile as the base stagnation point moves downstream of the measurement station (cf. data for $x/d = 0.75$, $I = 21.4 \times 10^{-3}$, Figure (41-c)). For $Re_{\infty, d} = 0.9 \times 10^4$, the profiles are diffusion dominated. As a result, the only apparent effect of an increase in the mass transfer rate is an increase in the width of the normalized mass-concentration profiles, commensurate with the displacement of the shear-layers by the increased base pressure. The effects for helium addition are qualitatively similar and

are not shown here.

Axial Distribution

To obtain a qualitative description of the axial distribution of mass concentration in the region between the two stagnation points, an approximate solution of the species conservation equation on the axis will be obtained, subject to the boundary conditions on the mass concentration at the base and at the rear stagnation point. The mass concentration at the base is determined directly by the injection parameter I, whereas the mass-concentration distribution along the u=0 locus, and hence the mass concentration at the rear stagnation point, are determined by the diffusional loss of mass through the outer transport layer by the requirement that the net efflux from the recirculating region exactly balances the mass added. The complexity of this second boundary condition prevents the complete analytic solution for the axial distribution and only its qualitative features will be given below.

From an examination of Figure (35), it is apparent that both the axial and the transverse diffusion terms are important on the axis. Then, in physical coordinates, the species conservation equation on the axis takes the elliptic form

$$\frac{u}{D}\frac{\partial C_i}{\partial x} = \frac{\partial^2 C_i}{\partial x^2} + \frac{\partial^2 C_i}{\partial y^2} \quad ,$$

where $\frac{\partial(\rho D)}{\partial C_i} = 0$ is assumed, and both thermal and barotropic diffusion are ignored. Using the non-dimensional coordinates

$$\tilde{X} = \frac{x - x_b}{x_r - x_b} \quad ,$$

$$\tilde{Y} = \frac{y}{x_r - x_b} \quad ,$$

where x_b is the location of the base stagnation point in physical coordinates, the equation takes the non-dimensional form

$$\frac{\partial^2 C_i}{\partial \tilde{X}^2} + \frac{\partial^2 C_i}{\partial \tilde{Y}^2} + \tilde{U}(\tilde{X}) \frac{\partial C_i}{\partial \tilde{X}} = 0 \quad ,$$

where $$\tilde{U}(\tilde{X}) = \frac{u(\tilde{X})}{u_{max}} \cdot \frac{|u_{max}|(x_r - x_b)}{D} = Re(\tilde{X})\, Sc \, .$$

To facilitate a solution, the mass-concentration field near the axis is assumed to be self-similar, i.e.

$$C_i = C_{\mathbb{C}}(\tilde{X})\, F(\eta) \quad ,$$

where $$\eta = \tilde{Y} / \sigma(\tilde{X}) \quad .$$

Then $$\left.\frac{\partial^2 C_i}{\partial \tilde{Y}^2}\right|_{\tilde{Y}=0} = C_{\mathbb{C}}(\tilde{X}) \frac{F''_{(0)}}{\sigma(\tilde{X})^2} \quad ,$$

where $F''_{(0)}$ is unspecified, and the species conservation equation on the axis takes the form

$$\frac{d^2 C_{\mathbb{C}}}{d\tilde{X}^2} + \tilde{U}(\tilde{X}) \frac{dC_{\mathbb{C}}}{d\tilde{X}} + \Delta(\tilde{X})\, C_{\mathbb{C}}(\tilde{X}) = 0 \quad ,$$

where $$\Delta(\tilde{X}) = \frac{F''_{(0)}}{\sigma(\tilde{X})^2}$$

The general solution of this equation for arbitrary $\tilde{U}(\tilde{X})$, $\sigma(\tilde{X})$ is

$$C_{\mathbb{C}}(\tilde{X}) - C_{\mathbb{C}}(0) = \left.\frac{dC_{\mathbb{C}}}{d\tilde{X}}\right|_{\tilde{X}=0} \cdot \int_0^{\tilde{X}} \frac{d\xi}{E(\xi)} - \int_0^{\tilde{X}} \frac{1}{E(\xi)} \int_0^{\xi} \Delta(\xi') E(\xi') C_{\mathbb{C}}(\xi')\, d\xi'\, d\xi \quad ,$$

where

$$E(\tilde{X}) = \exp\left[\int_0^{\tilde{X}} \tilde{U}(\xi)\, d\xi\right] \quad .$$

Two parameters, $\tilde{U}(\tilde{X})$ and $\Delta(\tilde{X})$, occur in this solution; however, it is not in a convenient form from which the qualitative features of the axial

decay may be obtained, both because of the parabolic dependence on the boundary conditions, and because of the integral nature of the solution. To obtain a qualitative understanding of the mass-concentration field, it is sufficient to examine the special case for which $\tilde{U}$ and Δ are independent of $\tilde{X}$. Then, the species equation

$$\frac{d^2 C_{\mathfrak{L}}}{d\tilde{X}^2} + \tilde{U} \frac{d C_{\mathfrak{L}}}{d\tilde{X}} + \Delta C_{\mathfrak{L}}(\tilde{X}) = 0$$

has the solution

$$C_{\mathfrak{L}}(\tilde{X}) = A e^{\frac{\tilde{U}}{2}(\alpha-1)\tilde{X}} + B e^{-\frac{\tilde{U}}{2}(\alpha+1)\tilde{X}} ,$$

where

$$\alpha = \left[1 - \frac{4\Delta}{\tilde{U}^2}\right]^{\frac{1}{2}} .$$

From the elliptic nature of the problem, the boundary conditions are taken at the extremities, $\tilde{X} = 0, 1$, giving the result

$$A = -\frac{\left[C_{\mathfrak{L}}(0) e^{-\tilde{U}\alpha} - C_{\mathfrak{L}}(1) e^{-\frac{\tilde{U}}{2}(\alpha-1)}\right]}{\left[1 - e^{-\tilde{U}\alpha}\right]} ,$$

$$B = \frac{\left[C_{\mathfrak{L}}(0) - C_{\mathfrak{L}}(1) e^{-\frac{\tilde{U}}{2}(\alpha-1)}\right]}{\left[1 - e^{-\tilde{U}\alpha}\right]} .$$

The complexity of the solution in this region is apparent. However, from the form of the solution, the basic features of the axial distribution can be determined. Of primary importance is the conclusion that the presence of the rear stagnation point imposes as the solution of the species equation the linear superposition of a positive and a negative exponential function. The negative exponential corresponds to the decay from a source at the base stagnation point into a uniform flow of infinite extent with lateral diffusion; whereas, the positive exponential

represents the decay toward the base of the mass concentration supplied by a source at the rear stagnation point, whose strength is determined by the outer flow as a consequence of the coupling in the subcritical region.

As $\tilde{U} = ReSc \to \infty$, the boundary layer character of the solution becomes evident. In this limit,

$$\alpha \approx 1 \quad ,$$

and the solution becomes

$$C_{\mathcal{L}}(\tilde{X}) = C_{\mathcal{L}}(0) \frac{[e^{-\tilde{U}\tilde{X}} - e^{-\tilde{U}}]}{[1 - e^{-\tilde{U}}]} + C_{\mathcal{L}}(1) \frac{[1 - e^{-\tilde{U}\tilde{X}}]}{[1 - e^{-\tilde{U}}]} \quad .$$

Under these circumstances, the solution represents a thin, exponentially decaying boundary layer with a characteristic thickness $\delta_b \sim \tilde{U}^{-1}$. This is precisely the base boundary layer proposed by Scott and Eckert[19] for the transfer of heat or mass from the base into the recirculating vortex at infinite Reynolds number.

In the present experiments, however,

$$\tilde{U} = ReSc \sim 0(1) \quad ,$$

and the axial diffusion depth is of the order of the distance between the two stagnation points, $\delta_b \sim \tilde{U}^{-1} \approx 1$. Under these circumstances, the base transport layer is no longer thin, but dominates the near-wake distribution (Figures (35), (37)) and represents a generalization of the layer proposed by Scott and Eckert to the low Reynolds number case. The present solution also differs from the stagnation point solution by Hayday,[30] principally because of the importance of the transverse diffusion terms in the species conservation equation.

Two length scales appear in the solution for small values of $\tilde{U}$. The first is associated with the product ReSc through the velocity, i.e. $\tilde{X} \sim \frac{1}{\tilde{U}}$, and reflects the importance of counter-current diffusion in determining the axial decay, as discussed above. The second scaling is associated with the transverse diffusion, i.e. $\tilde{X} \sim \frac{1}{\sqrt{\Lambda}} = \frac{\sigma}{\sqrt{|F''(0)|}}$, and demonstrates the influence on the axial decay of transverse diffusion into the sink provided by the outer flow. Both υ and $\tilde{U}$ are non-trivial functions of $Re_{\infty, d}$, Sc, and I through the influence of these parameters on the near-wake flow-field structure (Figures (35), (41)).

In the solution presented above, three major difficulties occur which obviate the use of the solution in any but a qualitative discussion. First, from Figures (35), (41), the assumption Δ = const. is valid for $Re_{\infty, d} = 0.9 \times 10^4$, but is incorrect at the higher Reynolds number because of the fundamental changes which occur in the shape of the mass-concentration profiles near the base with increasing I. Second, the assumption $\tilde{U}$ = const. is very rough and does not specify the proper value of $\tilde{U}$ = ReSc. More properly, $\tilde{U}$ should be assumed to be parabolic, i.e. $\tilde{U} \sim \tilde{X}(1-\tilde{X})$ (see Figure (19)), and the integral solution, given previously, should be used. Finally, and most seriously, is the question of the establishment of the boundary conditions $C_{\mathfrak{C}_L}(0)$ and $C_{\mathfrak{C}_L}(1)$, discussed previously.

Figure (38) illustrates the effect of molecular weight on the axial mass-concentration profiles for a constant value of the injection parameter I. For this case a decrease in molecular weight for a fixed value of I results in a decreased mass concentration. It is apparent from the above discussion that no simple scaling exists for the influence of

molecular weight; however, it is fortuitous that an adequate correlation of the axial mass-concentration data for both molecular weight and the mass transfer parameter I can be obtained by the correlation of the mole fraction X_i with the injection parameter I at selected axial stations (see Figure (39)). For $Re_{\infty, d} = 3 \times 10^4$, the mole fraction correlates with the injection parameter between the base and $x/d = 1.0$. For $x/d \geq 1.5$, the data in Figure (38) exhibit the effects of the decreased Schmidt number for helium, manifested as an increased helium mole fraction for a given value of I. For $Re_{\infty, d} = 0.9 \times 10^4$, the Schmidt number effects for helium are pronounced at $x/d = 0.625$ because of the decreased Reynolds number in the recirculating zone, an effect which persists throughout the near-wake region.

IV. 2. The Near-Wake Flow with Mass Addition from the Forward Stagnation Region

Transverse Distribution

For mass addition from the forward stagnation region, the near-wake mass-concentration field is illustrated in the isometric plots in Figure (43) and the isograms in Figure (44). The species transferred from the forward stagnation region enter the near-wake flow field through mass-concentration boundary layers whose thickness upstream of separation is comparable to the viscous boundary-layer thickness. The mass-concentration distribution in these boundary layers dominates the boundary conditions for the distribution of mass concentration in the near-wake flow field, and sets the mass-concentration level at the base.

Figure (42) illustrates the mass-concentration profiles in the boundary layer upstream of separation ($x/d = 0.20$) for helium and

argon addition for $Re_{\infty, d} = 0.9$ and 3×10^4. For argon addition, a local maximum occurs in the mass-concentration distributions at a distance from the wall equal to nearly one half of the viscous boundary-layer thickness. The maximum overshoots the wall value by 3% for $Re_{\infty, d} = 3 \times 10^4$ and nearly 10% for $Re_{\infty, d} = 0.9 \times 10^4$, and is the result of both probe interference effects and the diffusion upstream into the low speed boundary-layer flow near the wall of the relatively low mass-concentration gas from the vicinity of the base. Both processes are a consequence of the fact that the boundary-layer profiles have been measured approximately one boundary-layer thickness upstream of separation, and this distribution is not expected to persist further upstream. Similar results were not recorded for the addition of helium because of the lack of sensitivity in the measurement of helium concentrations in the vicinity of the wall.

The above results suggest that barotropic diffusion may contribute to the formation of the local maximum in the boundary layer profile. Barotropic diffusion results from the centrifugal forces associated with the expansion of the flow and provides a mass-transport distribution in the boundary layer that is similar in form to that provided by ordinary diffusion, the direction of the transport being a function of molecular weight. As a consequence, barotropic diffusion can only enhance the effects of ordinary diffusion in the boundary layer, and for this reason, the local maximum occurring in the profiles cannot be accounted for by the effects of barotropic diffusion.

The extensions of these boundary-layers into the near-wake flow are the narrow mass-transport layers which provide the outer boundary

conditions on the mass-concentration field in the region of reversed flow. These outer layers, shown in Figures (43) and (45), are a consequence of the transition of the dominant transport mechanism from one of diffusion for the inner recirculating flow to one of convection for the outer flow, and form the outer transport layers in the two layer model proposed by Scott and Eckert,[19] as described previously.

The transverse profiles for argon exhibit a nearly uniform region between the $u = 0$ loci (Figure 43) as a consequence both of the effects of diffusion within the recirculating vortex and of the decrease in the mass concentration of the injected gas along the undisturbed dividing streamline by the diffusional loss of the injected species through the outer transport layers. This causes a reduction of the mass concentration at the rear stagnation point below that at the base, and provides the second boundary condition for the axial decay of mass concentration in the near wake, as discussed previously.

A local maximum occurs off the axis, followed by a rapid decay of the mass concentration in the outer transport layer. On the body, the local maximum occurs for $\psi > 0$ (Figure (42)). As the rear stagnation point is approached, the local maximum is displaced toward the axis by lateral diffusion and by the convergence of the shear flow in the vicinity of the neck (see Figure (44)), but does not coincide with the $\psi = 0$ streamline upstream of the rear stagnation point, as can be inferred from Figure (43).

The profiles described above are qualitatively similar to a profile obtained by Mohlenhoff[10] in the recirculating zone of a uniformly porous cylinder for helium addition; however, no direct comparison

can be made because of the more complex boundary conditions used by Mohlenhoff. The present results also qualitatively resemble a theoretical model used by Reeves and Lees[1] to represent the analogous total enthalpy profiles for a cold cylinder. The analogy to the heat transfer model of Scott and Eckert[19] is one in which the flow is dominated by the outer transport layer, i. e. heat transfer from the forward stagnation region, with an adiabatic base. This case is discussed in detail in Appendix A.

For the addition of helium (Figures (43), (44)), the near-wake profiles assume a less complex form because of the increased diffusivity. At $Re_{\infty, d} = 3 \times 10^4$, a local maximum occurs in the mass-concentration profiles for $x/d = 0.52$, but decays rapidly because of the effects of diffusion. Within the recirculating zone, at this Reynolds number, the profiles exhibit three distinct inflection points; however, for $Re_{\infty, d} = 0.9 \times 10^4$ the profiles for helium possess only a single inflection point.

The mass-concentration isograms are shown in Figure (44), superimposed on the characteristic features of the pressure field. For this case, the isolines exhibit some folding as a consequence of the existence of the local maximum, but otherwise lie nearly parallel to the shear-layer edge, as shown in the figure.

The normalized mass-concentration profiles for argon, shown in Figure (45), are independent of the mass transfer rate, and the normalization, $C_{\mathcal{L}}$, scales linearly with $\dot{M}$. The results for helium addition are qualitatively similar, and are not shown here. The characteristic widths of the mass-concentration profiles are again determined only by

the viscous shear layer (Figure (40)) and the diffusion coefficient, and are thus independent of mass transfer rate. For this flow, the mass-concentration wake edge (C_i) lies parallel to the shear-layer edge but is displaced into the outer flow beyond the shear-layer edge as a consequence of the boundary conditions at the base.

Axial Distribution

The axial distribution of mass concentration for the case of mass transfer from the forward stagnation region is given in Figure (46), with $Re_{\infty, d}$ and $\dot{M}as$ parameters. To obtain a qualitative understanding of this axial distribution, the approximate solution outlined previously will be employed. From the condition of a nearly uniform transverse distribution, $\Delta = 0$ and hence

$$\alpha = 1.$$

Therefore

$$C_{\mathfrak{L}}(\tilde{X}) = C_{\mathfrak{L}}(0) \frac{\left[e^{-\tilde{U}\tilde{X}} - e^{-\tilde{U}}\right]}{\left[1 - e^{-\tilde{U}}\right]} + C_{\mathfrak{L}}(1) \frac{\left[1 - e^{-\tilde{U}\tilde{X}}\right]}{\left[1 - e^{-\tilde{U}}\right]} .$$

This is the exponential boundary-layer solution given previously. Again $\tilde{U} = ReSc \sim 0(1)$ and hence $\delta_b \sim \tilde{U}^{-1} \approx 1$, i. e. the axial diffusion depth is of the order of the distance between the two stagnation points. Furthermore, because there is no source in the base region, the difference between the mass concentrations at the base and at the rear stagnation point results only from the decrease in the mass concentration of the injected species along the dividing streamline by diffusional loss through the outer transport layer. As a result, the two boundary conditions are nearly equal and the axial decay is extremely weak compared to that for base mass addition (cf. Figures (35), (37) and (43), (46)).

Transverse diffusion within the reversed flow provides a nearly uniform mass-concentration distribution throughout the region between the u = 0 loci. The results for helium, as a consequence of the increased diffusion coefficient, exhibit an axial distribution of mass concentration which decays more rapidly than that for argon (Figure (46-b)).

This case more closely parallels the stagnation point flow field analyzed by Hayday;[30] however, the boundary conditions and the molecular weight scaling contain multiple length scales and are again coupled to the flow, giving the weak axial decay shown in Figure (46).

IV. 3. The Intermediate-Wake Region

The far-wake flow field of a circular cylinder has been studied experimentally by McCarthy[7] and Behrens[9] at GALCIT, and the results have been favorably compared to the asymptotic far-wake calculations of Kubota[5] and Gold.[6] These results show that although the decay law for the outer-wake flow field is similar to that for the inner-wake flow, the length scales for the two processes are greatly different. The scale for the inner-wake flow is set by the influence of the near-wake boundary conditions, whereas the scale for the outer-wake flow is set by the influence of the boundary conditions generated by the bow shock wave.

For the asymptotic decay of the inner wake, an Oseen linearization of the boundary-layer equations yields a self-similar form for the small perturbations to the uniform field. The details of the near-wake flow field are contained in the boundary conditions and are accounted for in the solution by establishing a virtual origin of the coordinate system. The result of the Oseen calculation for the velocity

defect,

$$w = 1 - U$$

is given by

$$w = \theta_o \frac{M_{e_o}^2}{M_e^2} \frac{e^{-\frac{C_\infty Y^2}{4X}}}{\sqrt{X}} ,$$

where,

$$\theta_o = \frac{(\rho_e u_e \theta)_o}{2\rho_\infty u_\infty d} \left[\frac{C_\infty Re_{\infty, d}}{\pi}\right]^{\frac{1}{2}} ,$$

and X and Y are the coordinates in the incompressible plane, measured from the rear stagnation point, given by

$$X = \int_o^{x/d} \frac{\rho_e \mu_e u_e}{\rho_\infty \mu_\infty u_\infty} d(x/d) ,$$

$$Y = [C_\infty Re_{\infty, d}]^{\frac{1}{2}} \int_o^{y/d} \frac{\rho_e u_e}{\rho_\infty u_\infty} \frac{\rho}{\rho_e} d(y/d) ,$$

(cf. Gold[6]).

An extension of Kubota's[5] analysis to the mass-concentration field yields the solution for the diffusion from a delta function source at the origin as the asymptotic result;

$$C_i = \frac{\dot{m}_i}{2\rho_\infty u_\infty d} \left[\frac{C_\infty Re_{\infty, d} Sc}{\pi}\right]^{\frac{1}{2}} \frac{e^{-\frac{Sc\, Y^2}{4X}}}{\sqrt{X}} .$$

This result assumes a delta function source at the origin and that $w << 1$, i.e., to first order, $U = 1$.

The presence of the rear stagnation point, and the finite width of the mass-concentration profiles at the origin, require the existence of an intermediate-wake region in which the mass-concentration and velocity fields experience a transition from the distributions imposed

at the rear stagnation point by the near-wake flow to their respective asymptotic far-wake distributions given above. In this region, the mass-concentration field is strongly dependent on the boundary conditions at the rear stagnation point, and weakly dependent on the accelerating axial velocity.

To account for the accelerating centerline velocity, the functional form of $U_{\mathbb{C}}(X)$ may be obtained either from the momentum equation or from experimental data. Figure (47) shows the experimental centerline velocity profile for the undisturbed wake, for $Re_{\infty, d} = 0.9 \times 10^4$, together with an analytic representation

$$U_{\mathbb{C}} = \frac{X}{a+X} \quad ,$$

where a is obtained by matching the data at X = 4.0. This form has the proper limiting behavior for small X. For large X it yields the asymptotic limit $w \rightarrow a/X$ as $X \rightarrow \infty$, instead of the limit $w \rightarrow a/\sqrt{X}$ required by the Oseen solution. However, the asymptotic behavior of the velocity field is unimportant in the calculation of the axial mass-concentration decay because the Oseen linearization is used in the asymptotic far field. Similar calculations have not been performed on the data for $Re_{\infty, d} = 3 \times 10^4$ because of the occurrence of transition in the intermediate-wake flow field at this Reynolds number (see Section III-4).

The boundary conditions on the mass-concentration field are illustrated in Figures (41), (45), (48), which show that the mass-concentration profiles in the vicinity of the neck can be described by their centerline mass concentration, which scales directly as the mass

transferred, and by a characteristic width, which is a function of molecular weight and the mode of mass addition. In the physical plane, the characteristic width can be either the half width, $W_{\frac{1}{2}}$, or the wake edge (C_i) defined by the maximum slope intercept with the zero mass concentration level. In the incompressible plane, Figure (48a) shows that for argon the measured transverse mass-concentration profiles in the vicinity of the neck approach a Gaussian form with increasing axial distance. These profiles exhibit a characteristic width $Y = \sigma_c$, for which $C_i/C_{\mathcal{L}} = 1/e$. Further, for argon mass addition, Figures (39), (44) show that the viscous and mass-concentration wake edges nearly coincide. In addition, Figure (40) demonstrates that at a fixed value of X, the ratio $W_{\frac{1}{2}}/(y/d)_e$ is independent of mass addition and hence the lateral scale for the mass-concentration wake depends mechanically on the lateral scale for the viscous wake, i.e. $\sigma_c = \sigma_c(\sigma_u)$ is independent of the mass transfer rate.

The boundary conditions outlined above will now be used to calculate the intermediate-wake centerline mass-concentration distribution for argon mass addition. The results for helium addition are more complex and are not within the scope of the present theory. Those results will be discussed separately below.

Neglecting axial diffusion, which will be justified a posteriori, the species conservation equation on the axis becomes

$$u/D \frac{\partial C}{\partial x} = \frac{\partial^2 C}{\partial y^2} \quad .$$

In addition, conservation of the injected species provides the integral relation

$$\dot{m}_i = 2\int_o^\infty \rho u\, C_i\, dy = \text{const.} \quad .$$

Using the modified Howarth transformations to the incompressible plane given previously, these equations take the form

$$Sc\ U \frac{\partial C}{\partial X} = \frac{\partial^2 C}{\partial Y^2} \quad ,$$

$$\int_N^\infty UC\, dY = \int_X^\infty UC\, dY \quad ,$$

where

$$U = u/u_e$$

$$Sc = \nu/D = \text{const.} \quad .$$

It is convenient at this point to introduce the assumption that both the mass-concentration and the velocity profiles are self-similar, i.e.,

$$\frac{C}{C_{\mathfrak{L}}(X)} = F(Y/\sigma_c(X)) = F(\eta_c) \quad ,$$

$$\frac{1-U}{1-U_{\mathfrak{L}}(X)} = F^*(Y/\sigma_u(X)) = F^*(\eta_u) \quad .$$

Therefore,

$$\frac{\partial^2 C}{\partial Y^2} = \frac{C_{\mathfrak{L}}(X)}{\sigma_c^2(X)} F''(\eta_c) \quad ,$$

and

$$Sc\ U\ F_o \frac{d\, C_{\mathfrak{L}}(X)}{dX} = \frac{C_{\mathfrak{L}}(X)}{\sigma_c^2(X)} F_o'' \quad .$$

The integral equation then yields the algebraic result

$$\sigma_c(X) = \frac{\sigma_{c_N} C_N [b + U_N]}{C_{\mathfrak{L}}(X)[b + U_{\mathfrak{L}}(X)]} \quad ,$$

where

$$b = \frac{\int_0^\infty F(\eta_c)d\eta_c}{\int_0^\infty F(\eta_c)F^*(\eta_u)d\eta_c} - 1 \quad .$$

To simplify the calculations, it is assumed that the scales for the velocity and the mass-concentration profiles are the same, and that both possess Gaussian distributions (see Figure (48)), i.e.,

$$F(\eta) = F^*(\eta) = e^{-\eta^2} \quad ,$$

and $$\sigma_c(X) = \sigma_u(X) \quad .$$

As a consequence,

$$b = \sqrt{2} - 1 \quad .$$

Since $F_o = 1$, $F_o'' = -2$ for a Gaussian profile; therefore,

$$Sc\ U_{\mathbb{C}_L}(X)\ \frac{d\,C_{\mathbb{C}_L}(X)}{dX} = -\frac{2\,C_{\mathbb{C}_L}(X)}{\sigma(X)^2} \quad .$$

Using the expression for $\sigma(X)$, the equation becomes

$$\frac{[b+U_{\mathbb{C}_L}(X)]^2}{U_{\mathbb{C}_L}(X)}\,dX = -\frac{Sc\,\sigma_N^2 C_N^2}{2}[b+U_N]^2\,\frac{d\,C_{\mathbb{C}_L}(X)}{C_{\mathbb{C}_L}(X)^3} \quad .$$

Using the assumed analytic form for the axial velocity $U_{\mathbb{C}_L}(X)$, the differential equation is directly integrable. If the origin and the boundary conditions are taken at the neck, the solution becomes

$$\frac{C_{\mathbb{C}_L}(\xi)}{C_N} = \left\{1 + \frac{8}{Sc\sigma_N^2[b+U_N]^2}\left[\xi - \frac{a}{2}\ell n\left(\frac{a+X_N+\xi}{a+X_N}\right) + \left(\frac{3}{2} - \sqrt{2}\right)a\,\ell n\left(\frac{X_N+\xi}{X_N}\right)\right]\right\}^{-\frac{1}{2}},$$

where

$$\xi = X - X_N \quad .$$

The nature of the solution is best determined by examining the behavior of the solution for large and small ξ. For small ξ,

$$\frac{C_{\mathbb{C}}(\xi)}{C_N} \rightarrow 1 - \beta\,\xi \quad ,$$

where $$\beta = \frac{8}{Sc\,\sigma_N^2\,[b+U_N]^2}\left[1 - \frac{a}{2(a+X_N)} + \left(\frac{3}{2} - \sqrt{2}\right)\frac{a}{X_N}\right] .$$

For large ξ,

$$\frac{C_{\mathbb{C}}}{C_N} \rightarrow (\beta^*\xi)^{-\frac{1}{2}} \quad ,$$

where $$\beta^* = \frac{8}{Sc\,\sigma_N^2\,[b+U_N]^3} \quad .$$

Thus, for large ξ the solution approaches the decay law given by the Oseen linearized solution, while for small ξ the decay is less rapid.

Although, as shown in Figure (48a), the transverse mass-concentration profiles are bell-shaped at the neck, the axial decay cannot be adequately represented by calculating the transverse profile curvature on the axis from the curvature of the Gaussian profile fitted to the data at $C/C_N = 1/e$. To improve the accuracy of the theoretical estimate, an effective value of the curvature at the neck is calculated by fitting the solution for the axial decay to the data at $\xi = 8$, and in this way accounting both for the initial non-Gaussian behavior of the transverse profiles, and for the effects of finite aspect ratio discussed in Section IV. 4. The results for the axial decay are shown in Figures (49) and (50) for the case of argon addition from both the forward and the base stagnation regions. The difference in the axial decay for the two modes of injection is a consequence of the differences in the initial profile width, σ_N, at the neck.

For the addition of helium, the present theory is inadequate in two respects. First, Figure (48b) demonstrates that, irrespective of the mode of mass transfer, the transverse distribution of helium mass concentration in the vicinity of the neck deviates greatly from the self-similar Gaussian form. Second, near the origin the axial diffusion term becomes important and must be included in the analysis. More specifically, the analysis presented above assumes that axial diffusion is negligible, i. e.,

$$\frac{\partial^2 C}{\partial x^2} \Big/ \frac{\partial^2 C}{\partial y^2} \ll 1 \quad .$$

Transforming to the incompressible plane,

$$\frac{\partial^2 C}{\partial x^2} \Big/ \frac{\partial^2 C}{\partial y^2} = \frac{C_\infty}{Re_{\infty,d}} \left[\frac{T_{\mathfrak{L}}(X)}{T_\infty}\right]^2 \frac{\partial^2 C}{\partial X^2} \Big/ \frac{\partial^2 C}{\partial Y^2} \quad .$$

From the solution, near $\xi = 0$, this becomes,

$$R = \frac{\partial^2 C}{\partial x^2} \Big/ \frac{\partial^2 C}{\partial y^2}$$

$$\approx -\frac{24\, C_\infty}{Re_{\infty,d}} \left[\frac{C_{\mathfrak{L}}(X)}{C_N}\right]^4 \left[\frac{T_{\mathfrak{L}}(X)}{T_\infty} \cdot \frac{\sigma(X)}{Sc\, q_N^2 [b+U_N]^2}\right]^2 \left[1 - \frac{a}{2(a+X)} + \frac{(\frac{3}{2} - \sqrt{2})a}{X}\right]^2 .$$

This ratio may be evaluated from the solution and gives, for base mass transfer of argon, $R = 1.6 \times 10^{-2}$ for $\xi = 0$, and $R = 1.95 \times 10^{-3}$ for $\xi = 4.0$. Using the same solution for helium, however, $R = 0.630$ for $\xi = 0$, and $R = 4.5 \times 10^{-3}$ for $\xi = 4.0$. Therefore, the near-field solution, $\xi \to 0$, obtained above is invalid for helium addition. The far-field solution is valid, however, and will be used to determine the virtual origin for the asymptotic far wake in the following discussion.

For the mass-concentration wake, the virtual origin, ξ_o, is defined as the intercept with the line $C_{\mathcal{L}}/C_N = 1.0$ of the extrapolation of the asymptotic solution $C_{\mathcal{L}}/C_N \rightarrow (\beta^* \xi)^{-\frac{1}{2}}$, shown as a straight line of slope $-\frac{1}{2}$ in the log-log plot in Figure (50). From the solution,

$$\xi_o = 1/\beta^* \sim Sc\ \sigma_N^2 \quad ,$$

as shown by the extrapolation of the solution curve in Figure (50). Figure (51) demonstrates this dependence for the data for argon and includes a single data point for helium addition from the base. The point $\sigma_N = 0$ corresponds to the source solution of the Oseen linearized equations.

For mass addition from the forward stagnation point, the data in Figures (40), (45) show that the virtual origin is independent of the mass transfer rate. For base mass addition, the virtual origin moves slowly rearward with increasing mass transfer primarily as a consequence of the increase in the width of the viscous layer, demonstrated in Figures (29), (41), with a secondary influence caused by the changes in the axial velocity profile with increasing base mass transfer.

IV. 4. Mass Balance

As a quantitative check on the mass-concentration profiles in the near wake, a mass balance of the form

$$\frac{\dot{m}_{calc.}}{\dot{m}_i} = \frac{2}{\dot{m}_i} \int_o^\infty \rho u\, C_i\, dy$$

has been calculated using the measured, corrected Pitot and static pressures, and assuming $\gamma = 1.4$, as discussed in Appendix D. The integral was evaluated in the vicinity of the neck, and gives the result

that, for $Re_{\infty, d} = 3 \times 10^4$ at $x/d = 3.0$, the ratio of the calculated mass flux to the injected mass is $\dot{m}_{calc.}/\dot{m}_i = 0.7705$, for argon at $I = 4.28 \times 10^{-2}$. This result implies a loss of 23% of the injected mass.

The above calculation assumes a uniform spanwise mass-concentration distribution that terminates abruptly at the fences. This is, in fact, not the case. Within the recirculating zone, the measurements of the spanwise pressure distribution shown in Figure (5) demonstrate that the fences effectively isolate the central portion of the flow. However, measurements of the spanwise static-pressure distribution in the vicinity of the neck by Ramaswamy* show that an outflow exists near the fences. This outflow is of sufficient magnitude that an oil flow pattern is observed around the fences in the vicinity of the neck. Lateral diffusion, coupled with this lateral convection toward the side walls of the tunnel, generates a non-uniform spanwise mass-concentration profile that extends from the centerline to the tunnel side wall, bypassing the fences in the region downstream of reattachment.

The finite aspect ratio has no influence on the mass concentrations in the near wake because the fences isolate the recirculating flow. Downstream, in the vicinity of the neck, however, spanwise diffusion and mixing increase the rate of decay of the centerline mass concentration with increasing axial distance, but are not expected to influence the normalized transverse distribution. The rate of deviation from an ideal two-dimensional flow will be most pronounced in the vicinity of the neck, where the increased static pressure enhances the

* Ramaswamy, M. A.: Private Communication

spanwise convection. The three-dimensional nature of the flow in the intermediate wake is accounted for in the solution presented above by a decrease in the effective value calculated for σ_N through the matching of the solution to the experimental data.

In the ideal case, far downstream, the spanwise profile will again become uniform with a value of 60% of the value expected in the absence of spanwise diffusion, as a consequence of the increase of the spanwise dimension. This region is beyond the range of the present measurements, however. No quantitative estimate has been made of the effect of the three-dimensional nature of the flow on the axial mass-concentration distribution because of the important contribution of the unknown spanwise convection.

V. SUMMARY AND EXTENSION OF RESULTS

V. 1. The Near-Wake Flow

Forward Stagnation Region Mass Transfer

Mass addition from the forward stagnation region has no measurable influence on the near-wake pressure field for moderate mass transfer rates.

The species transferred from the forward stagnation region enter the near wake through mass-concentration boundary layers whose thickness upstream of separation is comparable to the viscous boundary-layer thickness. The extensions of these boundary layers into the near-wake flow are the narrow mass-transport layers which provide the outer boundary conditions on the mass-concentration field in the region of reversed flow, and which dominate the transport of mass into the outer flow.

Because there is no source in the base region, the dividing streamline is closed, and the distribution of mass concentration within the recirculating flow is determined primarily by the mass-concentration distribution on the dividing streamline. As a consequence of diffusion, the resulting mass-concentration field in the region of reversed flow is nearly uniform in the transverse direction. The axial mass-concentration profile in this field decays weakly downstream from the base as a consequence of the decrease in the mass concentration along the dividing streamlines by diffusional loss through the outer transport layers, and the subsequent convection toward the base of the resulting lower mass concentration gas in the vicinity of the rear stagnation point.

The transverse mass-concentration profiles that result in the near wake exhibit an overshoot in the vicinity of the $\psi = 0$ streamline, and possess a transverse scale comparable to that defined by the viscous shear-layer edge.

As a consequence of the convergence of the viscous shear layers in the vicinity of the rear stagnation point, the transverse mass-concentration profiles downstream of the rear stagnation point asymptotically approach a Gaussian form in the incompressible plane. The lateral scale of these profiles is independent of mass transfer rate, and the magnitude increases linearly with the mass transfer rate.

Base Mass Transfer

For the range of mass transfer rates investigated, a recirculating vortex exists in the near-wake flow, and mass addition from the base produces a change in the base pressure proportional to the momentum flux of the injected species. The mechanism which determines this change is the establishment of a stagnation point off the base, formed by the balance of momentum between the injected fluid and the reversed flow, and the consequent impression of the injected fluid on the free shear layer near separation. The generalization of the base pressure, or characteristic near-wake pressure, is the pressure at the base stagnation point. This pressure, and the influence of mass addition on the entire near-wake flow field, are completely correlated by the ratio of the momentum flux of the injected fluid to the momentum flux in the cylinder boundary layer upstream of separation, through the parameter

$$I = \frac{\dot{m}_i}{2\dot{m}_{B.L.}}\sqrt{\frac{\mathcal{M}_{Air}}{\mathcal{M}_i}} = \frac{\text{const}\,\dot{m}_i}{\sqrt{Re_{\infty,d}}}\sqrt{\frac{\mathcal{M}_{Air}}{\mathcal{M}_i}} \quad .$$

The near-wake mass-concentration field for mass addition from the base is determined by the counter-current diffusion of the injected species against the recirculating flow. Because the product $ReSc \approx 0(1)$ for the reversed flow, the resulting axial mass-concentration profile decays rapidly downstream from the base with a characteristic length scale of the order of the separation distance between the two stagnation points.

In the region between the two stagnation points both the axial and the transverse diffusion terms must be retained in the axial species conservation equation, hence the solution of the equation depends on the value of mass-concentration at both stagnation points. The boundary conditions at the base are imposed directly by the mass transfer, while the boundary conditions at the rear stagnation point are determined by the outer transport layer in a manner similar to that for mass addition from the forward stagnation region. The outer transport layer is coupled to the reversed flow through the mass-concentration boundary condition imposed by the flow in the vicinity of the u=0 locus.

In the vicinity of the rear stagnation point, the transverse mass-concentration profiles again asymptotically approach a Gaussian form in the incompressible plane in a manner analogous to that for mass addition from the forward stagnation region. The lateral scale of these profiles is a function both of the boundary conditions on the body and of the mass transfer rate.

V. 2. The Intermediate-Wake Region

In the intermediate-wake region, immediately downstream of the neck, the effects of mass addition from the forward stagnation region, and from the base, are unified in a single theory. In this region, for the addition of argon, the axial diffusion terms are negligible, and the mass-concentration field in the incompressible plane takes the form

$$C_i = C_{\underline{C}}(\xi)\, e^{-Y^2/\sigma(\xi)^2} \quad ,$$

where,

$$\frac{C_{\underline{C}}(\xi)}{C_N} = \left\{ 1 + \frac{8}{Sc\, \sigma_N^2 [b+U_N]^2} \left[\xi - A\, \ell n \left(\frac{B+\xi}{B}\right) + C\, \ell n \left(\frac{D+\xi}{D}\right) \right] \right\}^{-\frac{1}{2}} ,$$

$$\xi = X - X_N$$

The influence of the near-wake flow occurs through the boundary conditions at the neck in the profile parameter σ_N, which depends strongly on the mass-transfer boundary condition on the body.

The asymptotic far-wake solution, valid for any molecular weight, corresponds to that for the diffusion from a point source located at a virtual origin which depends on the boundary conditions. The intermediate-wake result establishes that the location of the virtual origin is proportional to the parameter $Sc\, \sigma_N^2$, where $\sigma_N = 0$ corresponds to a delta function source at the neck, $\xi = 0$.

V. 3. The Regimes of Mass Transfer

For mass addition from the base, three regimes of mass transfer in separated flows have been proposed, both here and in the literature.

For the first two regimes, the mass entrainment required by the shear layers is not satisfied by the mass addition, and a distinct recirculating vortex will exist.

The first regime is defined by the fact that the momentum flux of the injected fluid is negligible compared to the momentum flux in the reversed flow. Under these conditions, Chapman's[16] arguments, that the base pressure changes through the effect of mass addition on the entrainment in the shear layers, are valid and lead to the dependence of the base pressure on the mass flux of the injected fluid. However, on the basis of the present experiments, this regime does not exist for the near-wake of a circular cylinder. Furthermore, it is felt that if this regime does exist for experimentally realizable separated flows, it will occur only as a limiting case.

In the second regime, the subject of the present investigation, the momentum flux of the injected fluid is comparable to the momentum flux in the reversed flow, and determines the changes in the pressure field with mass transfer through the interaction of the injected fluid with the subcritical free shear layer. A qualitatively similar region is expected to exist for the case of mass addition from the base of a slender wedge, for example, despite the differences imposed by the supercritical expansion and catastrophic separation from the nearly fixed separation point (cf. Batt,[20] Hama[31]). For the wedge, the characteristic momentum flux is that associated with the inner viscous layer (cf. Batt); although, for laminar flow, the proper Reynolds number scaling may also be obtained by considering the boundary-layer momentum flux, as in the case of a circular cylinder.

For the third regime, the mass entrainment in the shear layers is satisfied by the injection, and no recirculating flow exists. For this regime, the absence of a rear stagnation point implies that the momentum of the injected species no longer determines the changes in the pressure field, and that the near-wake field is determined by the mixing of two nearly parallel streams. The measurements of Chapkis, et. al.,[14] Lewis and Behrens,[32] and Lewis and Chapkis[33] for a slender wedge show that, in this regime, for both laminar and turbulent flow, the axial static pressure is approximately constant near the body and correlates with the volume flow of the injected species. The results for a circular cylinder are expected to be qualitatively similar. Herzog[12] has shown for the cylinder that, for mass transfer rates in this regime, the axial static pressure near the body is nearly constant, although no molecular weight correlation was attempted.

Previously Chow,[34] and Fuller and Reid,[35] have reported the existence of distinct regimes in the correlation of base pressure with increasing mass addition; however, in each case insufficient evidence is exhibited to determine whether there is a one-to-one correspondence with the regimes described above.

V. 4. Suggestions for Future Research

On the basis of the present experiments, several related investigations are suggested which will increase our understanding of mass addition in separated flows:

1. further experimental investigation of the influence of molecular weight on the near-wake pressure field to establish the range of validity of the three mass transfer regimes delineated above, and to

further define the mechanism occurring in each regime.

2. an experimental investigation of the wakes of slender bodies with mass addition to determine the influence of body geometry on the behavior of the pressure and mass-concentration fields.

3. an extension of the theoretical investigation of Klineberg[3] to include the effects of mass and heat transfer, utilizing the experimental results as a guide in choosing the profile functions, and in ordering the terms in the equations.

4. further theoretical and experimental investigations of the effects of mass addition on the stability of wake flows.

5. experimental investigations of the compressible free shear layer which include the effects of the mixing of dissimilar gases for both laminar and turbulent flow.

TABLE 1

Summary of Flow-Field Constants:

P_o(Nominal)	25	80
$Re_{\infty, d}$ (a)	0.905×10^4	2.953×10^4
M_∞	6.047	6.084
T_o(^oK)	408	408
P_o(psia)	24.4	79.4
μ_∞/μ_r (b)	0.20	0.195
$\dot{m}_{B.L.}$ $\frac{\#}{in\text{-}sec}$ (c)	4.28×10^{-5}	7.56×10^{-5}
$\dot{m}_f$ $\frac{\#}{in\text{-}sec}$ (c)	1.737×10^{-3}	5.510×10^{-3}

(a) $d = 0.200$ in.

(b) $\mu_r = 9.6093 \times 10^{-7}$ $\frac{\#}{in\text{-}sec}$ Lennard-Jones model after McCarthy[7], Figure 61.

(c) Mass flux per unit span. See Appendix C.

$M_\infty = 6.0$

$Re_{\infty,d} = 6.65 \times 10^4$

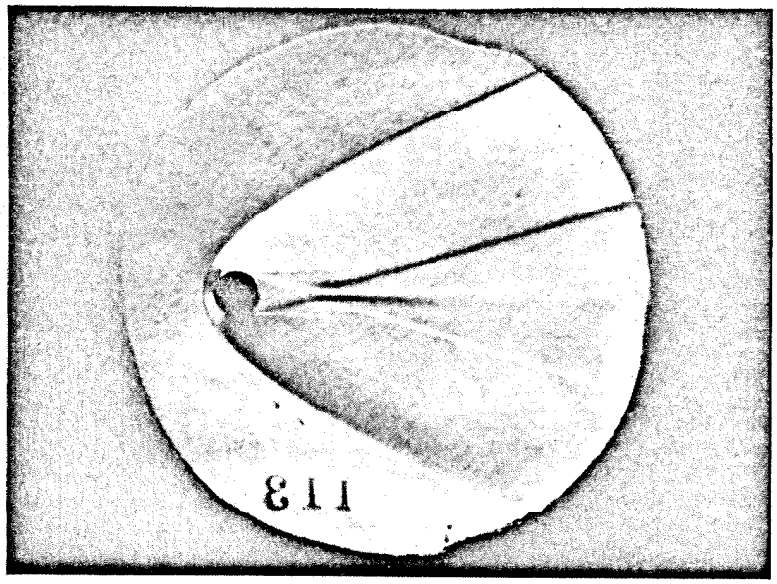

a. Schlieren Photograph Ref. 7

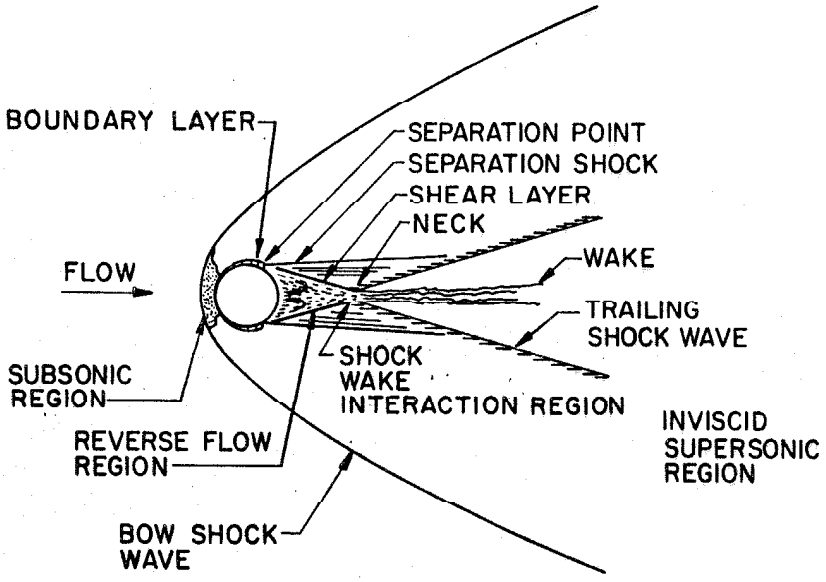

b. Flow Field Schematic Ref. 12

Fig. 1 HYPERSONIC FLOW OVER A CIRCULAR CYLINDER

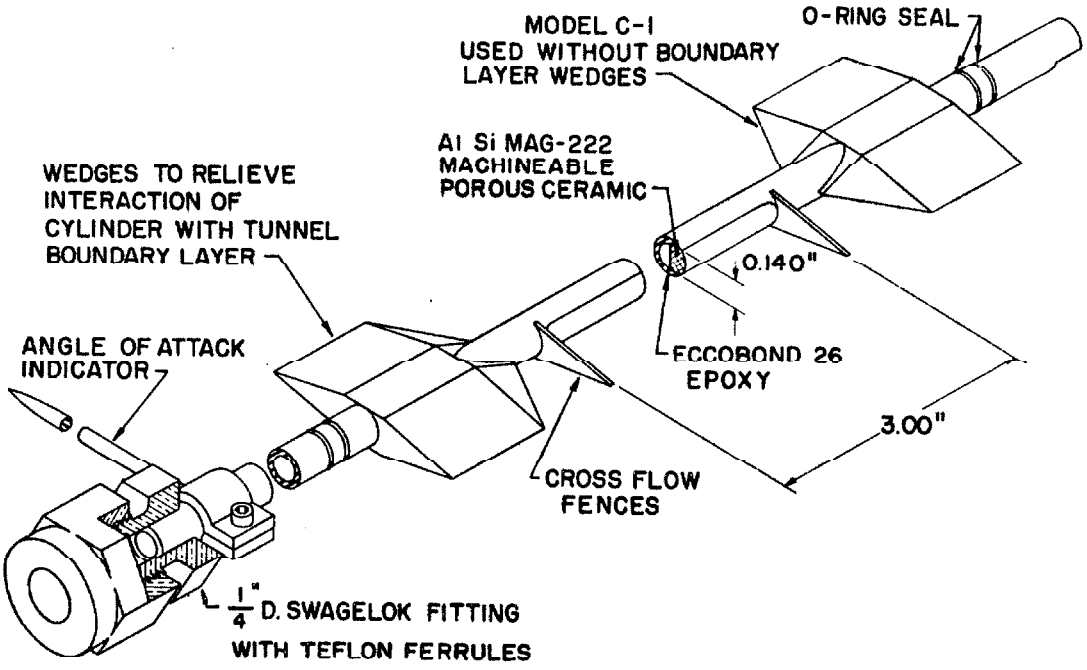

a. POROUS INJECTION MODELS C-1, C-4

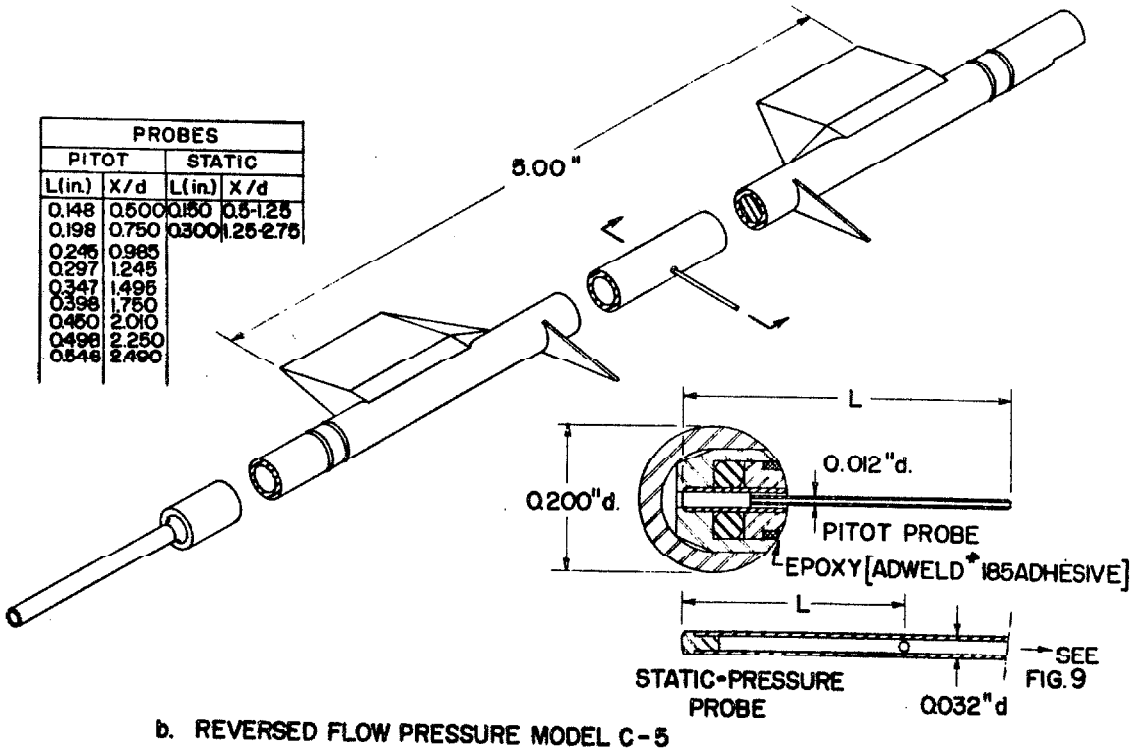

b. REVERSED FLOW PRESSURE MODEL C-5

Fig. 2 WINDTUNNEL MODELS

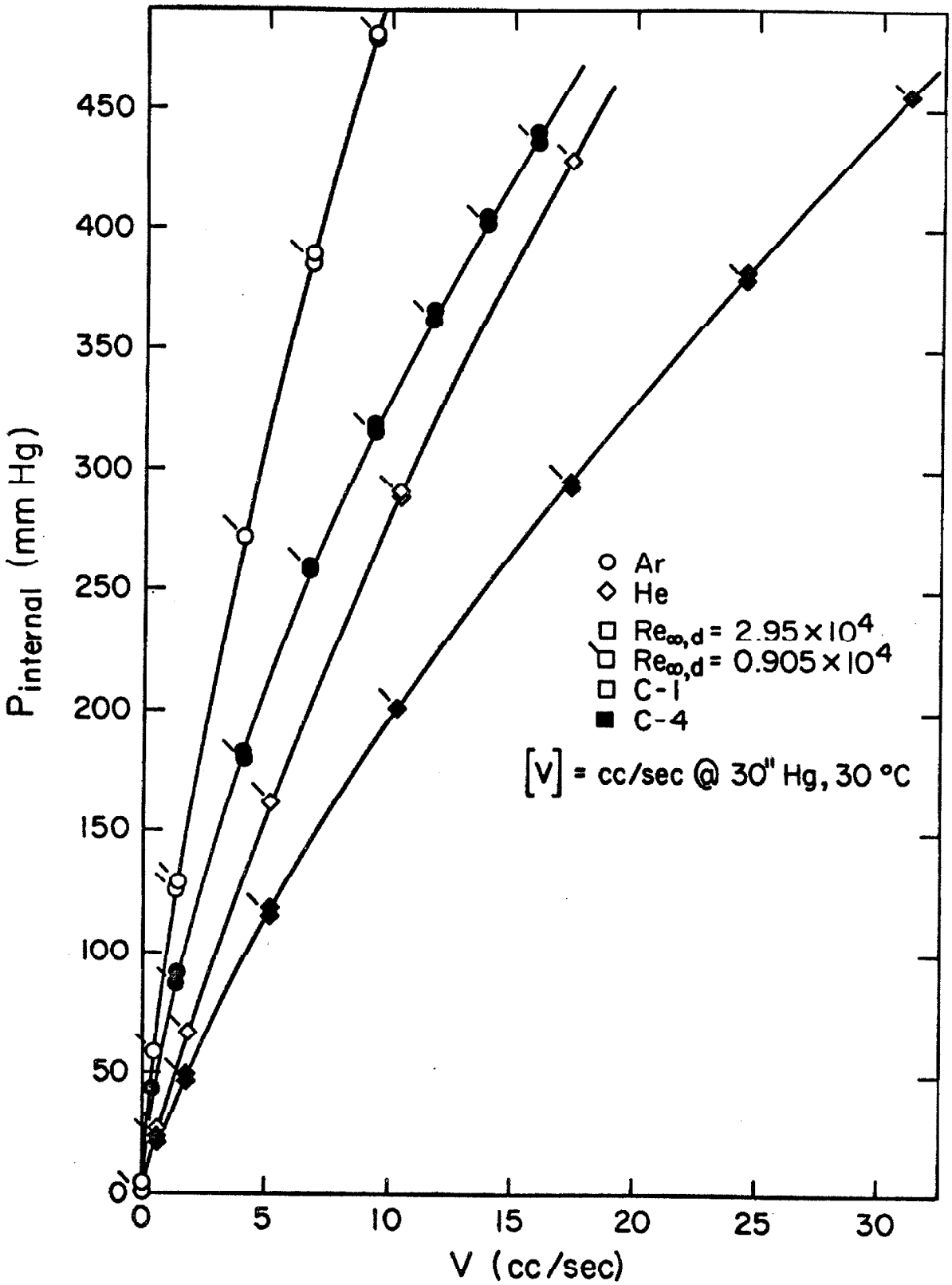

Fig. 3 MODEL PLENUM PRESSURE

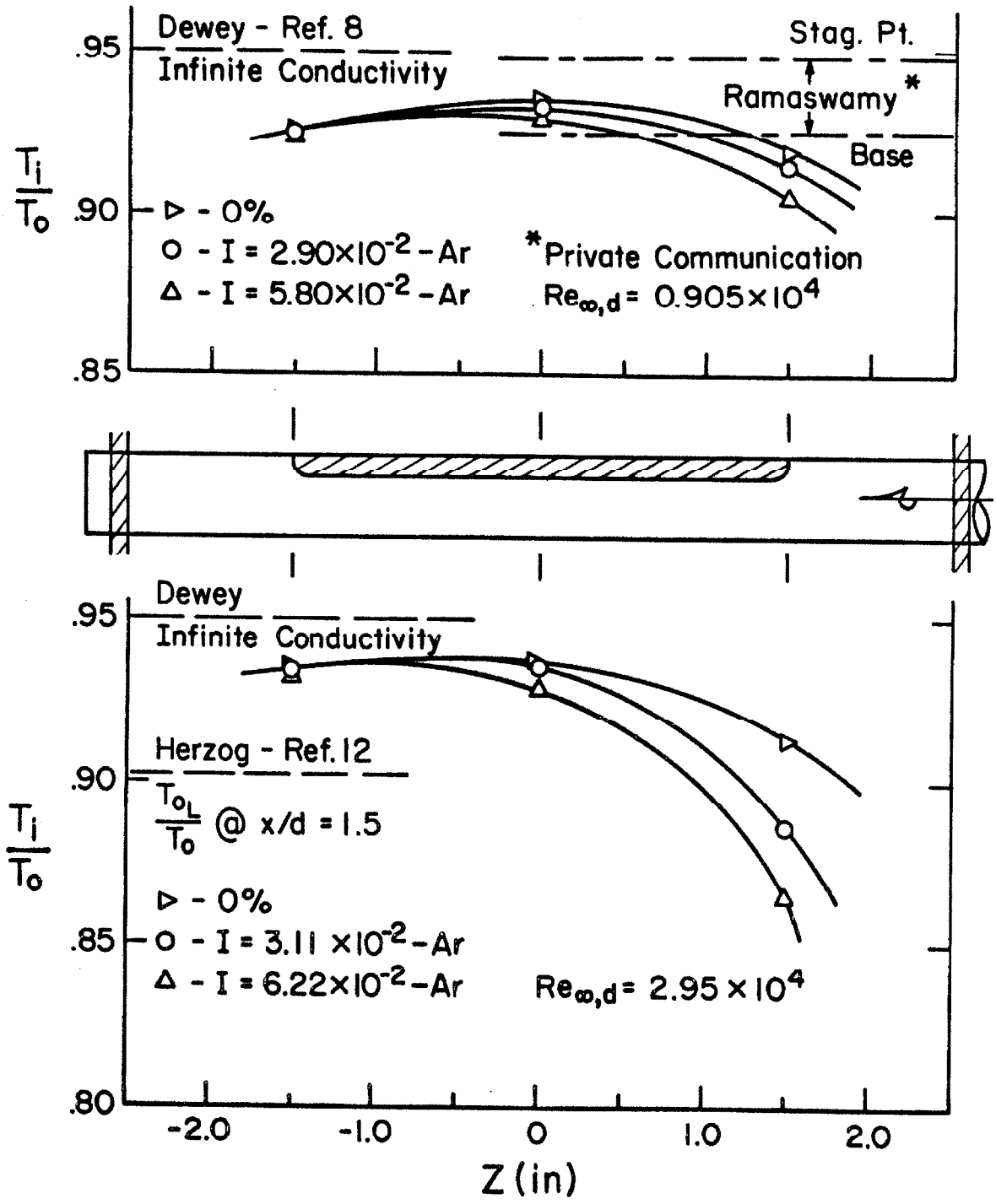

Fig. 4 MODEL PLENUM TEMPERATURE

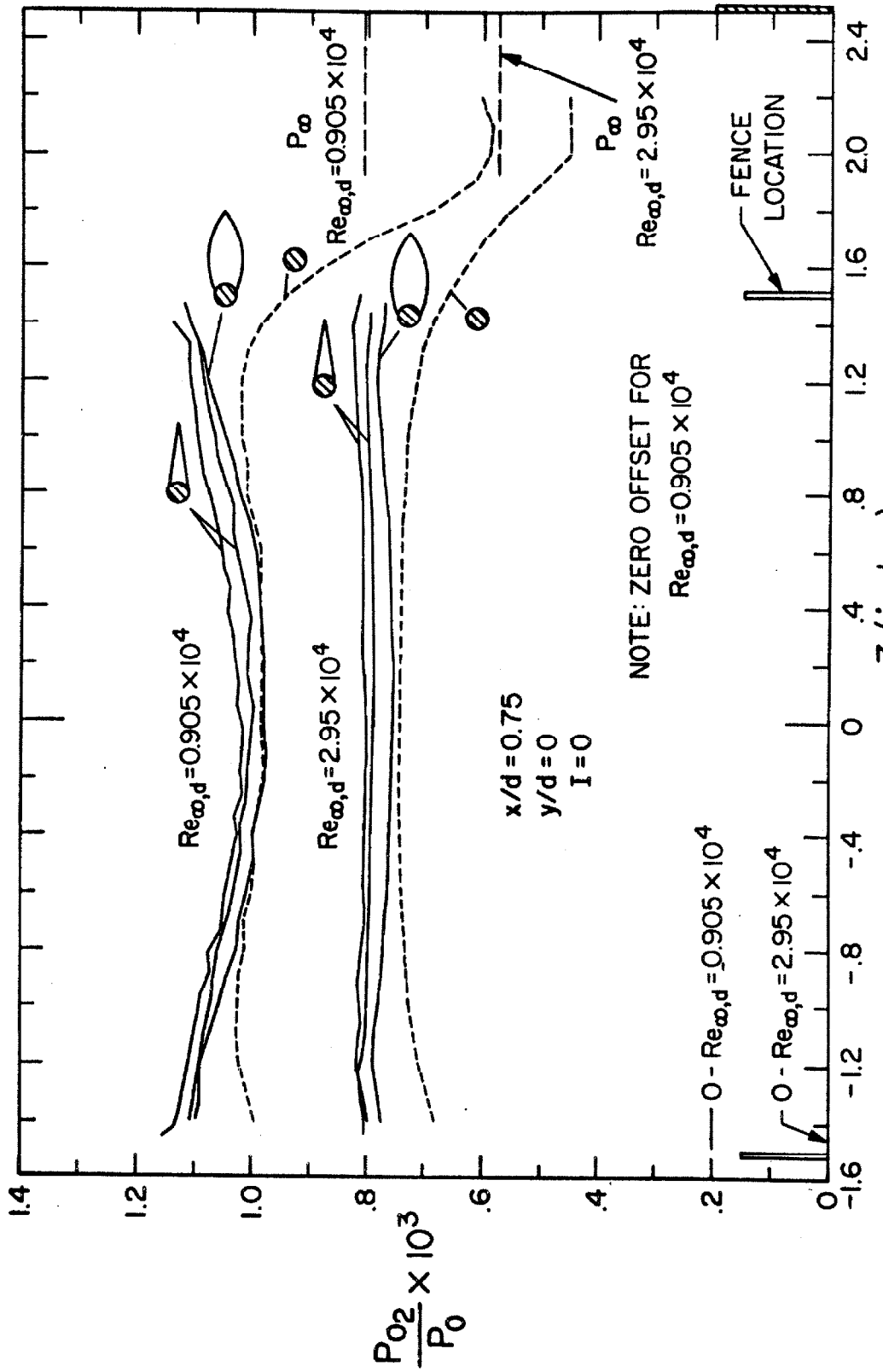

Fig. 5 EFFECT OF FENCE GEOMETRY ON THE SPANWISE DISTRIBUTION OF BASE PRESSURE

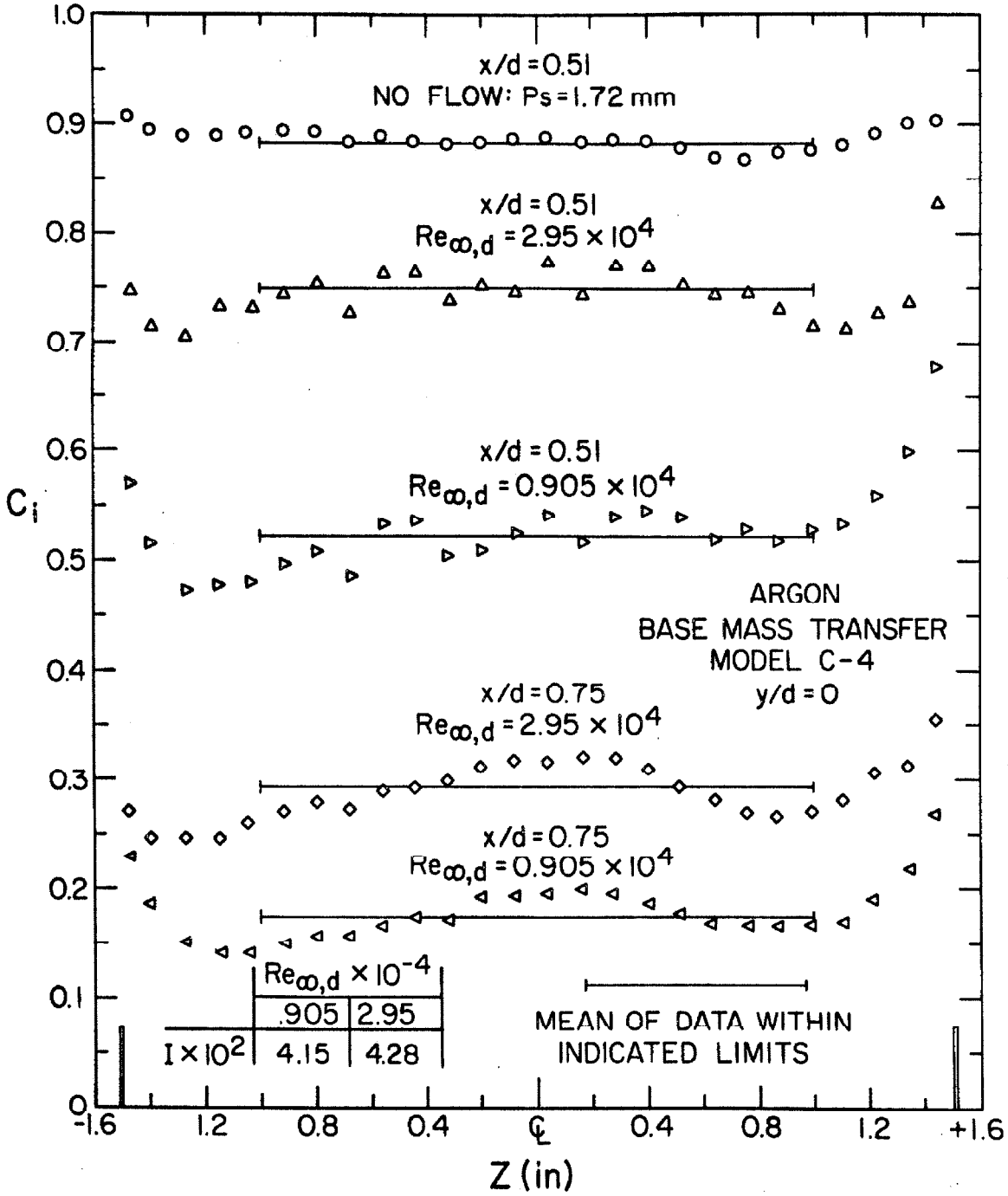

Fig. 6 NEAR-WAKE SPANWISE MASS-CONCENTRATION DISTRIBUTION

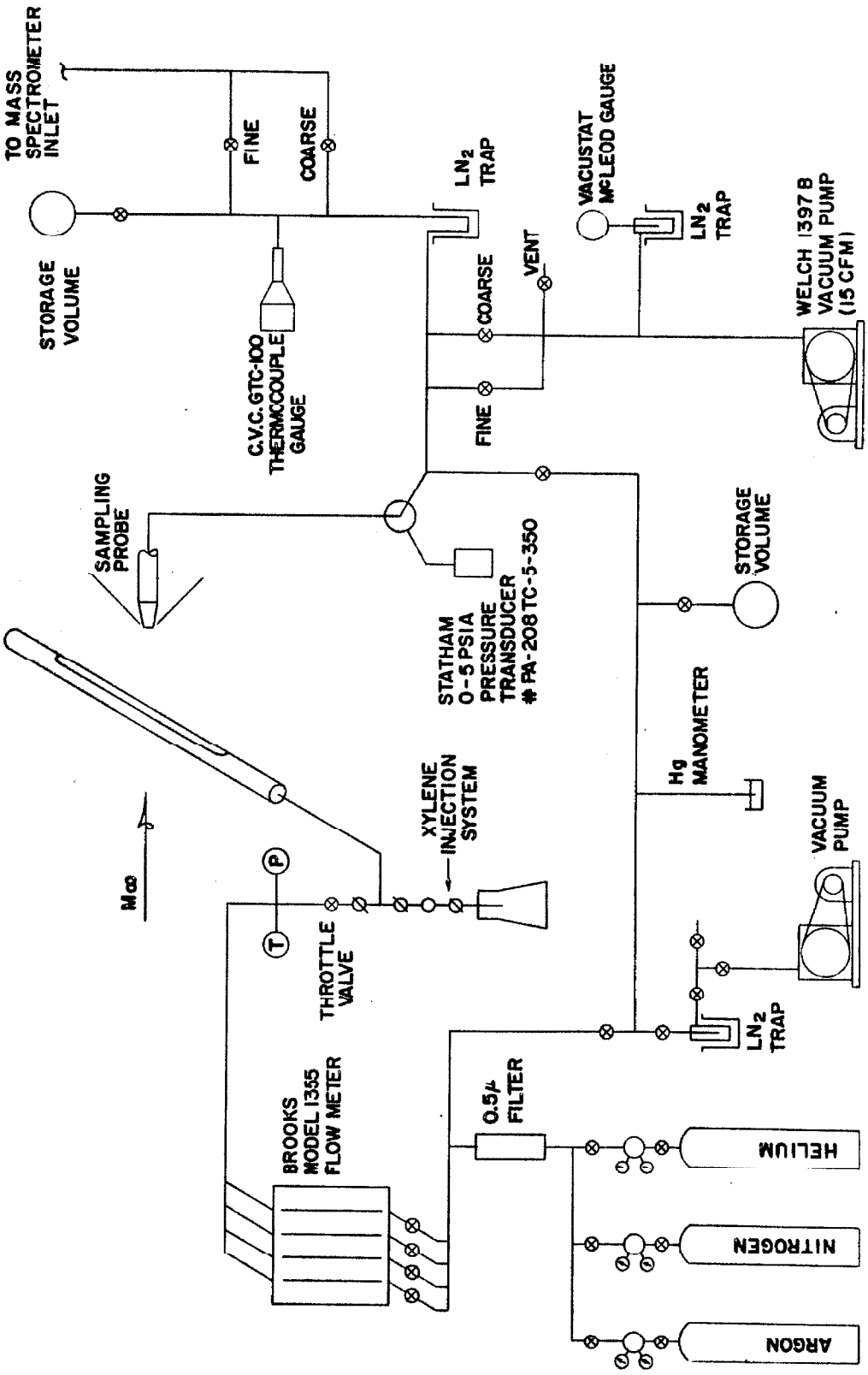

Fig.7 MASS INJECTION AND SAMPLING INLET APPARATUS

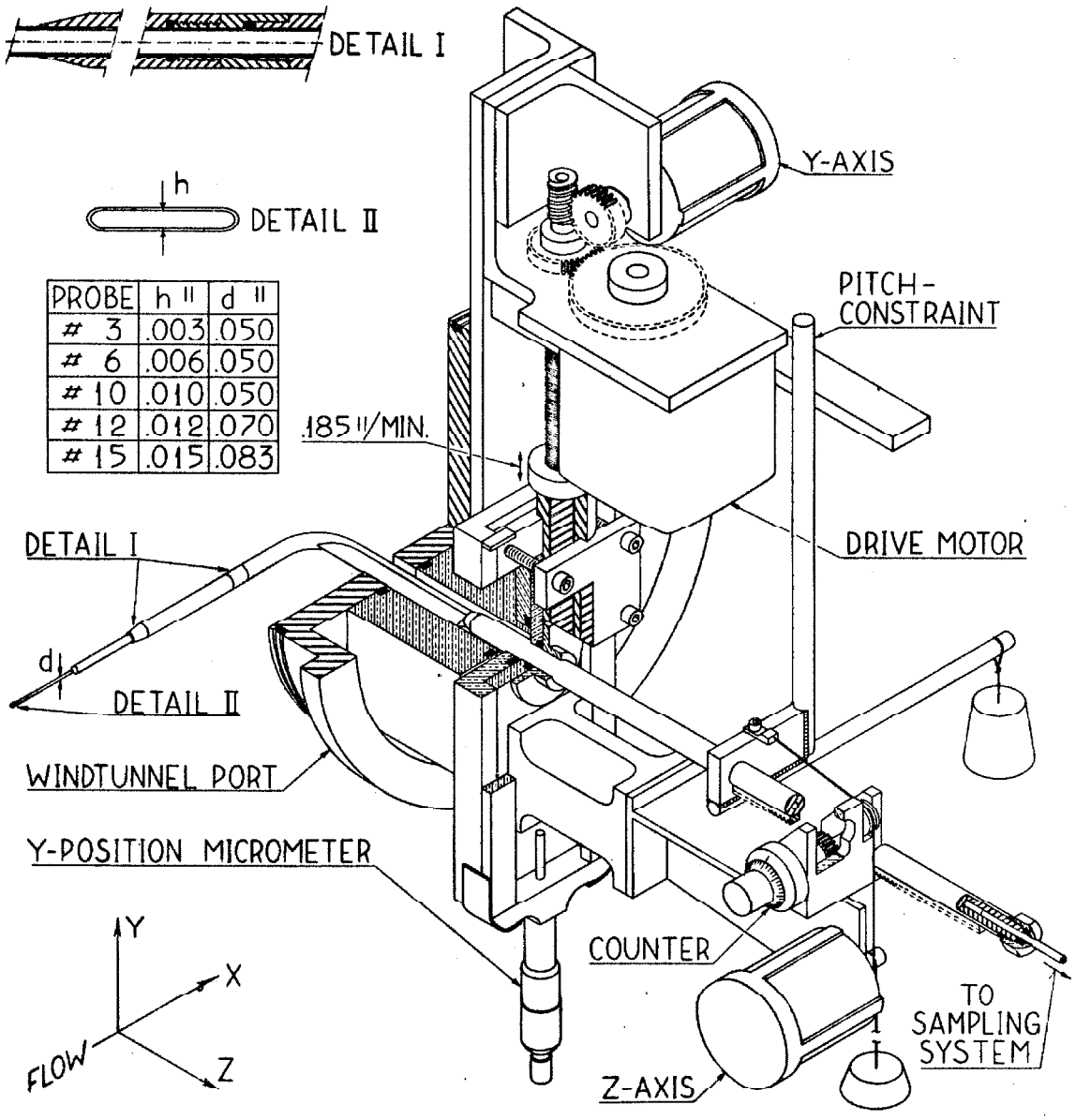

FIGURE 8
SPANWISE TRAVERSE MECHANISM

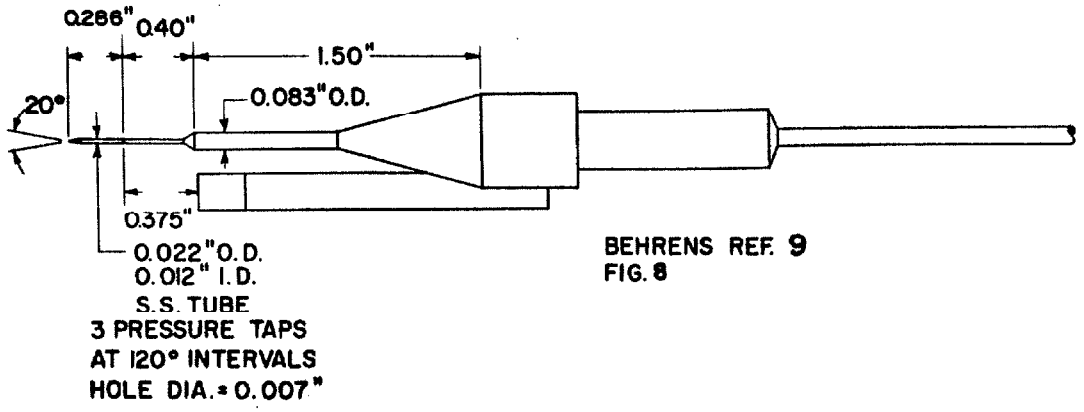

a. FAR-WAKE STATIC PROBE

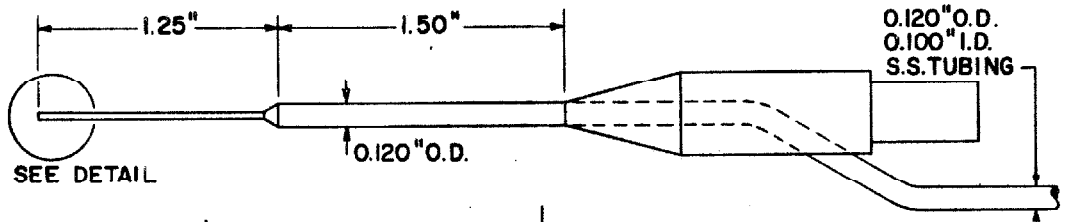

b. STATIC PROBES

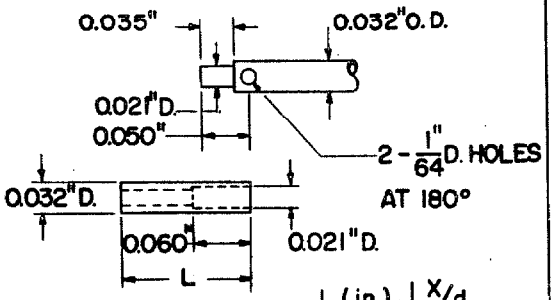

L (in.)	X/d
0.035	0.75
0.085	1.0
0.135	1.25
0.185	1.50
0.235	1.75
0.285	2.0-3.0

c. PITOT-SAMPLING PROBES

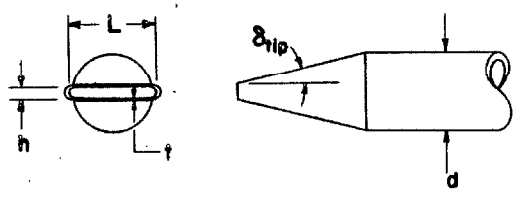

h (in.)	L (in.)	d (in.)	δ tip	t (in.)
0.002	0.043	0.050		< 0.001
0.003	0.043	0.050	4.66°	0.003
0.005	0.042	0.050	12.60° (SHANK 3.166°)	0.002
0.009	0.0920	0.083	6.40°	0.0015
0.013	0.0915	0.083	4.875°	0.0018

Fig. 9 PRESSURE AND SAMPLING PROBES

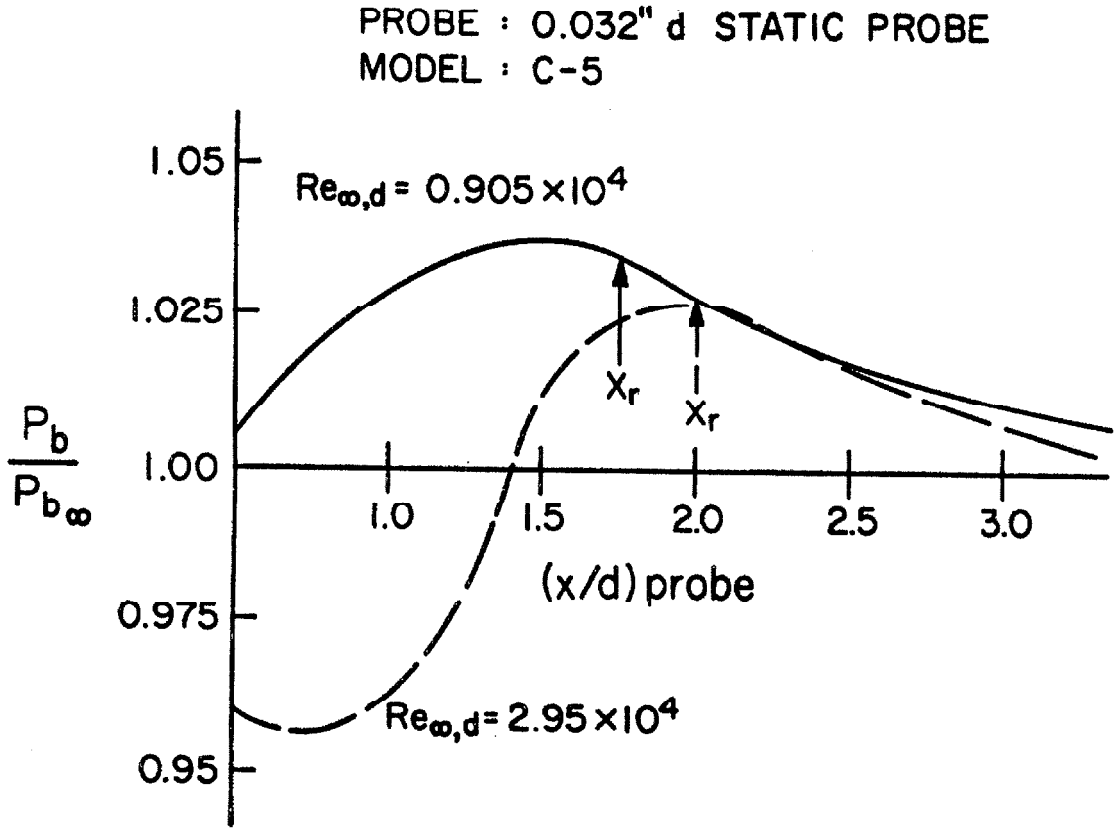

Fig. 10 EFFECT OF PROBE ON MEASURED BASE PRESSURE

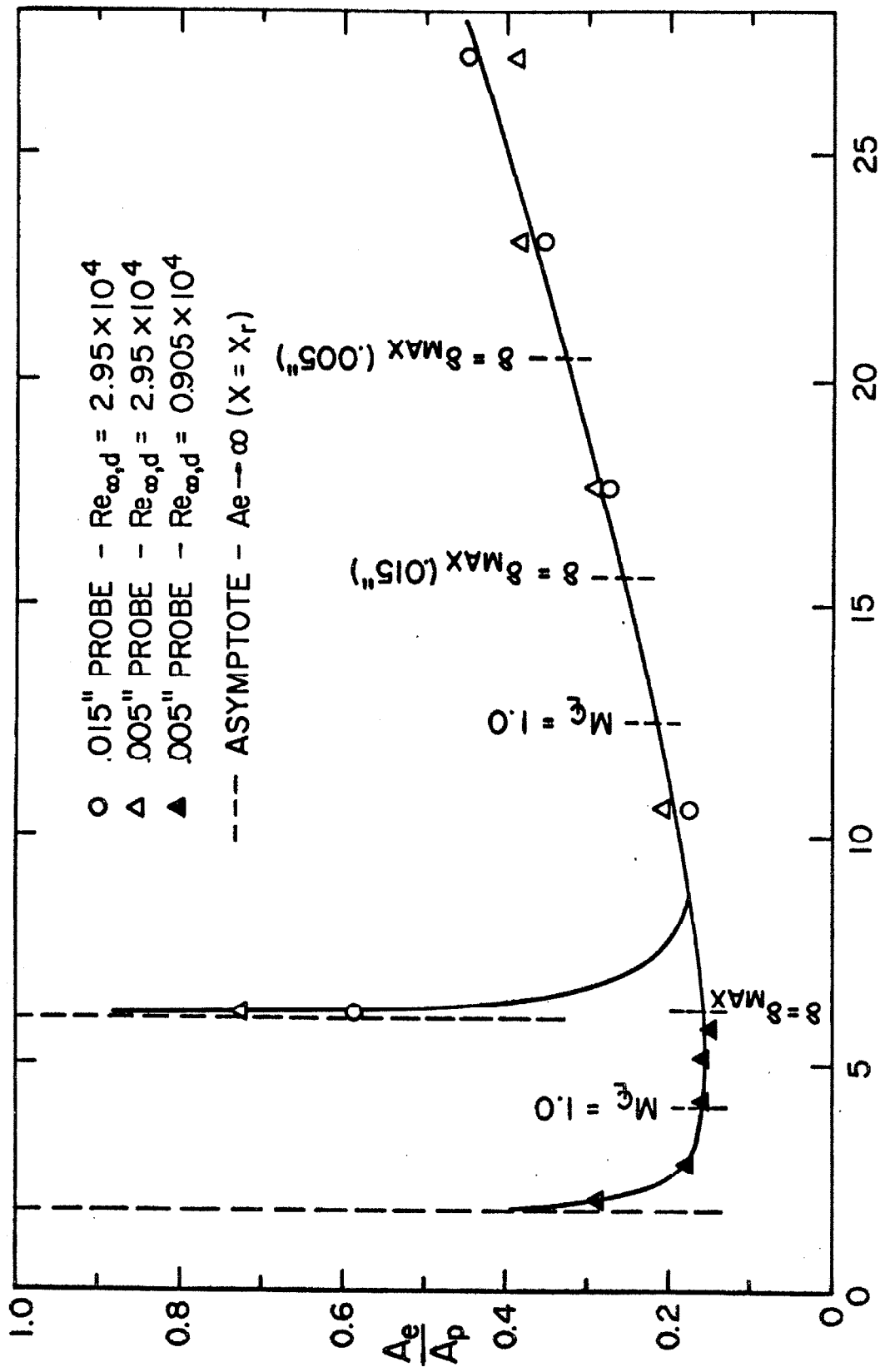

Fig.11 THE EFFECTIVE AREA OF THE SAMPLING PROBE

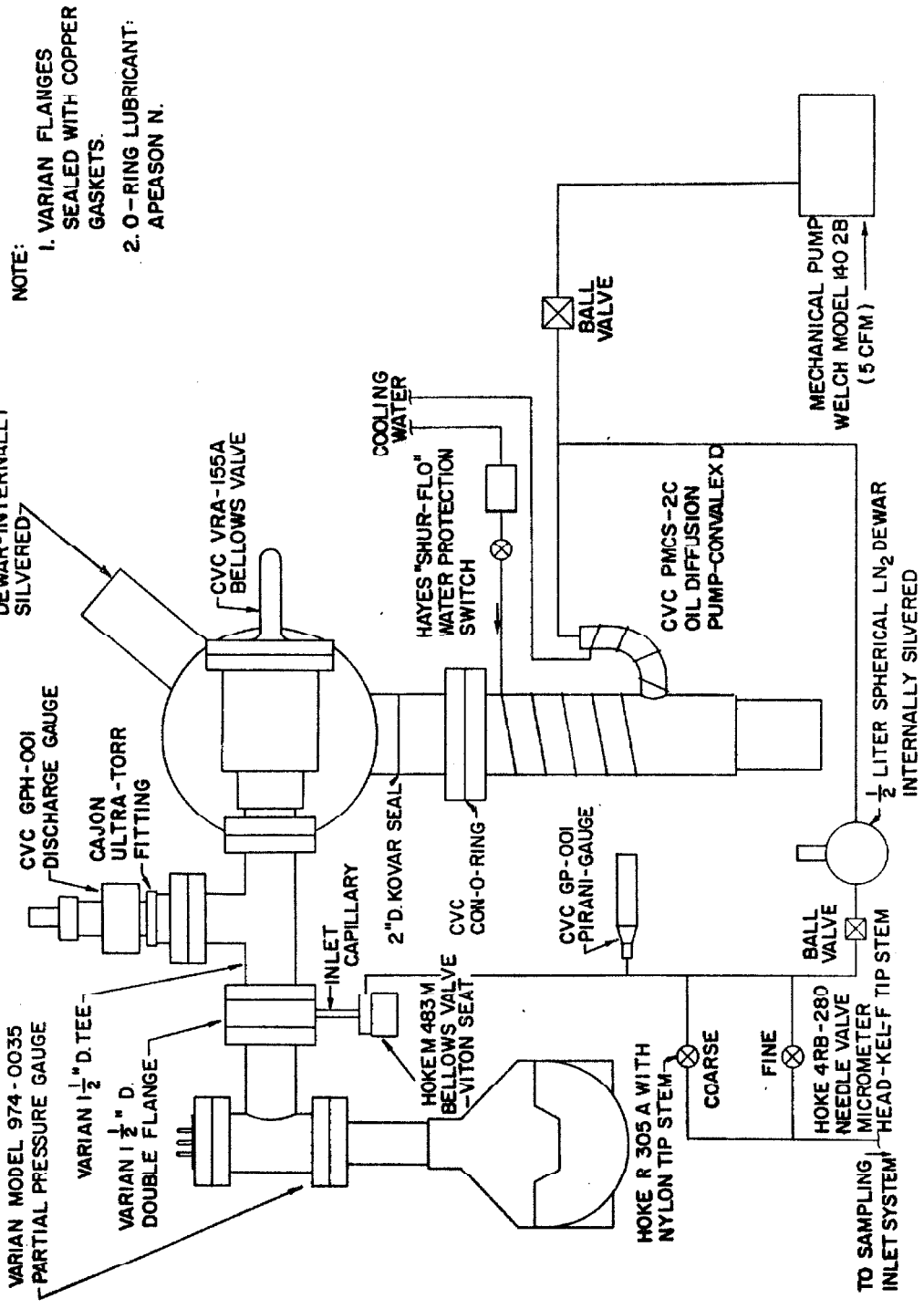

Fig.12 MASS-ANALYSIS SYSTEM

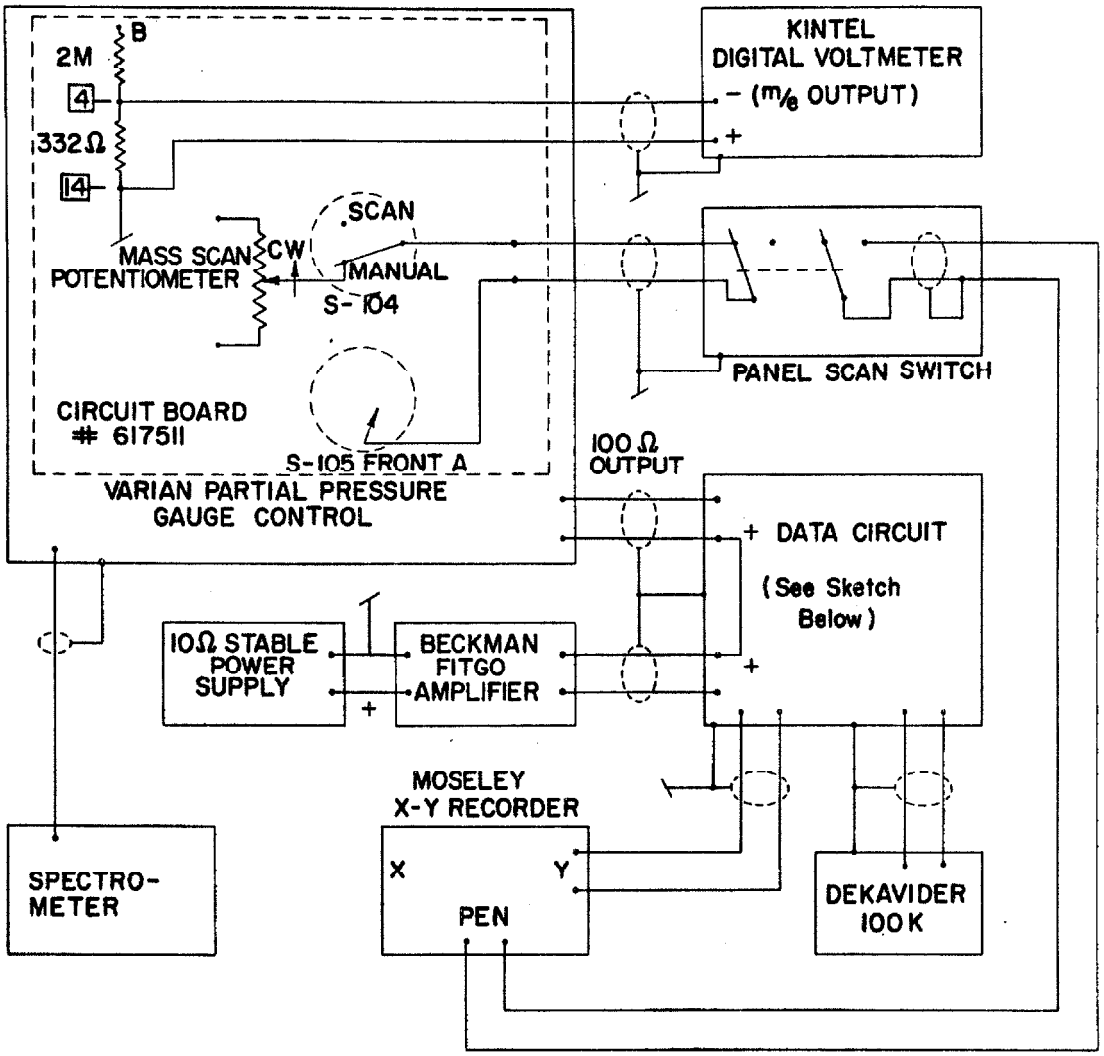

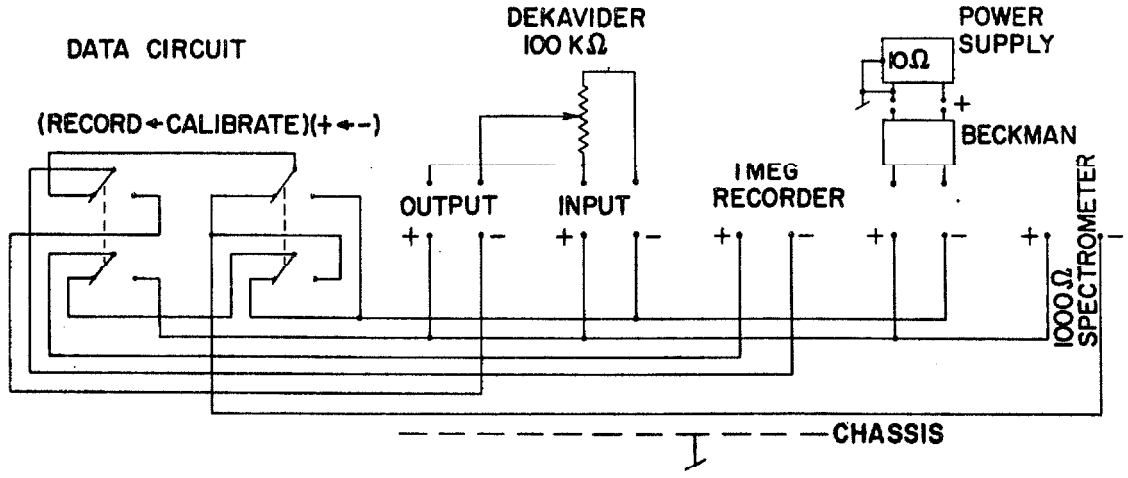

Fig. 13 MEASUREMENT CIRCUIT

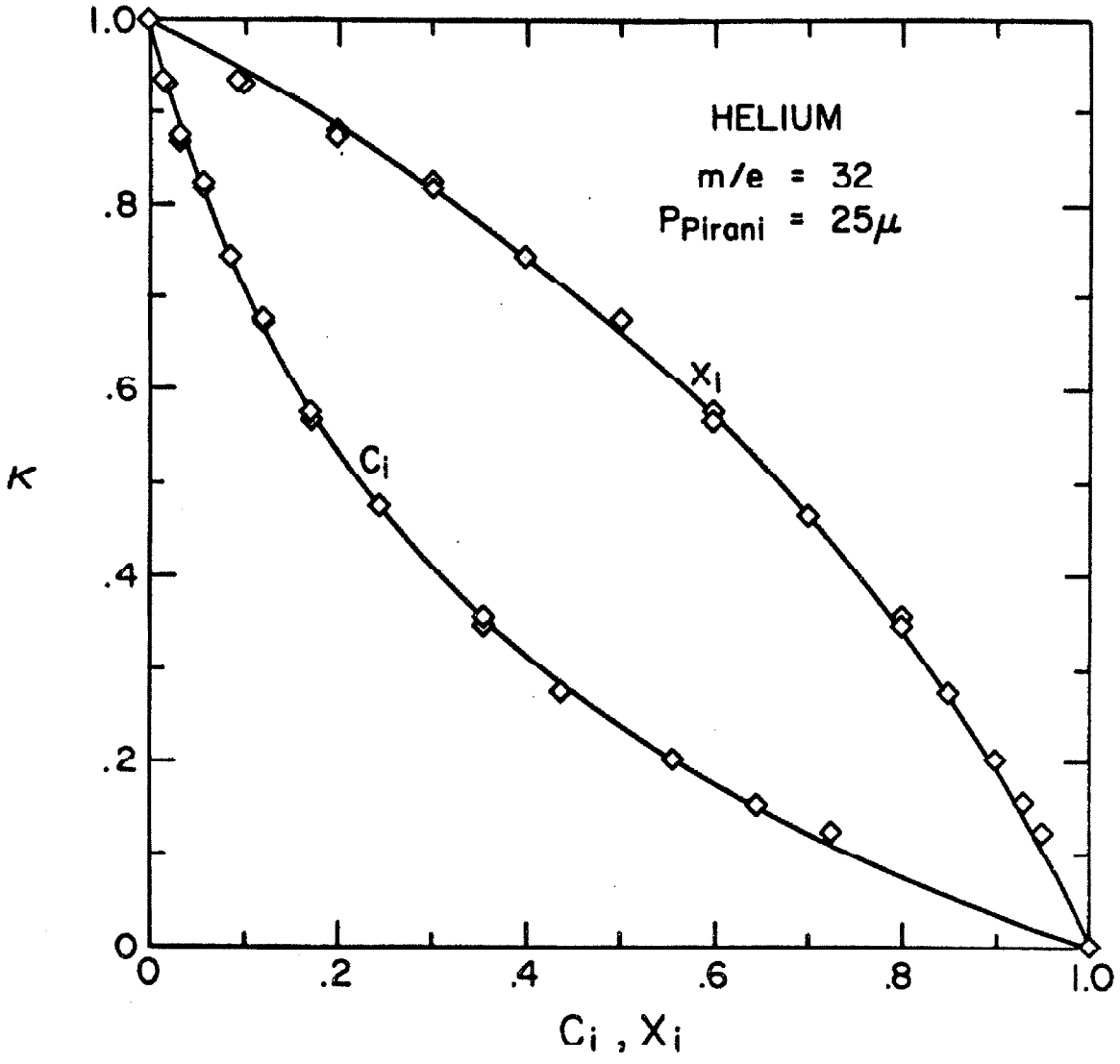

Fig. 14a NORMALIZED SPECTROMETER OUTPUT AS A FUNCTION OF MASS FRACTION (CI) AND MOLE FRACTION (XI).

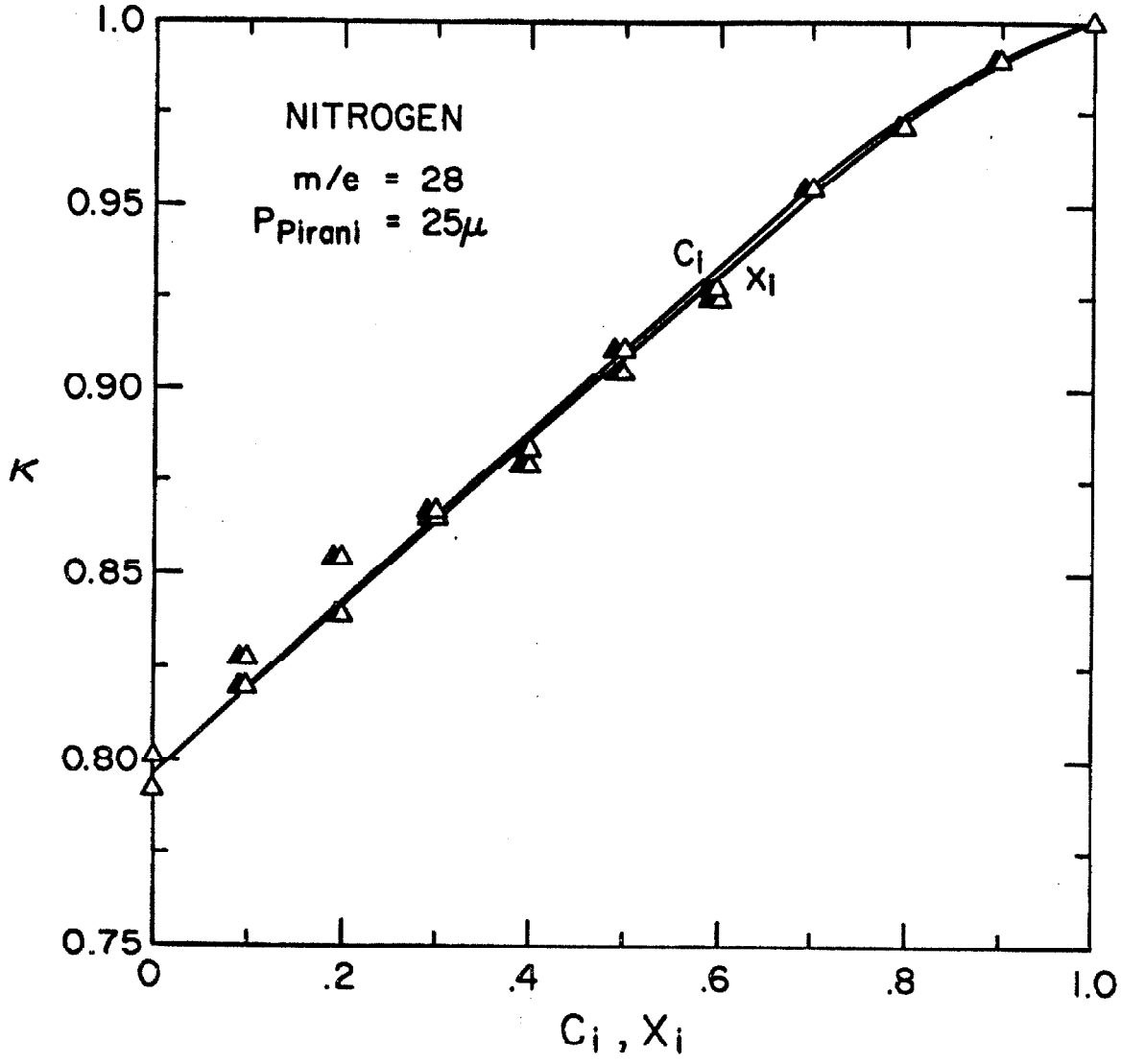

Fig. 14 b NORMALIZED SPECTROMETER OUTPUT AS A FUNCTION OF MASS FRACTION (CI) AND MOLE FRACTION (XI).

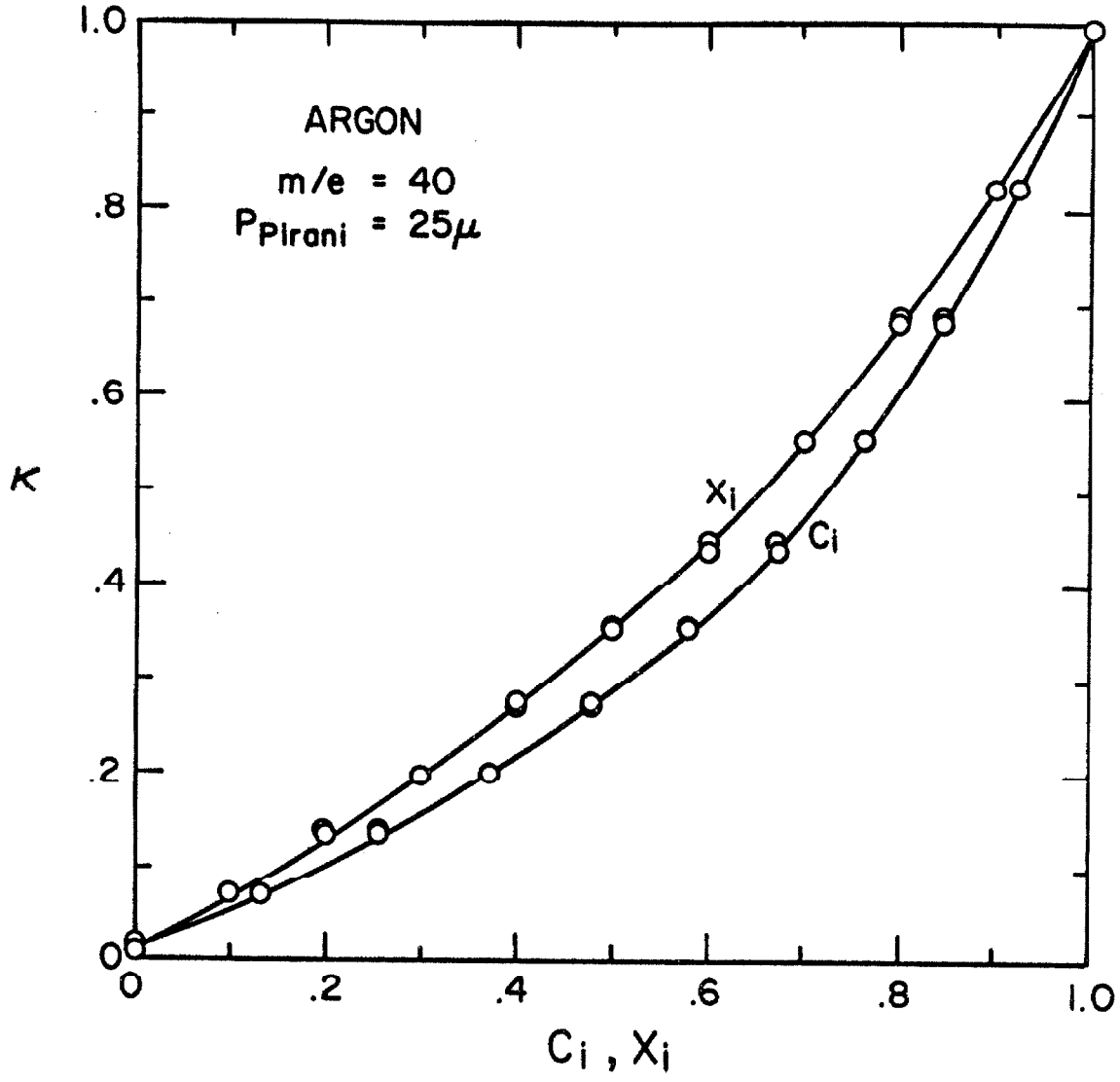

Fig. 14c NORMALIZED SPECTROMETER OUTPUT AS A FUNCTION OF MASS FRACTION (Ci) AND MOLE FRACTION (Xi).

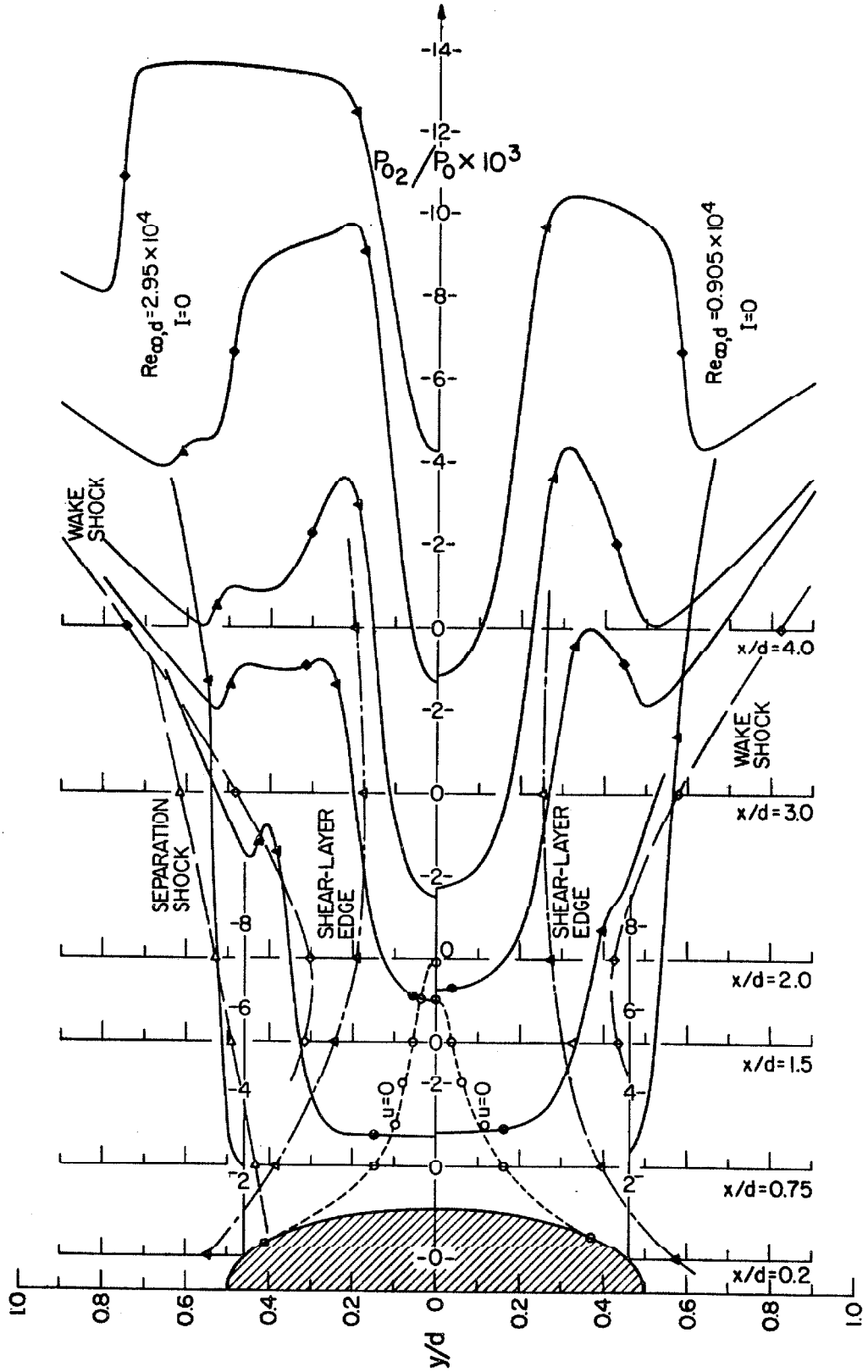

Fig. 15 NEAR-WAKE PRESSURE FIELD

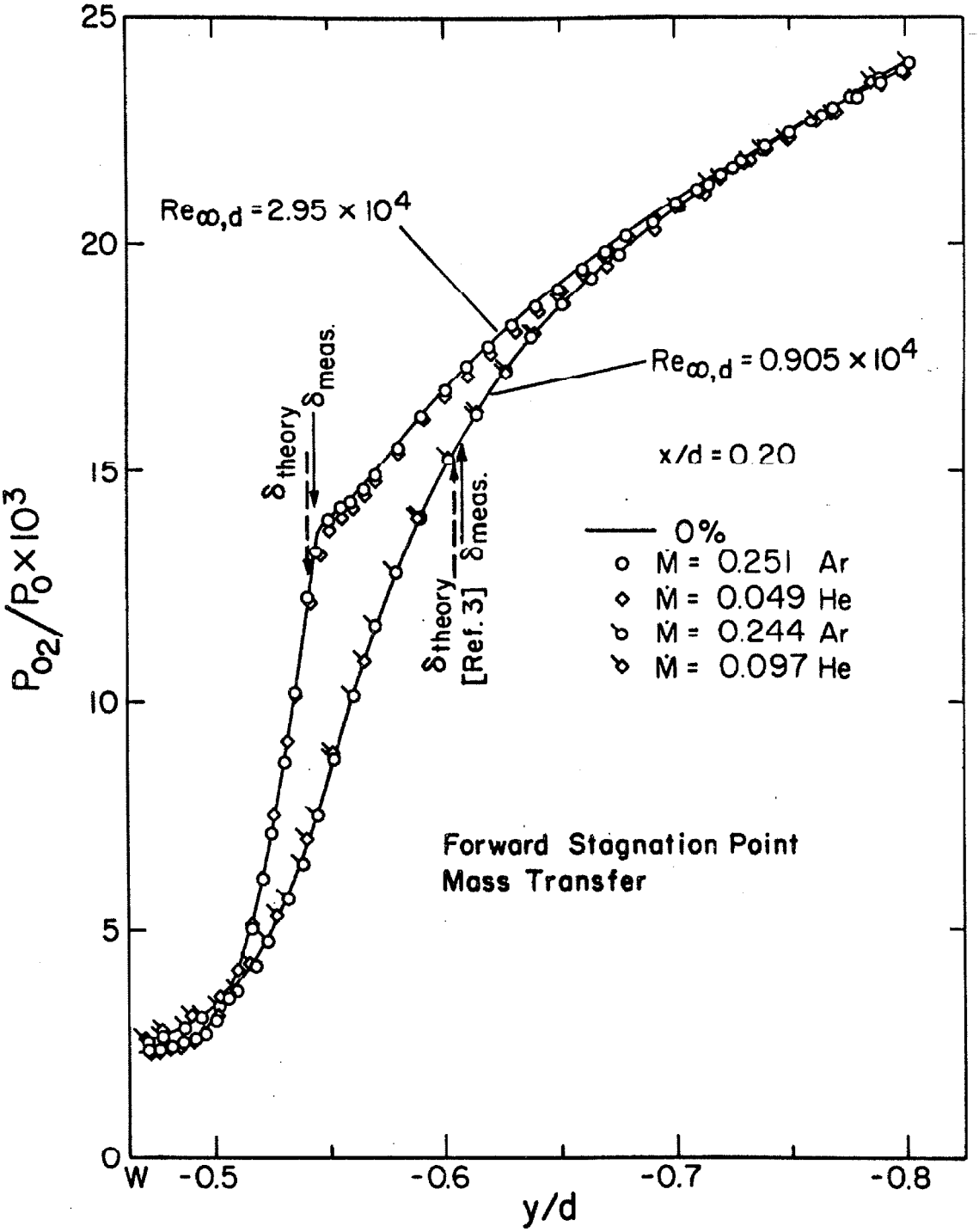

Fig. 16 EFFECT OF MASS ADDITION ON CYLINDER BOUNDARY LAYER.

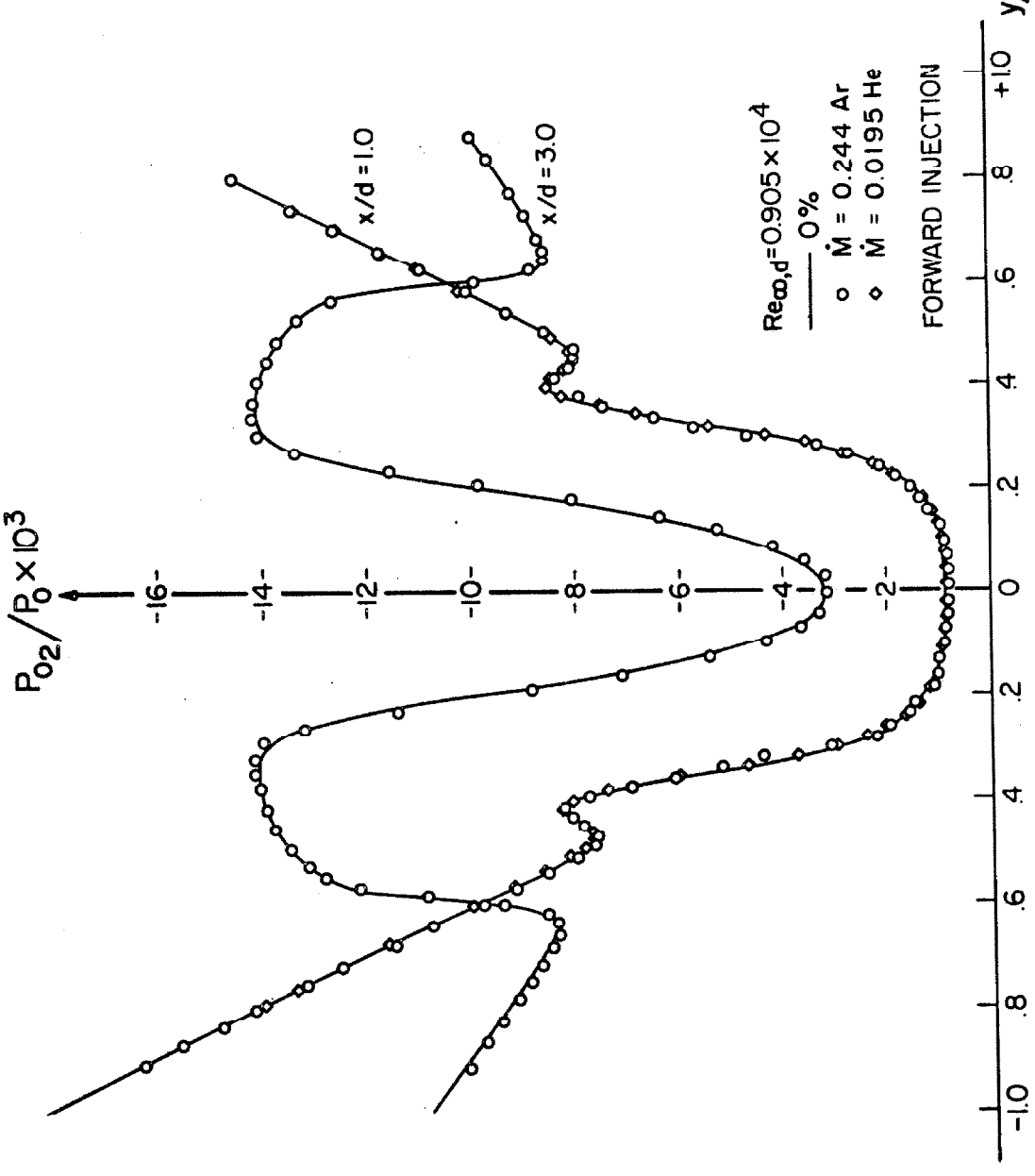

Fig. 17a EFFECT OF MASS TRANSFER ON NEAR-WAKE PITOT PRESSURE

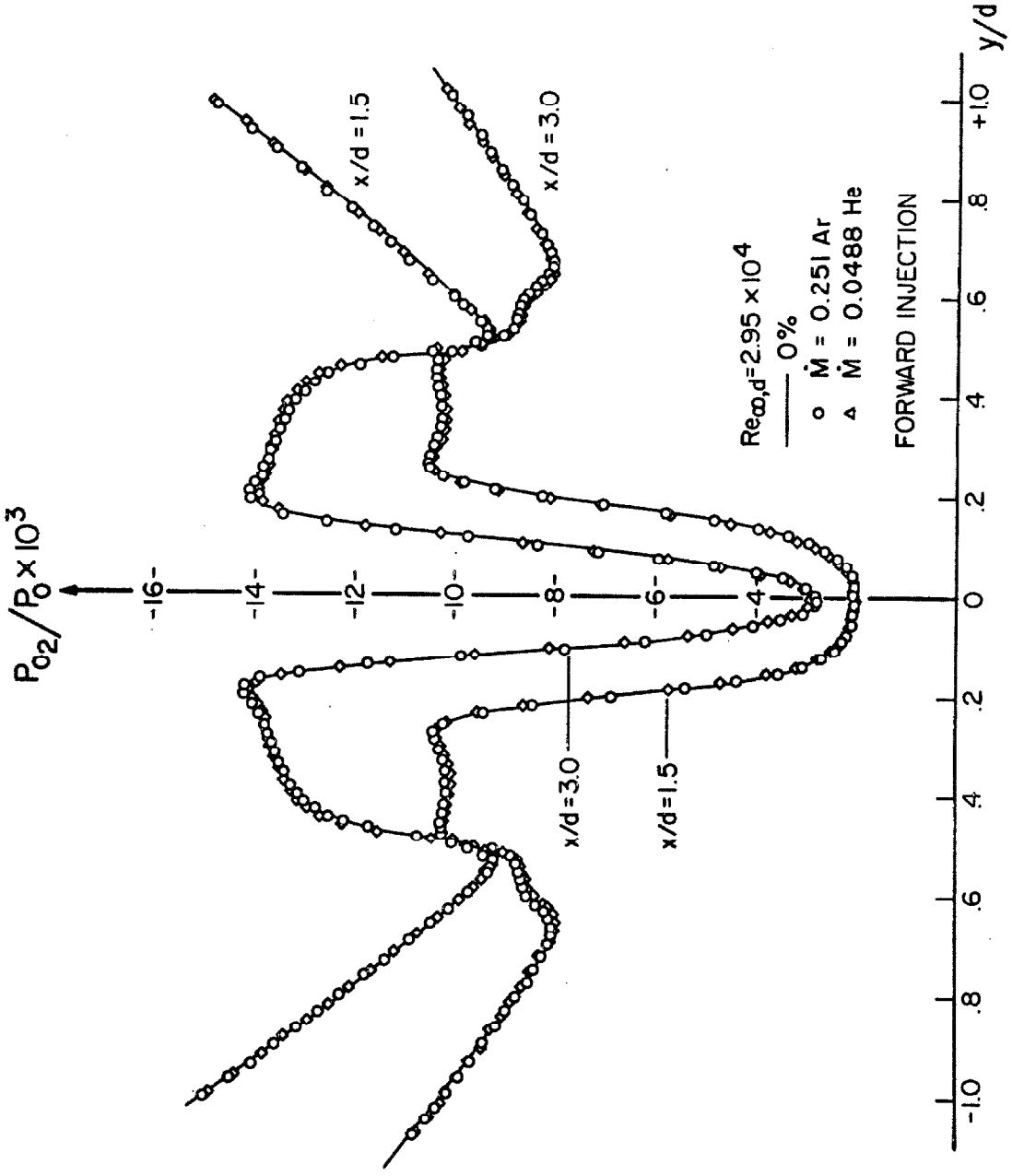

Fig. 17b EFFECT OF MASS TRANSFER ON NEAR-WAKE PITOT PRESSURE

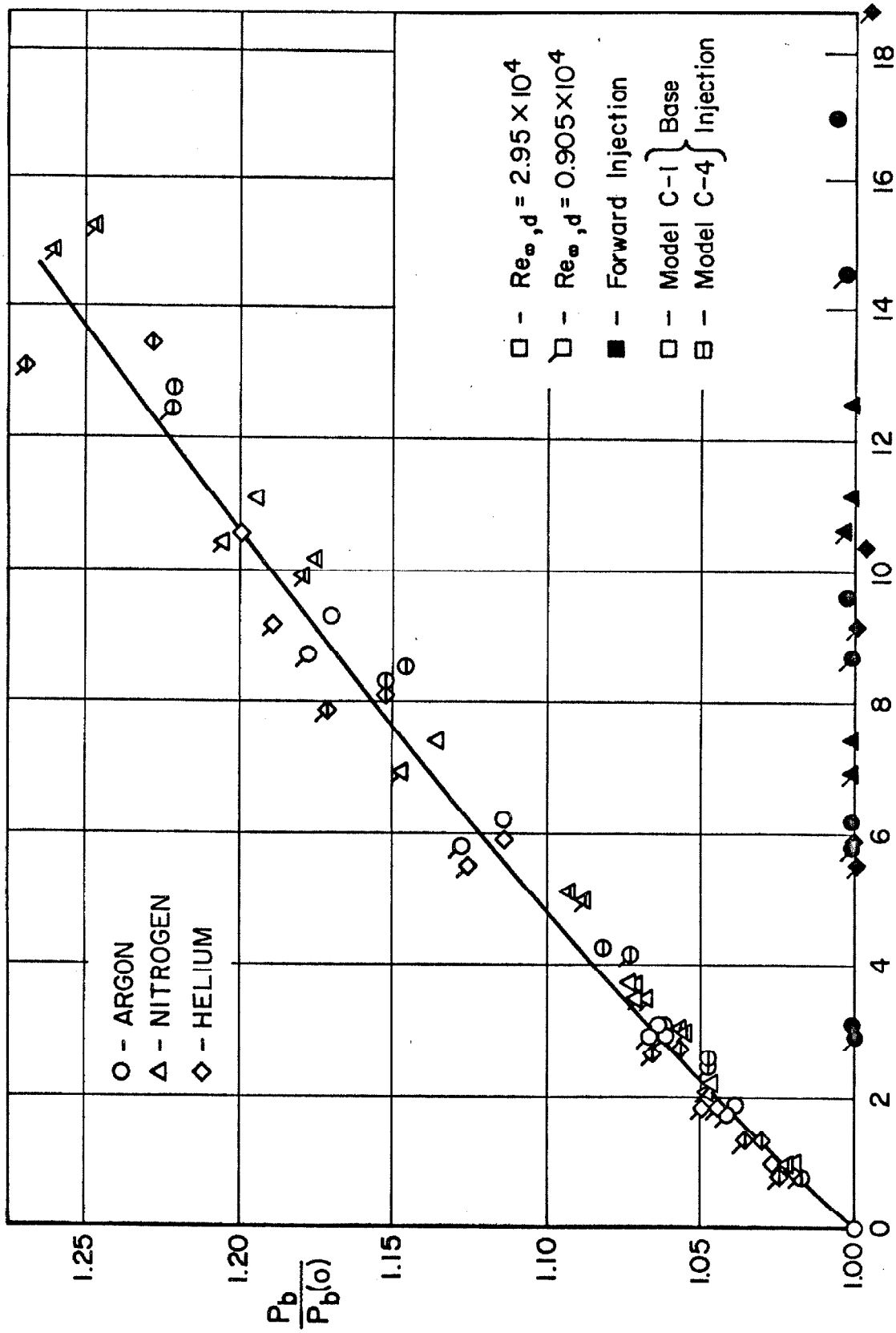

Fig. 18 VARIATION OF BASE PRESSURE WITH MASS ADDITION

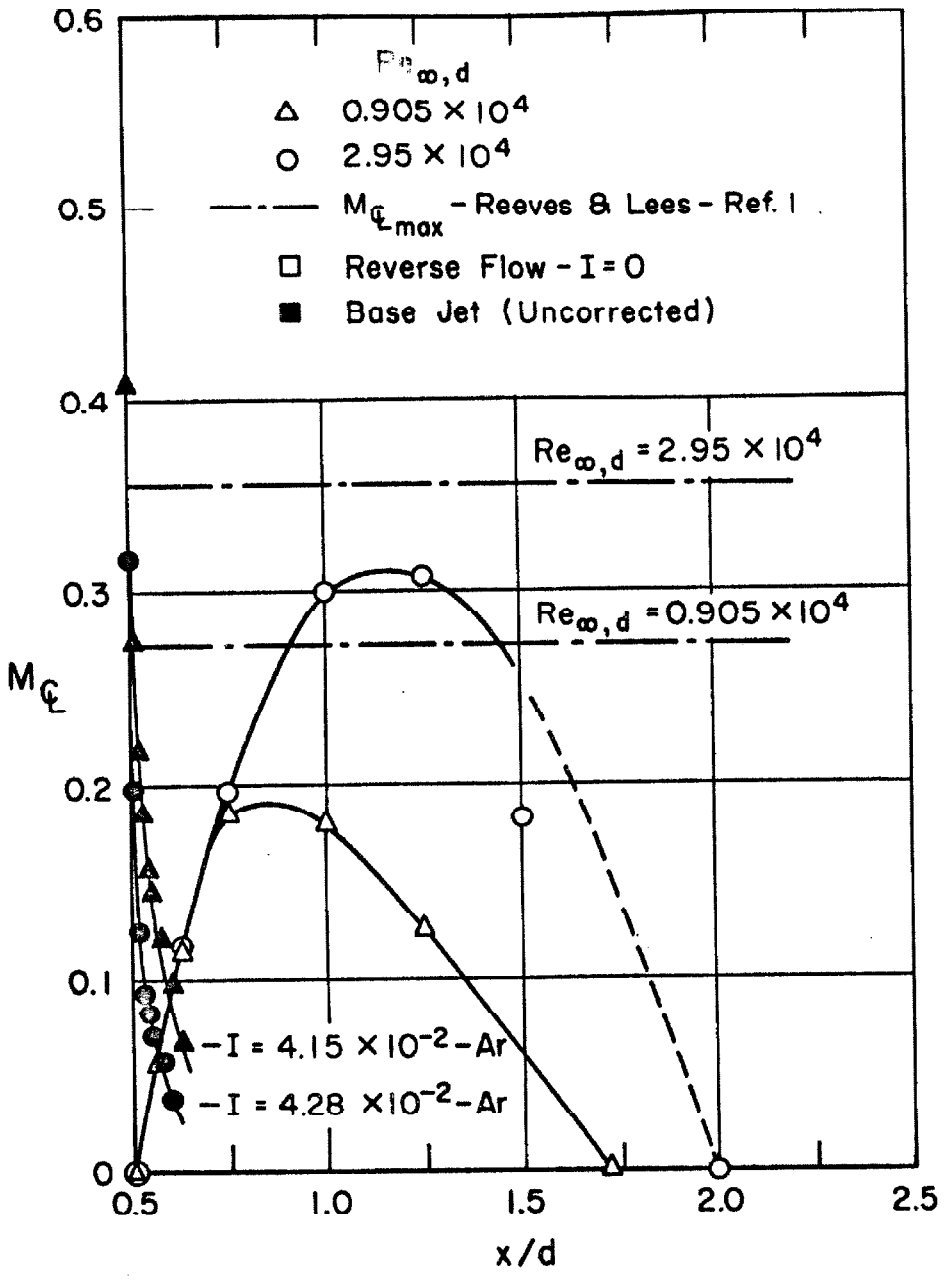

Fig. 19 REVERSE FLOW CENTERLINE MACH NO. DISTRIBUTION

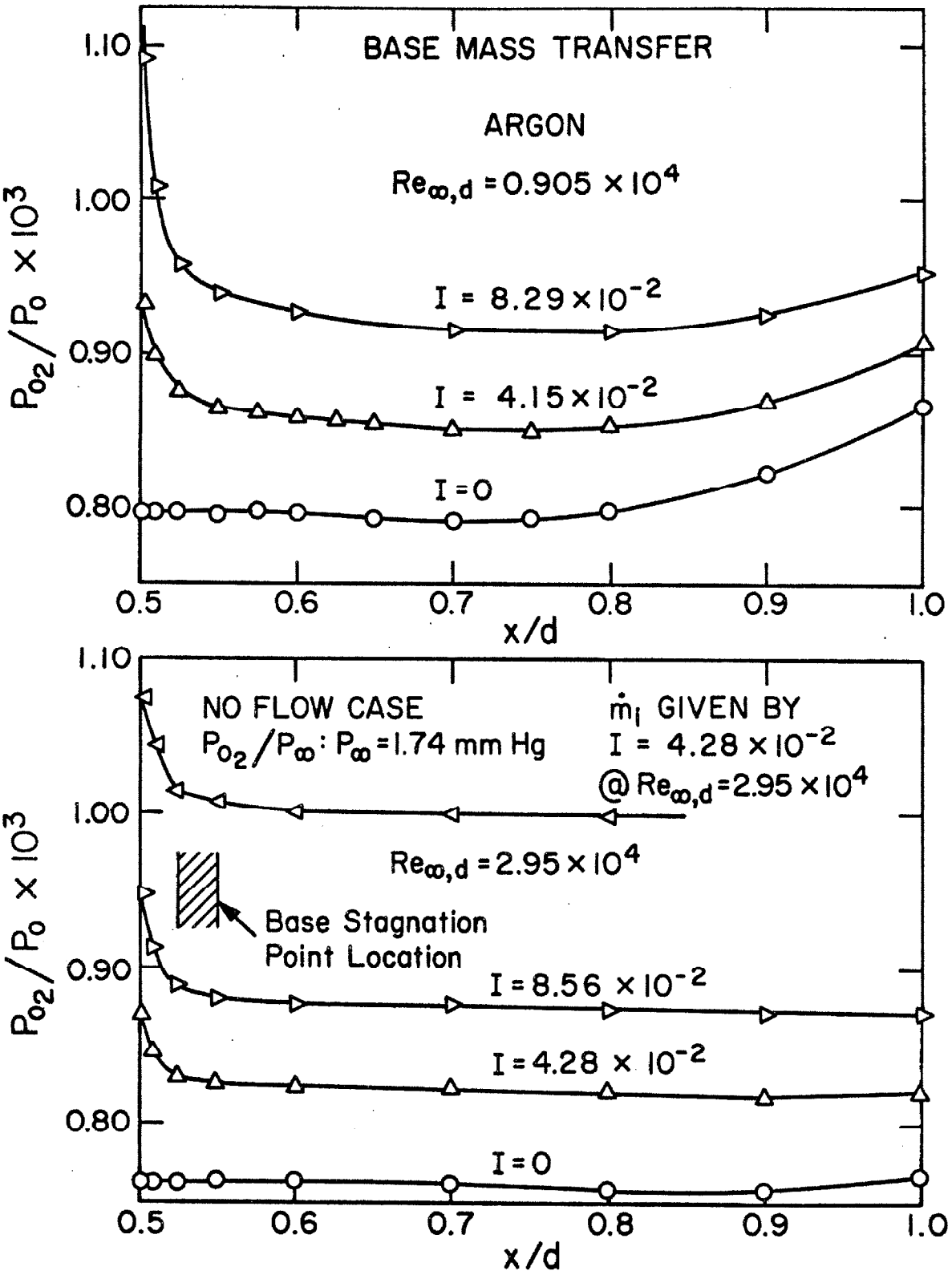

Fig. 20 PITOT-PRESSURE DISTRIBUTION IN THE BASE JET.

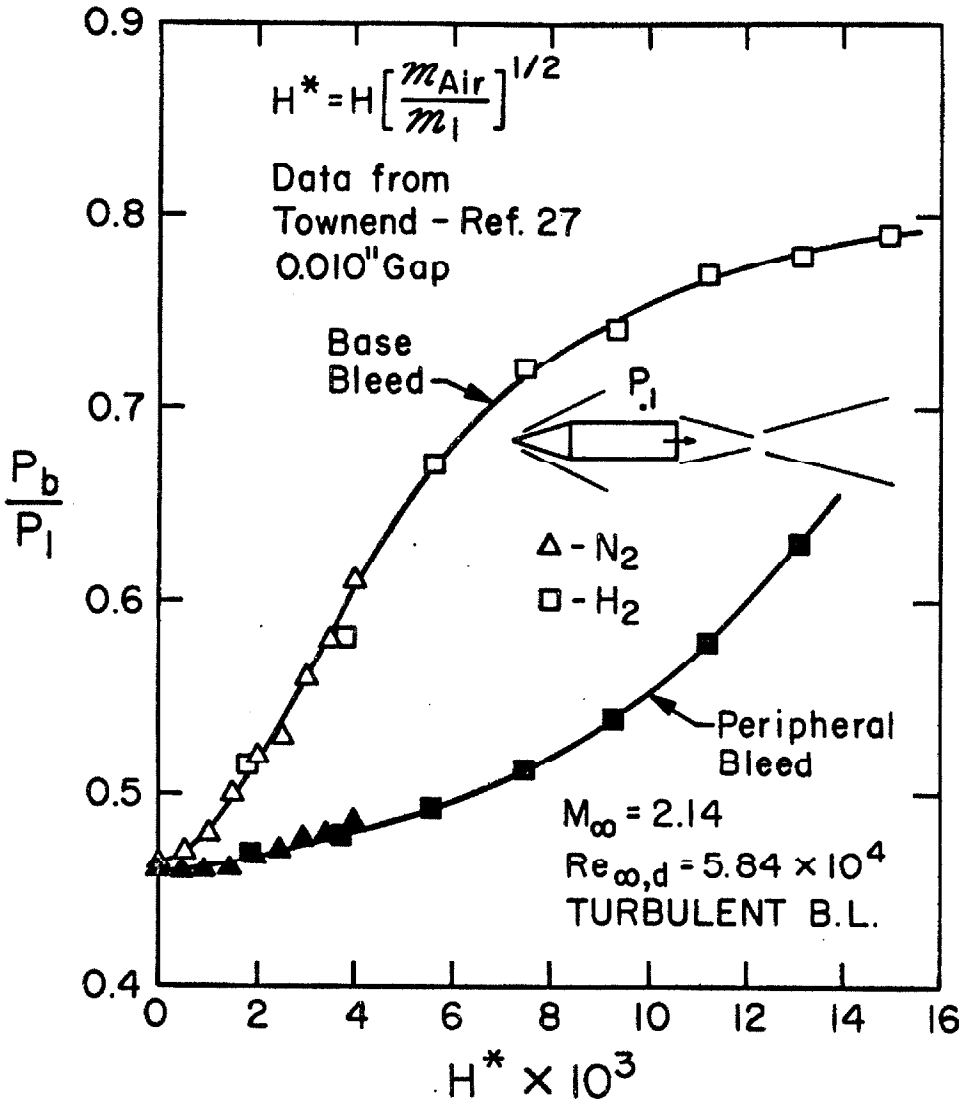

Fig. 21 BASE PRESSURE CORRELATION FOR A CONE – CYLINDER.

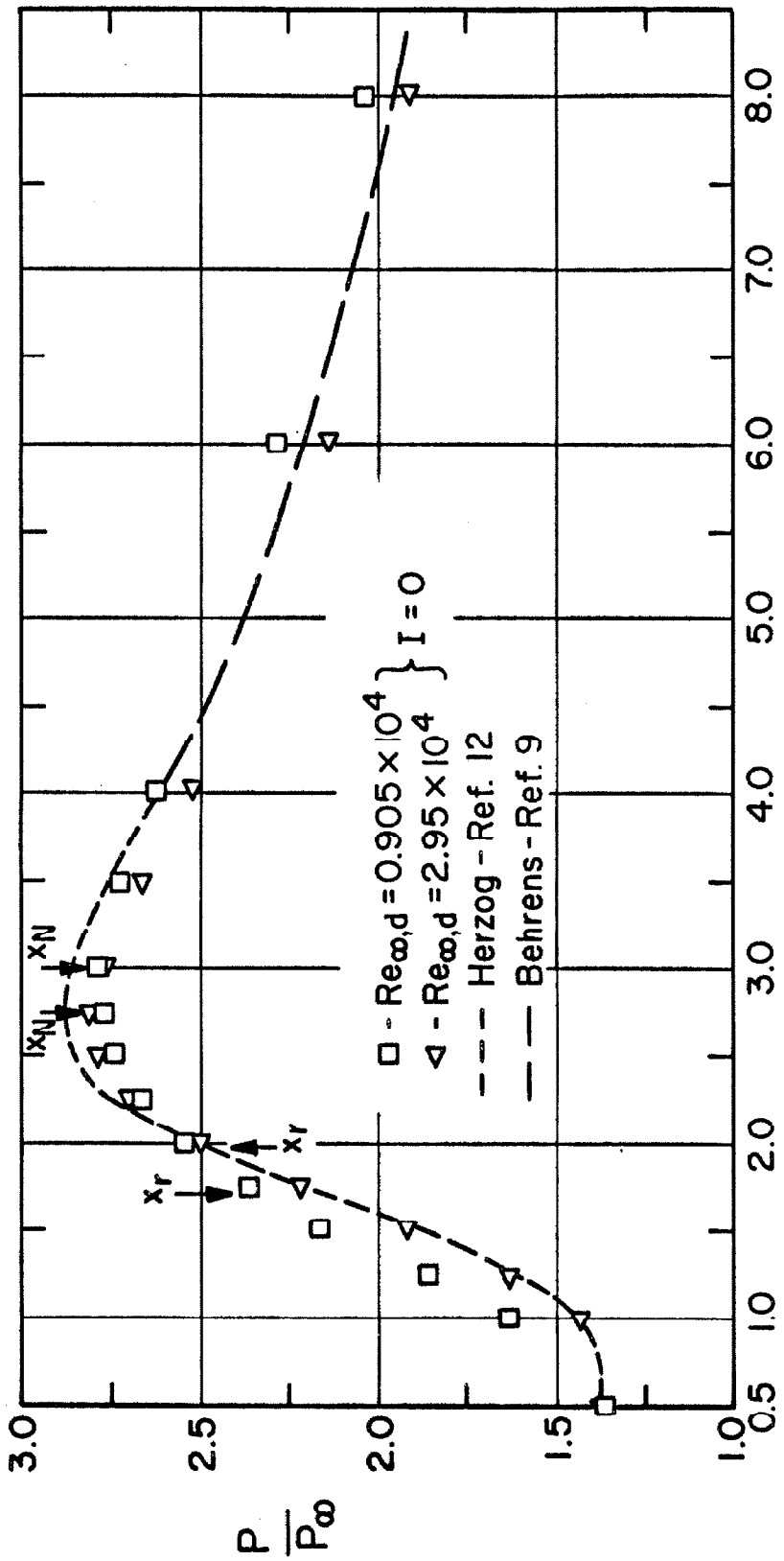

Fig. 22 AXIAL STATIC PRESSURE

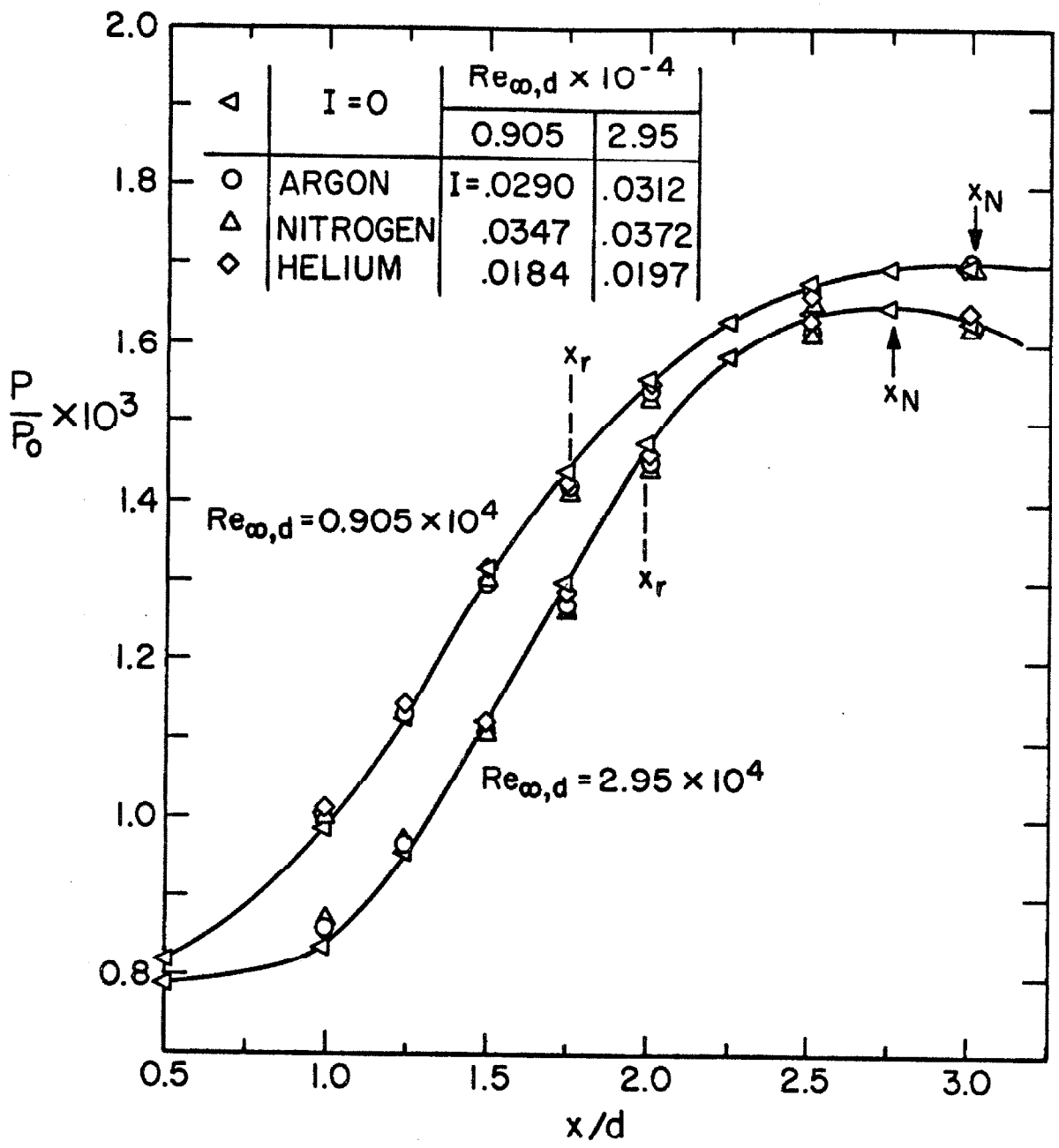

Fig. 23 AXIAL STATIC PRESSURE WITH BASE MASS TRANSFER

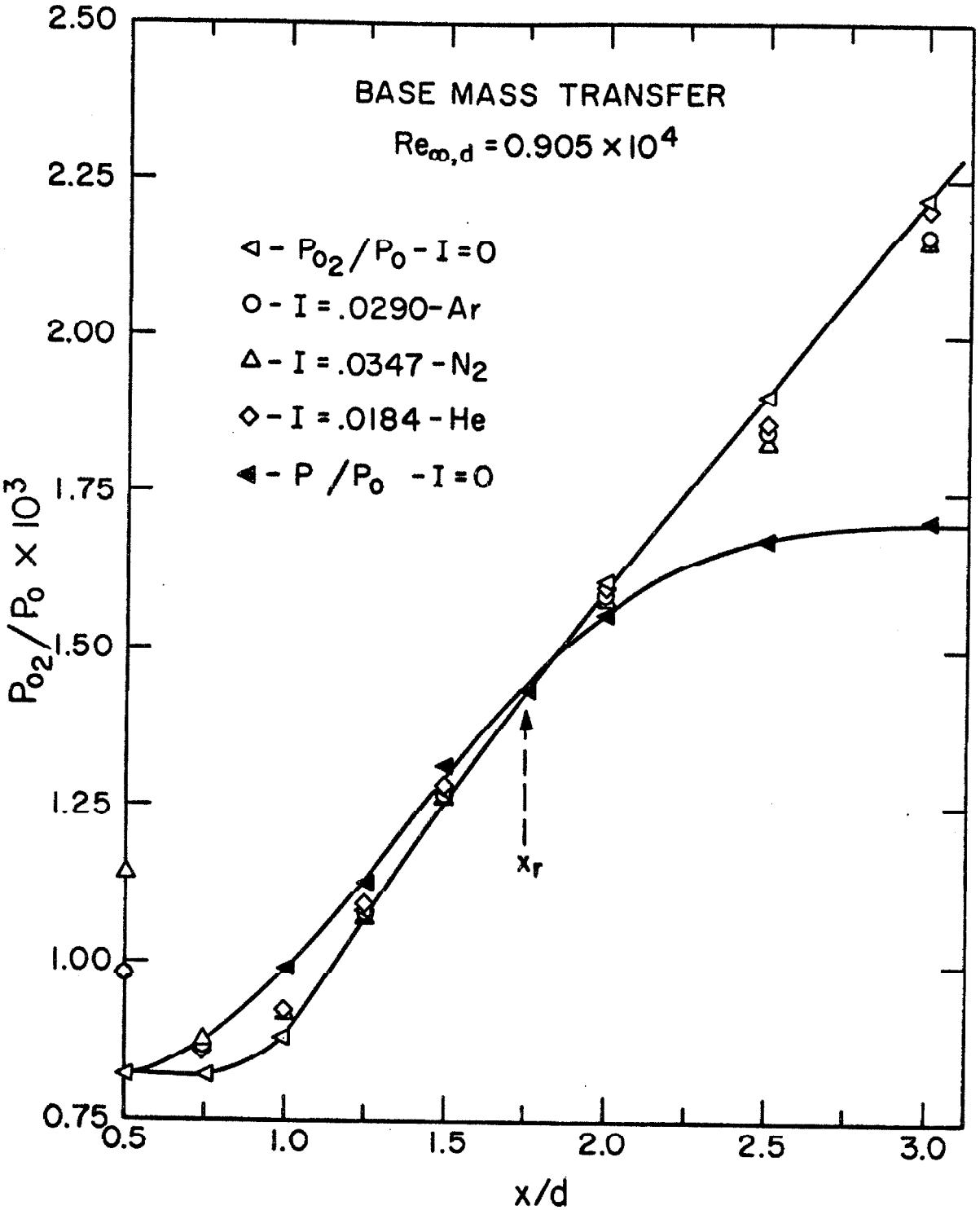

Fig.24a NEAR-WAKE AXIAL PITOT PRESSURE WITH BASE MASS TRANSFER

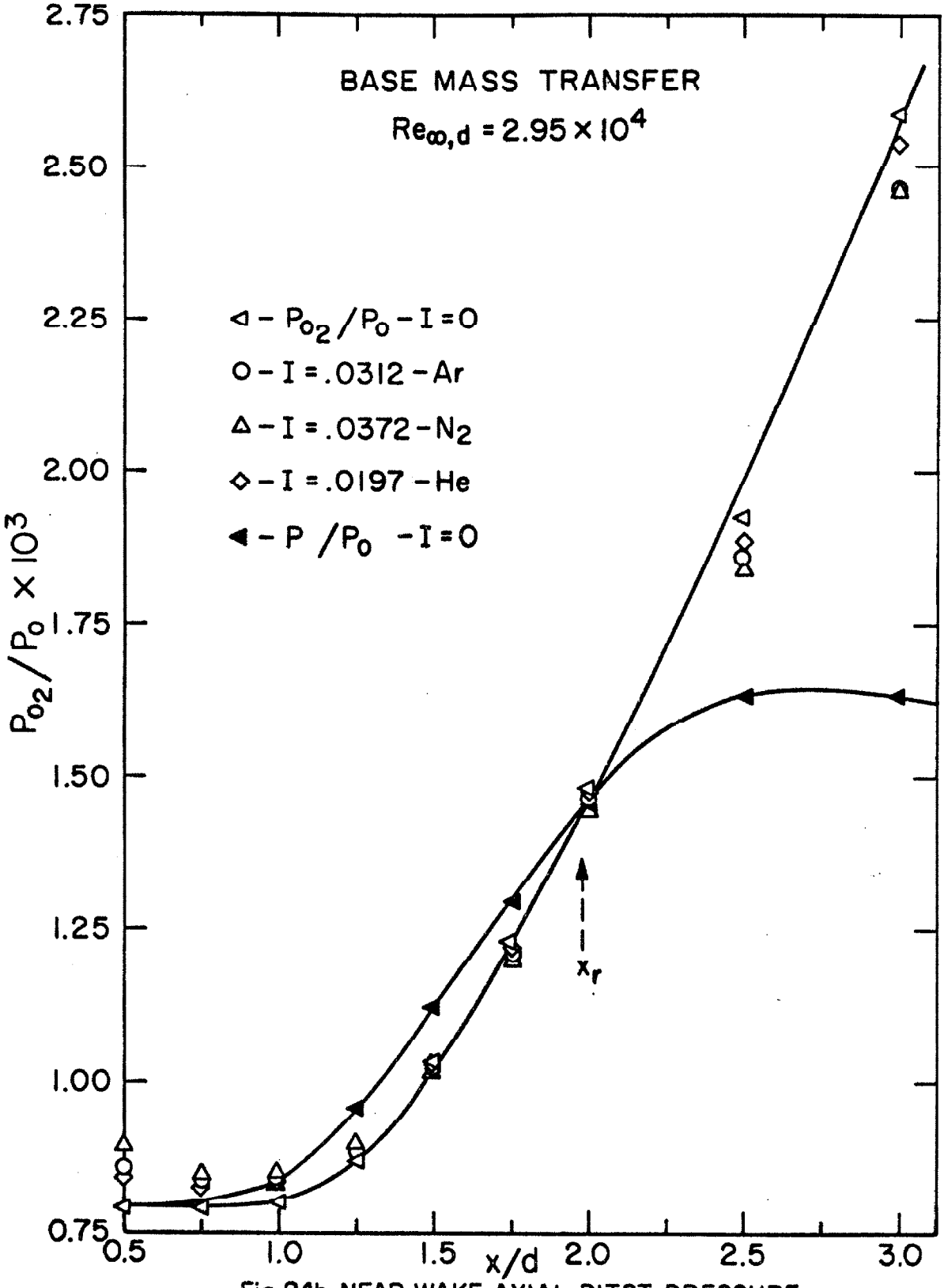

Fig.24b NEAR-WAKE AXIAL PITOT PRESSURE WITH BASE MASS TRANSFER

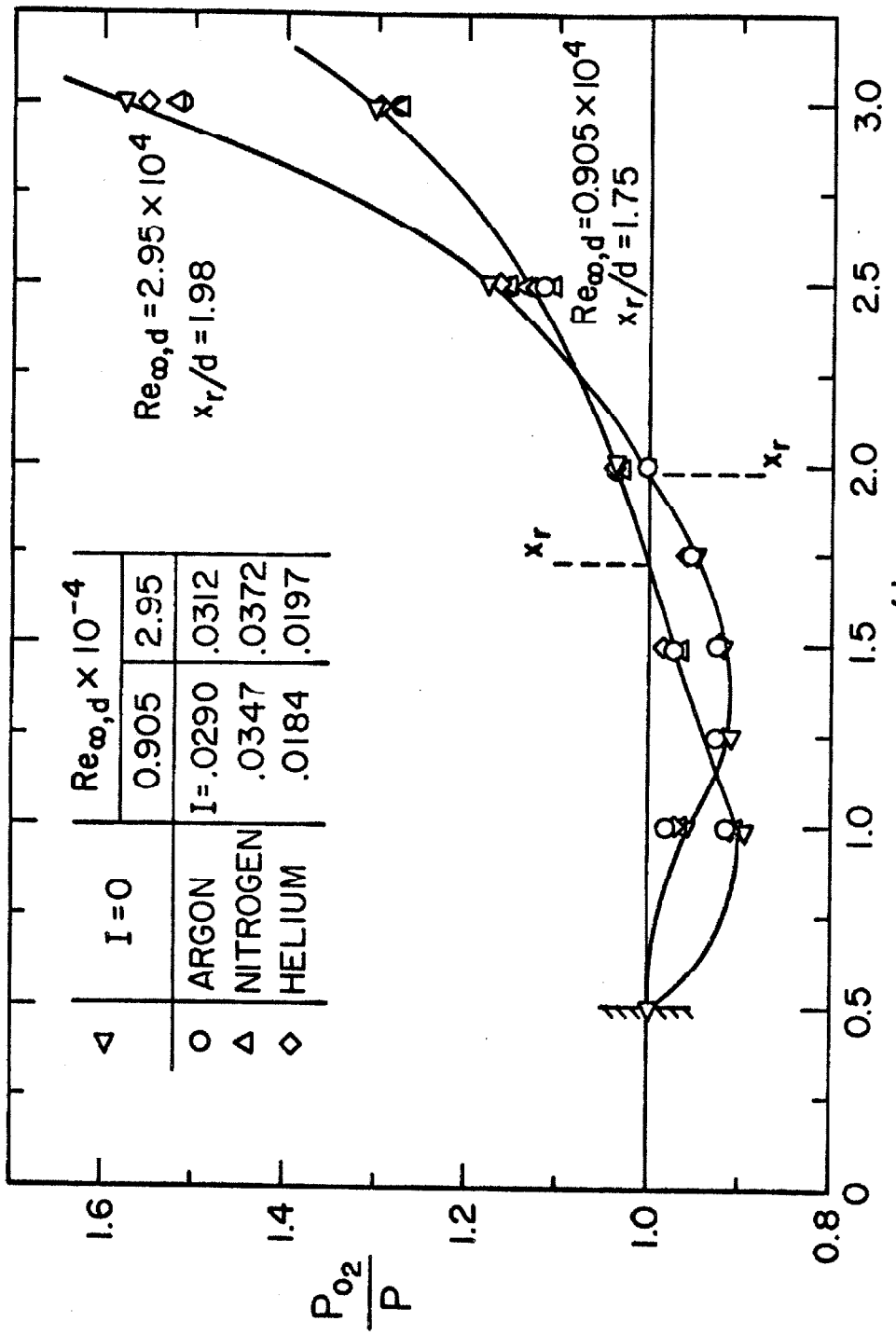

Fig. 25 REAR STAGNATION POINT DEFINITION WITH BASE MASS TRANSFER.

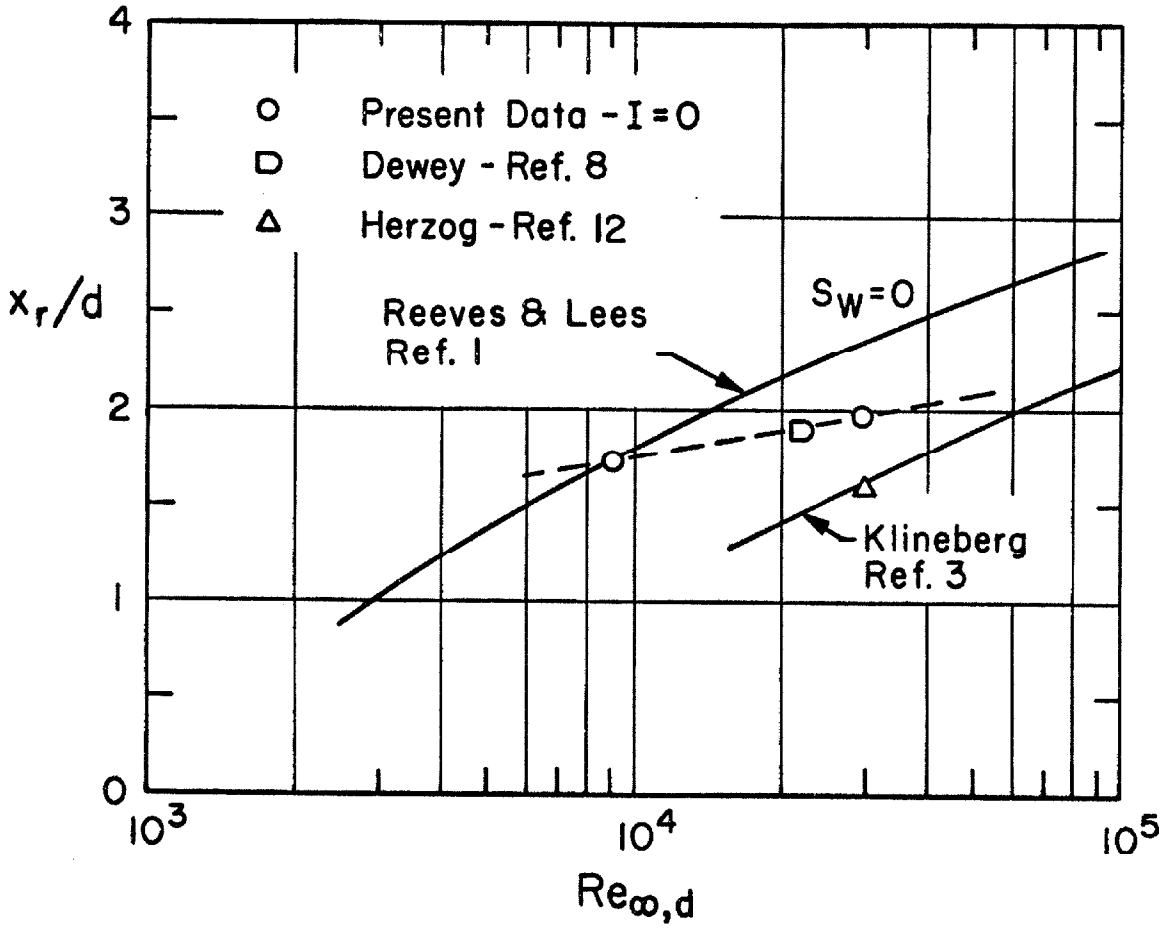

Fig. 26 LOCATION OF REAR STAGNATION POINT

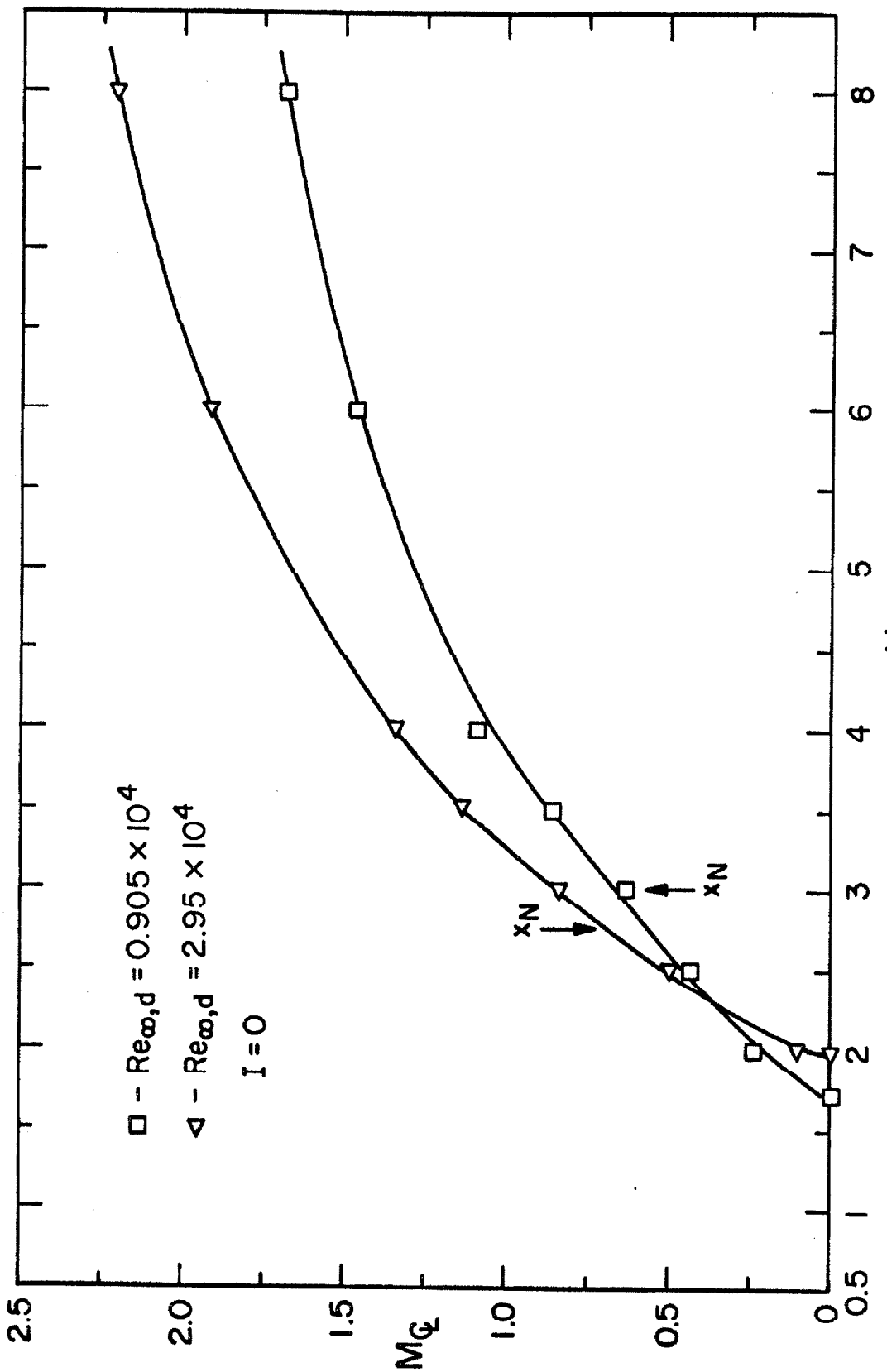

Fig. 27 CENTERLINE MACH NUMBER.

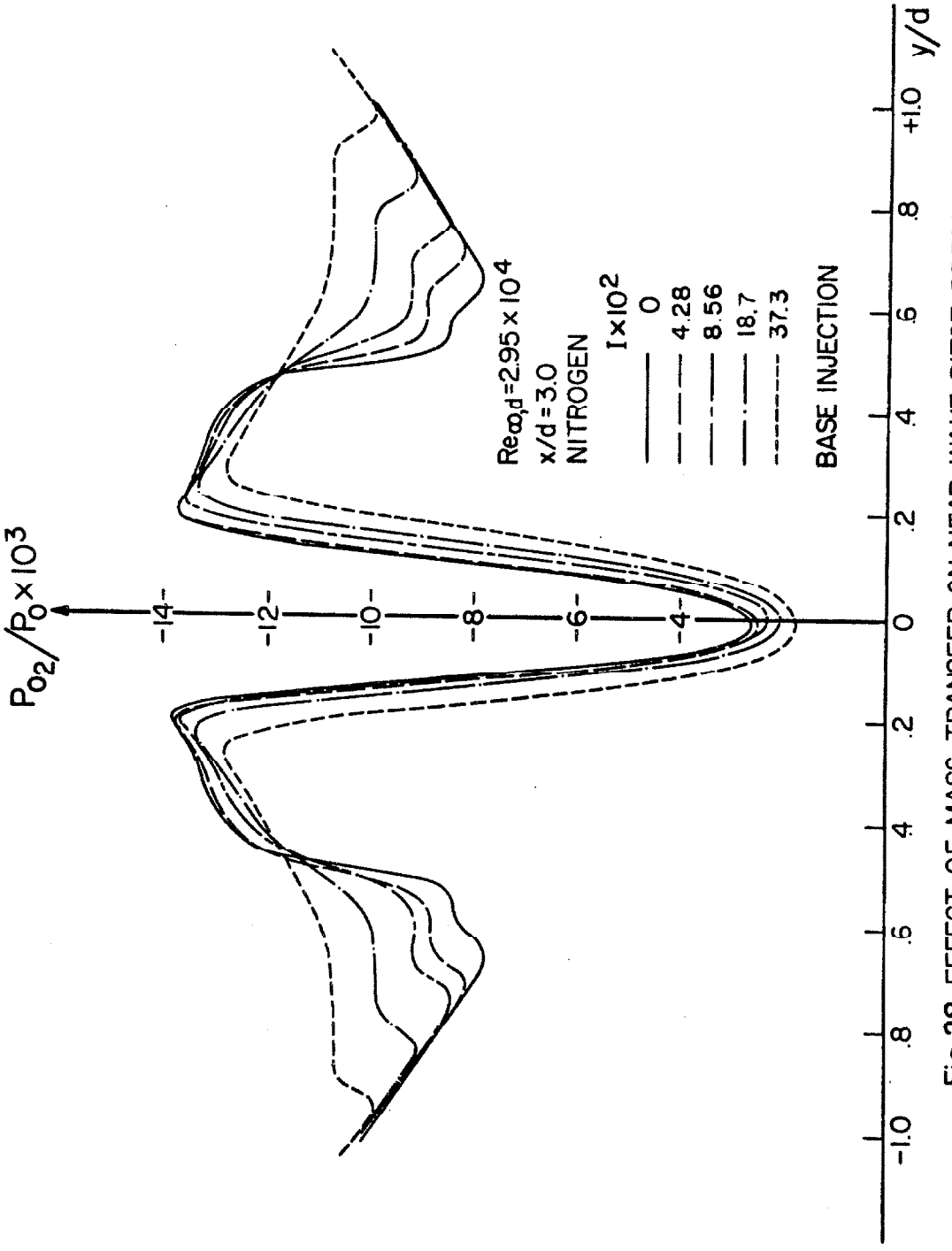

Fig.28 EFFECT OF MASS TRANSFER ON NEAR-WAKE PITOT PRESSURE

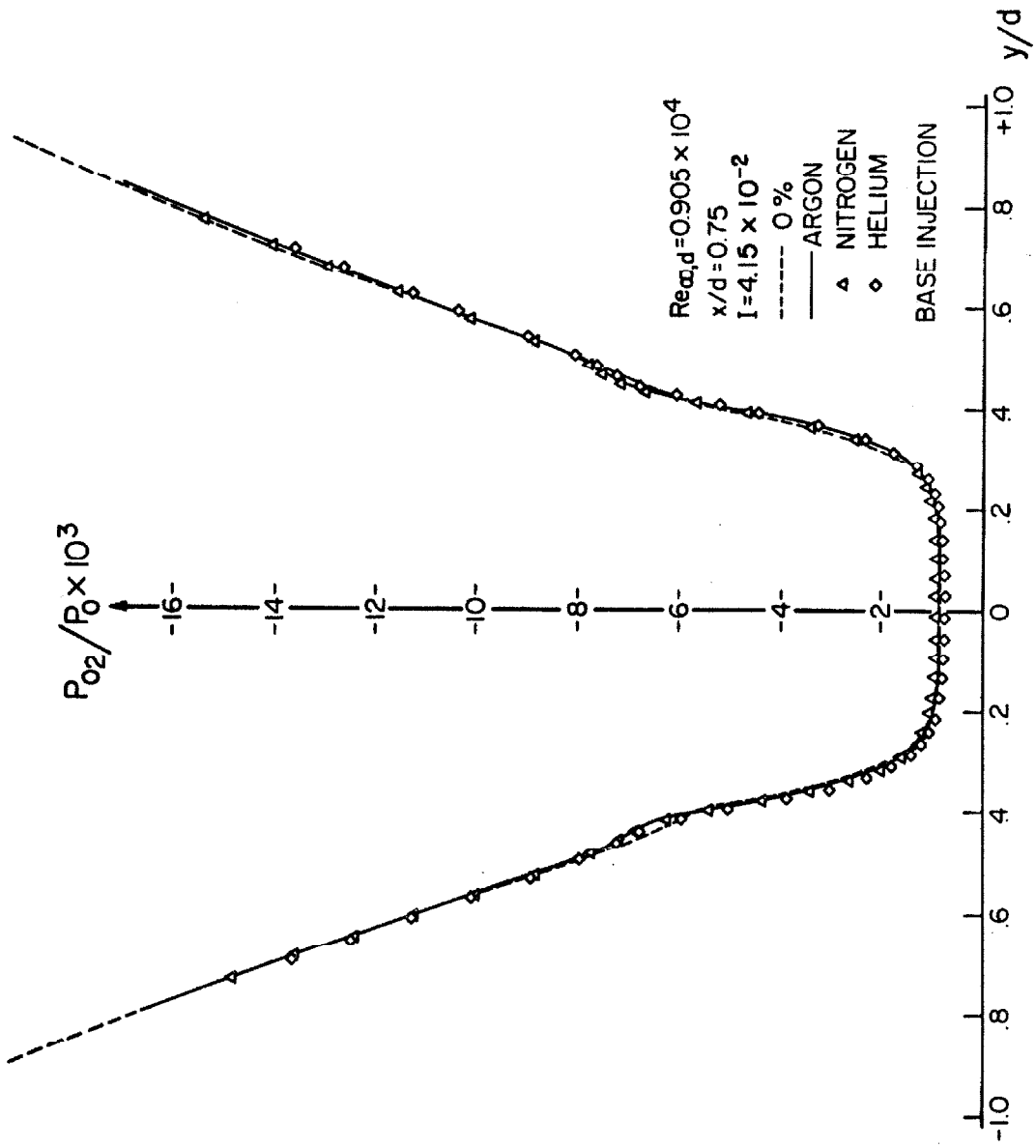

Fig. 29 a EFFECT OF MASS TRANSFER ON NEAR-WAKE PITOT PRESSURE

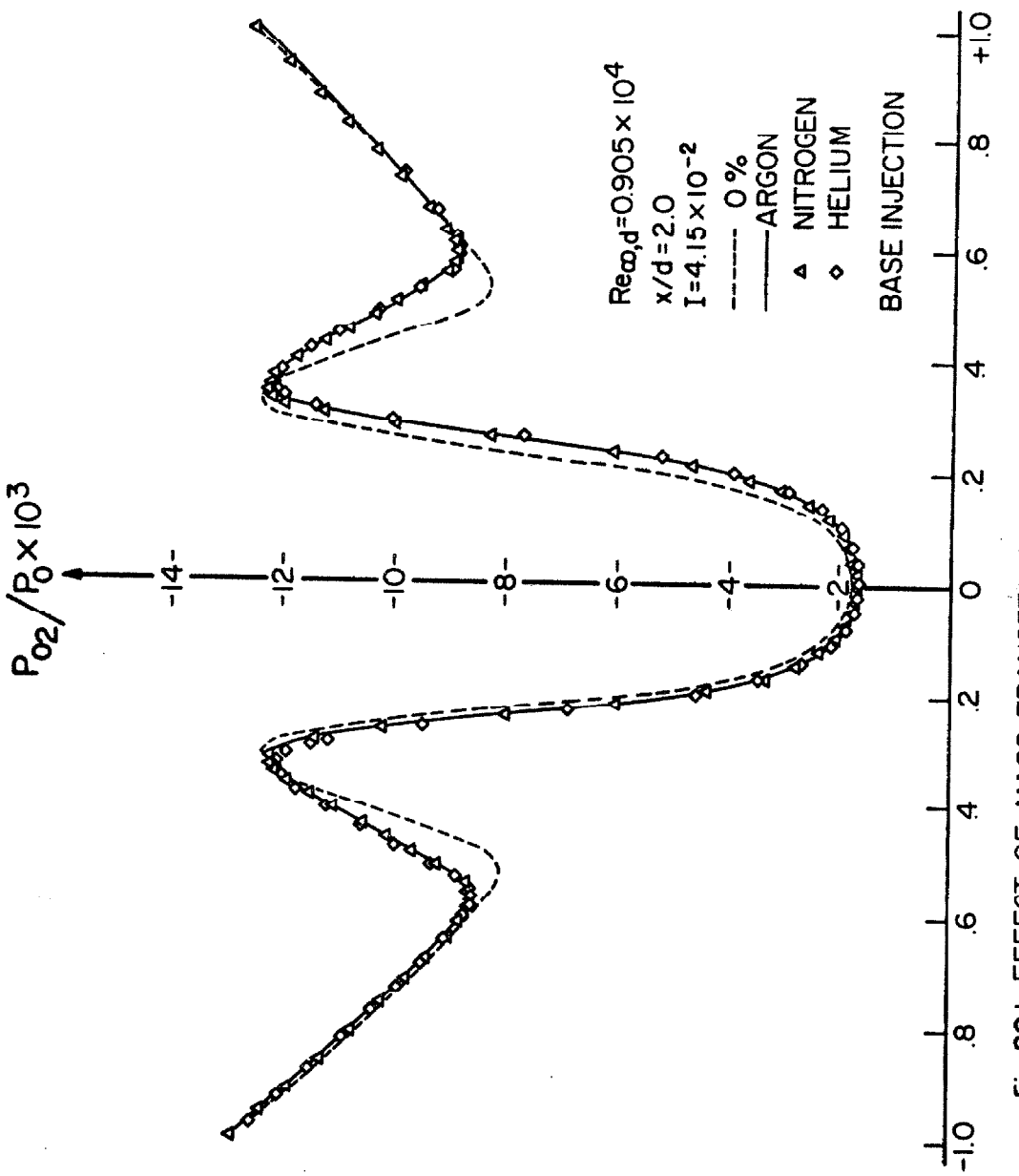

Fig.29 b EFFECT OF MASS TRANSFER ON NEAR-WAKE PITOT PRESSURE

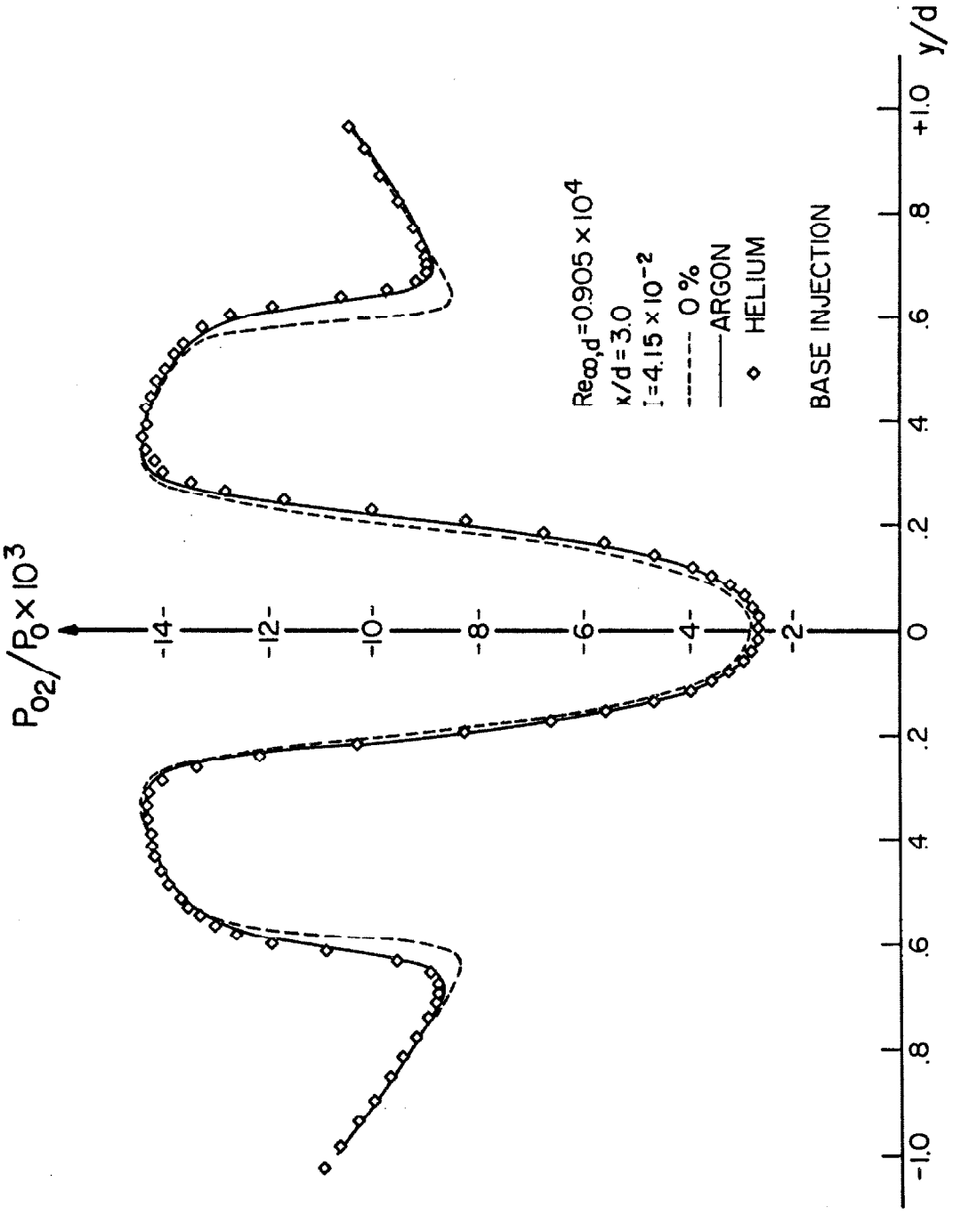

Fig. 29c EFFECT OF MASS TRANSFER ON NEAR-WAKE PITOT PRESSURE

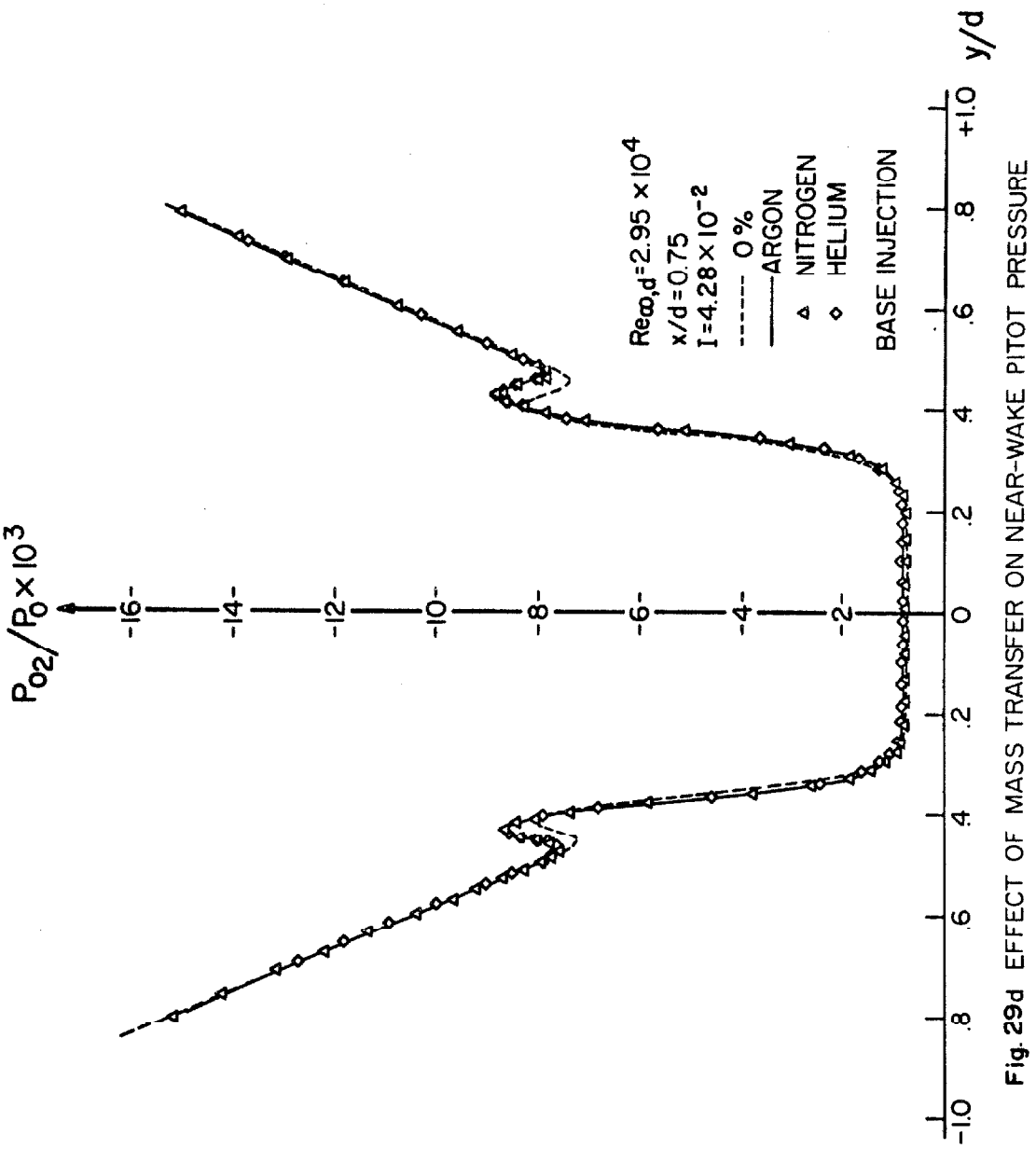

Fig. 29d EFFECT OF MASS TRANSFER ON NEAR-WAKE PITOT PRESSURE

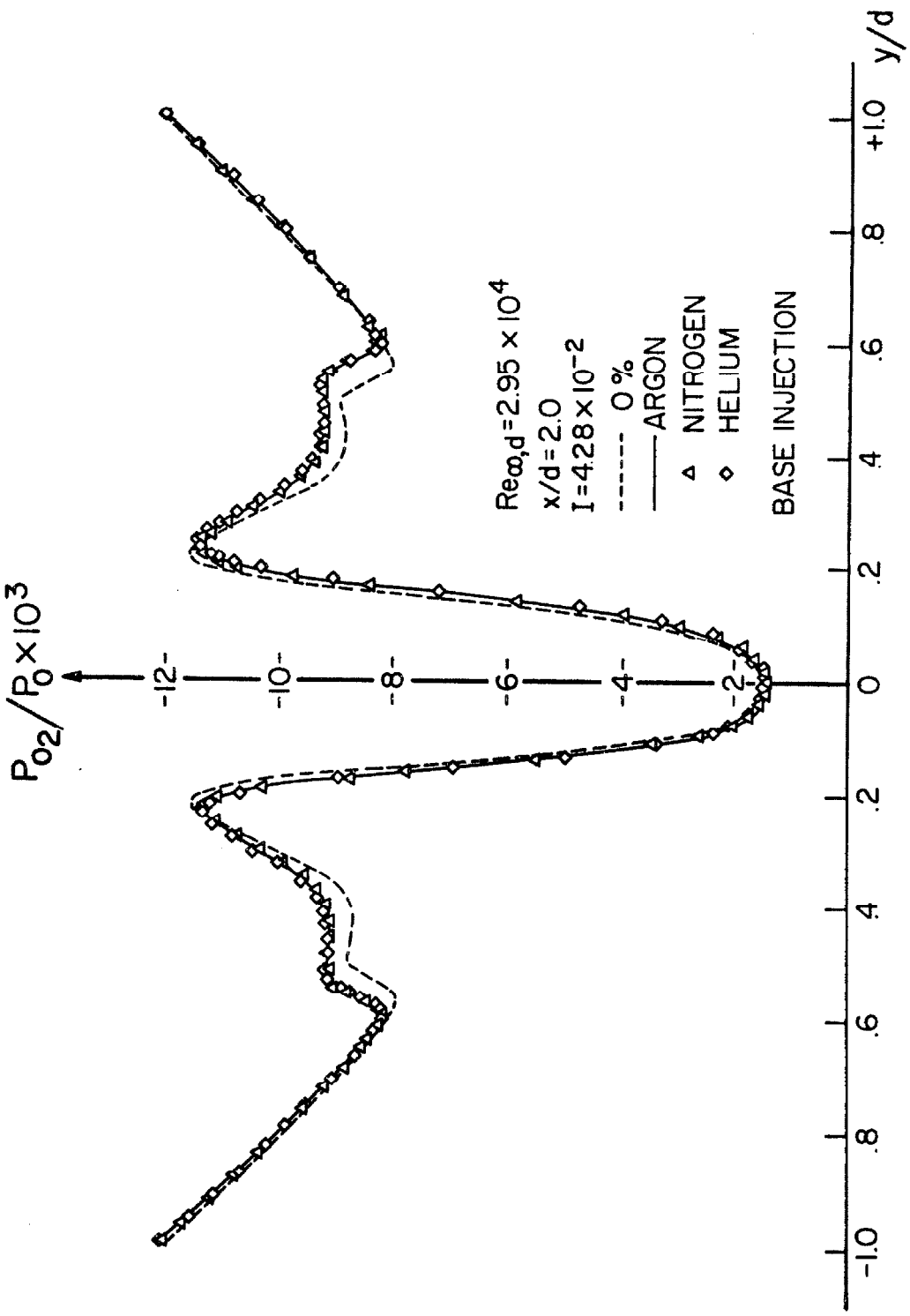

Fig. 29 e EFFECT OF MASS TRANSFER ON NEAR-WAKE PITOT PRESSURE

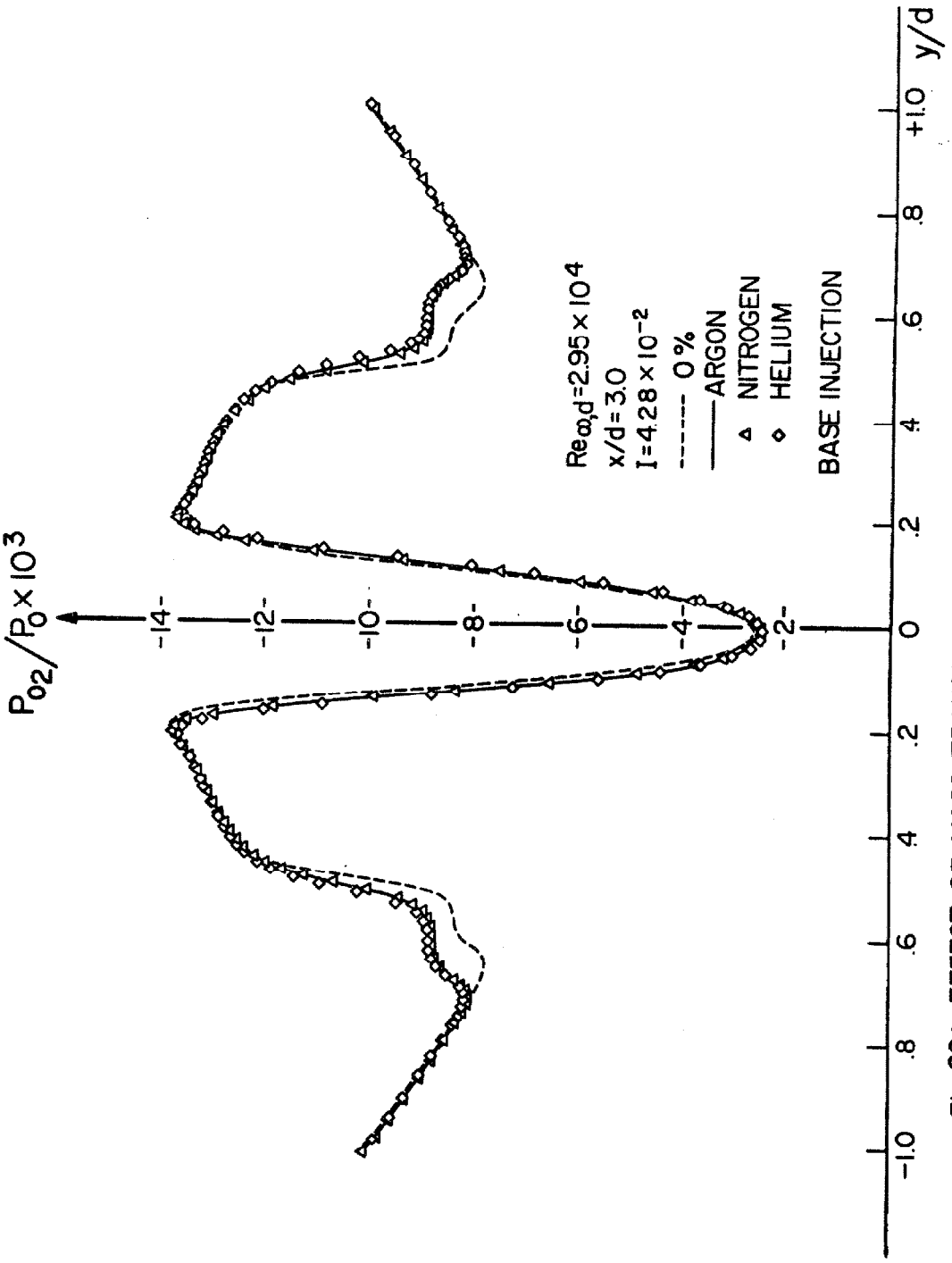

Fig. 29f EFFECT OF MASS TRANSFER ON NEAR-WAKE PITOT PRESSURE

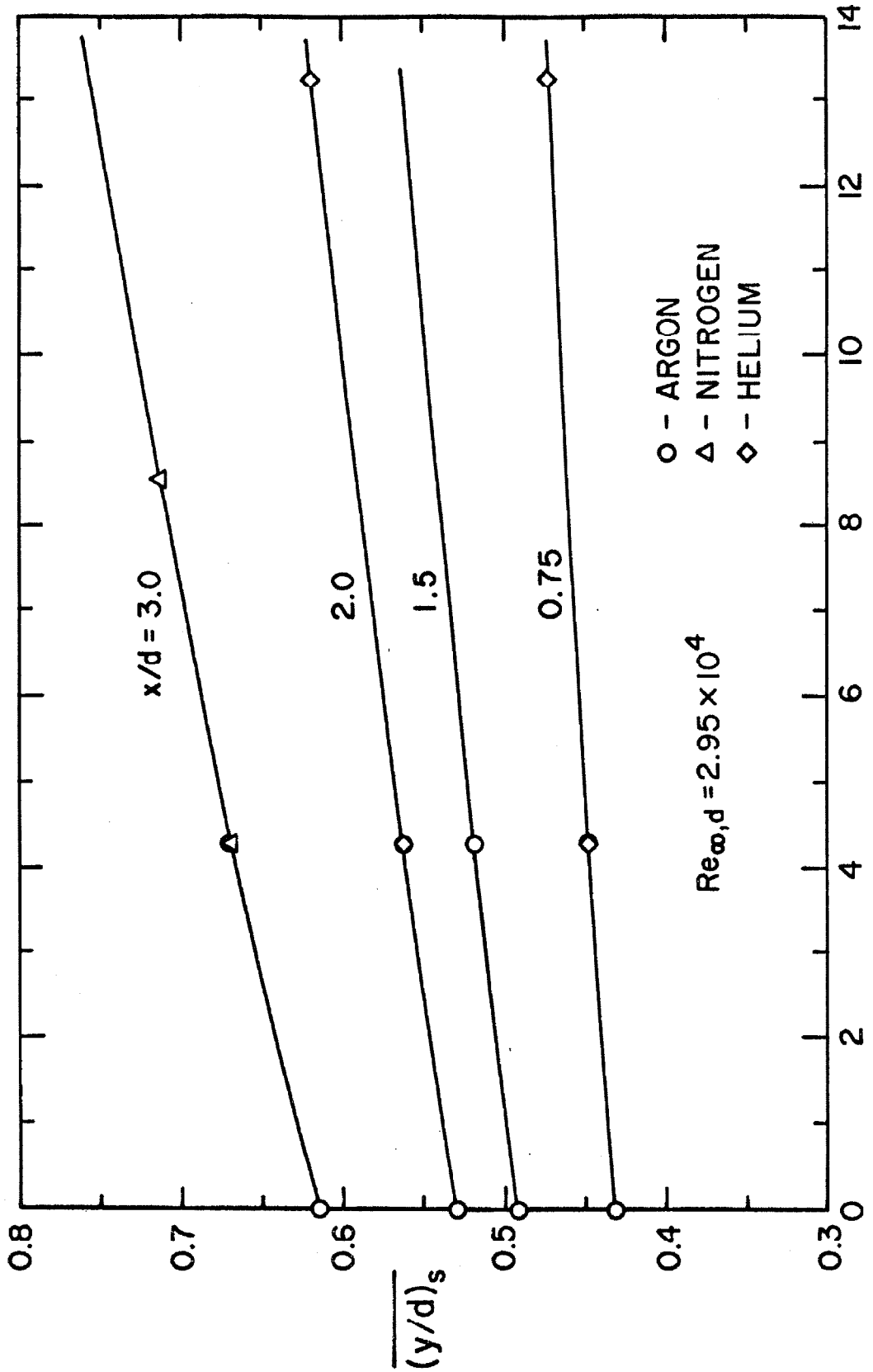

Fig. 30 SEPARATION SHOCK LOCATION WITH BASE MASS TRANSFER.

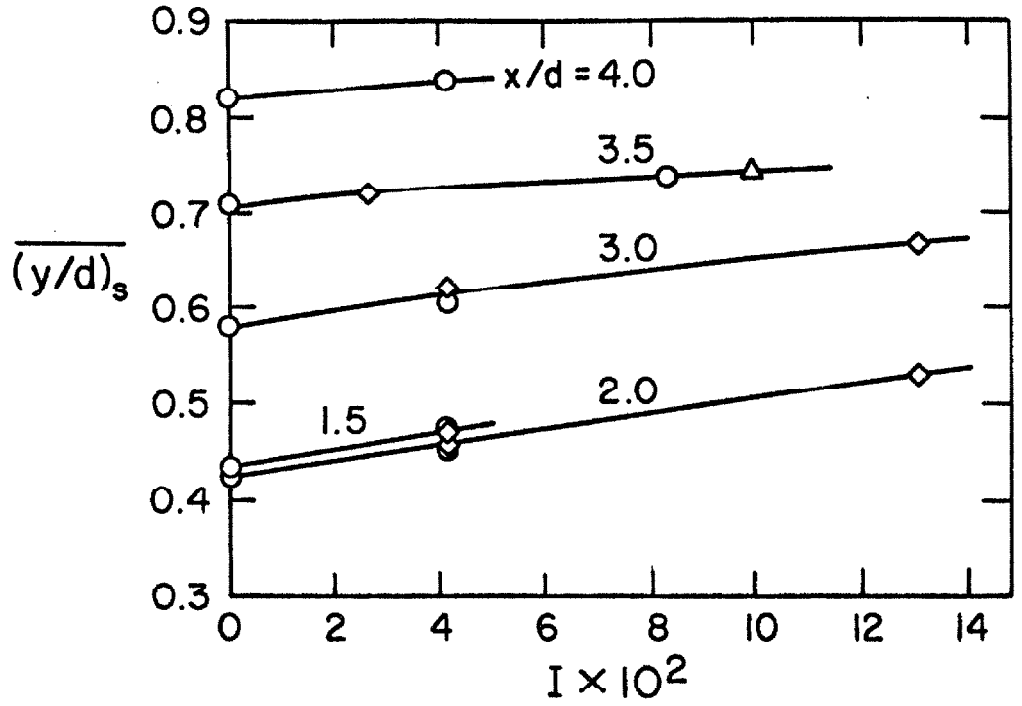

a. $Re_{\infty,d} = 0.905 \times 10^4$

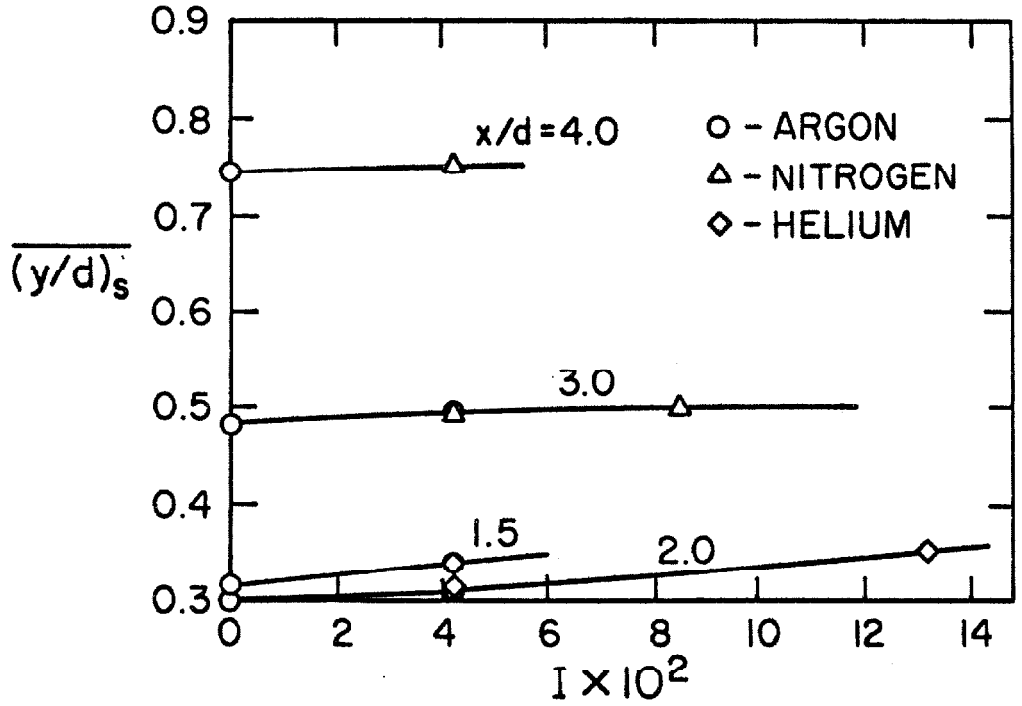

b. $Re_{\infty,d} = 2.95 \times 10^4$

Fig. 31 WAKE SHOCK LOCATION WITH BASE MASS TRANSFER

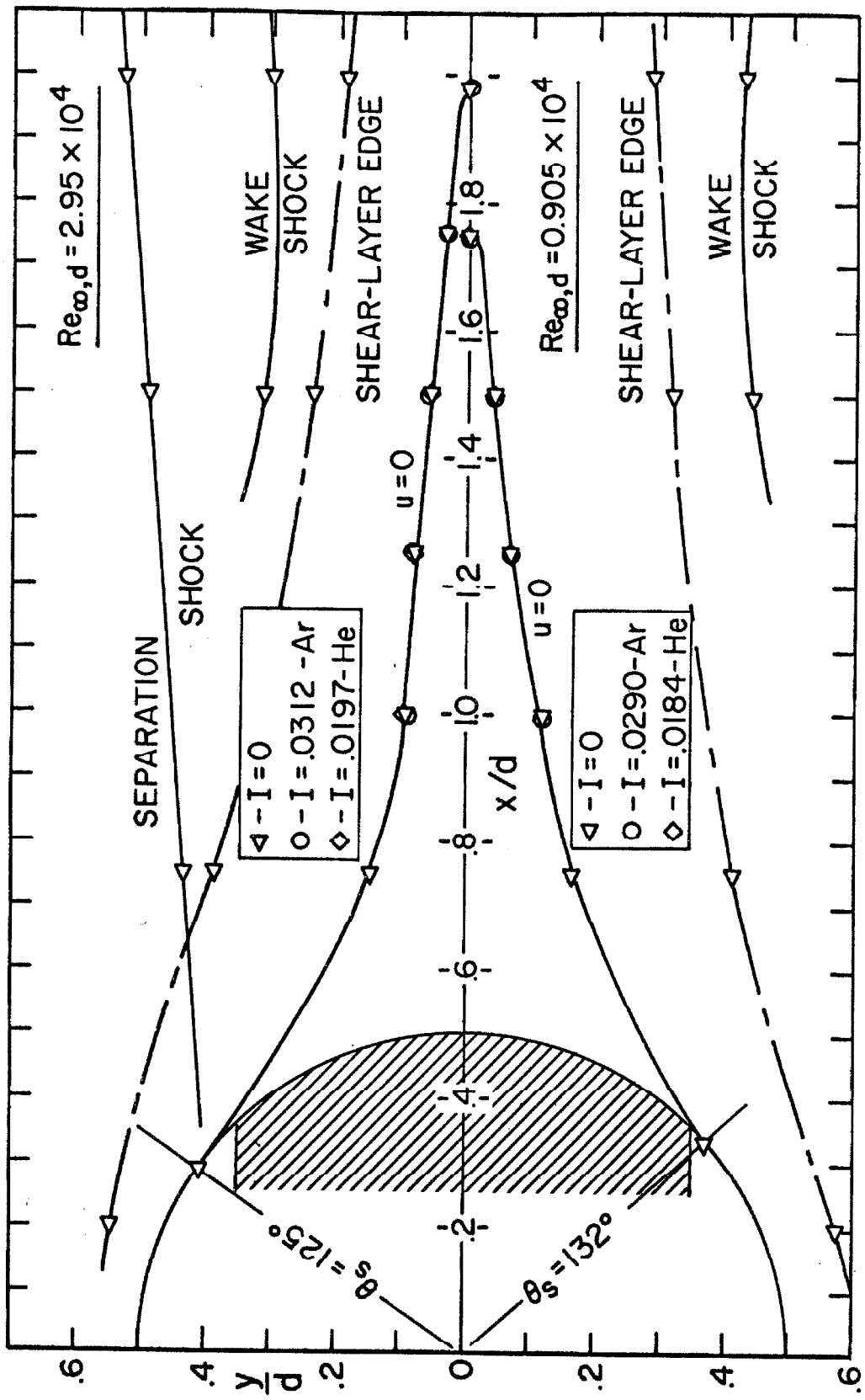

Fig. 32 NEAR-WAKE FLOW FIELD STRUCTURE WITH BASE MASS TRANSFER.

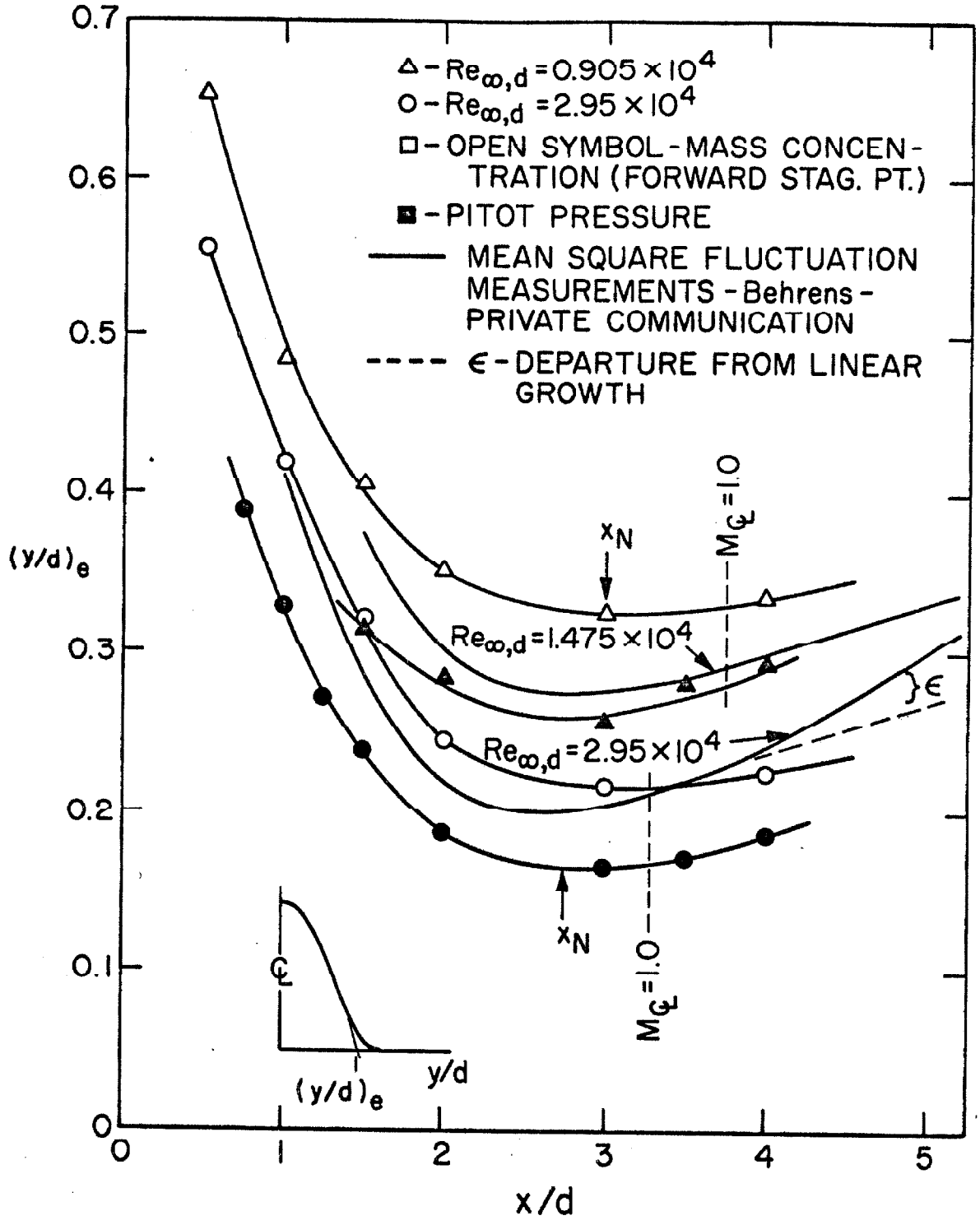

Fig.33 EXPERIMENTAL WAKE WIDTHS.

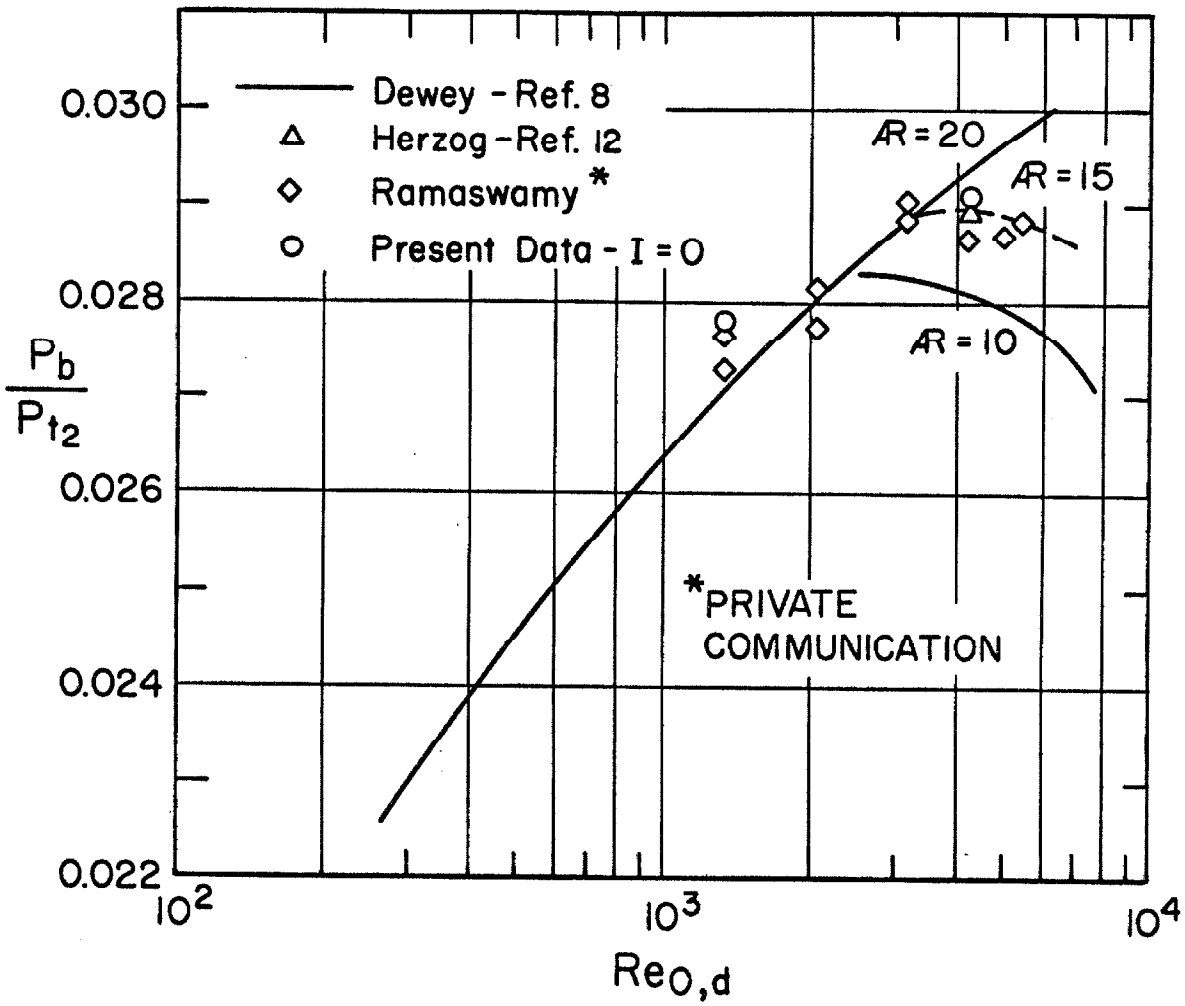

Fig.34 BASE PRESSURE VARIATION WITH REYNOLDS NUMBER

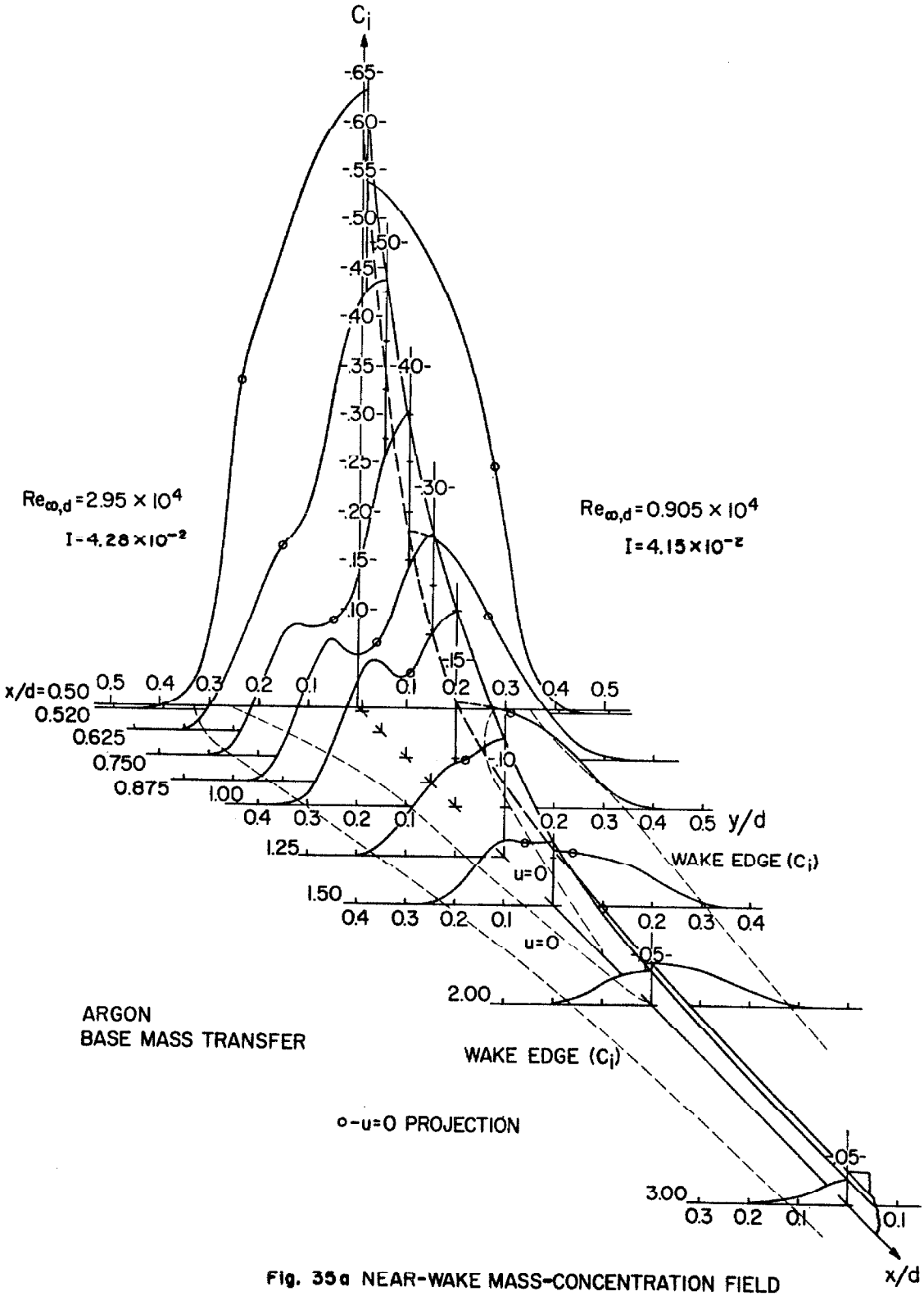

Fig. 35a NEAR-WAKE MASS-CONCENTRATION FIELD

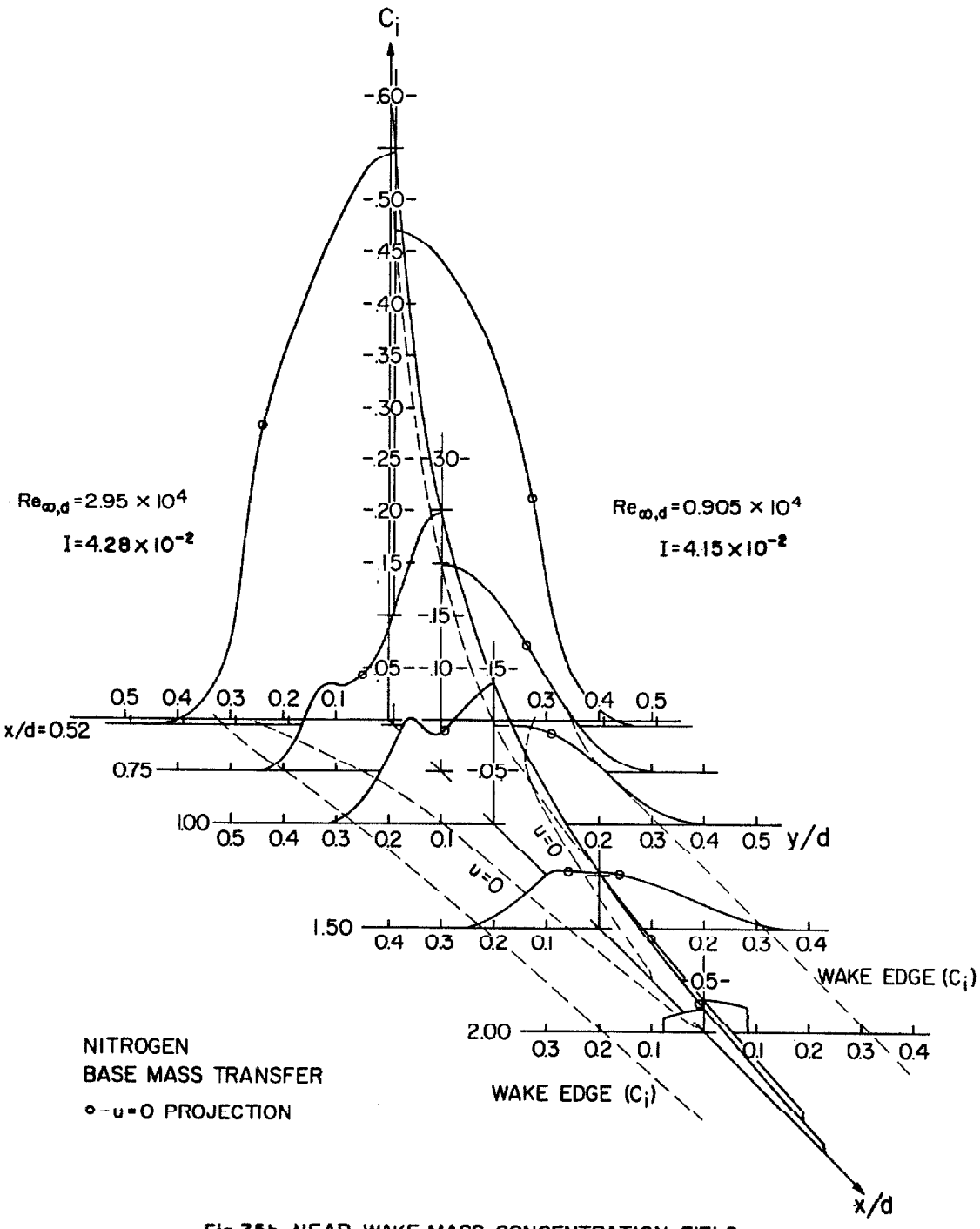

Fig. 35b NEAR-WAKE MASS-CONCENTRATION FIELD

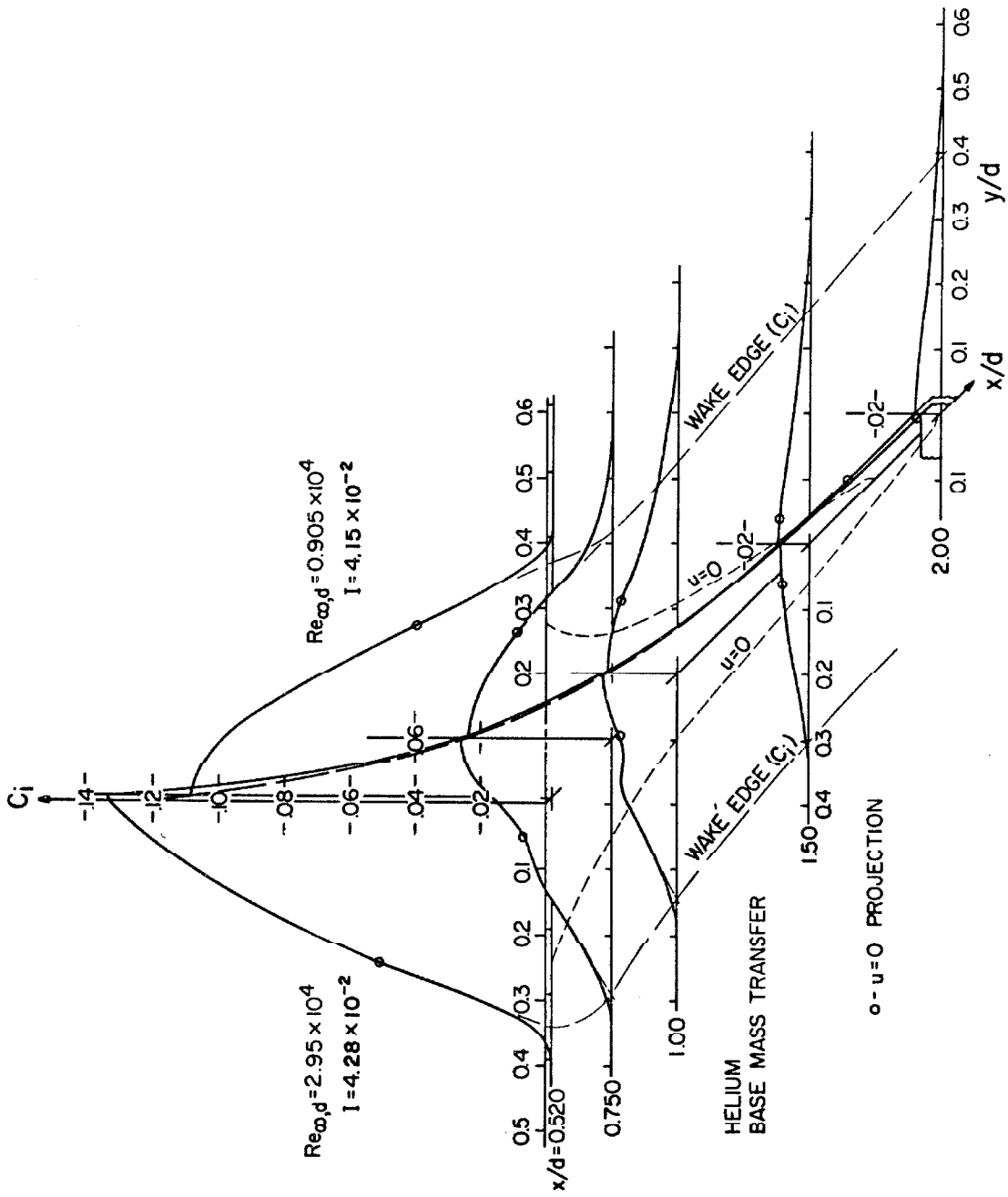

Fig. 35c NEAR-WAKE MASS-CONCENTRATION FIELD

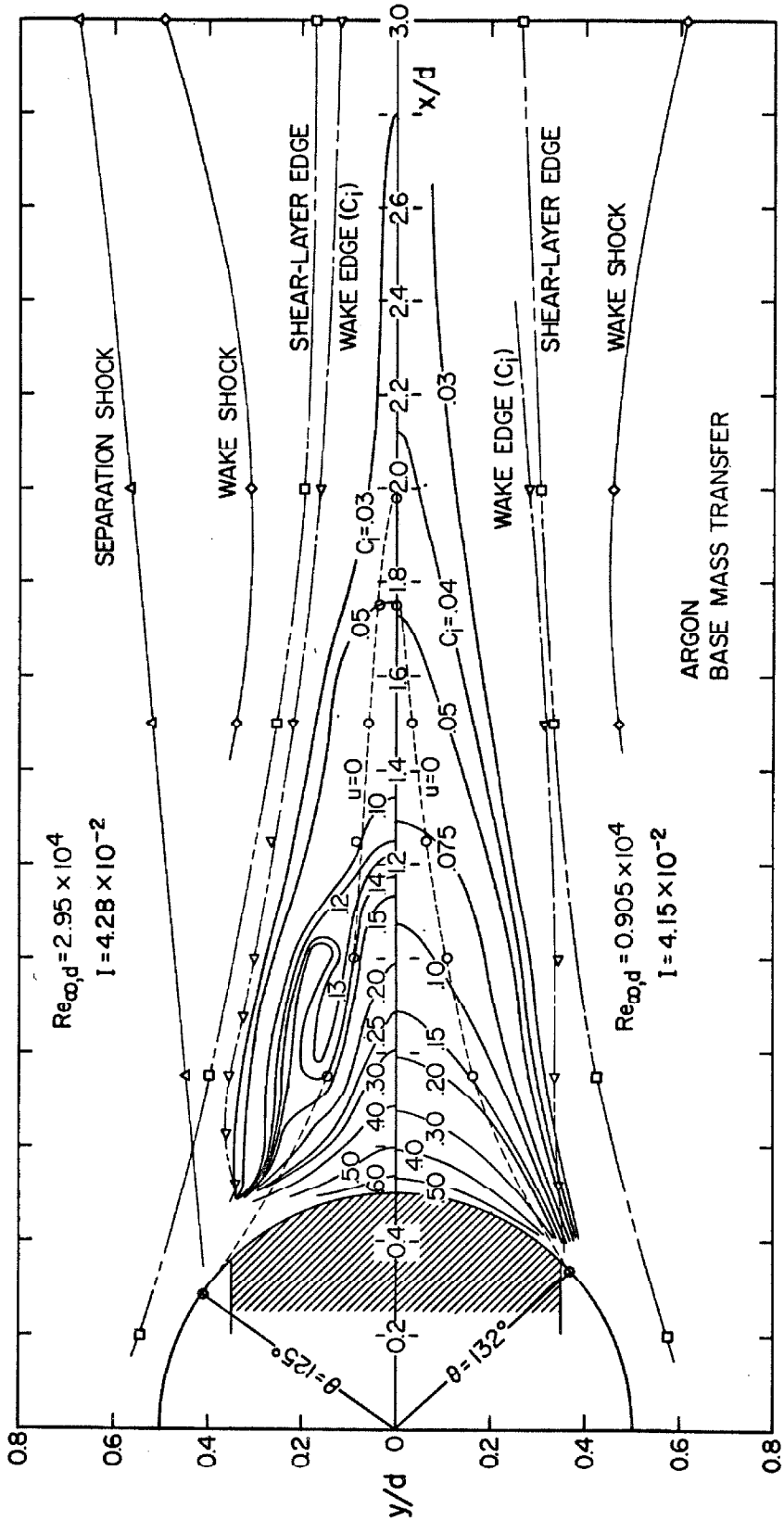

Fig. 36a MASS-CONCENTRATION ISOGRAM

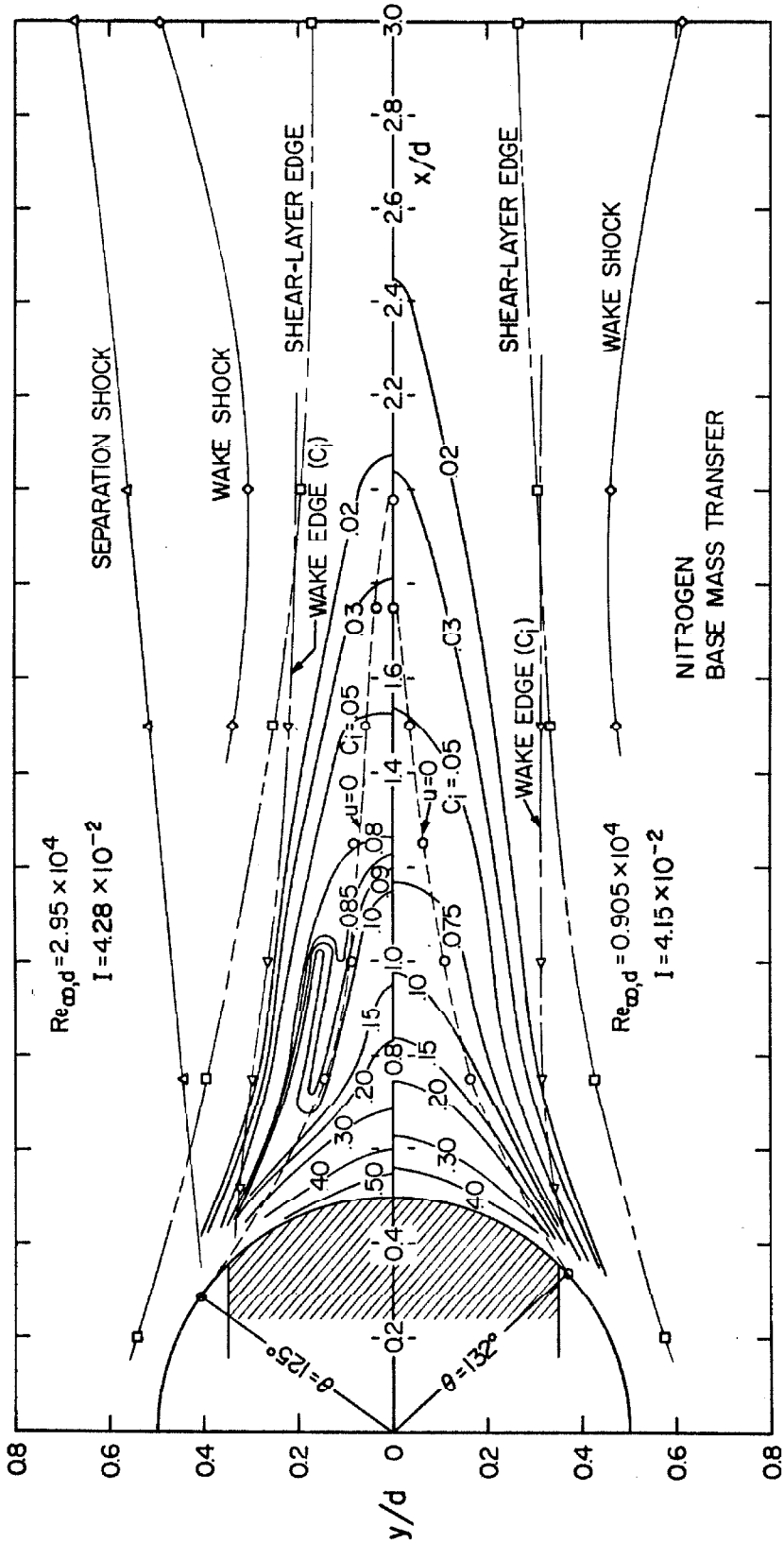

Fig. 36b. MASS-CONCENTRATION ISOGRAM

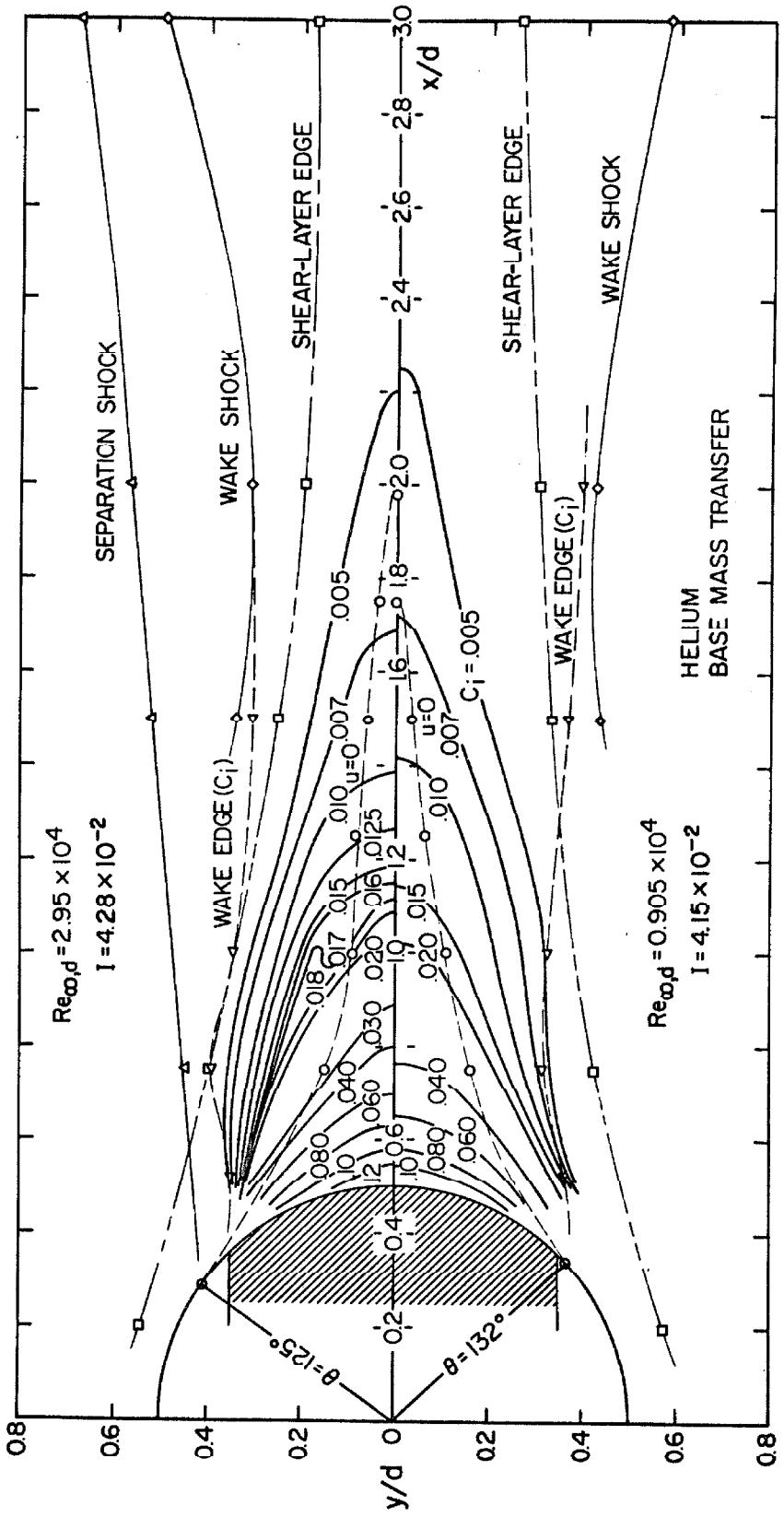

Fig. 36c MASS-CONCENTRATION ISOGRAM

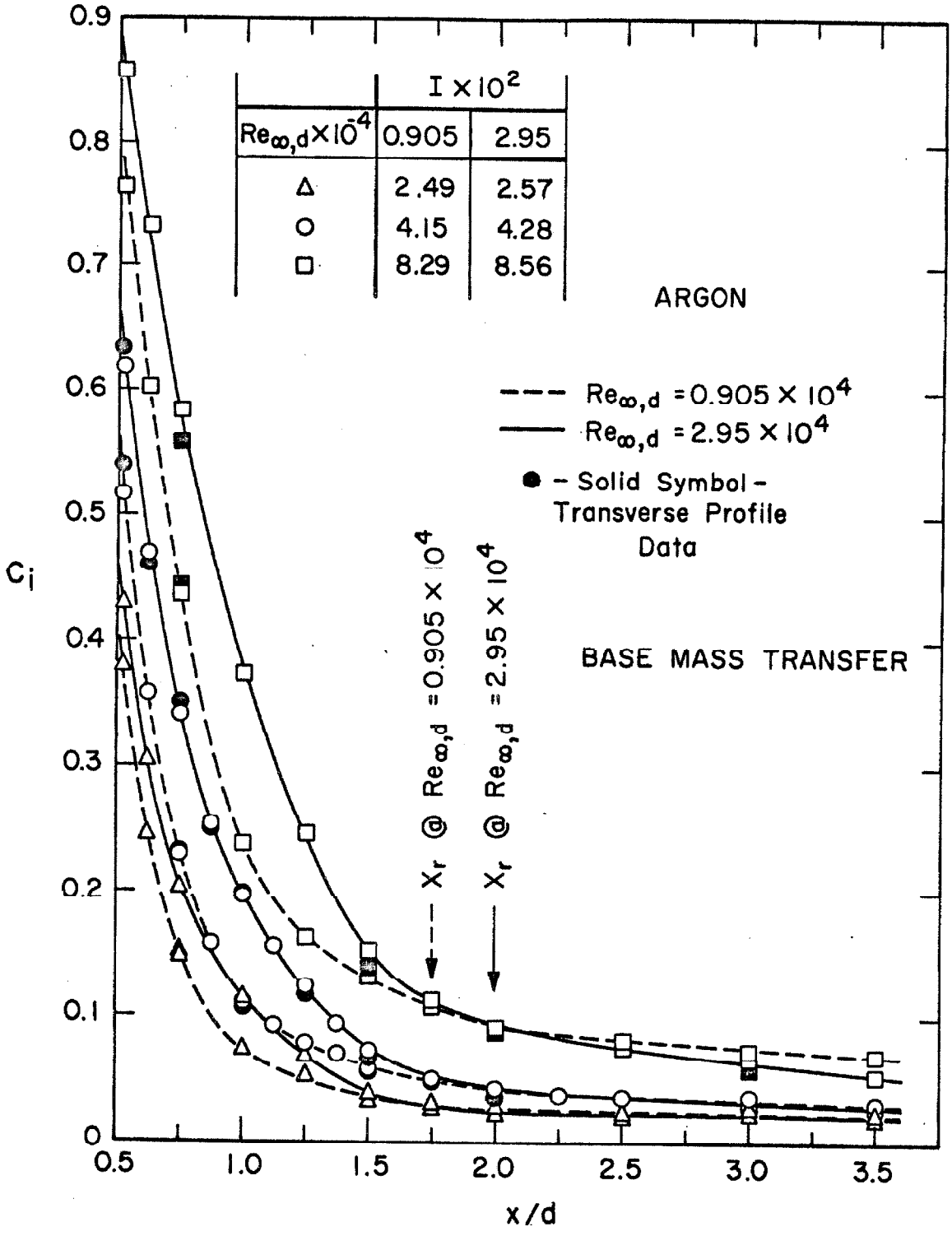

Fig. 37a NEAR-WAKE CENTERLINE MASS-CONCENTRATION PROFILES.

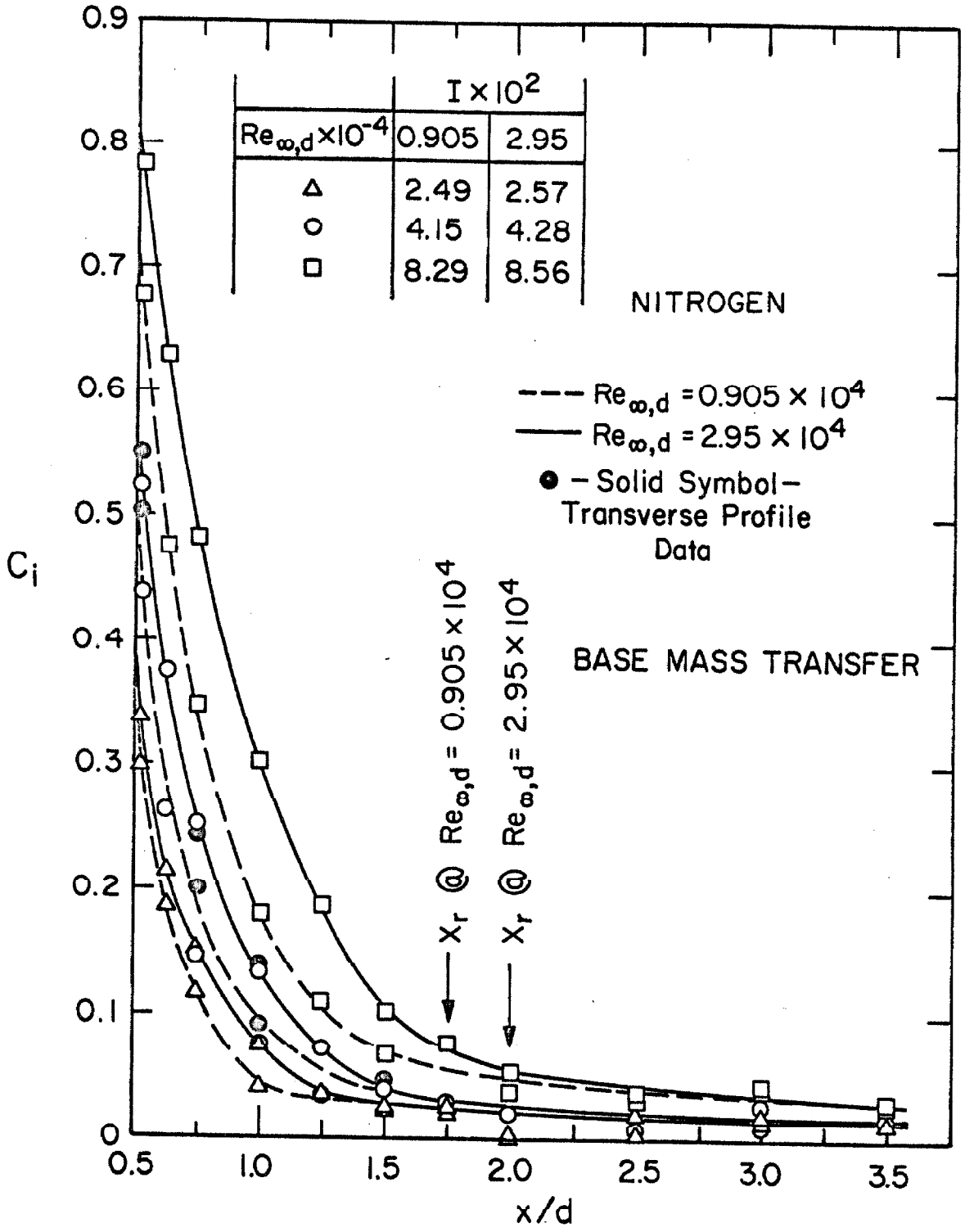

Fig. 37 b NEAR-WAKE CENTERLINE MASS-CONCENTRATION PROFILES.

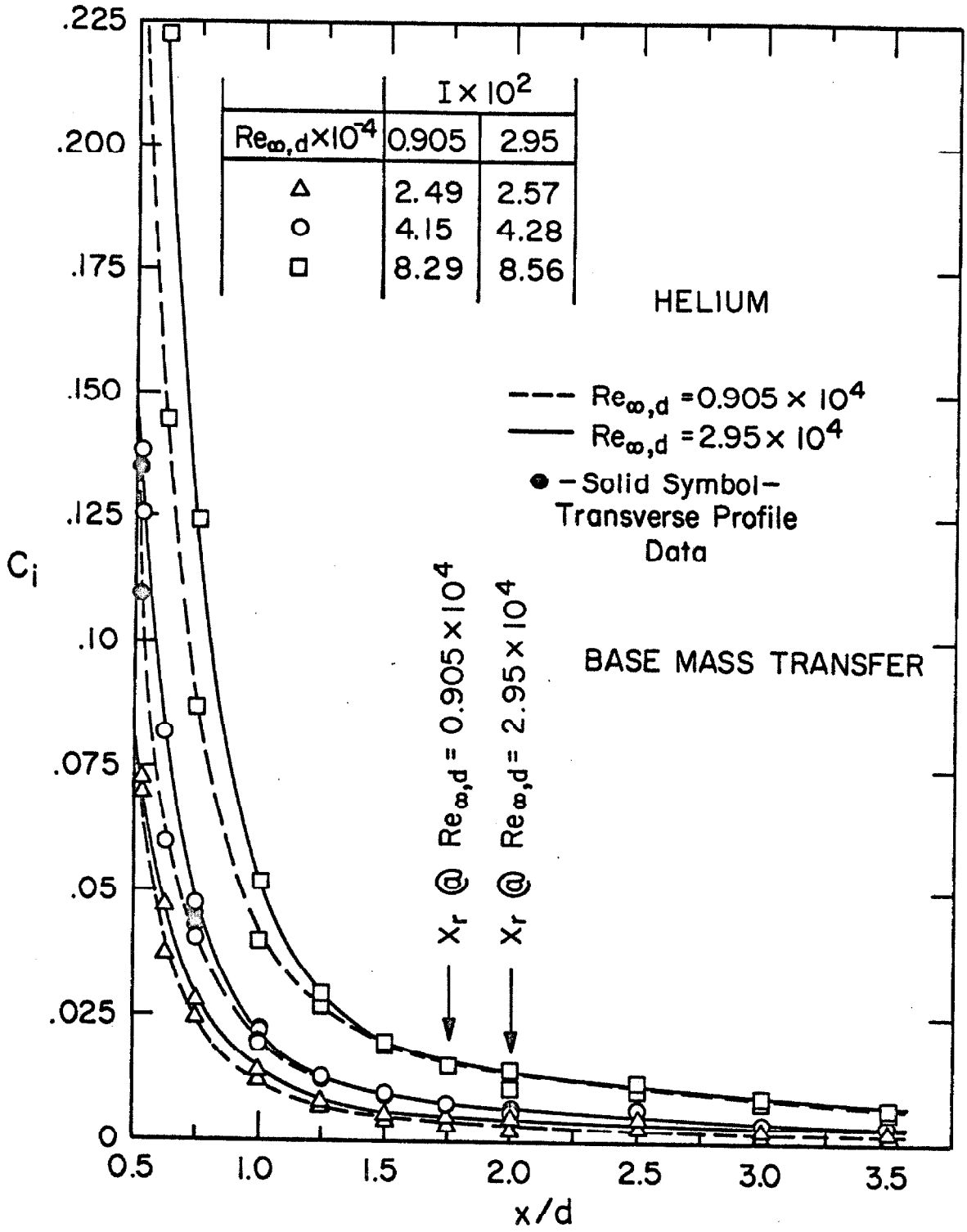

Fig. 37c NEAR-WAKE CENTERLINE MASS-CONCENTRATION PROFILES.

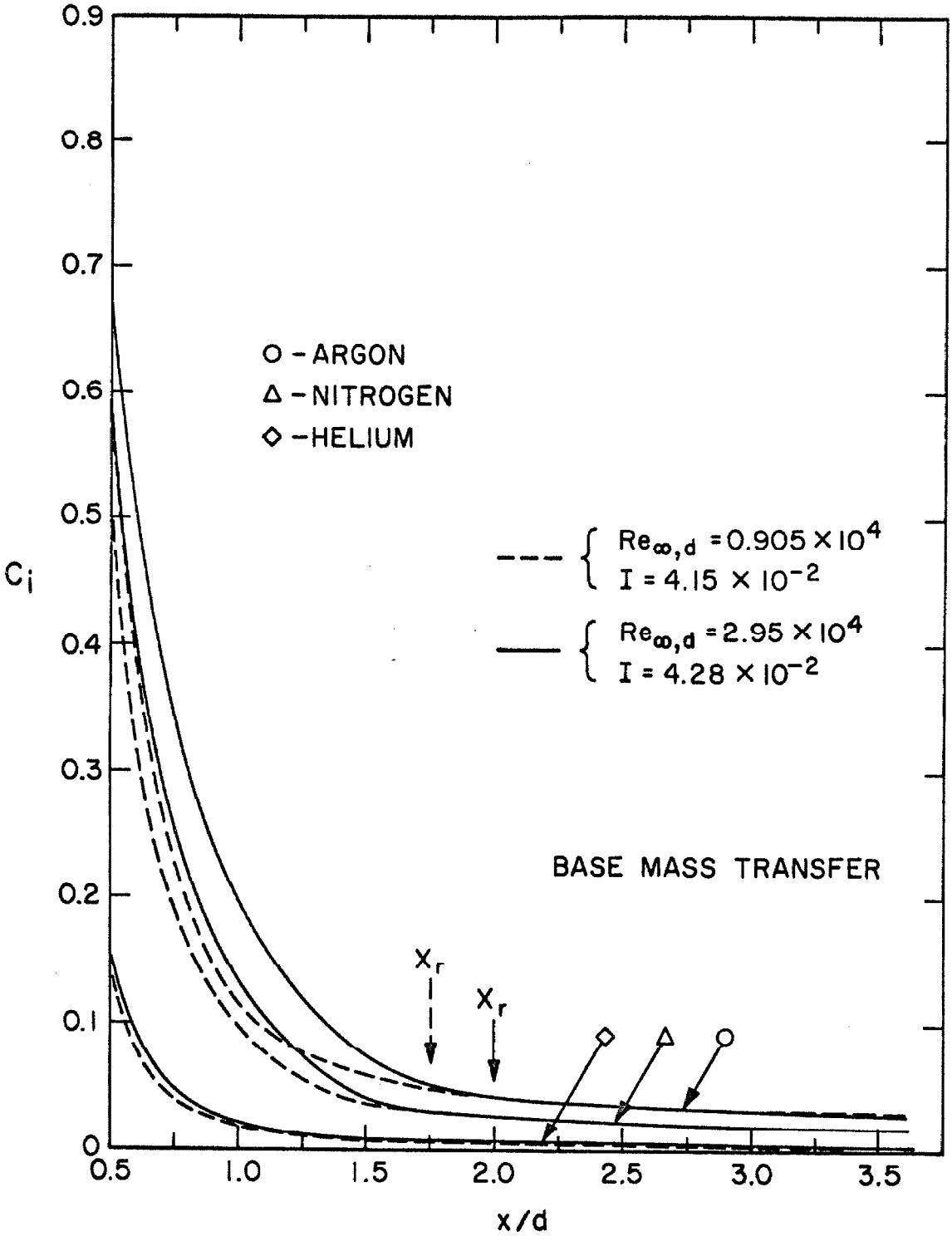

Fig. 38 NEAR-WAKE CENTERLINE MASS-CONCENTRATION PROFILES

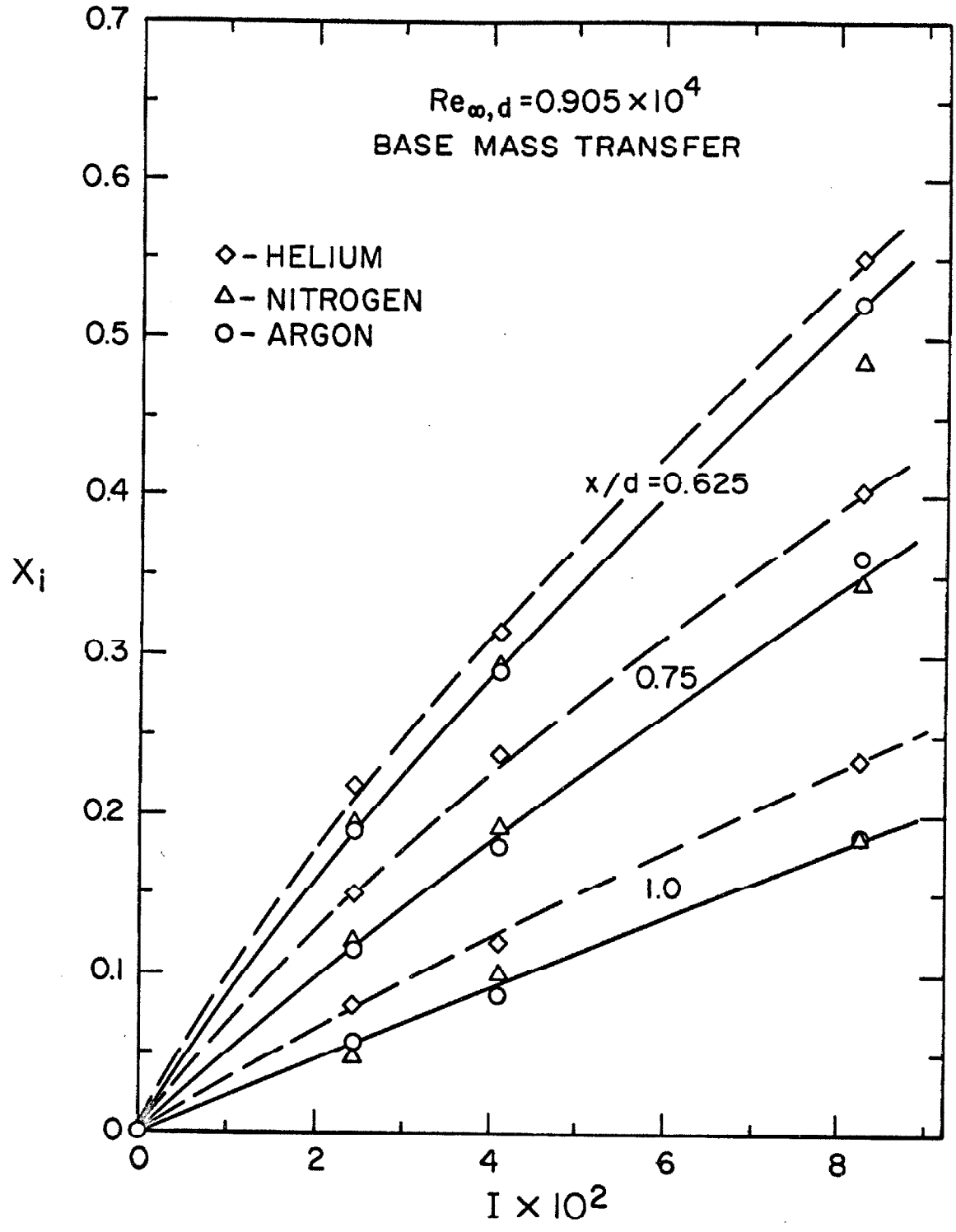

Fig. 39a NEAR-WAKE CENTERLINE MOLE-FRACTION DEPENDENCE ON MASS TRANSFER PARAMETER

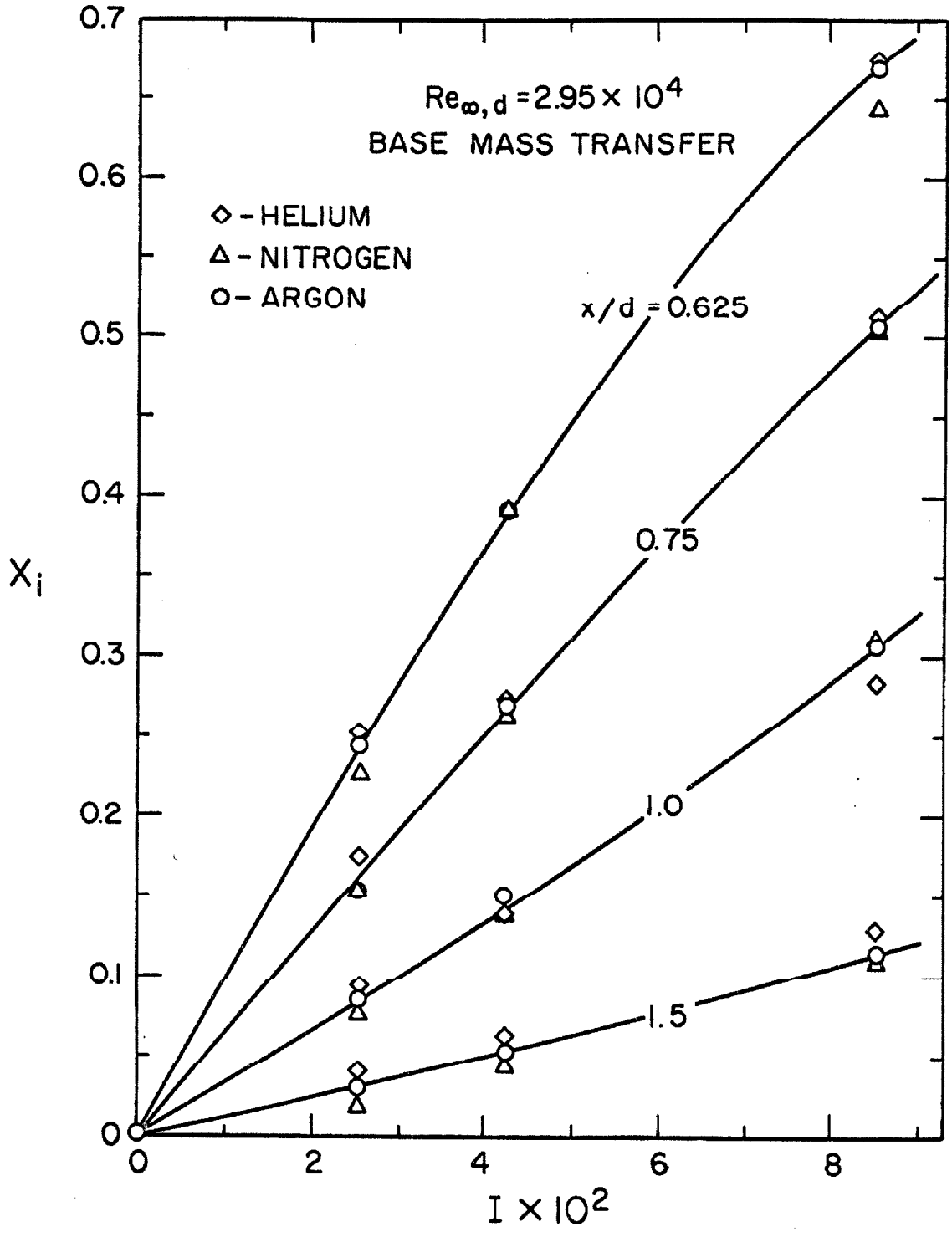

Fig. 39b NEAR-WAKE CENTERLINE MOLE-FRACTION DEPENDENCE ON MASS TRANSFER PARAMETER

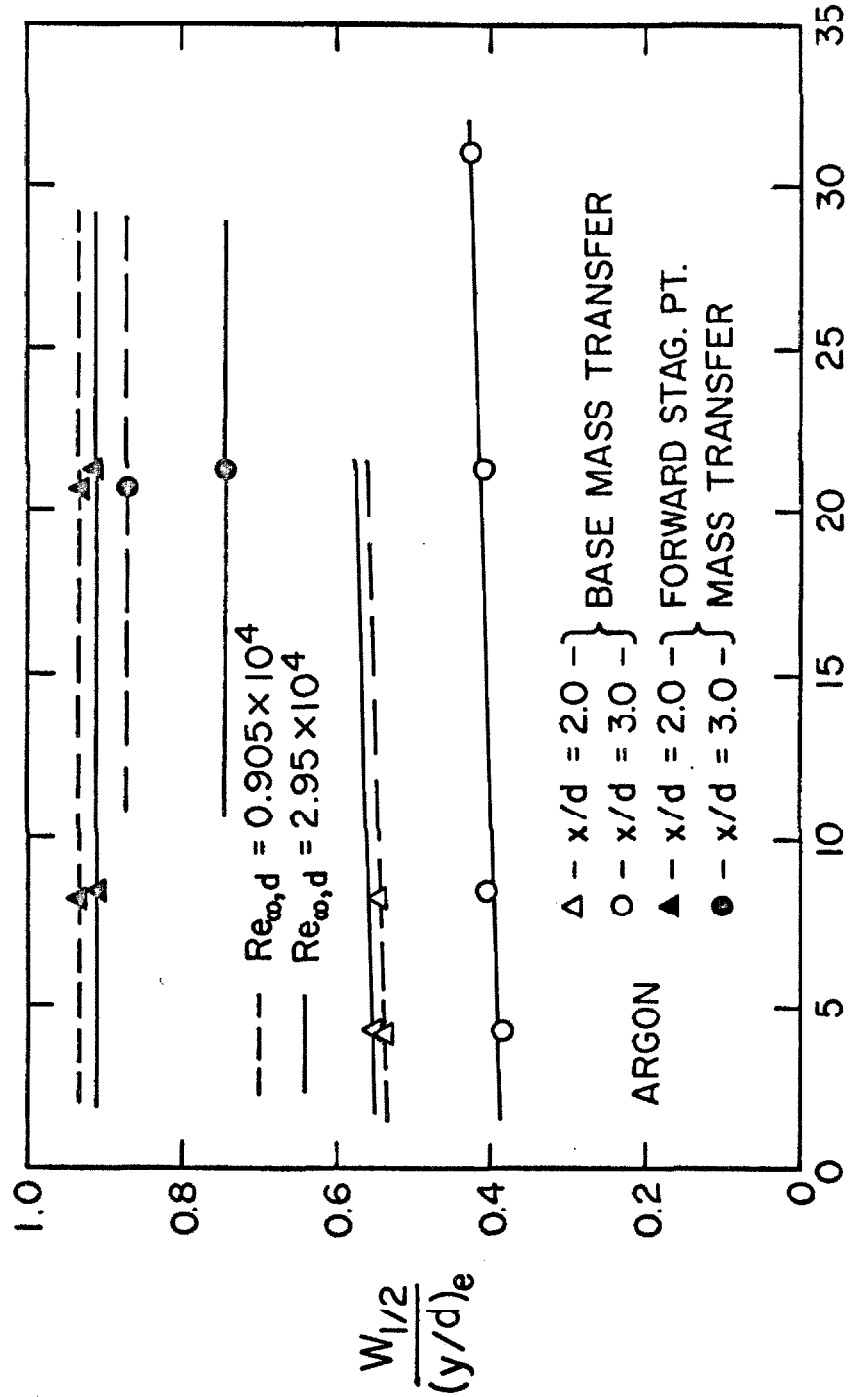

Fig. 40 MASS-CONCENTRATION PROFILE WIDTH

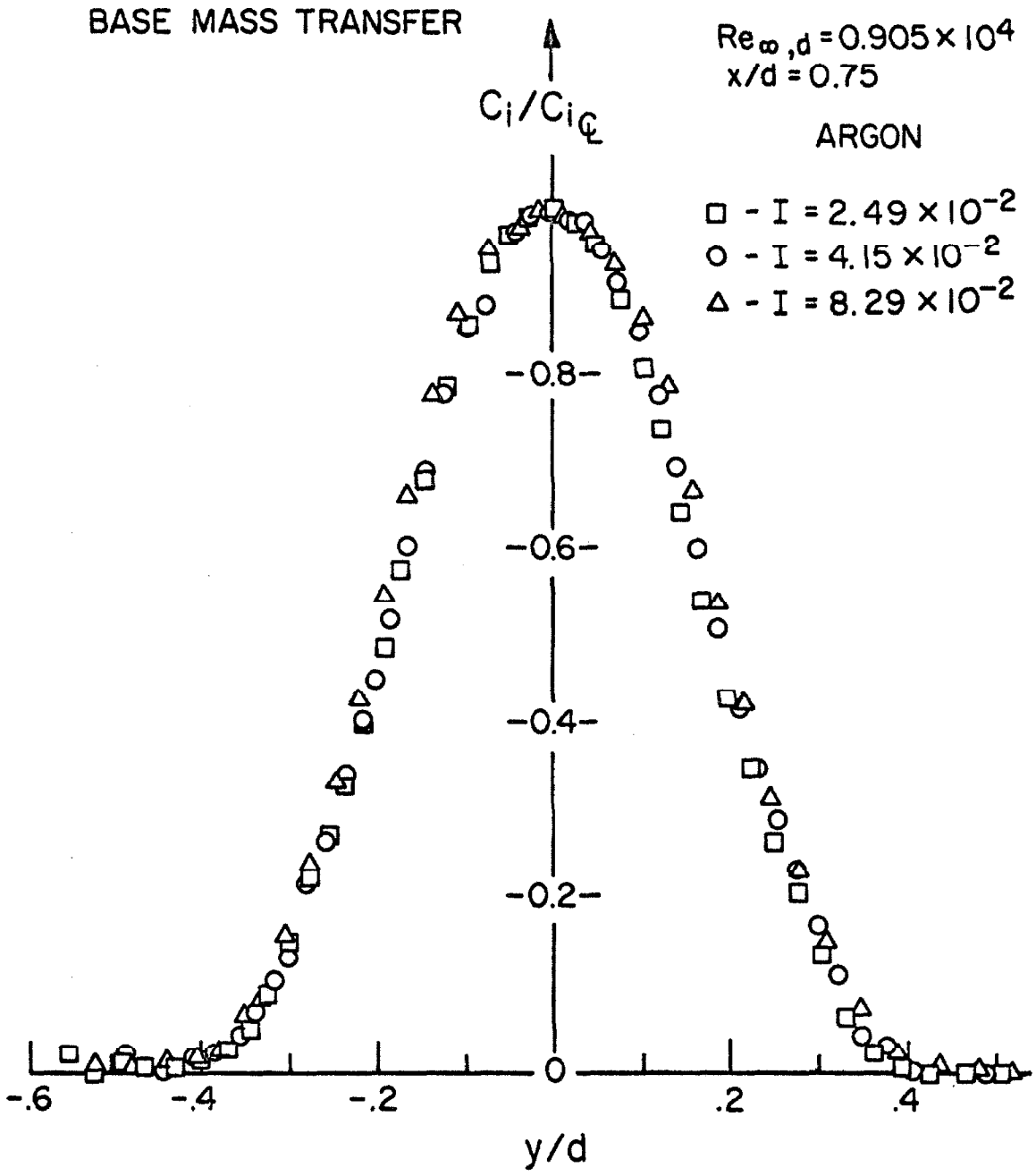

Fig. 41a THE EFFECT OF THE INJECTION PARAMETER ON THE MASS-CONCENTRATION FIELD.

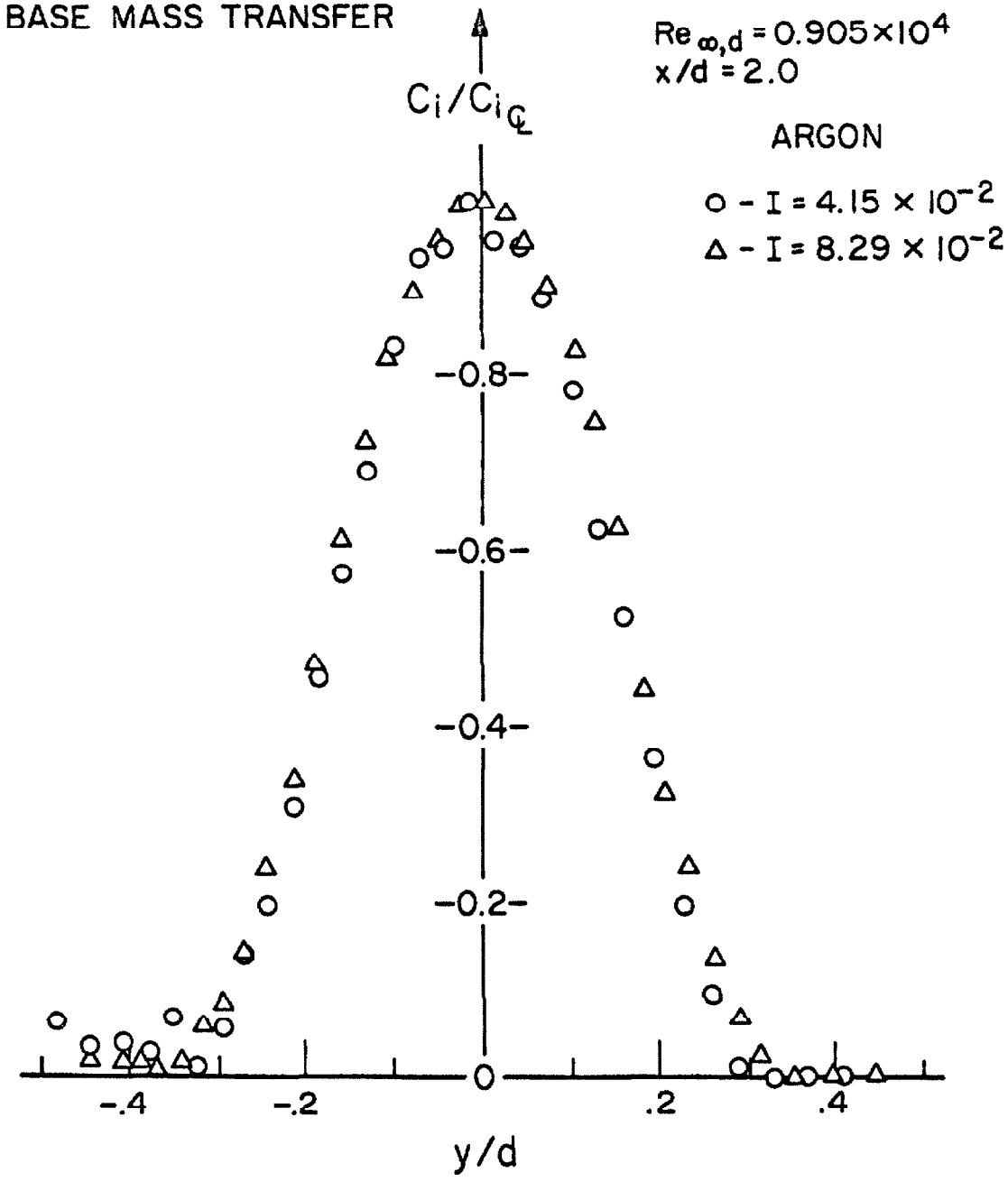

Fig. 41b THE EFFECT OF THE INJECTION PARAMETER ON THE MASS-CONCENTRATION FIELD.

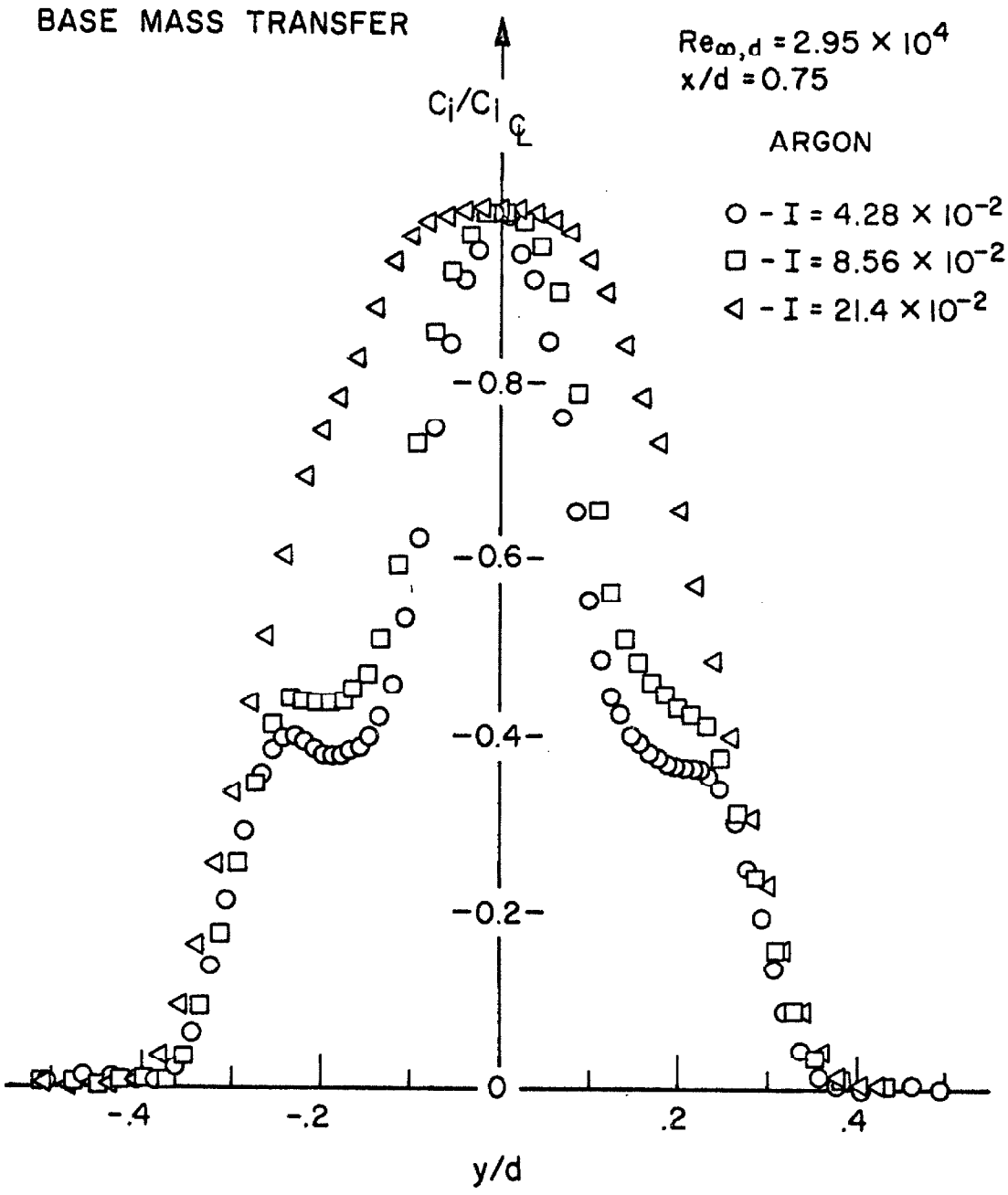

Fig. 41c THE EFFECT OF THE INJECTION PARAMETER ON THE MASS-CONCENTRATION FIELD.

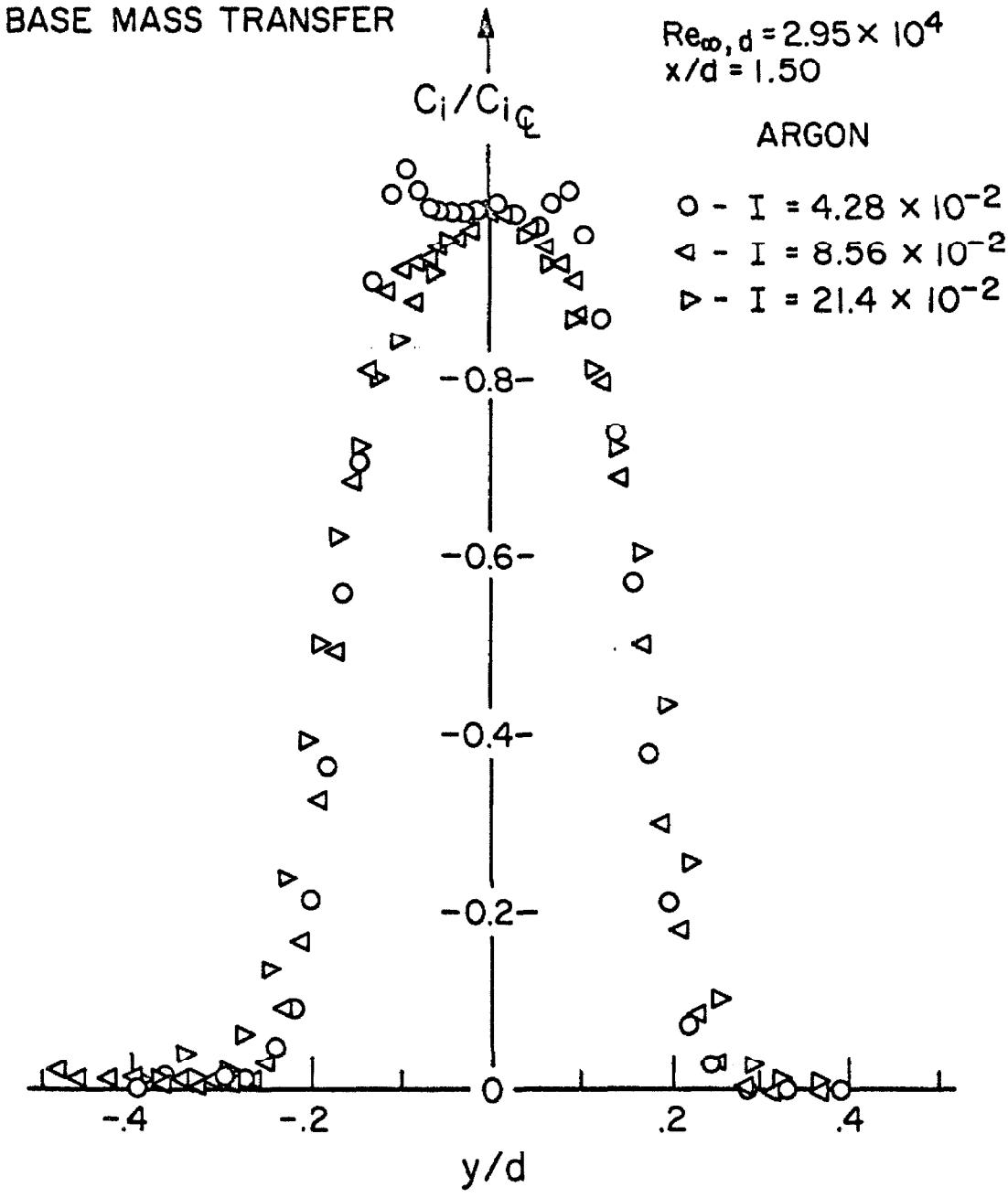

Fig. 41d THE EFFECT OF THE INJECTION PARAMETER ON THE MASS-CONCENTRATION FIELD.

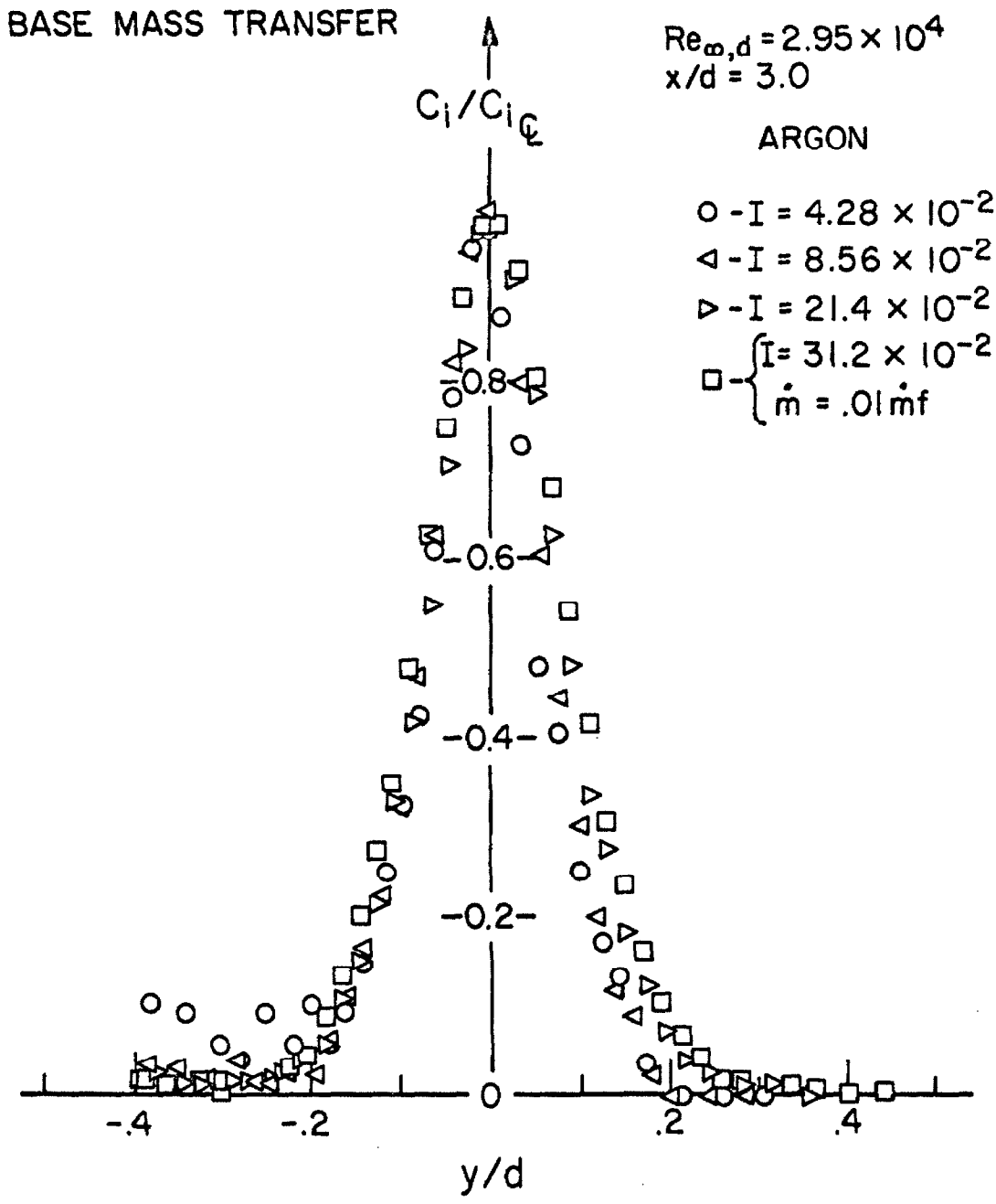

Fig. 41e THE EFFECT OF THE INJECTION PARAMETER ON THE MASS-CONCENTRATION FIELD.

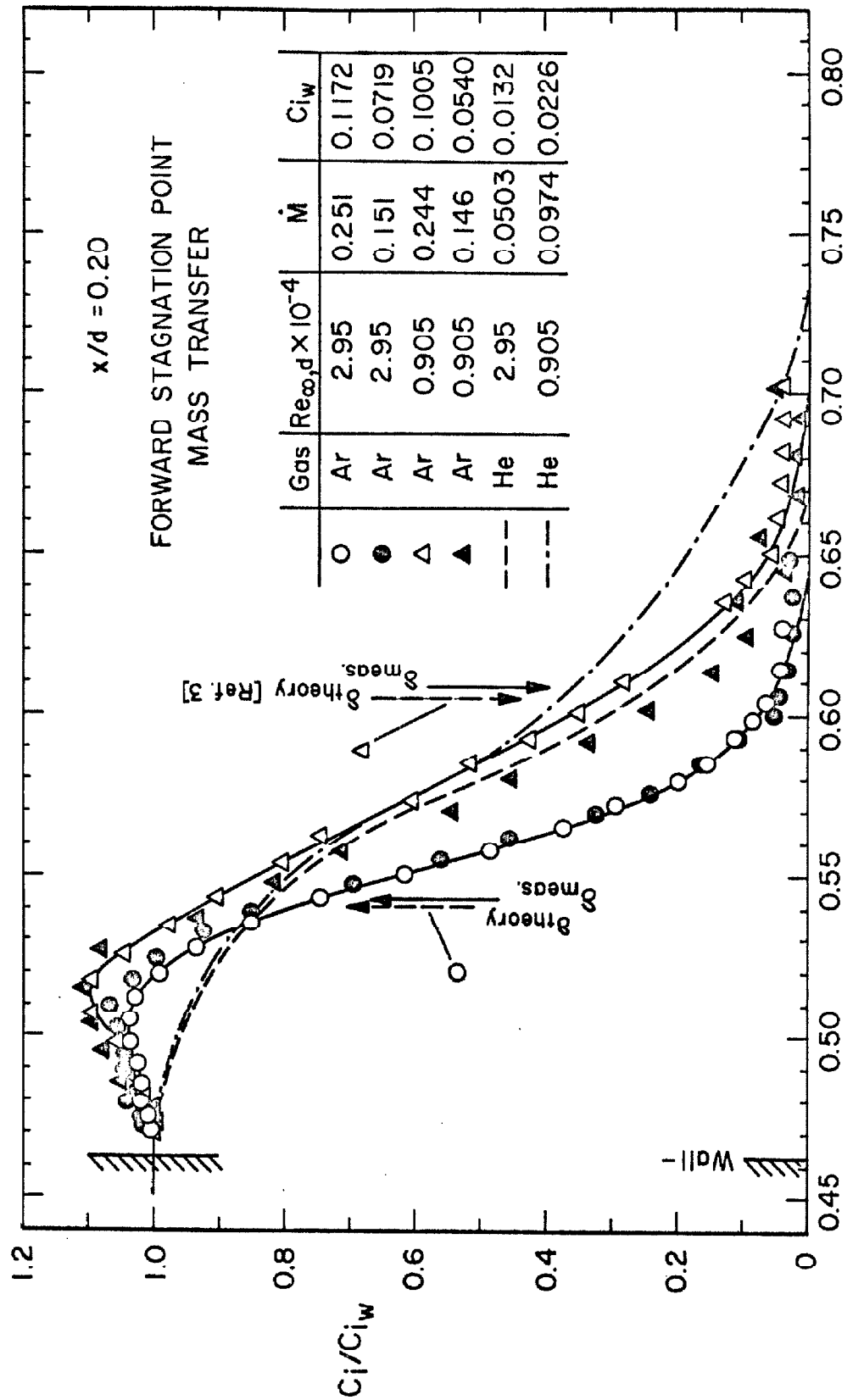

Fig. 42 CYLINDER BOUNDARY-LAYER MASS CONCENTRATION UPSTREAM OF SEPARATION

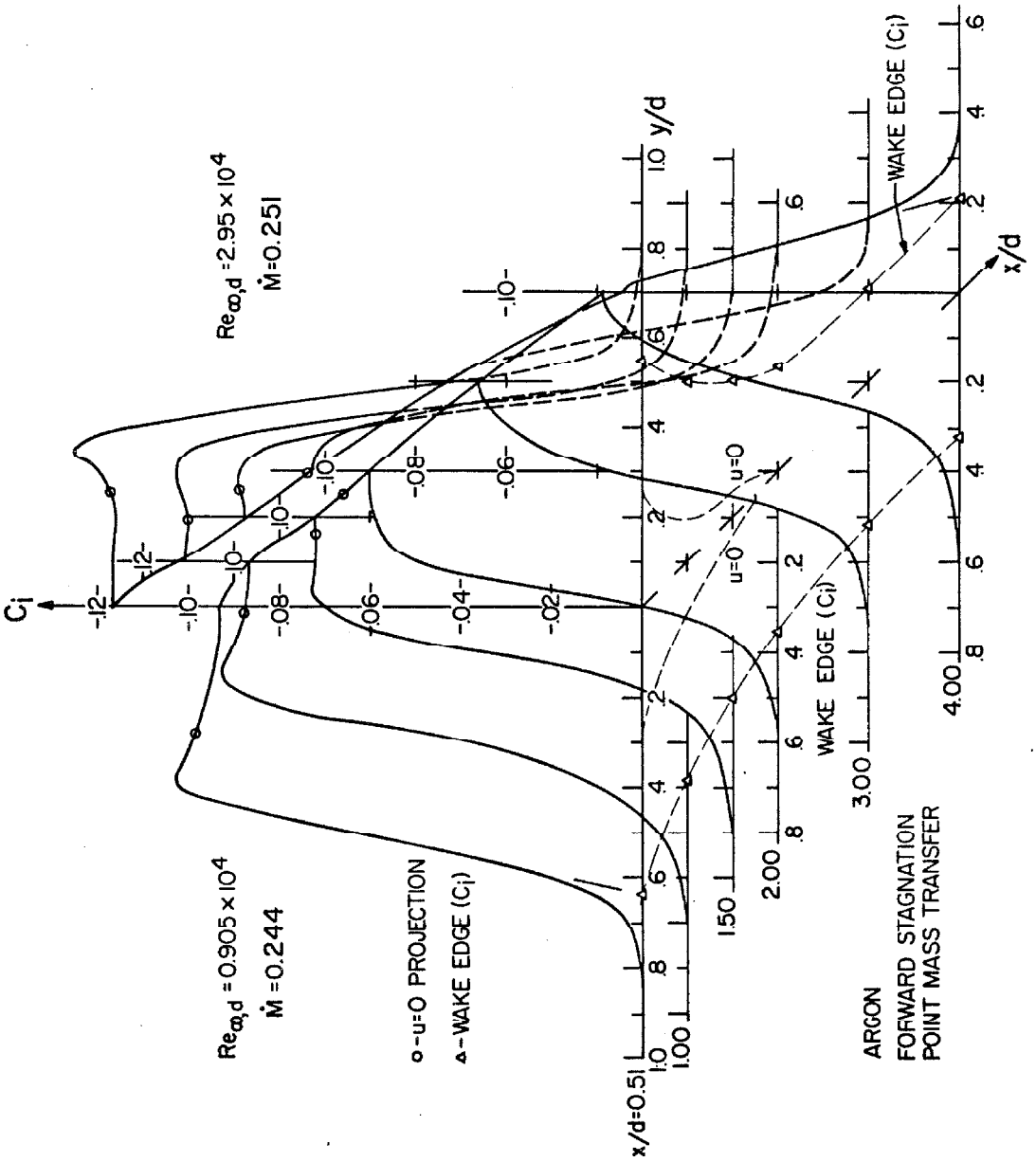

Fig. 43a NEAR-WAKE MASS-CONCENTRATION FIELD

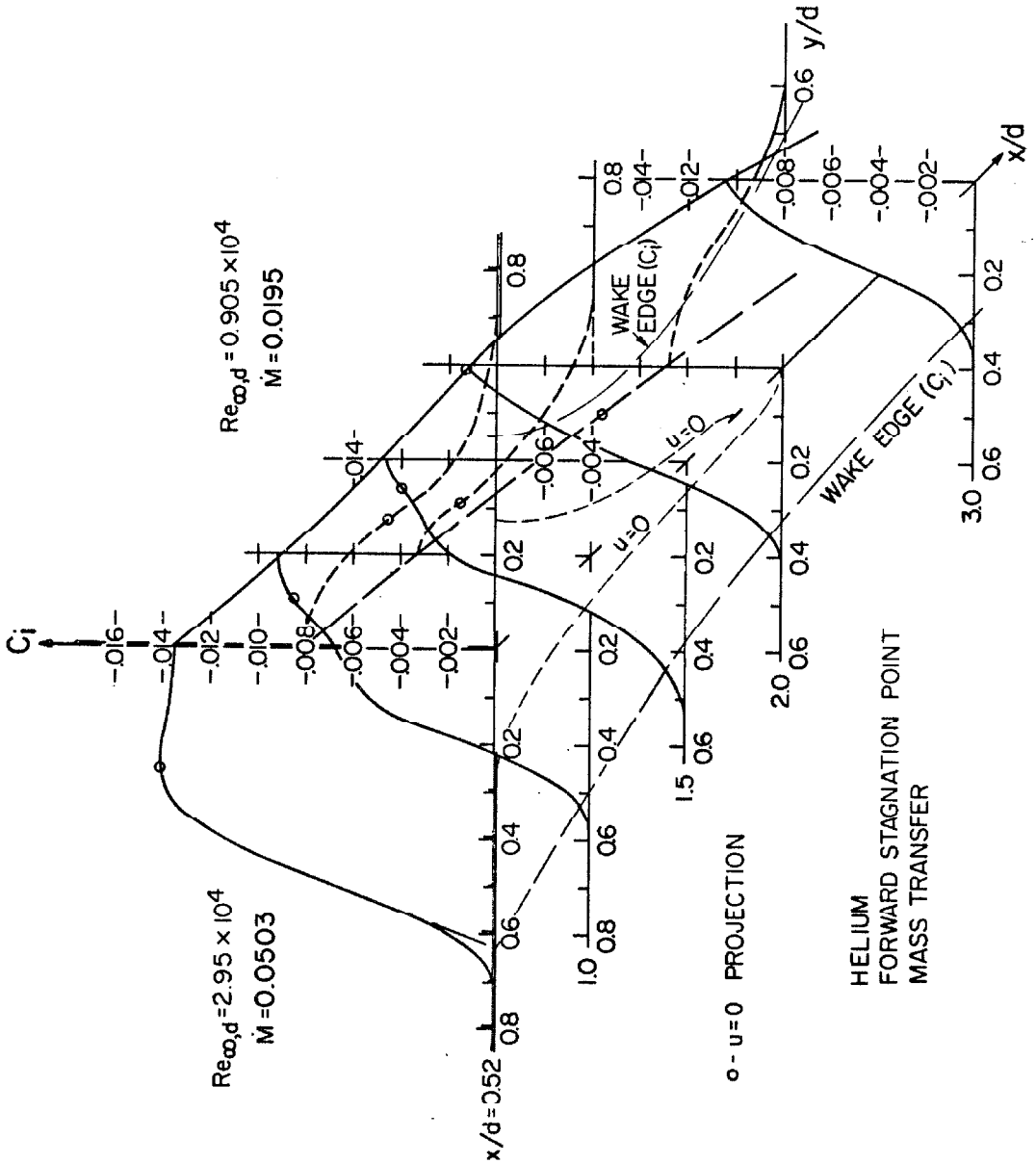

Fig.43b NEAR-WAKE MASS-CONCENTRATION FIELD

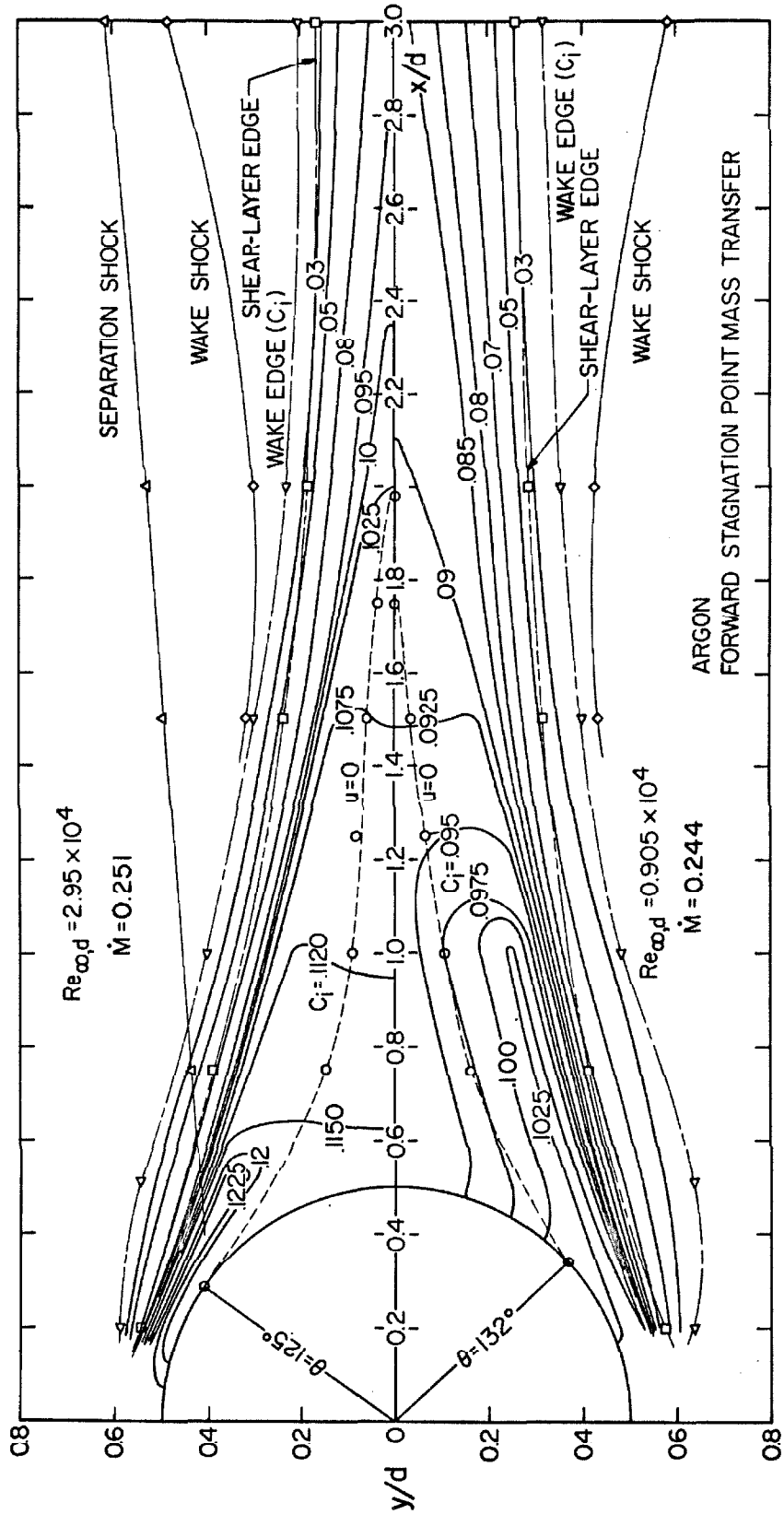

Fig. 44a MASS-CONCENTRATION ISOGRAM

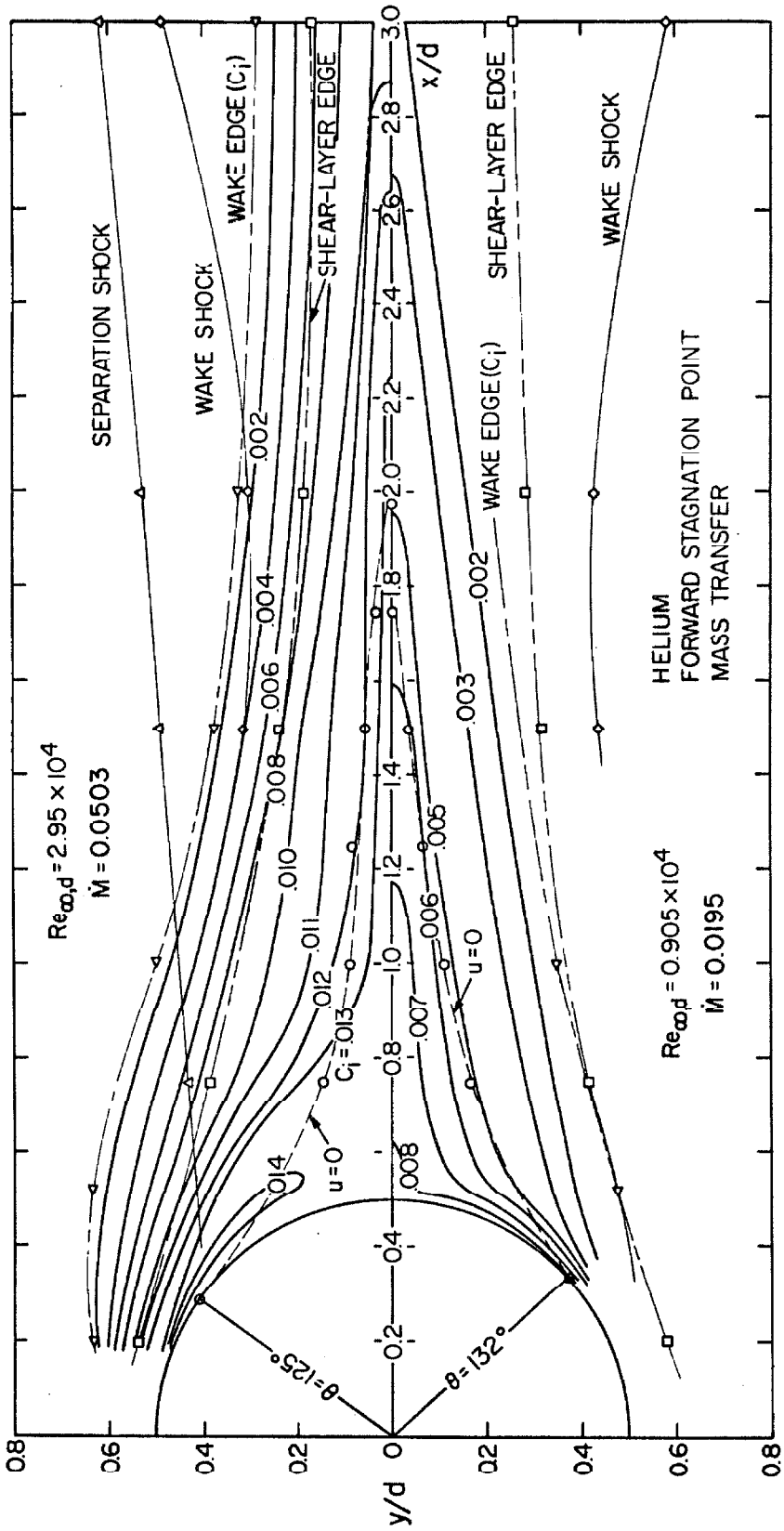

Fig. 44b MASS-CONCENTRATION ISOGRAM

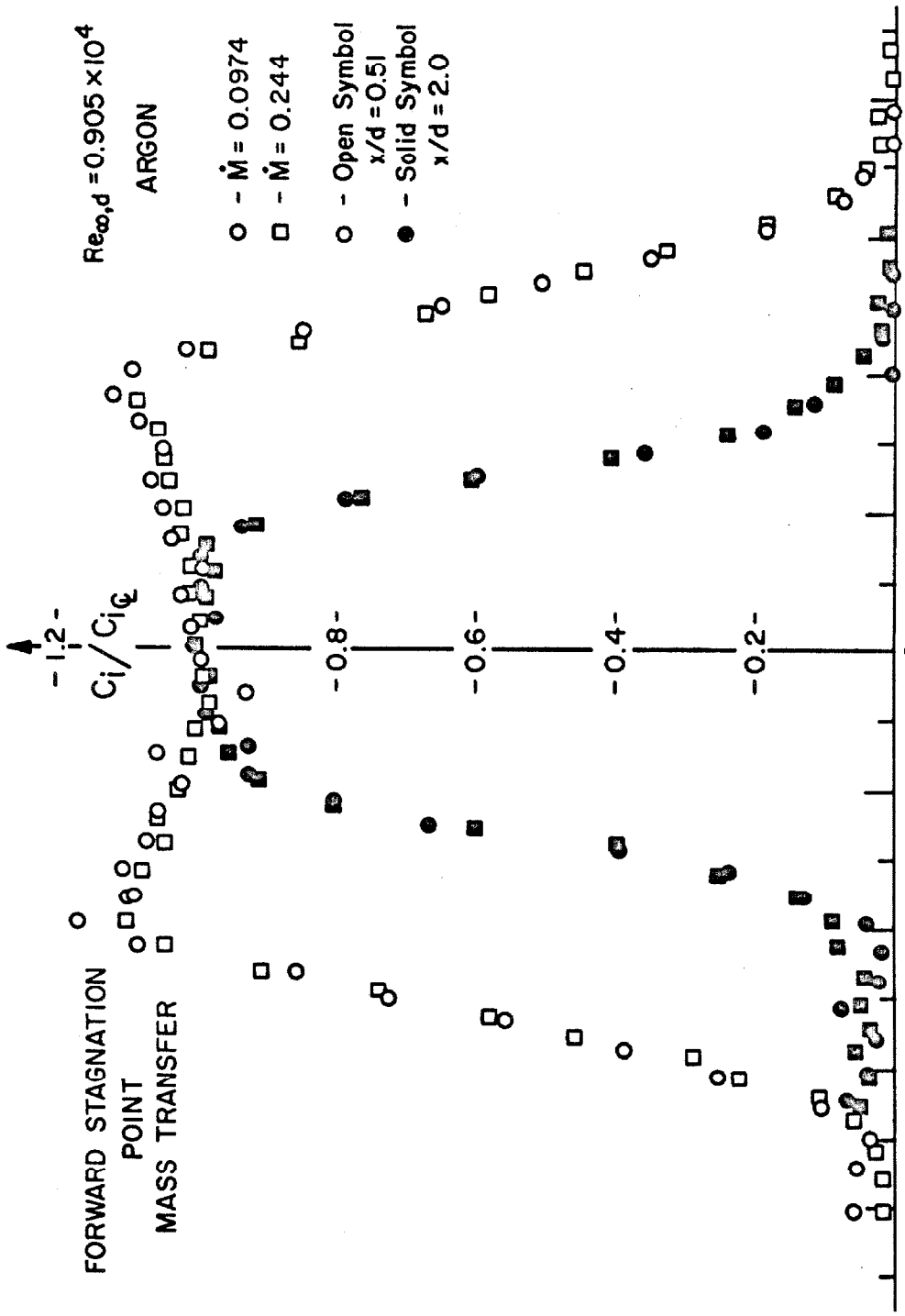

Fig. 45 a THE EFFECT OF THE INJECTION PARAMETER ON THE MASS-CONCENTRATION FIELD.

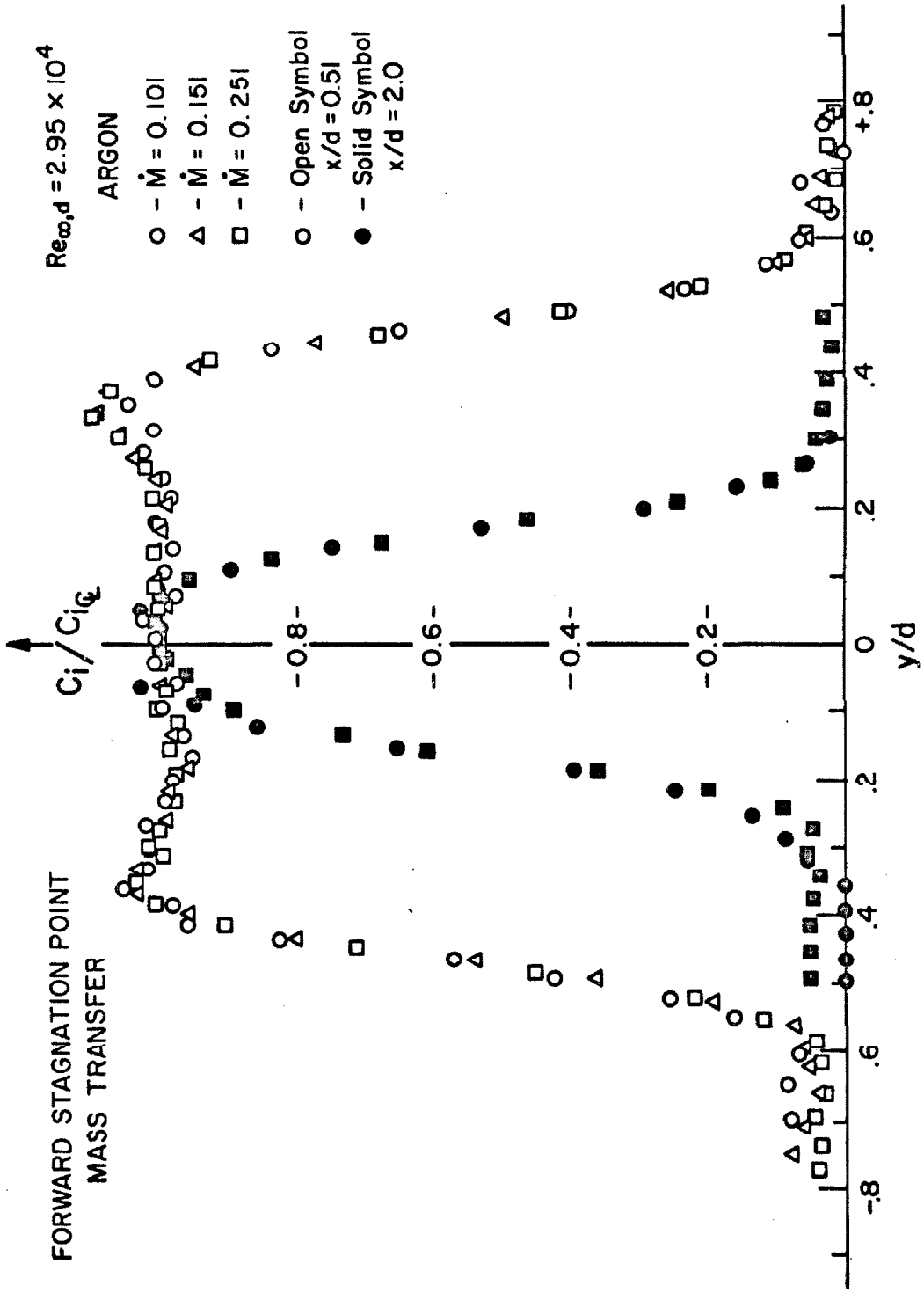

Fig. 45b THE EFFECT OF THE INJECTION PARAMETER ON THE MASS-CONCENTRATION FIELD.

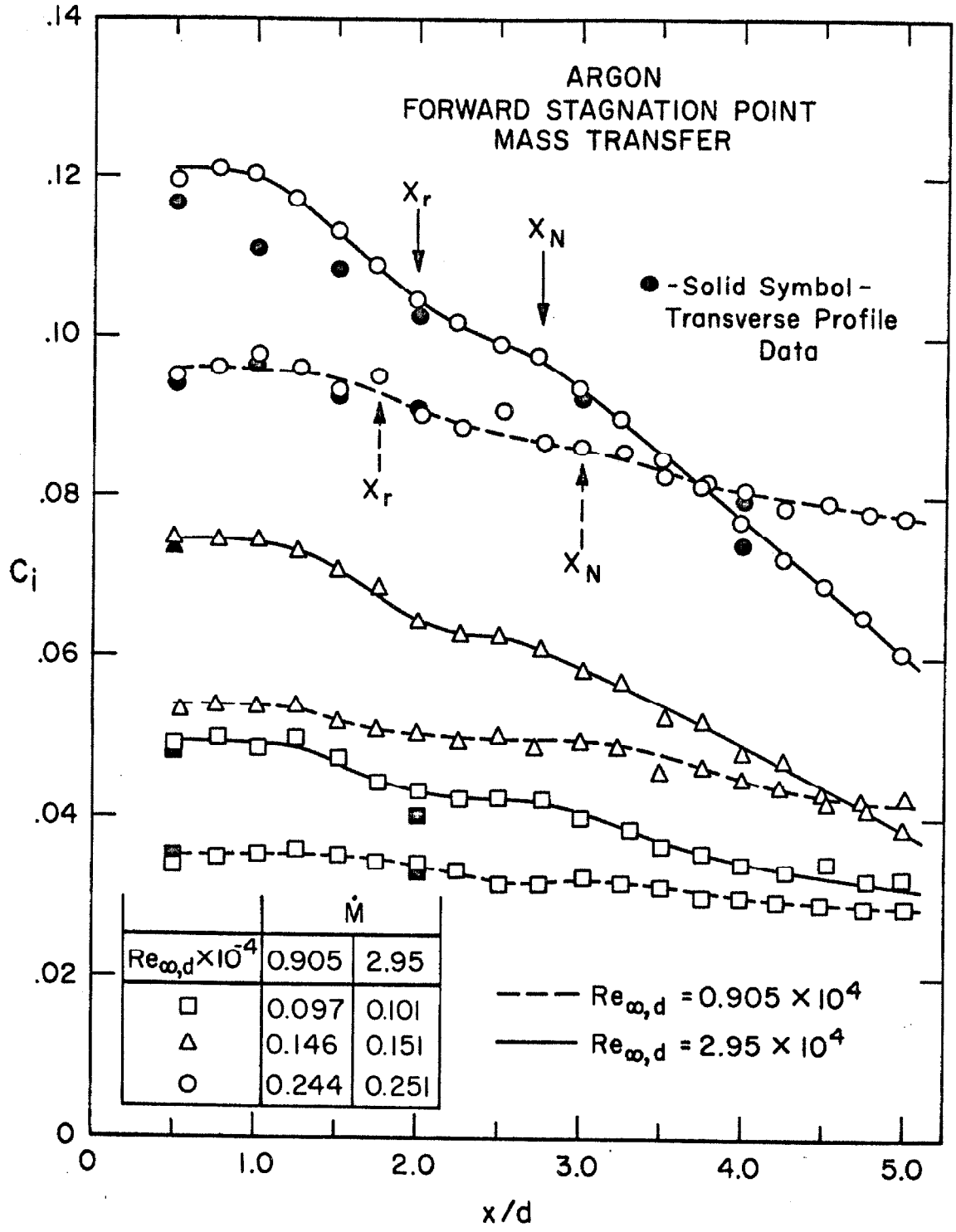

Fig. 46a NEAR-WAKE CENTERLINE MASS - CONCENTRATION PROFILES.

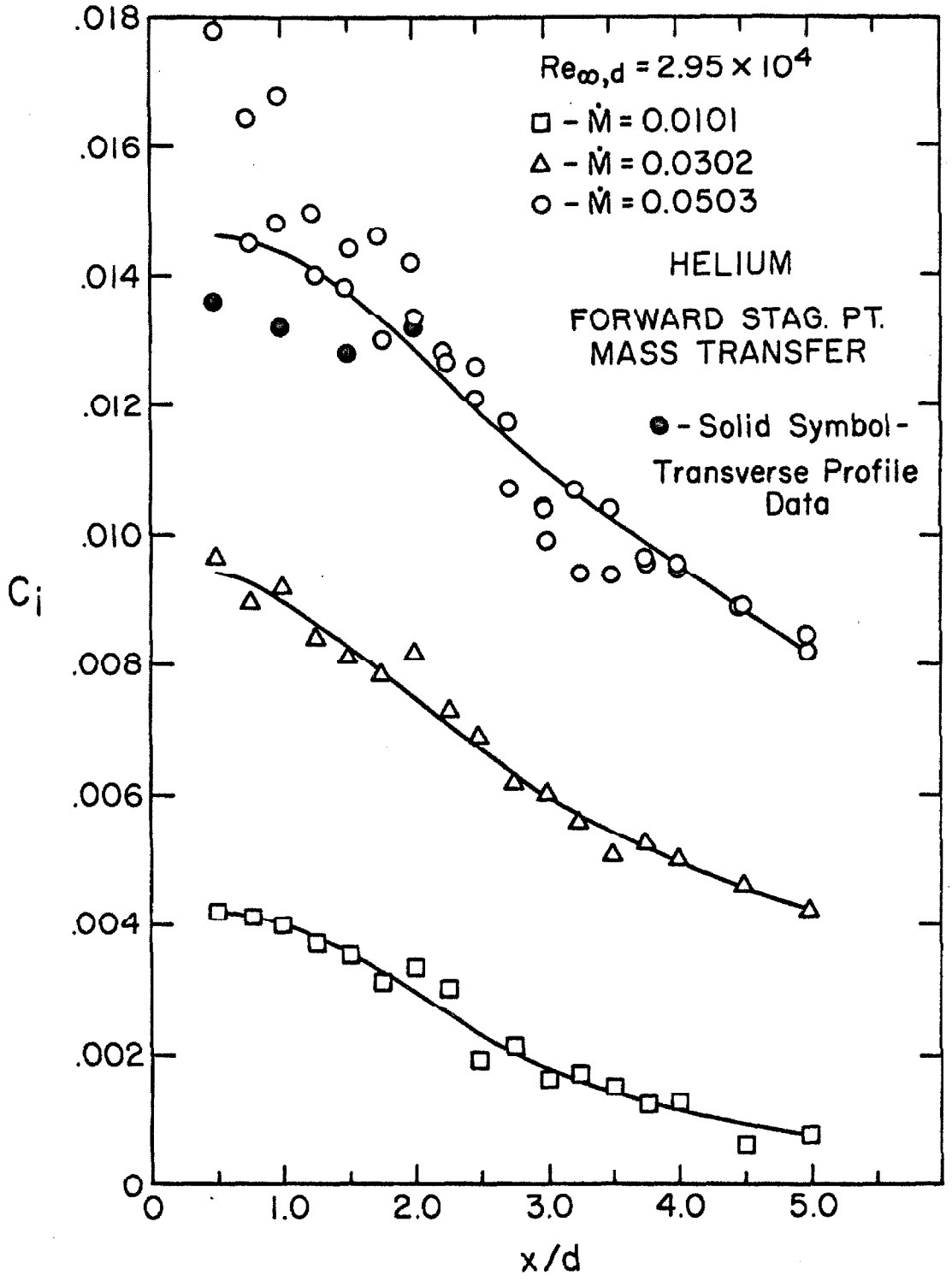

Fig. 46b NEAR-WAKE CENTERLINE MASS-CONCENTRATION PROFILES.

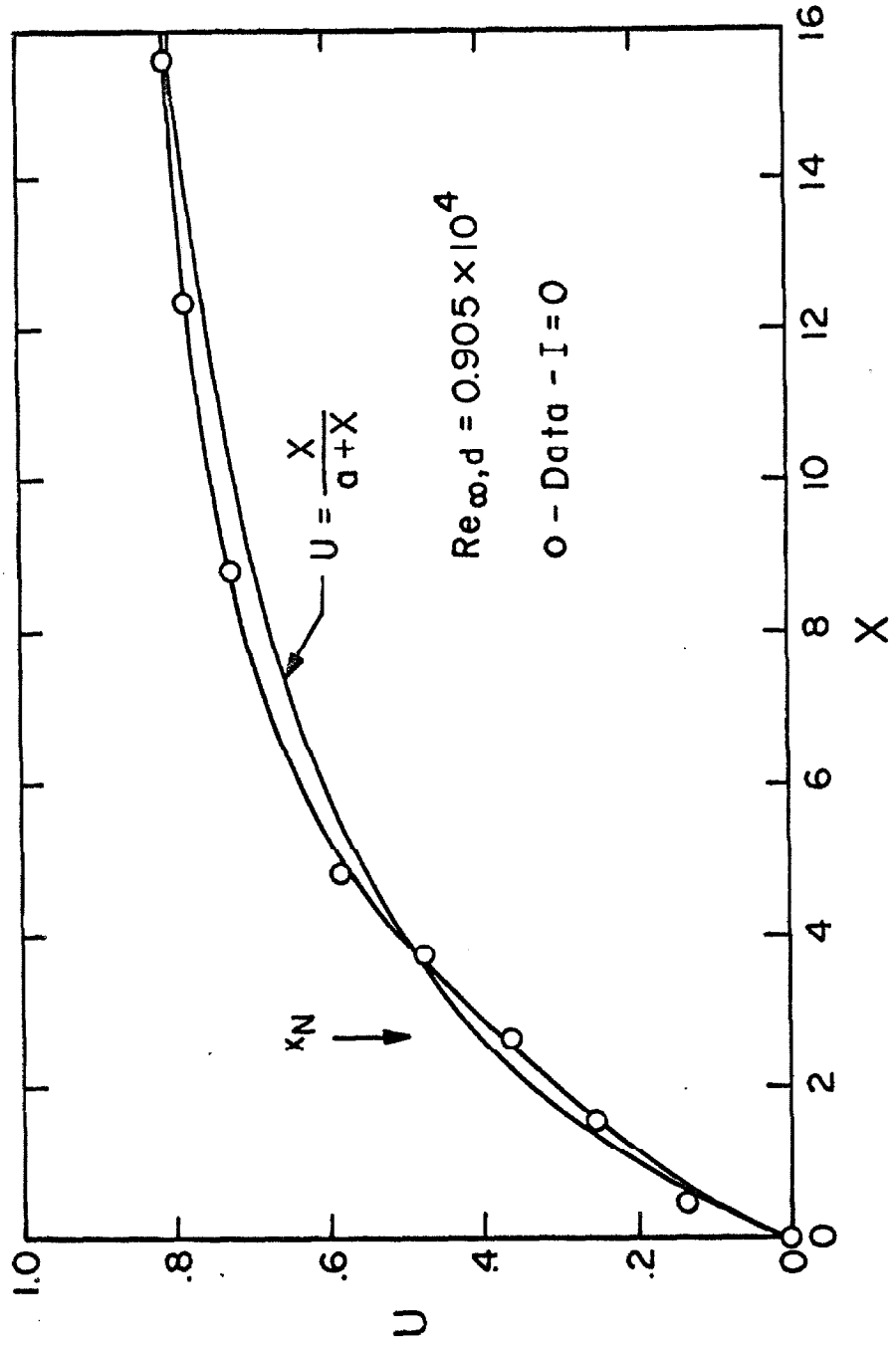

Fig. 47 AXIAL VELOCITY IN THE INTERMEDIATE WAKE

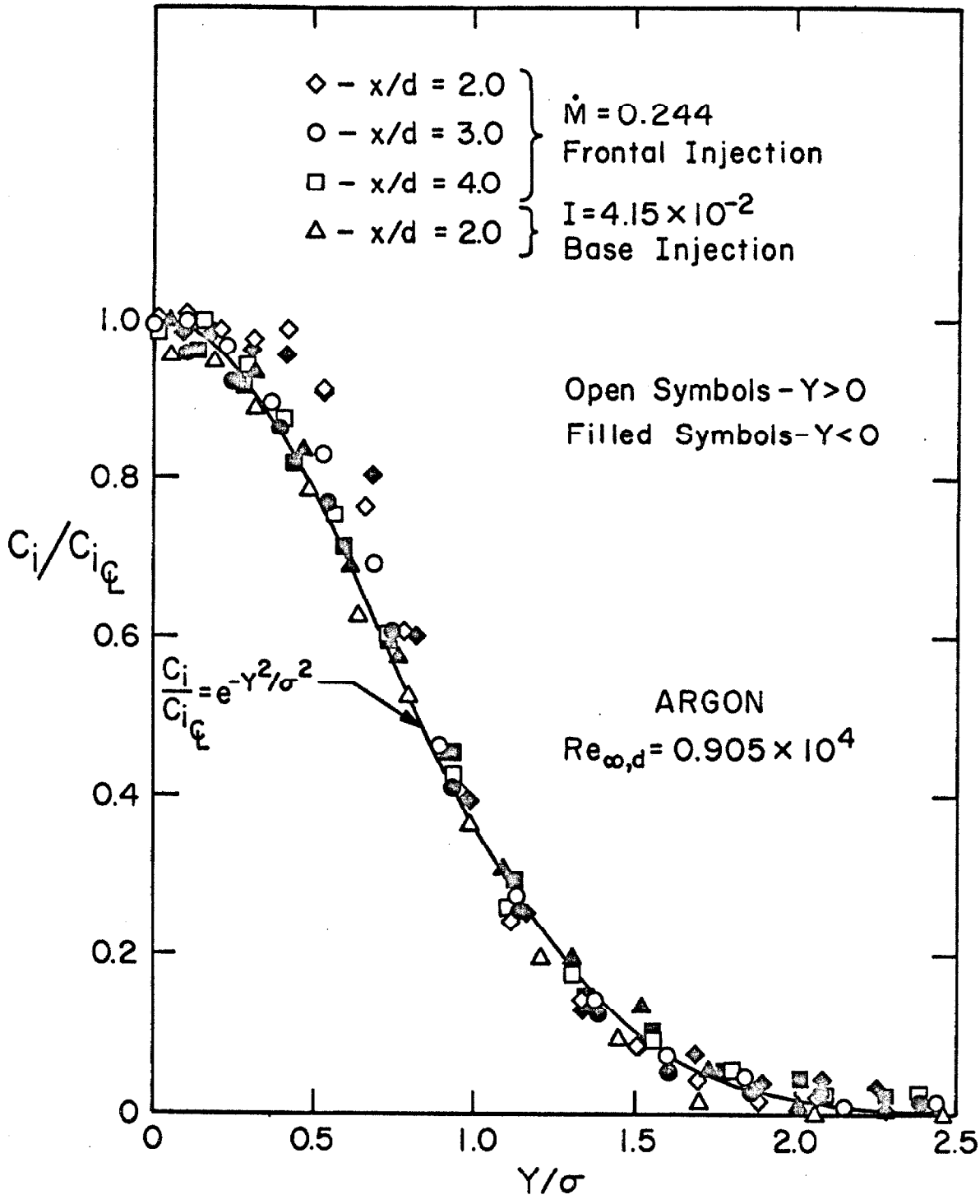

Fig. 48a MASS-CONCENTRATION DISTRIBUTION IN THE INTERMEDIATE WAKE

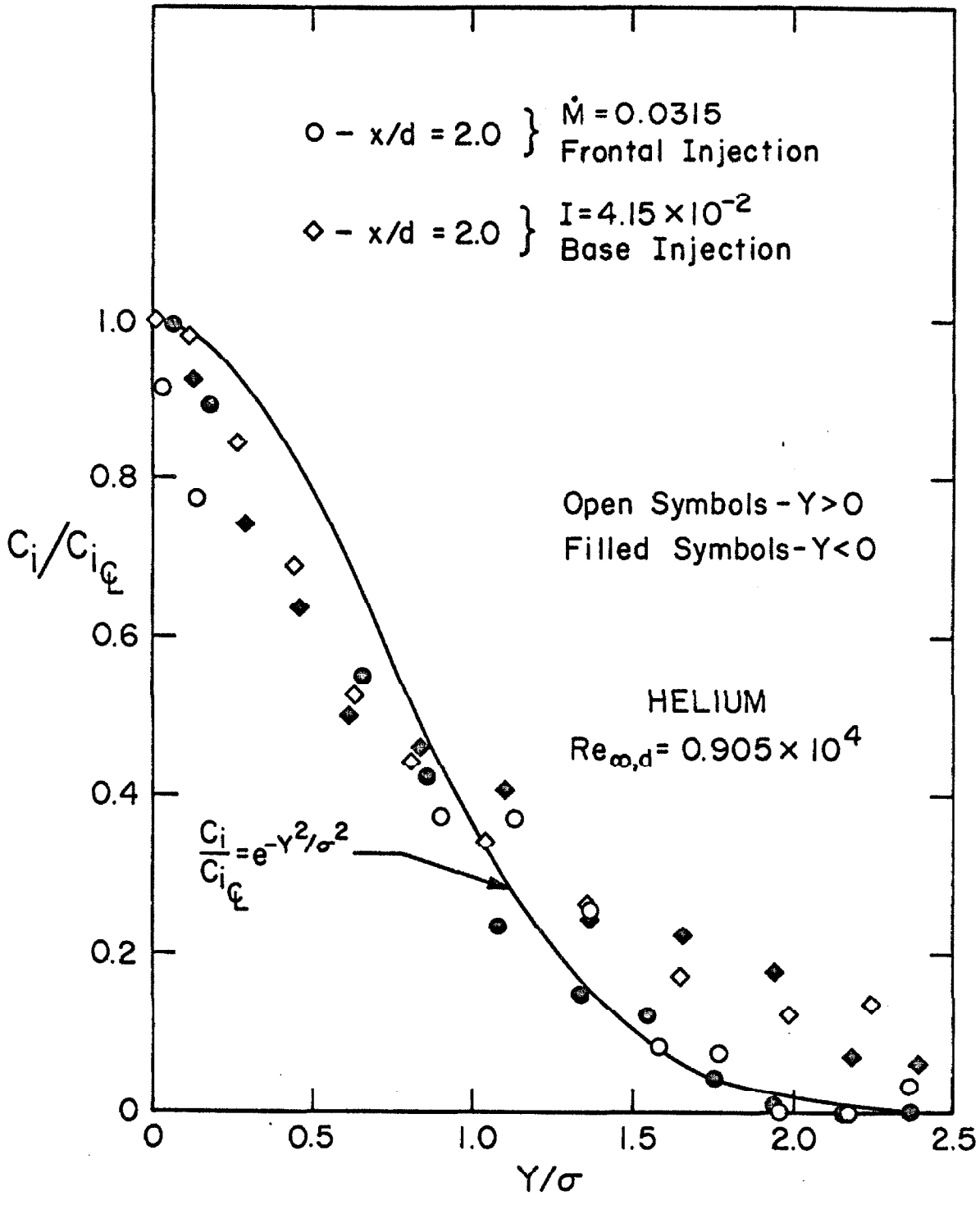

Fig. 48b MASS-CONCENTRATION DISTRIBUTION IN THE INTERMEDIATE WAKE

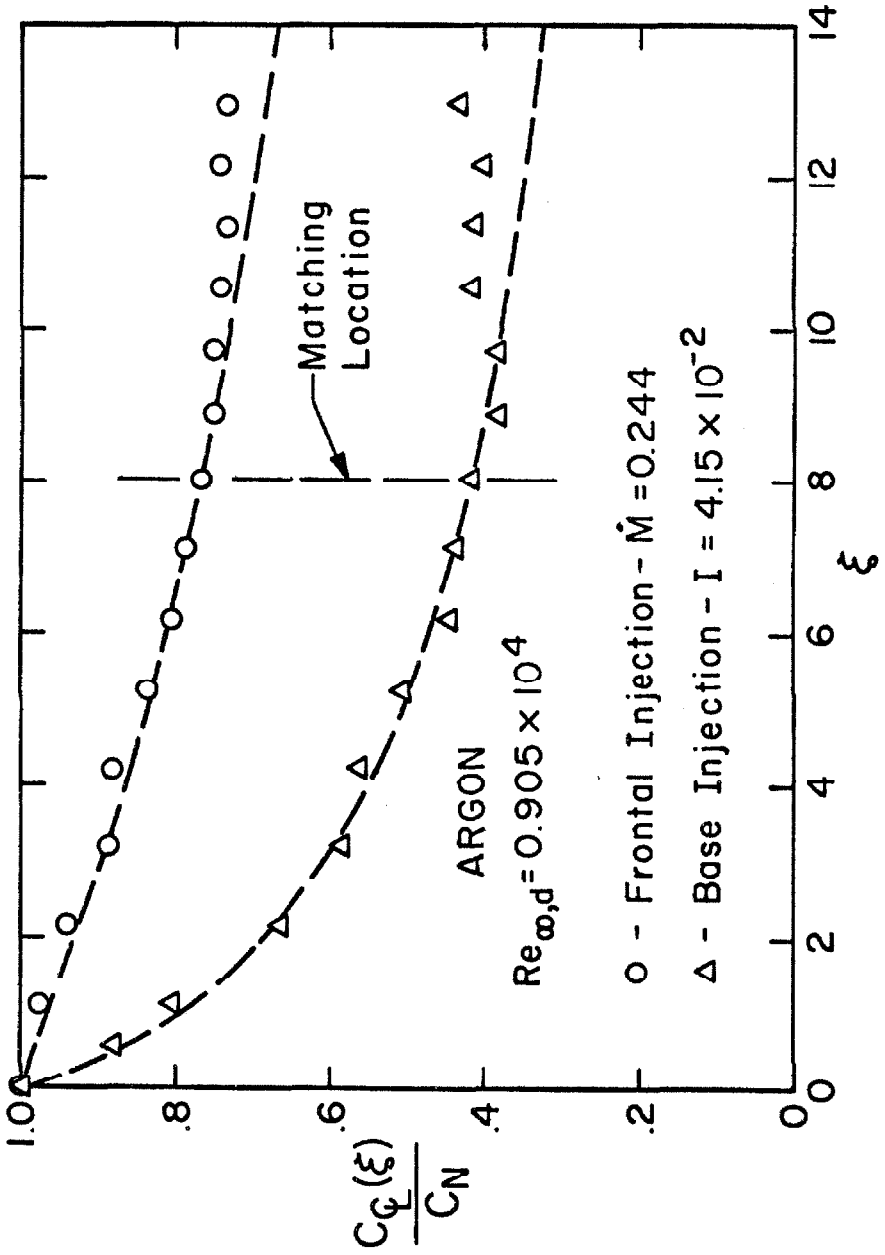

Fig. 49 CENTERLINE MASS-CONCENTRATION IN THE INTERMEDIATE WAKE

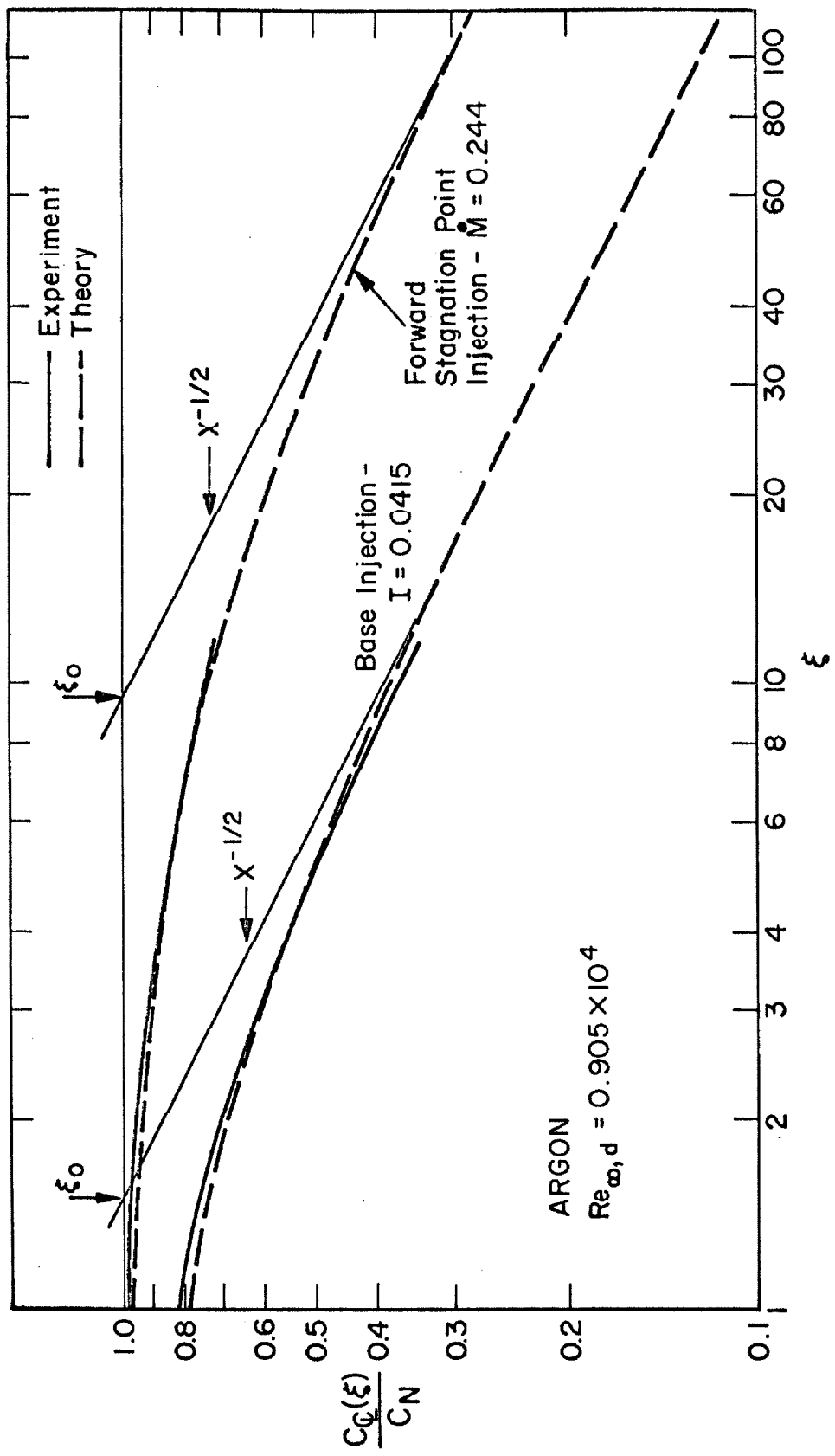

Fig. 50 CENTERLINE MASS CONCENTRATION IN THE INTERMEDIATE WAKE

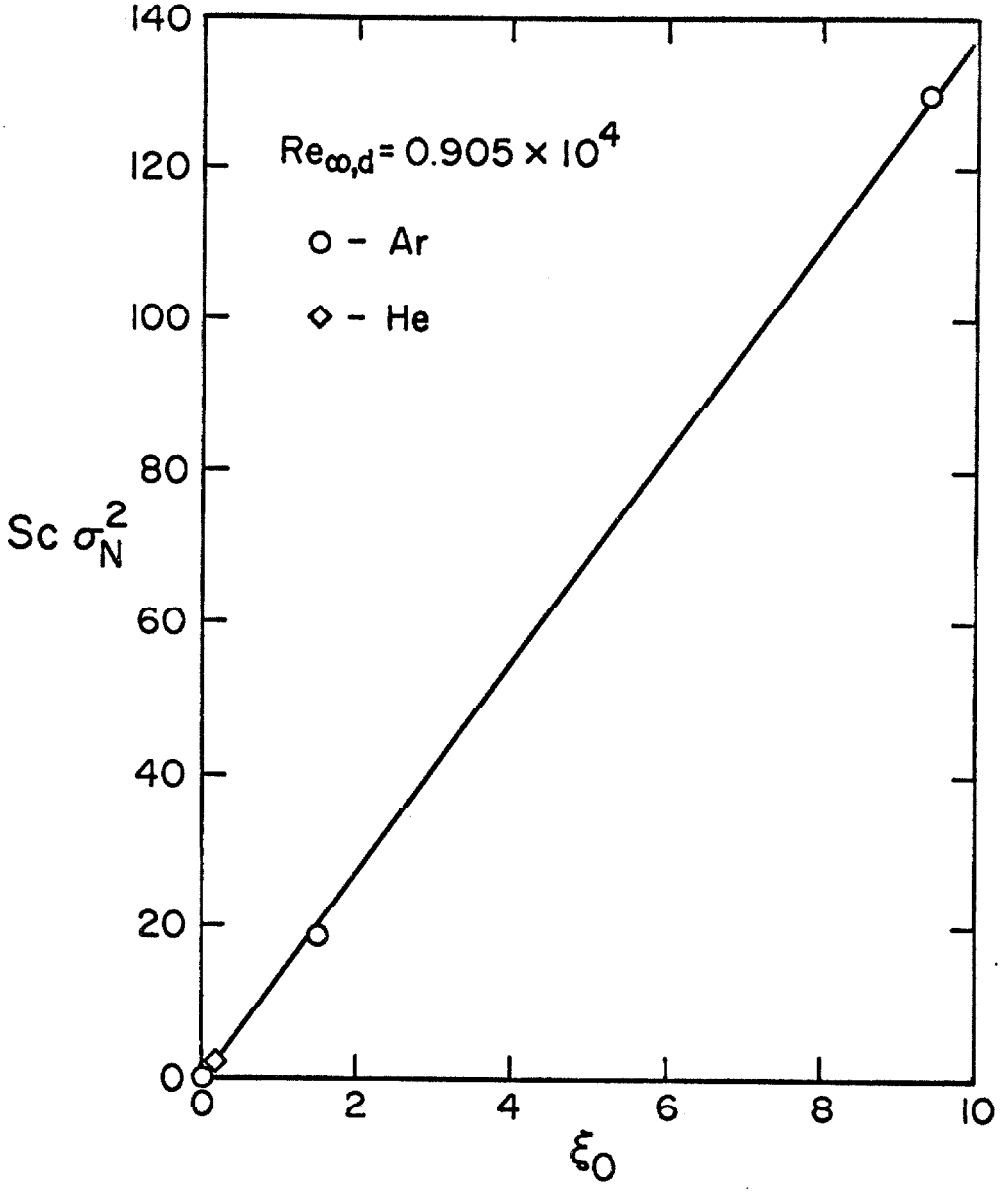

Fig. 51 VIRTUAL ORIGIN FOR THE ASYMPTOTIC FAR WAKE

APPENDIX A

HEAT TRANSFER--MASS TRANSFER ANALOGY

For the near-wake flow of a circular cylinder, an analogy exists between mass addition and heat transfer. In both cases, the problem reduces to one of the diffusion of a scalar quantity, e.g., mass, total enthalpy, within the separated flow in the near wake, and the convection of the scalar downstream into the far-wake flow. If the thermal and barotropic diffusion terms are neglected in the species conservation equation, an assumption that is particularly valid in the low Mach number near-wake flow of a circular cylinder, and if the dissipation terms are neglected in the energy equation, i.e. Pr = 1, an assumption which is certainly not justifiable in certain regions of the flow, then the species equation takes a form similar to the energy equation written in terms of $S = \frac{H-He}{He}$, the normalized total enthalpy defect parameter used by Reeves and Lees.[1] The following conditions then specify the analogy:

$$Sc \rightarrow Pr \quad ,$$

$$C_i - C_{i_e} \rightarrow S = \frac{H-H_e}{He} \quad .$$

For the general case of heat transfer for a circular cylinder in hypersonic flow, the heat transferred is a maximum at the forward stagnation point and decays rapidly as the flow progresses around the body. For the theoretical model, the boundary conditions for the transfer of heat will be idealized to $\partial T/\partial \eta \neq 0$ over the forward stagnation region, and to $\partial T/\partial \eta = 0$ over the region extending somewhat upstream of separation and downstream to the base. These assumptions

can be partially justified by the existence of the insulating base boundary layer (cf. Scott and Eckert[19]) and by an examination of the data given in Chapter IV. The mass transfer analog of this theoretical model is mass addition from the forward stagnation region, for which the transfer of mass is restricted to the forward stagnation region, and a zero mass flux boundary condition is preserved over the remainder of the cylinder. The enthalpy defect parameter S is then analogous to $C_i - C_{i_e}$, where the foreign species models the case $S_w > 0$, i.e., $C_{i_w} > 0$, $C_{i_e} = 0$; the species in the primary stream models the case $S_w < 0$, i.e., $C_{i_w} < 1$, $C_{i_e} = 1.0$. Under these conditions, the direction of species and total temperature diffusion are the same, and hence the two scalars will be analogous. The influence of molecular weight is felt through its influence on the Schmidt number, Sc. For the addition of argon in air, $Sc \approx Pr$, independent of mass concentration. For helium addition, because $Sc = Sc(C_i)$, the analogy is to a non-linear dependence $Pr = Pr(T)$ (see Appendix D).

For mass addition from the base, the analogous heat transfer boundary conditions are those of an adiabatic flow upstream of separation, with base heat transfer. However, this does not represent a physically interesting analog.

APPENDIX B

TWO-DIMENSIONALITY OF THE NEAR-WAKE FLOW

A two-dimensional near-wake flow field is characterized by the necessary, but not sufficient, condition that the static pressure is independent of the spanwise dimension. In addition, for flows with heat and mass transfer, the temperature and mass-concentration fields must also be independent of the spanwise dimension; i.e., spanwise convection and diffusion must be negligible.

The interaction of a circular cylinder with the wind tunnel sidewall boundary layer produces a complex, three-dimensional, separated flow, reported by Sykes,[36] which extends three to four diameters ahead of the cylinder and generates pressure disturbances that extend into the near-wake region by disturbing the pressure field near the wall. The interaction is manifested in the spanwise base-pressure distribution, shown in Figure (5), as a decrease in the base pressure below the free-stream static pressure in the region near the wall. The resulting spanwise convection toward the wall produces a non-uniform distribution of mass concentration in the case of mass transfer from the cylinder. However, the existence of a strong outflow isolates the central portion of the span from perturbations in pressure or mass concentration originating at the wall. This has been experimentally verified by monitoring the pressure and mass-concentration fields associated with the introduction of argon at the wall both upstream and downstream of the model station.

To prevent the outflow and its associated degradation of the mass-concentration field, crossflow fences were mounted on the models.

as illustrated in Figure (2). The results for the spanwise pressure field within the region bounded by the fences are shown in Figure (5). At the higher Reynolds number, the fences serve to create a more uniform pressure distribution, with no evidence of spanwise convection. At the lower Reynolds number, a perturbation due to the fences themselves results in an increase in the base pressure near the fence. However, the induced pressure gradient is much less severe than that existing without fences.

Figure (6) demonstrates that the spanwise mass-concentration distributions, plotted with the axial position and Reynolds number as parameters, are uniform over the central portion of the span, i. e. $|z/d| \leq 5.0$. In addition, a survey is shown which was taken with the tunnel evacuated to a pressure representative of the cylinder base pressure, but without flow in the tunnel, to demonstrate the uniformity of the porous material alone, in the absence of the primary flow. Within the central region of the span, the mass-concentration distribution in the latter case is uniform to $\pm 2\%$. Under flow conditions, however, at the same axial station ($x/d = 0.51$), the mass-concentration field is uniform to $\pm 7\%$. At an axial station $x/d = 0.75$, the mass-concentration field is nonuniform, with variations of $\pm 14\%$ A careful study of these perturbations indicates that small initial non-uniformities in the mass-concentration field are preserved and amplified with increasing axial distance from the model. This amplification phenomenon seems to be characteristic of flows with a distribution of scalar quantities, e. g. heat, mass concentration, and is thought to occur as a result of the inherently three-dimensional structure of the separated flow. In

contrast, when discrete jets occur because of imperfections in model construction, the pressure field rapidly recovers to a uniform distribution with increasing axial distance from the model.

Further downstream, near the end of the fences, the spanwise static-pressure measurements of Ramaswamy,* for x/d = 2.0, 3.0, corroborated by an oil flow pattern observed on the fences, demonstrate the existence of a convective outflow that is responsible for the overall reduction in the spanwise mass concentrations reported in Section IV.4.

From these measurements, it is concluded that, within the recirculating zone, with the use of fences, no three-dimensional effects occur which dominate the distribution of pressure or mass concentration. Certainly three-dimensional effects exist, as reported by Ginoux,[37] and others, but their effects on the spanwise distribution of scalar quantities are of second order, as demonstrated by the mass-concentration measurements. Downstream of the rear stagnation point, however, three-dimensional effects are present and influence the distribution of mass concentrations (cf. Section IV.4).

---

* Ramaswamy, M. A. - Private Communication.

APPENDIX C

MASS-FLUX CALCULATIONS

C. 1. The Mass Flux in the Cylinder Boundary Layer at Separation

The laminar boundary layer on a circular cylinder has been calculated by Klineberg[3] (see also Reeves and Lees[38]) using the assumption of local similarity and the results of measured static-pressure distributions reported by McCarthy.[7] These results will be utilized to calculate the boundary-layer mass flux at the point of separation.

From elementary considerations, the mass flux per unit span is given by:

$$\dot{m}_{B.L.} = \int_0^{\delta} \rho u \, dy \quad ,$$

$$\therefore \quad \dot{m}_{B.L.} = \tfrac{1}{2} \frac{\rho_e u_e}{\rho_\infty u_\infty} \mu_\infty \frac{Re_{\infty, d}}{\sqrt{Re_{N, d}}} \left[\frac{\delta}{r} \sqrt{Re_{N, d}} - \frac{\delta^*}{r} \sqrt{Re_{N, d}} \right] .$$

If an adiabatic, locally similar solution for the boundary layer is assumed, which is coupled to an inviscid, isentropic expansion of the outer flow from the forward stagnation point, according to the static-pressure distribution measured by McCarthy, the results of Klineberg can be utilized in the following manner.

Using the Stewartson transformation to transform the flow into the incompressible plane,

$$d\bar{Y} = \frac{\rho a_e}{\rho_N a_N} dy \quad ,$$

and defining

$$U = \frac{u}{u_e}$$

the displacement thickness becomes

$$\delta^* = \int_o^{\delta} (1 - \frac{\rho u}{\rho_e u_e}) \, dy \quad ,$$

$$\therefore \qquad \delta^* = \frac{a_N \rho_N}{a_e \rho_e} \int_o^{\delta_i} (\frac{\rho_e}{\rho} - U) \, d\bar{Y} \, .$$

If the boundary layer is considered to be of constant total temperature, then

$$\frac{\rho_e}{\rho} = \frac{T}{T_e} = 1 + \frac{(\gamma-1)}{2} M_e^2 \, [1 - (\frac{u}{u_c})^2] \, .$$

$$\therefore \; \delta^* = \frac{a_N \rho_N}{a_e \rho_e} \left\{ [1 + \frac{(\gamma-1)}{2} M_e^2] \, \delta_i^* + \frac{(\gamma-1)}{2} M_e^2 \, \theta_i \right\} \, ,$$

where

$$\delta_i^* = \int_o^{\delta_i} [1 - U] \, d\bar{Y} \, ,$$

$$\theta_i = \int_o^{\delta_i} U [1 - U] \, d\bar{Y} \, .$$

The form parameter $\aleph$ is defined as $\aleph = \theta_i / \delta_i^*$.

Then,

$$\frac{\delta^*}{r} \sqrt{Re_{N,d}} = \frac{a_N \rho_N}{a_e \rho_e} \left\{ 1 + \frac{(\gamma-1)}{2} (1+\aleph) M_e^2 \right\} \frac{\delta_i^*}{r} \sqrt{Re_{N,d}} \quad ,$$

or, following Klineberg, if the parameter δ_r^* is defined as

$$\delta_r^* = \tfrac{1}{2} Re_{N,d} \left[\frac{\delta_i^*}{r} \right]^2 \quad ,$$

$$\therefore \; \frac{\delta^*}{r} \sqrt{Re_{N,d}} = \frac{a_N \rho_N}{a_e \rho_e} \left\{ 1 + \frac{(\gamma-1)}{2} (1+\aleph) M_e^2 \right\} (2 \delta_r^*)^{\frac{1}{2}} \quad .$$

Klineberg has assumed that for $s/r > 1.20$, the form parameter of the boundary layer ($\aleph$) is constant, i.e., that the boundary-layer profile is unchanged in shape, but continues to grow parabolically with

increasing Reynolds number. Using Klineberg's results, in the vicinity of separation the mass flux in the boundary layer increases $\approx 1\%$/degree of expansion around the cylinder. The separation point on the cylinder, in the absence of mass addition, occurs at $\theta_s = 125°$ for $Re_{\infty, d} = 3 \times 10^4$ and $\theta_s = 132°$ for $Re_{\infty, d} = 0.9 \times 10^4$. An arbitrary location, $\theta = 122.5°$ ($s/r = 2.136$), was chosen for the calculation of the boundary-layer mass flux upstream of separation.

Under the above conditions, from the results of Klineberg,

$$M_e = 3.307 \ ,$$

$$\frac{\delta}{r}\sqrt{Re_{N, d}} = 15.413 \ ,$$

$$\frac{\delta^*}{r}\sqrt{Re_{N, d}} = 8.551 \ .$$

Using the assumption that the external flow is obtained by an inviscid, isentropic expansion from the condition behind a normal shock at M_∞, the boundary-layer mass flux can be rewritten as:

$$\dot{m}_{B.L.} = \tfrac{1}{2}\frac{M_e}{M_\infty}\left[\frac{1+\frac{(\gamma-1)}{2}M_\infty^2}{1+\frac{(\gamma-1)}{2}M_e^2}\right]^{\frac{\gamma+1}{2(\gamma-1)}} \frac{P_{o_e}}{P_o}\,\mu_\infty \frac{Re_{\infty, d}}{\sqrt{Re_{N, d}}} \cdot \left[\frac{\delta}{r}\sqrt{Re_{N, d}} - \frac{\delta^*}{r}\sqrt{Re_{N, d}}\right] ,$$

where, from the above assumptions,

$$Re_{N, d} = \frac{1}{6} Re_{\infty, d} \ ,$$

$$\frac{P_{o_e}}{P_o} = \left.\frac{P_{o_e}}{P_o}\right|_{M_\infty} .$$

Using the appropriate values of the free-stream constants obtained from Table 1, the results of the boundary-layer mass flux calculation are indicated in Table C-1, where $\dot{m}_{B.L.}$ is the mass flux per unit span in the cylinder boundary layer.

C. 2. Intercepted Free-Stream Mass Flux

A second parameter used for comparison of the data is the free-stream mass flux per unit span intercepted by the cross-sectional area of the model

$$\dot{m}_f = \rho_\infty u_\infty d$$

$$\therefore \dot{m}_f = d \frac{P_\infty}{P_o} M_\infty P_o \left[\frac{\gamma}{R T_o}\right]^{\frac{1}{2}} \left[\frac{T_o}{T_\infty}\right]^{\frac{1}{2}} .$$

Again, using the appropriate values of the free-stream constants obtained from Table 1, the results are indicated in Table C-1.

TABLE C-1

P_o	25 (psia)	80 (psia)
$Re_{\infty, d}$	0.905×10^4	2.953×10^4
$\dot{m}_{B.L.}$ ($\frac{\#}{in\text{-}sec}$)	4.28×10^{-5}	7.56×10^{-5}
$\dot{m}_f$ ($\frac{\#}{in\text{-}sec}$)	1.737×10^{-3}	5.510×10^{-3}

Mass-Flux Parameters for the Circular Cylinder as a Function of Reynolds Number.

APPENDIX D

DEPENDENCE OF THE FLOW FIELD ON MASS CONCENTRATION

The assumption of small mass concentrations, i.e., that the thermodynamic properties of the gas correspond to those of air, has been used in the flow field calculations in the near wake. The validity of this assumption must be examined for the molecular weights of interest.

For a binary mixture (cf. Baron[39]), the gas constant R and the specific heat C_p take particularly simple forms,

$$R = R_1 + (R_i - R_1)\, C_i \quad ,$$

i.e.,

$$R = R_1 \left[1 + \frac{m_1 - m_i}{m_i} C_i \right] ,$$

and

$$C_p = C_{p_1} + (C_{p_i} - C_{p_1}) C_i \quad .$$

The specific heat ratio γ, however, takes a non-linear form,

$$\gamma = \frac{\gamma_1 \left[C_{p_1} + (C_{p_i} - C_{p_1}) C_i \right]}{\left[C_{p_1} + \left(C_{p_i} \frac{\gamma_1}{\gamma_i} - C_{p_1} \right) C_i \right]} \quad ,$$

and is plotted in Figure (D-1) as a function of mass concentration for helium and argon in air.

The dynamic viscosity μ can be taken to be independent of mass concentration for small concentrations, but is otherwise given by the Chapman-Enskog formulation. The Schmidt number, $Sc = \nu/D$ is then dependent on both mass concentration and molecular weight (cf. Chapman and Cowling[40]). To illustrate the behavior, the Schmidt number for binary mixtures of argon, nitrogen and helium with air are shown

in Figure (D-1) as a function of the mass concentration C_i at 273° K. The Schmidt number depends on temperature as $S_c \sim T^{\frac{1}{4}}$.

The conclusion is that for argon and nitrogen addition, the assumption of constant properties is reasonable. However, for helium $\frac{d\gamma}{dC_i}$ and $\frac{\partial S_c}{\partial C_i}$ are large for $C_i \to 0$ (see Figure (D-1)) and the assumption of constant properties must be reevaluated. This assumption is justified only by virtue of the fact that for a comparable value of I, the mass concentrations for helium are much less than those for argon, as discussed in Chapter IV.

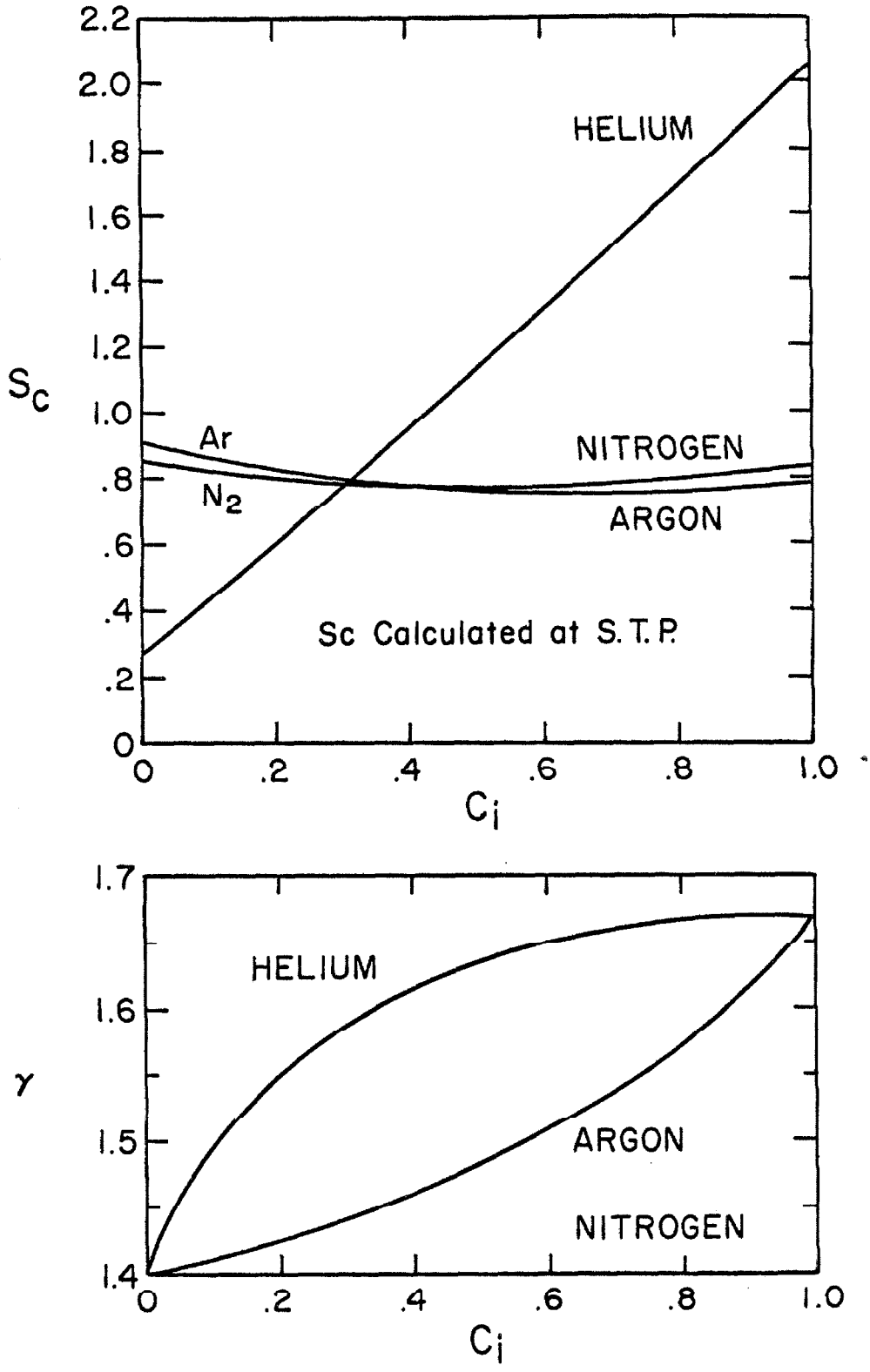

Fig.D-1 THERMODYNAMIC COEFFICIENTS FOR BINARY MIXTURES WITH AIR.

REFERENCES

1. Reeves, B. L. and Lees, L.: "Theory of Laminar Near Wake of Blunt Bodies in Hypersonic Flow," AIAA J., 3, No. 11, 2061 (Nov., 1965).

2. Grange, J.-M., Klineberg, J. M. and Lees, L.: "Laminar Boundary-Layer Separation and Near-Wake Flow for a Smooth Blunt Body at Supersonic and Hypersonic Speeds," AIAA J., 5, No. 6, 1089 (June, 1967).

3. Klineberg, J. M.: "Theory of Laminar Viscous-Inviscid Interactions in Supersonic Flow," Ph. D. Thesis, California Institute of Technology, Pasadena, Calif. (1968).

4. Crocco, L. and Lees, L.: "A Mixing Theory for the Interaction between Dissipative Flows and Nearly Isentropic Streams," J. A. S., 19, No. 10, 649 (Oct., 1952).

5. Kubota, T.: "Laminar Wake with Streamwise Pressure Gradient," GALCIT Hypersonic Research Project, Internal Memorandum No. 9 (May, 1962).

6. Gold, H.: "Laminar Wake with Arbitrary Initial Profiles," AIAA J., 2, No. 5, 948 (May, 1964).

7. McCarthy, J. F., Jr.: "Hypersonic Wakes," GALCIT Hypersonic Research Project, Memorandum No. 67 (July, 1962).

8. Dewey, C. F., Jr.: "Measurements in Highly Dissipative Regions of Hypersonic Flows. Part II. The Near Wake of a Blunt Body at Hypersonic Speeds," Ph. D. Thesis, California Institute of Technology, Pasadena, California (1963).

9. Behrens, W.: "Flow Field and Stability of the Far Wake behind Cylinders at Hypersonic Speeds," Ph. D. Thesis, California Institute of Technology, Pasadena, California (1966).

   Also, Behrens, W.: "The Far Wake behind Cylinders at Hypersonic Speeds. Part I: Flowfield," AIAA J., 5, No. 12, 2135 (Dec., 1967).

10. Mohlenhoff, W.: "Experimental Study of Helium Diffusion in the Wake of a Circular Cylinder at M = 5.8," GALCIT Hypersonic Research Project, Memorandum No. 54 (May, 1960).

11. Kingsland, L.: "Experimental Study of Helium and Argon Diffusion in the Wake of a Circular Cylinder at M = 5.8," GALCIT Hypersonic Research Project, Memorandum No. 60 (June, 1961).

REFERENCES (Continued)

12. Herzog, R. T.: "Nitrogen Injection into the Base Region of a Hypersonic Body," GALCIT Hypersonic Research Project, Memorandum No. 71 (August, 1964).

13. Ginoux, J. J.: "Effects of Gas Injection in Separated Supersonic Flows," TCEA TN-7 (February, 1962), Von Kármán Institute, Rhode-Saint-Genese, Belgium.

14. Chapkis, R. L.: Fox, J., Hromas, L. and Lees, L.: "An Experimental Investigation of Base Mass Injection in the Laminar Wake behind a 6-Degree Half-Angle Wedge at M = 4.0," AGARD Conference Proceedings No. 19, Fluid Physics of Hypersonic Wakes, Vol. I (May, 1967).

15. Korst, H. H., Page, R. H. and Childs, M. E.: "A Theory for Base Pressures in Transonic and Supersonic Flow," University of Illinois, Engineering Experiment Station, M. E. Technical Note - 392-2 (March, 1955).

16. Chapman, D. R.: "Theoretical Analysis of Heat Transfer in Separated Flows," NACA TN-3792 (1956).

17. Chapman, D. R.: Kuehn, D. M. and Larson, H. K.: "Investigation of Separated Flows in Supersonic and Subsonic Streams with Emphasis on the Effects of Transition," NACA TN-1356 (1958).

18. Chow, R. R.: "On the Separation Phenomena of Binary Gas Mixture in an Axisymmetric Jet," U. C. Berkeley, TR-HE 150-175, (1959).

19. Scott, C. J. and Eckert, E. R. G.: "Heat and Mass Exchange in the Supersonic Base Region," AGARD Conference Proceedings #4, Separated Flows. Part I, 429 (May, 1966).

20. Batt, R. G.: "Experimental Investigation of Wakes behind Two-Dimensional Slender Bodies at M = 6," Ph. D. Thesis, California Institute of Technology, Pasadena, California (1967).

21. Sherman, F. S.: "New Experiments on Impact-Pressure Interpretation in Supersonic and Subsonic Rarefied Air Streams," NACA TN 2995 (Sept., 1953).

22. Behrens, W.: "Viscous Interaction Effects on a Static Pressure Probe at M = 6," AIAA J., 1, No. 12, 2864 (Dec., 1963).

23. Masson, B. S.: "Diffusive Separation of a Gas Mixture Approaching a Sampling Probe," U. C. Berkeley, TR-HE-150-206 (1962).

REFERENCES (Continued)

24. Reis, V. H. and Fenn, J. B.: "Separation of Gas Mixtures in Supersonic Jets," J. Chem. Phys., 39, No. 12, 3240 (Dec., 1963).

25. Coles, D. E.: "Measurements in the Boundary Layer on a Smooth Flat Plate in Supersonic Flow," Ph. D. Thesis, California Institute of Technology, Pasadena, Calif. (1953).

26. Chapman, D. R.: "Laminar Mixing of a Compressible Fluid," NACA TN 1800 (Feb., 1949) or NACA Rep. 958 (1950).

27. Townend, L. H.: "Some Effects of Stable Combustion in Wakes Formed in a Supersonic Stream," R. A. E. Tech. Note, No. Aero. 2872 (March, 1963).

28. Kendall, J. M., Jr.: "Experimental Investigation of Leading Edge Shock Wave-Boundary Layer Interaction at Hypersonic Speeds," GALCIT Hypersonic Research Project, Memorandum No. 30 (January, 1956).

29. Behrens, W.: "Far Wake behind Cylinders at Hypersonic Speeds: Part II. Stability," AIAA J., 6, No. 2, 225 (February, 1968).

30. Hayday, A. A.: "Mass Transfer cooling in a Laminar Boundary Layer in Steady Two-Dimensional Stagnation Flow," University of Minnesota TN-19 (April, 1958).

31. Hama, F. R.: "Experimental Studies on the Lip Shock," AIAA J., 6, No. 12, 212 (February, 1968).

32. Lewis, J. E. and Behrens, W.: "Fluctuation Measurements in the Near Wake of a Slender Wedge at Mach 4. 0 With and Without Base Injection," AIAA Paper No. 68-100 (January, 1968).

33. Lewis, J. E. and Chapkis, R. L.: "Experimental Investigation of the Effect of Base Injection on the Turbulent Near Wake of a Slender Body at Mach 4. 0," T. R. W. Systems Preprint (1968).

34. Chow, W. L.: "On the Base Pressure Resulting from the Interaction of a Supersonic External Stream with a Sonic or Supersonic Jet," J. A. S., 26, No. 3, 176 (March, 1959).

35. Fuller, L. and Reid, J.: "Experiments on Two-Dimensional Base Flow at M = 2. 4," A. R. C. -R & M #3064 (British), (1958).

36. Sykes, D. M.: "The Supersonic and Low-Speed Flows Past Circular Cylinders of Finite Length Supported at One End," J. F. M. 12, Part 3, 267 (1962).